

**WHAT DROVE MONGOLIAN MESOZOIC VOLCANISM: WAS IT
CRUSTAL OR MANTLE PROCESSES?**

Thesis submitted for the degree of
Doctor of Philosophy
At the University of Leicester

Thomas Chay Sheldrick
Department of Geology
University of Leicester
August 2018

WHAT DROVE MONGOLIAN MESOZOIC VOLCANISM: WAS IT CRUSTAL
OR MANTLE PROCESSES?

Thomas Sheldrick

Mesozoic intraplate volcanism occurred over a wide region of East Asia. Although there are a variety of hypotheses to explain the volcanism, the lack of studies on the Mesozoic volcanism from Mongolia has hindered the ability to test these hypotheses. Furthermore, the existence of the Palaeozoic and Mesozoic Mongol-Okhotsk Ocean is evident from the Mongol-Okhotsk suture, which stretches from central Mongolia to the Sea of Okhotsk. Insufficient palaeomagnetic data has led to difficulties in reconstructing the history, geometry and closure of this ocean. However, this ocean closure may have implications for Mesozoic magmatic/metasomatism processes.

Samples were collected from traverses parallel and perpendicular to, the Mongol-Okhotsk suture. Newly discovered low-silica adakite-like (LSA) and high-silica adakite (HSA) samples from eastern and south-central Mongolia, on the southern side of the Mongol-Okhotsk suture, are used to investigate the possibility of a southward-subducting Mongol-Okhotsk oceanic slab. The LSA are interpreted as being derived from a lithospheric mantle wedge that has undergone metasomatism by slab melts. This mantle was likely metasomatised by a southward-subducting Mongol-Okhotsk slab associated with the closure of the Mongol-Okhotsk Ocean. Two alternative models are proposed to explain the petrogenesis of the HSA samples: (1) a southward-subducting Mongol-Okhotsk slab underwent partial melting during the closure of the Mongol-Okhotsk Ocean and assimilated minor mantle and crustal material; or (2) basaltic underplating of a thickened (>50 km; >1.5 GPa), eclogite lower crust, foundered into the underlying mantle, assimilated minor mantle material and finally underwent crustal contamination.

Mongolian basaltic samples >107 Ma have geochemical signatures consistent with a metasomatised subcontinental lithospheric mantle source. However, the geochemistry also indicates increasing asthenospheric input throughout the Mesozoic (~220-107 Ma), with enough lithosphere being stripped away by 107 Ma for asthenospheric mantle derived magmatism to predominate.

An extensive comparative study, using geochemical data from the literature, on volcanic samples from Russia, Mongolia, the North China Craton and Korea is combined with this new data. The North China Craton magmatism also has a geochemical signature consistent with increasing asthenospheric input throughout the Mesozoic. Both Mongolia and the North China Craton switch to asthenospheric magmatism at ~107 Ma; this might reflect a largescale process for Late Mesozoic magmatism in East Asia.

Acknowledgements

Embarking on this PhD part-time, whilst working full-time, has been a long, but overall enjoyable (bittersweet) endeavour. This acknowledgement section is far from exhaustive, nevertheless, I attempt to briefly thank the people that have helped me directly, or indirectly.

Firstly, thanks to my supervisor, Tiffany Barry, who has remained very enthusiastic and has always made time to discuss and debate different aspects of this project. I was lucky to have got such an enthusiastic supervisor who just enjoys discussing science. These few lines don't give her the credit she deserves.

Thanks to my family for always encouraging me to follow my ambitions; It would be difficult, if not impossible, to overpraise them.

Thanks to Batulzii Dash for field assistance (and some accommodation). Thanks also to Ade Band, Sophie Nicholson, Annika Szameitat, Michael Morton, Gregor Hahn, Jordan Bestwick, Martha Papadopoulou, Dan Smith, Tom Harvey, Sarah Lee, Andy Saunders, Douwe van Hinsbergen, Pamela Kempton, Tom "Gibbon" and Callum Ewan. Similarly, appreciations to the various technical staff that have assisted me. Thanks also to my offshore colleagues on the metal prison: Stephen Nwabuzor, Murray Crone, Andy McKenzie, Trevor Philips, Robert Starling and Adrian Denham.

PROJECT OVERVIEW

Intraplate magmatism, by its very definition, offers an opportunity to study magmatic processes far from subduction zones and constructive margins. Mantle plumes have been the favoured explanation for many areas of intraplate magmatism (e.g., Schilling, 1973; Hauri, 1996; Yarmolyuk and Kovalenko, 2001), although the mantle plume theory has also been challenged (e.g., Foulger, 2011). Other models such as slab break-off (e.g., Davies et al., 1995; Meng, 2003), lithospheric delamination (e.g., Bird, 1978; Dash et al., 2015), convective removal (e.g., Hawkesworth et al., 1995) and decompression melting away from constructive margins (e.g., Raddick et al., 2002) have been amongst the common alternatives to mantle plumes. Unsurprisingly, due to the complexity of different geological processes, the causes of intraplate magmatism are hotly debated (e.g., Yarmolyuk and Kovalenko, 2001; Barry et al., 2003; Meng, 2003; Foulger, 2011; Hunt et al., 2012; Dash et al., 2015; Sheldrick et al., 2018). Understanding geological processes behind intraplate magmatism not only presents important questions for petrogenesis, but also for other areas of geoscience including mineral exploration (e.g., Tran et al., 2016 and references therein), Earth climate (e.g., Saunders et al., 2009) and tectonics (e.g., Bars et al., 2018).

Mesozoic to Cenozoic intraplate magmatism in Eastern Asia stretches from the Great Xing'an Mountains in northeast China to the far-east of Russia (e.g., Yarmolyuk and Kovalenko, 2001; Badarch et al., 2002; Fan et al., 2003; Meng, 2003 and Wang et al., 2006), largely within a Neoproterozoic to Mesozoic orogen known as the Central Asian Orogenic Belt (e.g., Windley et al., 2007; Xiao et al., 2015 and references therein). This widespread, low-volume magmatism is located within the east Asian continental interior and erupted far away from continental margins; its cause remains enigmatic (e.g., Yarmolyuk and Kovalenko, 2001; Meng, 2003; Windley et al., 2010; Dash et al., 2015). Such long-lived volcanism is perhaps the best opportunity to understand the natural processes behind intraplate magmatism and its auxiliary effects (e.g., metasomatism processes, lithospheric destruction and replacement, mineral genesis).

This study utilises a combination of geochemical and petrological data: major- and trace-element data, Sr-Nd-Pb-Hf isotopes and $^{40}\text{Ar}/^{39}\text{Ar}$ radiometric dating to investigate what caused Mongolian Mesozoic volcanism and by inference, what caused volcanism across the Central Asian Orogenic Belt. This thesis is separated into four main chapters:

Chapter 1 – An introduction to the Central Asian Orogenic Belt: regional tectonics and magmatism (a brief literature review).

Chapter 2 – Constraining lithospheric removal and asthenospheric input to melts in Central Asia: A geochemical study of Triassic to Cretaceous magmatic rocks in the Gobi Altai (Mongolia).

Chapter 3 – Evidence for southward subduction of the Mongol-Okhotsk oceanic plate: implications from Mesozoic adakitic lavas from Mongolia.

Chapter 4 – Evaluating the wider scale context of magmatism across East Asia: a regional comparison with data from Russia, Mongolia, The North China Craton and Korea.

Table of Contents

CHAPTER 1

AN INTRODUCTION TO THE CENTRAL ASIAN OROGENIC BELT: REGIONAL TECTONICS AND MAGMATISM.

1. PROJECT AMBITIONS	1-3
REGIONAL TECTONICS	
1.1 An overview of Mongolia and the Central Asian Orogenic Belt	3-8
1.2 The Mongol-Okhotsk Ocean and Suture	8-11
1.2.1 The Mongol-Okhotsk slab and seismic tomography	11-13
1.3 The Palaeo-Pacific (Izanagi) plate	13-15
1.4 The Solonker Suture	15
1.5 REGIONAL MAGMATISM	
1.5.1 Triassic magmatism	15-17
1.5.2 Jurassic magmatism	18-19
1.5.3 Cretaceous magmatism	19-23
1.5.4 Cenozoic magmatism	23-27
1.6 MESOZOIC MAGMATIC MODELS	
1.6.1 Slab roll-back and asthenospheric upwelling	27-28
1.6.2 Convective mantle lithosphere removal	29
1.6.3 Slab break-off in the Mongol-Okhotsk region	30
1.6.4 Bi-directional delamination	30
1.6.5 Sinking of subducted oceanic slabs	31
1.6.6 Mongol-Okhtosk slab window	32
1.6.7 Mantle plume	32-33
1.7 SUMMARY	33-34

CHAPTER 2

CONSTRAINING LITHOSPHERIC REMOVAL AND ASTHENOSPHERIC INPUT TO MELTS IN CENTRAL ASIA: A GEOCHEMICAL STUDY OF TRIASSIC TO CRETACEOUS MAGMATIC ROCKS IN THE GOBI ALTAI (MONGOLIA)

Chapter abstract	35
2. INTRODUCTION AND GEOLOGICAL BACKGROUND	36-38
2.1 PETROGRAPHY	38-46
2.2 GEOCHEMISTRY OF THE GOBI LAVAS AND INTRUSIVES	

2.2.1 Major-element variations	46-48
2.2.2 Trace-element and REE variations	48-52
2.3 FRACTIONAL CRYSTALLISATION	52-56
2.4 ISOTOPE VARIATIONS & CRUSTAL CONTAMINATION	57-61
2.5 SOURCE & MELTING CONDITIONS	
2.5.1 A changing source	61-69
2.5.2 Peridotite vs. pyroxenite source: geochemical indicators	69-73
2.5.3 Mixing between lithospheric and asthenospheric mantle melts	73-75
2.6 DISCUSSION	75-80
2.7 SUMMARY	80

CHAPTER 3

EVIDENCE FOR SOUTHWARD SUBDUCTION OF THE MONGOL-OKHOTSK OCEANIC PLATE: IMPLICATIONS FROM MESOZOIC ADAKITIC LAVAS FROM MONGOLIA

Chapter abstract	81
3. ADAKITE PETROGENESIS	
3.1.1 What is an adakite?	82-83
3.1.2 Adakitic melts	79-80
3.1.3 Melting models for adakite petrogenesis	83-84
3.1.4 Mongolian and Chinese rocks with adakite geochemistry	85-89
3.2 GEOLOGICAL SETTING	89-90
3.3 PETROLOGY	
3.3.1 Petrological observations	91-94
3.3.2 Probe analysis	95-100
3.4 ARGON DATING	100-101
3.5 GEOCHEMICAL RESULTS	
3.5.1 Rock classification and major-element variations	101-106
3.5.2 Trace-element and REE variations	106-110
3.5.3 Comparative summary	110
3.6 FRACTIONAL CRYSTALLISATION	110-112
3.7 MAJOR-ELEMENT, TRACE-ELEMENT AND REE COMPARISONS	
3.7.1 Mg# numbers and their significance	113-115

3.7.2 Na ₂ O abundances in slab and lower crust melts: melt reactions within the mantle	115-117
3.7.3 Th/U and K ₂ O/Na ₂ O ratios	117-119
3.7.4 Cr and Ni abundances	119-121
3.7.5 Nb/Ta and Zr/Hf ratios	
3.7.5.1 Nb/Ta ratios	121-123
3.7.5.2 Zr/Hf ratios	123-124
3.7.6 Major-element comparisons with high-pressure basalt partial melts	124-127
3.7.7 Summary	128
3.8 ISOTOPE VARIATIONS AND CRUSTAL INPUT	128-133
3.9 DISCUSSION	133-136

CHAPTER 4

EVALUATING THE WIDER SCALE CONTEXT OF MAGMATISM ACROSS EAST ASIA: A REGIONAL COMPARISON WITH DATA FROM RUSSIA, MONGOLIA, THE NORTH CHINA CRATON AND KOREA.

Chapter abstract	137
4.1 INTRODUCTION	138
4.2 PETROLOGY	138-143
4.3 ARGON DATING	144-145
4.4 GEOCHEMICAL RESULTS	
4.4.1 Rock classification and major-element variations	145-146
4.5 GEOCHEMICAL VARIATIONS	
4.5.1 K/La ratios through time and space	147-148
4.5.2 Δ Nb through time and space	149-152
4.5.3 ⁸⁷ Sr/ ⁸⁶ Sr _(i) isotopes through time and space	152-154
4.5.4 ϵ Nd _(i) values through time and space	154-157
4.5.5 Pb isotopes through time and space	158-159
4.5.6 ϵ Hf _(i) values through time and space	159-160
4.6 DISCUSSION	
4.6.1 Comments on the mantle plume hypothesis	160-163
4.6.2 Towards an integrated model for the Mesozoic volcanism	163-165

CHAPTER 5	
CONCLUDING REMARKS AND FURTHER WORK	
5.1 OVERALL THESIS CONCLUSIONS	166-167
5.2 FURTHER WORK	
5.2.1 Constraining Mesozoic magmatism across Eastern Asia	168
5.2.2 Additional Hf isotope analysis	168-169
5.2.3 Constraining the style and closure time of the Mongol-Okhotsk Ocean	169
5.2.4 Modelling magmatic upwelling from slab roll-back processes	169-170
Abbreviation list	171
Equation list	172-174
Reference list	175-188
Appendix A	
Samples and analytical methods (XRF and ICP-MS)	189-190
Isotope (Sr-Nd-Pb-Hf) preparation	191-195
Ar-Ar dating preparation	196-197
Appendix B	
New Mongolian samples plotted on a TAS diagram	198

CHAPTER 1

AN INTRODUCTION TO THE CENTRAL ASIAN OROGENIC BELT: REGIONAL TECTONICS AND MAGMATISM

1. PROJECT AMBITIONS

Despite there being abundant Mesozoic and Cenozoic volcanism across Mongolia and northern China, and much research on the North China volcanism (e.g., Meng, 2003; Barry et al., 2003; Dash et al., 2015; Sheldrick et al., 2018), little consensus has been reached about the cause of apparent lithospheric removal in the Mesozoic and associated magmatism across Eastern Asia. Models for Mesozoic and Cenozoic volcanism in East Asia are either region-specific (e.g., He, 2015; Yarmolyuk et al., 2015), or considered the volcanism collectively (e.g., Dash et al., 2015). Models which suggest cogenetic links for Mesozoic magmatism across the area range from Palaeo-Pacific slab roll-back (Ma et al., 2014; Bars et al., 2018), delamination processes (Dash et al., 2015 Sheldrick et al., 2018), or convective erosion above subducting or stagnant slabs associated with the closure of the Mongol-Okhotsk Ocean (Fritzell et al., 2016), Palaeo-Asian (Windley et al., 2010) and Palaeo-Pacific plate (He 2014, 2015).

Testing these models has been hindered, in part, due to a lack of data on the Mesozoic volcanism from Mongolia, or simply because regional views are not considered fully. This thesis aims to combine new data from southern and eastern Mongolia, with existing data from Russia and North China to test existing Mesozoic magmatic models and constrain lithospheric removal in Mongolia.

Furthermore, the Mongol-Okhotsk suture (see section 1.2 for further details) attests to the existence of the Mongol-Okhotsk Ocean (e.g., Seton et al., 2012). This ocean formed in the Carboniferous between the continental blocks of Siberia to the north and Amuria (Mongolia)–North China blocks to the south (e.g., Tomurtogoo et al., 2005; Cocks and Torsvik, 2007; van der Voo et al., 2015). The final closure time of the Mongol-Okhotsk Ocean is estimated to have occurred sometime between the Late Jurassic (~155 Ma) and the beginning of the Early Cretaceous (~120 Ma) and intrusions and marine fossils found in the Mongol-Okhotsk suture young from west to east, suggesting that the ocean closure

started in the west and ended in the east (e.g., Zonenshain et al., 1990; ; Halim et al., 1998; Kravchinsky et al., 2002; Tomurtogoo et al., 2005; van der Voo et al., 2015).

However, it is still debated how this Mongol-Okhotsk Ocean closed (e.g., Windley et al., 2010). Evidence for northwards subduction of the Mongol-Okhotsk oceanic slab includes arc-related calc-alkaline granodiorites, granites and quartz diorites (Zorin, 1999) in the Khentey and Dauria zones, seismic tomographic images of slabs (van der Voo et al., 1999) and numerical modelling results (Fritzell et al., 2016). Nevertheless, other models have advocated for southward subduction only (e.g., Seton et al., 2012), or bi-modal subduction (e.g., Windley et al., 2010; Wang et al., 2015; van der Voo et al., 2015). Thus, whether the Mongol-Okhotsk Ocean closed with bi-modal subduction along northern and southern margins or, whether subduction was just along one margin, remains a debated issue (Fritzell et al., 2016).

To help tackle the question of “what caused Mongolian Mesozoic volcanism” this thesis will try and address the following questions:

- What is the distribution of Mesozoic volcanism and is there any obvious age progression?
- How does the chemistry of volcanism change with time and spatial distribution?
- How does the chemistry of volcanism compare regionally (specifically with the North China Craton and Russia)?
- Can evidence for southward subduction of a Mongol-Okhotsk Oceanic plate be identified?
- Can this information help test models for Mesozoic magmatism?

To address these questions, a combination of major – and trace-element chemistry, Sr-Nd-Pb-Hf isotopes and ^{40}Ar - ^{39}Ar dating results will be used to test the following hypotheses:

- There is no age progression consistent with the previously proposed mantle plume model (Yarmolyuk et al., 2015).
- Mesozoic Mongolian volcanism will record geochemical changes consistent with the removal of lithospheric mantle and increased asthenospheric input.

- Mesozoic Mongolian volcanism will show geochemical switches at a similar time to volcanism in the North China Craton, consistent with a model of holistic magmatic processes.
- There will be Mesozoic volcanism with arc-like geochemical signatures consistent with a model of a southward-subducting Mongol-Okhotsk slab.

This study will combine detailed localised geochemical investigations on volcanism from the Gobi Altai (Chapter 2), with geochemical investigations on newly discovered adakitic rocks south of the Mongol-Okhotsk suture (Chapter 3) and finally undertake a large regional comprehensive geochemical study on volcanism across Eastern Asia (Chapter 4) to test the above hypotheses.

REGIONAL TECTONICS

1.1 An overview of Mongolia and the Central Asian Orogenic Belt

The Central Asian Orogenic Belt (**Fig. 1.1**; CAOB) has an age range from 1 Ga to 250 Ma (e.g., Sengör et al. 1993; Wilhem et al. 2012, and references therein) and extends for >4000 km from the Tian Shan of Central Asia in the west to the Sea of Okhotsk in the east (e.g., Briggs et al., 2007; Xiao et al., 2010; Kröner et al., 2013). Within the Mongolian and Siberian Altai, Precambrian microcontinents have been identified at Tuva-Mongolia, Baidrag-Dzabkhan, Khangai (Tarvagatai), Idermeg and Khangai-Argunsky (**Fig. 1.2**; Wilhem et al., 2012, and references therein). The Argunsky microcontinent was a part of ribbon-microcontinent, often referred to as the Khangai-Argunsky microcontinent; this ribbon continent is simply referred to as Khangai on Figure 1.2. Wilhem et al. (2012) use the term “zone” (**Fig. 1.2 & 1.3**) to constrain an area which contains distinctive geology, tectonic features, and is delimited by tectonic boundaries such as suture zones or major faults; they use the term “terrane” to refer to a collection of zones which have common affinities that allow for mutual correlations. Using the same terminology, a summary about the terranes in Mongolia (plus their associated zones) and microcontinents is given in Table 1.1.

Many of these microcontinents evolved together as independent ribbon-terrane (Wilhem et al. 2012). It has been proposed that the Tuva-Mongolian microcontinent (**Fig. 1.2**; Tuva-Mongolian and Hamar-Davaa zones) and Central Mongolian microcontinents (**Fig. 1.2**;

Baidrag-Dzabkhan, Khangai and Idermeg zones) formed one single ribbon-microcontinent in the Vendian-Cambrian. The peri-Siberian part of the orogen formed around the microcontinents of Tuva-Mongolia and Altai-Mongolia through the accretion of multiple island arcs, oceanic islands/seamount plateaus and via the formation of back-arc basins. These accretion-collision events created the formation of peri-Siberian sutures by the end of the Palaeozoic. The Mongol-Okhotsk Ocean (**Fig. 1.4**) then opened within this accreted continent in the Early-Middle Palaeozoic (Wilhem et al. 2012). Overall, it's clear that a

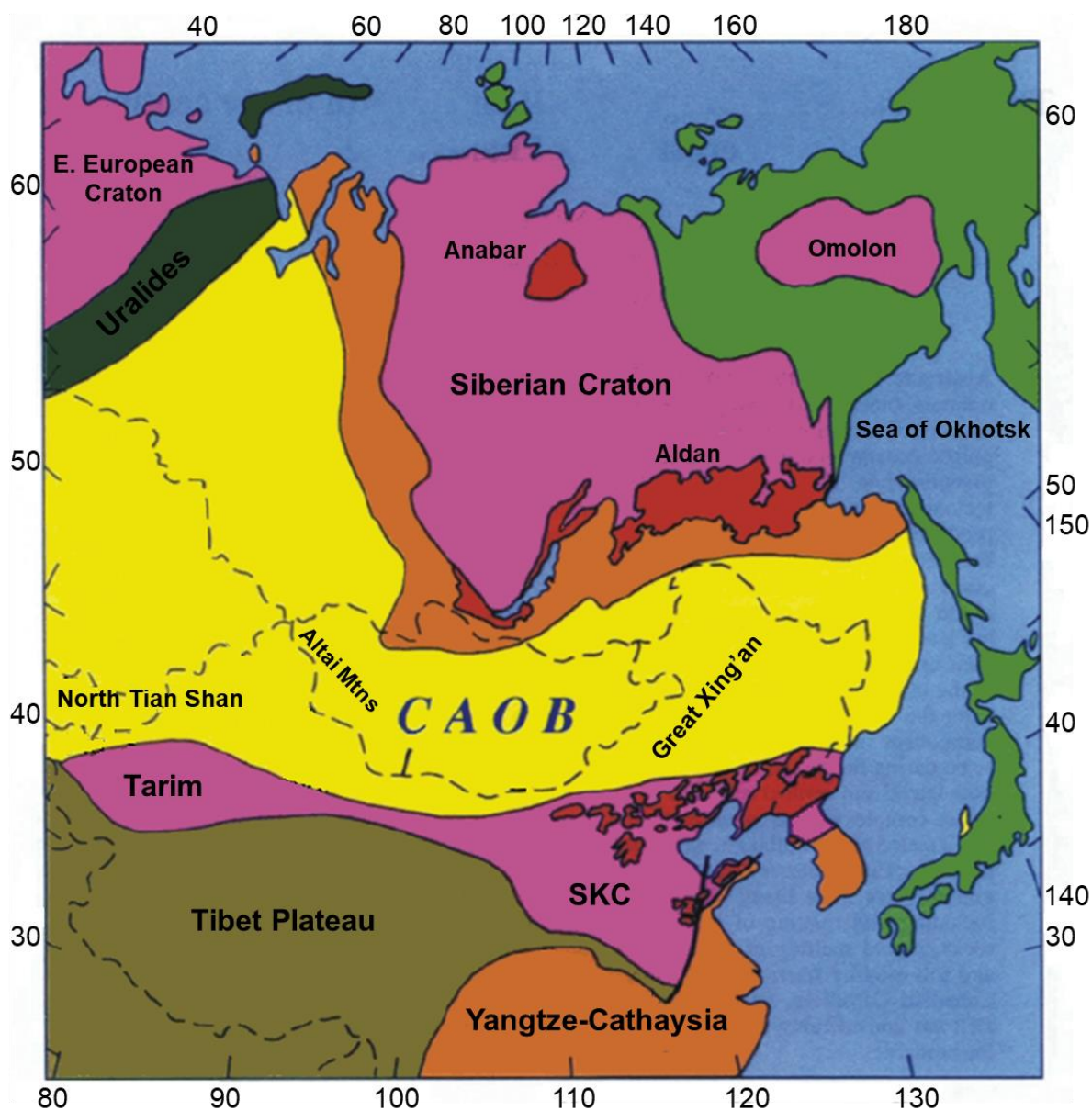


Figure 1.1: Schematic map of the Central Asian Orogenic Belt modified from Kröner and Rojas-Agramonte (2014) showing the domains with predominantly Neoproterozoic rocks (light brown), and Palaeozoic and younger rocks (yellow).

complicated tectonic history of accretion, extension and multiple ocean closures (e.g., the Dariv-Agardgh, Bayanhongor and Mongol-Okhotsk Ocean) has affected the terranes

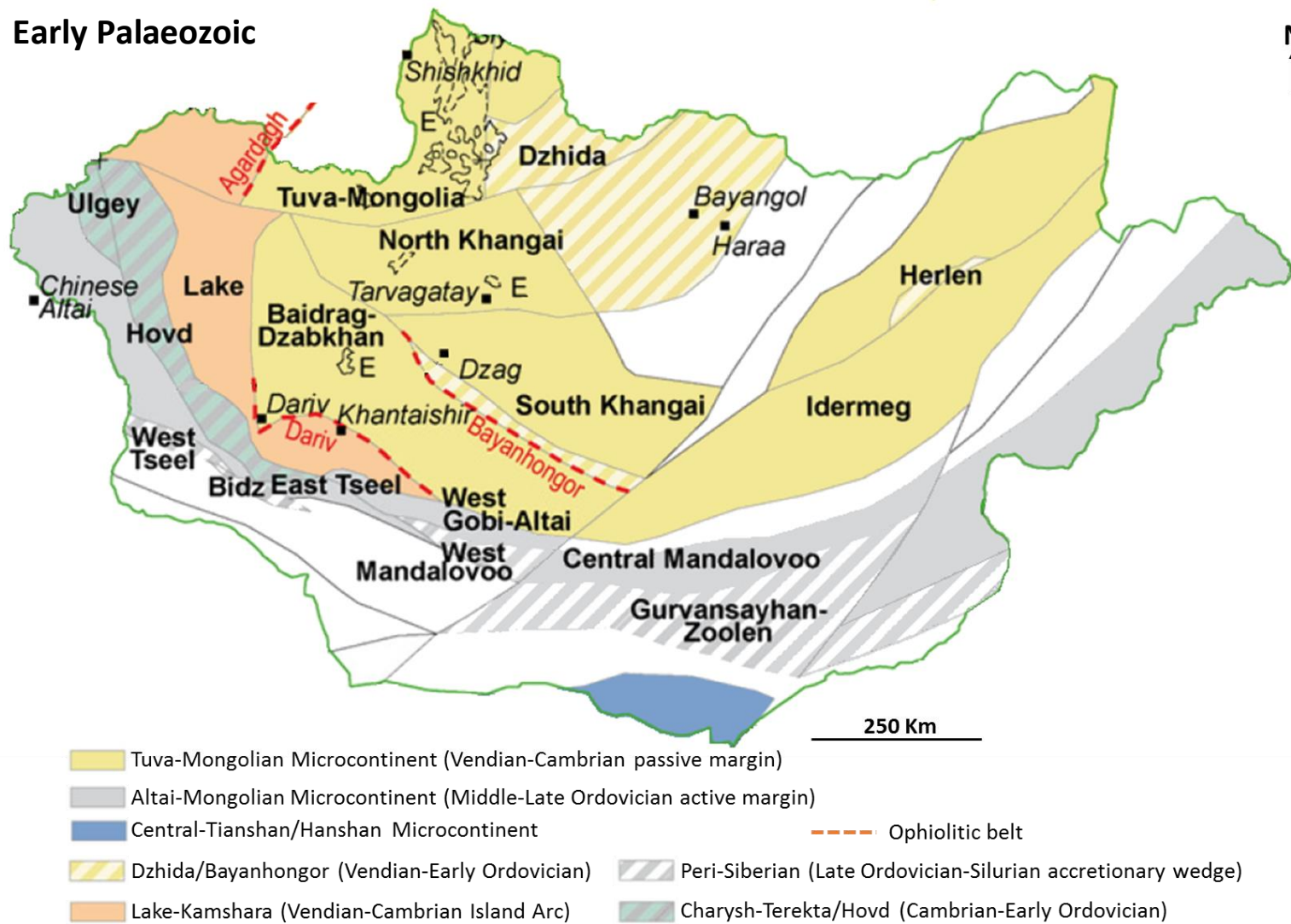


Figure 1.2: Early Palaeozoic terrane map of Mongolia modified from Wilhem et al. (2012).

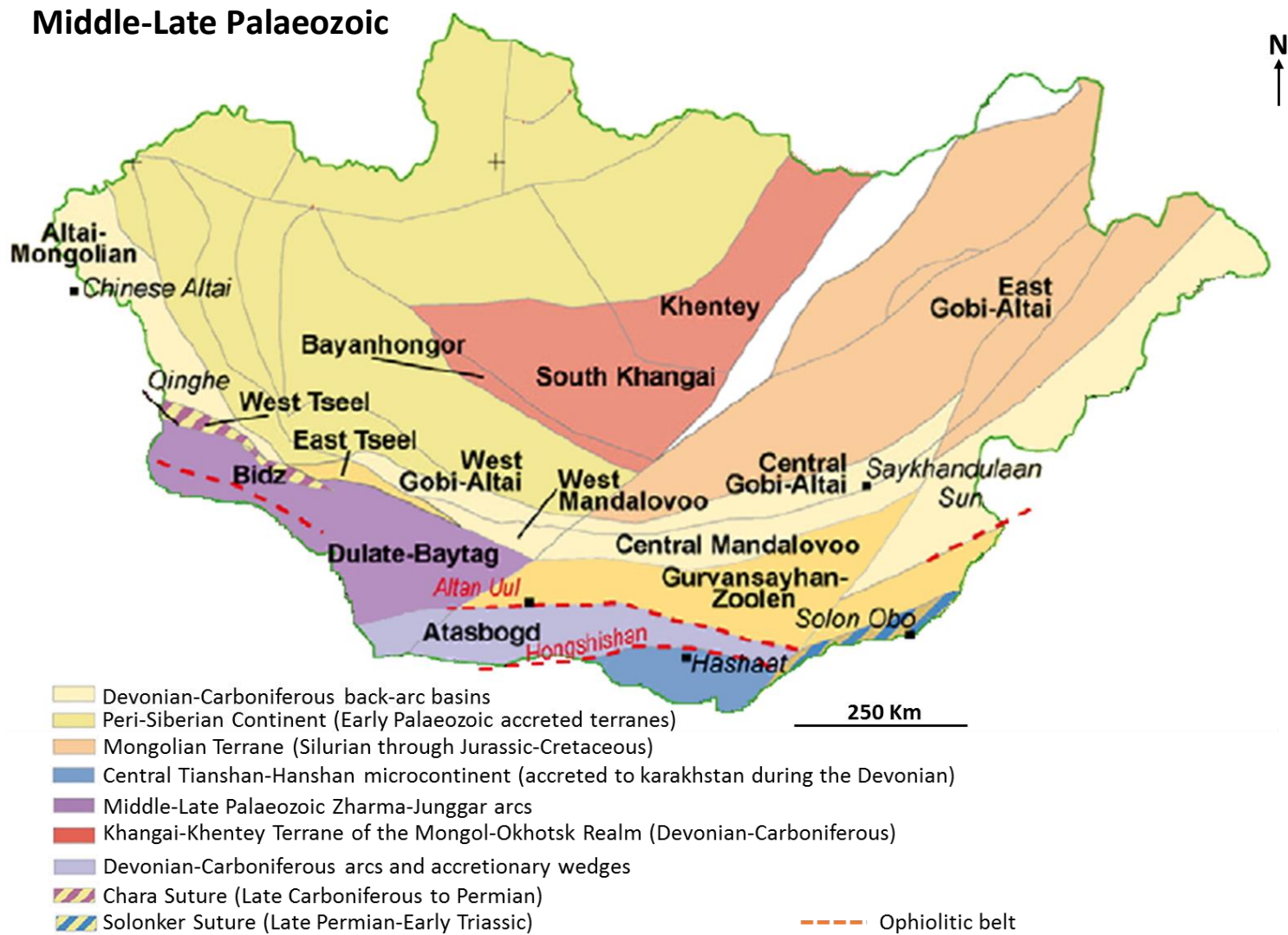


Figure 1.3: Middle-Late Palaeozoic terrane map of Mongolia modified from Wilhem et al. (2012).

Table 1.1: Summary of Early Palaeozoic Mongolian Microcontinents and Zones

<p>The Tuva-Mongolian Microcontinent</p> <p>The Tuva-Mongolian (Tuva-Mongolian and Hamar-Davaa zones) Microcontinent (Fig. 1.2) has been considered to be from Gondwana (e.g., Zonenshain et al. 1990; Wilhem et al. 2012, and references therein) or originated from Siberia which has been supported by palaeomagnetic data (e.g., Cocks and Torsvik, 2007). Carbonate sediments (Letnikova and Geletii, 2005) further suggest that this microcontinent was located in the Peri-Siberian topics in the Late Vendian-Cambrian (e.g., Wilhem et al. 2012, and referenced therein).</p>
<p>The Altai-Mongolian Microcontinent</p> <p>The Altai-Mongolian Microcontinent (Fig. 1.2) was accreted to Siberia after the Early Ordovician and believed to have a Gondwanan origin (e.g., Zonenshain et al., 1990; Mossakovsky et al., 1994; Wilhem et al. 2012, and references therein). Based on the presence of Precambrian detrital zircons in metasedimentary rocks and xenocrystic zircons in granitoids Glorie et al. 2011 and Jiang et al. 2011 concluded that this terrane has a Precambrian basement. However, from Hf isotope compositions of zircons in sediments, Cai et al. (2011) concluded that the Chinese Altai is made of juvenile Palaeozoic materials and thus has little Precambrian basement. Nevertheless, in southern Mongolia the presence of Precambrian crust in the East Tseel Zone (Fig. 1.2; Badarch et al. 2002; Helo et al. 2006) suggests that this Precambrian basement could extend eastwards into the South Gobi and West Mandalovoo Zone.</p>
<p>The Lake-Khamsara arc</p> <p>The external boundary of the Tuva-Mongolia Ribbon-terrane is defined by the Dariv-Agardagh ophiolitic belt (Fig. 1.2) which formed in a proto-intra oceanic arc associated with forearc and back-arc basins. The ophiolitic belt is juxtaposed to the Lake-Khamsara Zone. Geochemistry and geochronology suggests that the Lake-Khamsara Zone formed in the Vendian-Cambrian in an intra-oceanic arc environment and has a Proterozoic basement (Kröner et al. 2010; Kovach et al., 2011; Yarmolyuk et al., 2011). The Hovd and Ulgey Zones (to the west of the Lake-Khamsara Zone) was interpreted as the northern accretionary wedge to this arc (Badarch et al., 2002).</p>
<p>The Bayanhongor Zone</p> <p>The Bayanhongor Zone is located between the Baidrag-Dzabkhan and Khangai (Tarvagatai) microcontinents (Fig. 1.2) and is a relic of at least two oceans. Oceanic crust was dated at 660-640 Ma (U-Pb) by Jian et al. (2010) and is a relic of the Bayanhongor Ocean which finally disappeared during the Ordovician and was followed by Devonian thrust stacking (Wilhem et al. 2012, and references therein). Carboniferous fossiliferous shallow-marine limestones also suggest the extension of the Mongol-Okhotsk Ocean in the Bayanhongor area. Ophiolitic Permo-Triassic gabbros and lavas (ca. 298-210 Ma) were described by Jian et al. (2010) which is further supportive of this ocean. Slightly further to the east, the calc-alkaline Khentai batholith has also been explained by closure of the Mongol-Okhotsk Ocean (220-200 Ma; Kovalenko et al., 2004).</p>
<p>The Dzhida-Bayangol Zone</p> <p>This zone is mainly characterised by Vendian-Cambrian arcs and subduction-accretion complexes (e.g., Badarch et al. 2002). The presence of ophiolites and island arc volcanics (Naumova et al., 2006; Zorin et al. 2009) has been used to suggest the presence of the Dzhida-Bayangol Ocean and this is believed to have closed by the Early Ordovician (Wilhem et al. 2012, and references therein).</p>

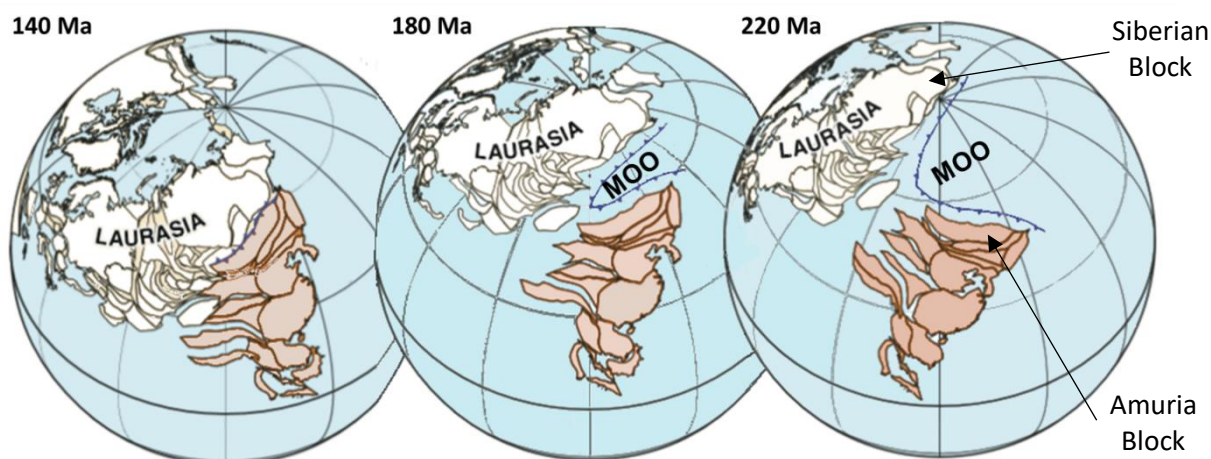


Figure 1.4: Edited plate reconstructions from vanderVoo et al. (2015). Plate reconstructions shown in palaeomagnetic reference frame, using apparent wander path of Torsvik et al. (2012) for Siberia. The South China block combined with the North China block at 220 Ma (Hacker et al., 2006). MOO – Mongol-Okhotsk Ocean.

within Mongolia. This geological history will undoubtedly have also affected the lithospheric mantle at depth (e.g., metasomatism processes), as well as the crust. Such potential modification processes can alter the geochemistry of magmatic rocks and this will be considered in more detail in later chapters.

1.2 The Mongol-Okhotsk Ocean and Suture.

The now-extinct Mongol-Okhotsk Ocean once separated the continental blocks of Siberia from southern Mongolia (Amuria) and the North China blocks. The existence of this palaeo-ocean is evident from the Mongol-Okhotsk Suture; this suture extends from central

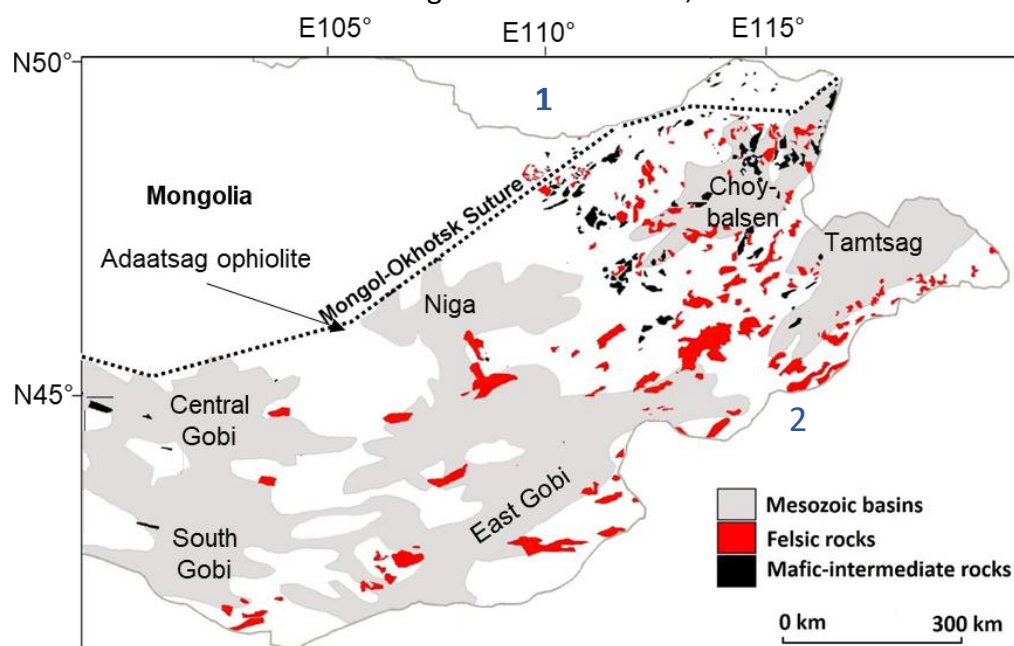


Figure 1.5: Sketch map of Mongolia showing the distribution of Mesozoic mafic to intermediate lavas. Felsic magmatism is shown, but age relationships are often not established. The distribution of volcanism is based on Mongolian government geological maps and field observations. The distribution of Mesozoic sedimentary basins is from Johnson et al. (2003). (1) Siberian Block (north of the Mongol-Okhotsk suture) and (2) Amuria Block (everything south of the Mongol-Okhotsk suture).

Mongolia, following the boundary between the Siberian and Amuria blocks, north to the Sea of Okhotsk (**Fig. 1.1, 1.5, 1.11**).

The continuation of the suture to the West is unclear, as the suture appears to disappear at longitudes west of $\sim 100^\circ\text{E}$ (e.g., van der Voo et al., 2015). The suture comprises of ophiolites (**Fig. 1.5**; Zonenshain et al., 1990; Tomurtogoo et al., 2005) and sediments containing marine fossils (Halim et al., 1998, and references therein). For such a large-scale ocean closure, the suture is not characterised by significant topological highs (**Fig. 1.6**).

Estimates for the opening of the Mongol-Okhotsk Ocean varies from Cambrian (Harland et al., 1990; $\sim 540\text{-}490$ Ma), Ordovician (Cock and Torsvik, 2007; $\sim 485\text{-}445$ Ma) to Permian (e.g., Zorin, 1999; Kravchinsky et al., 2002; $\sim 300\text{-}250$ Ma). The ambiguity of this timing is related to different definitions of the Mongol-Okhotsk Ocean, i.e. at what time associated terranes were in the configuration needed to form the ocean (e.g., Seton et al., 2012, and references therein). Nevertheless, $^{207}\text{Pb}/^{206}\text{Pb}$ dating of zircon grains (~ 325 Ma), from the Adaatsag ophiolite, in central Mongolia (**Fig. 1.5**; Tomurtogoo et al., 2005), indicates active seafloor spreading in the Carboniferous.

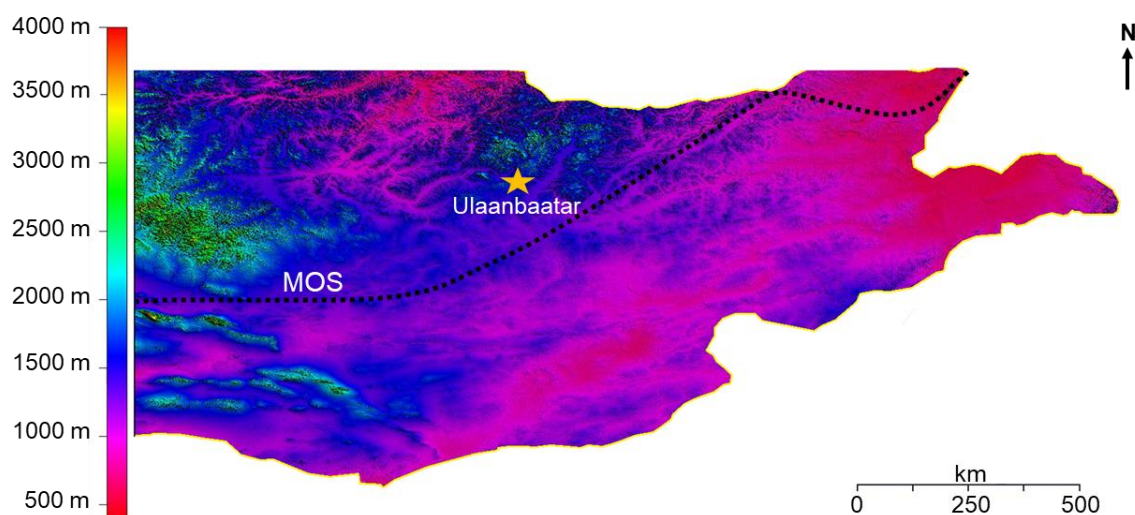


Figure 1.6: Elevation map for central and eastern Mongolia made from Shuttle Radar Topography Mission (SRTM) data. The SRTM data was downloaded from the Consortium for Spatial Information website and compiled in ArcGIS. The SRTM data has a resolution of 90 m with a vertical error <16 m. The approximate location of the Mongol-Okhotsk Suture (MOS) is shown.

The final closure of the Mongol-Okhotsk Ocean is also debated, according to Zonenshain et al. (1990) and Sengör & Natal'in (1996), the ocean closed in the Triassic in the west (Mongolia) and in the Late Jurassic in the east (Amur). However, based on palaeomagnetic

results, Enkin et al. (1990) and Scotese (2001) concluded that the ocean was still open in the Late Jurassic and closed in the Early Cretaceous. New palaeomagnetic data from Kravchinsky et al. (2002) constrain this further by concluding that the ocean closed largely during the Jurassic, with final closure at its eastern end in the Late Jurassic to earliest Cretaceous. Thus, the final closure of the ocean is suggested to have occurred sometime

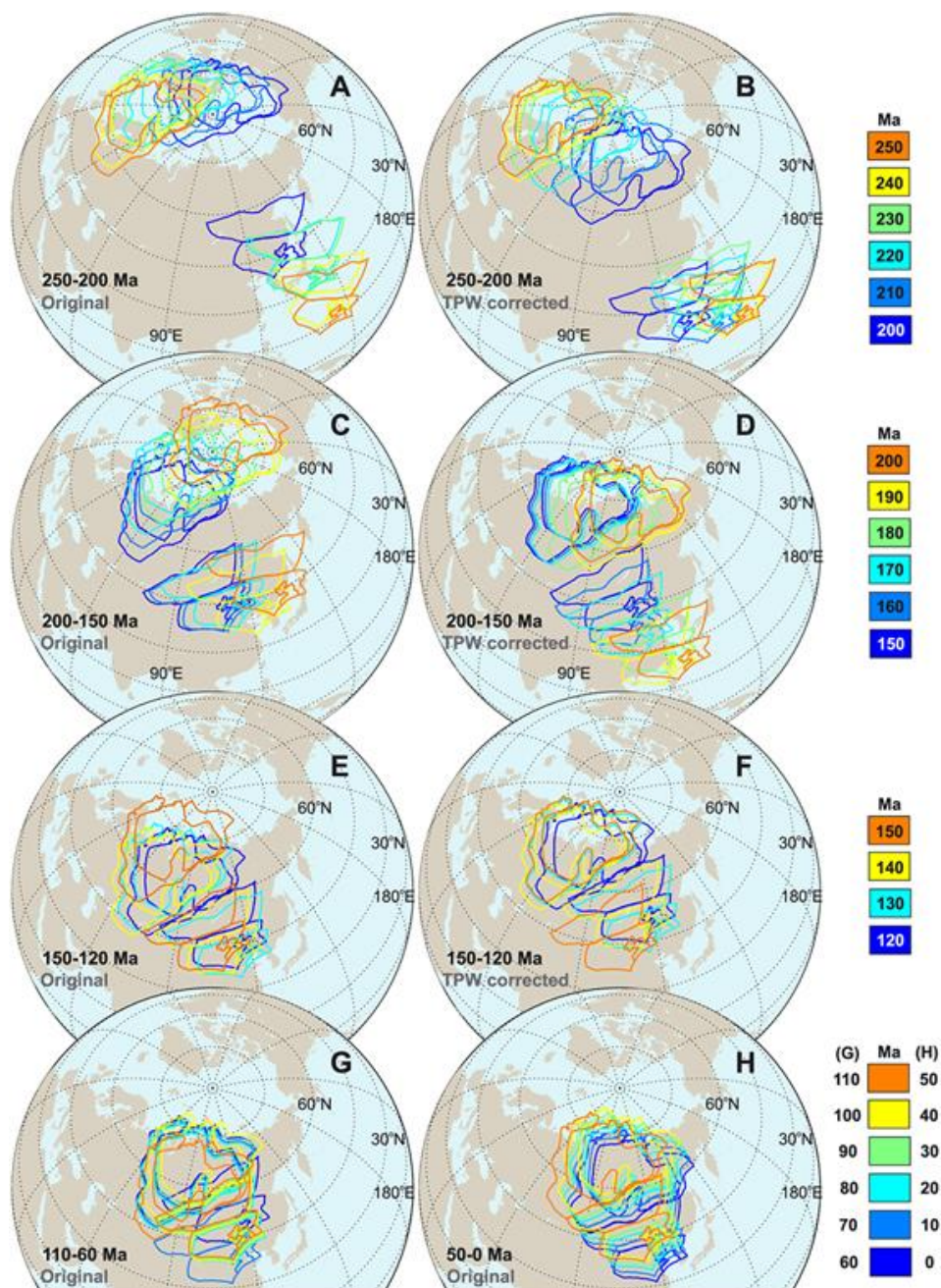


Figure 1.7: Reconstructions of Siberia and North China-Amuria since 250 Ma from Wu et al. (2017). Reconstructions on the left column are with respect to present day spin axis (the mantle) while reconstructions on the right have been corrected for True Polar Wander.

between the Late Jurassic (~155 Ma) and the beginning of the Early Cretaceous (~120 Ma). Nevertheless, as intrusions young from west to east along the Mongol-Okhotsk Suture, it

suggests the ocean closed in a scissor-like motion (e.g., Kravchinsky et al. 2002; Tomurtogt et al., 2005, and references therein).

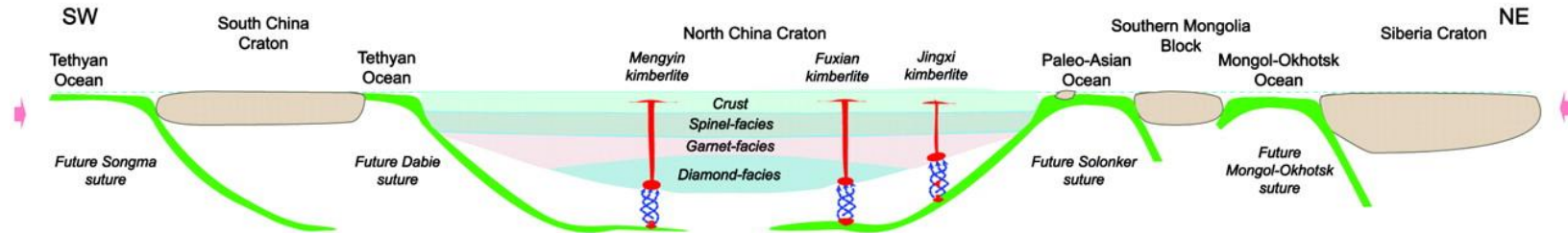
Modelling by Wu et al. (2017) suggests the closure of the Mongol-Okhotsk Ocean was in three major stages; between 250-200 Ma, 200-150 Ma and finally 150-120 Ma (**Fig. 1.7**). Their modelling proposes that during the first stage, approximately 62.5-76.1% of the Mongol-Okhotsk Ocean lithosphere subducted beneath Siberia and North China-Amuria with an average convergence rate of $\sim 8.8 \pm 0.6$ cm/yr. Due to the presence of “subduction” related magmatism on both sides of the Mongol-Okhotsk suture (e.g., Zorin, 1999) there have been interpretations of bi-modal subduction of the Mongol-Okhotsk Ocean (**Fig. 18**; e.g., Windley et al., 2010). Alternatively, the reconstructions from Seton et al. (2012) features subduction along the northern margin only, under Siberia. Numerical modelling by Fritzell et al. (2015) considered both subduction scenarios. Based on recreating seismic anomalies, modelling concluded that even if there was bi-modal subduction, subduction must have been dominant along the northern margin.

Such large amounts of subduction were postulated to occur predominantly on palaeotrenches in middle eastern Eurasia and, to a lesser extent, on continental-oceanic convergence near reconstructed Siberia and North China-Amuria. The second stage subducted approximately 14.2-30.6% of the Mongol-Okhotsk Ocean lithosphere, predominantly near North China-Amuria and southwest of Siberia. Subduction was concentrated in a zone stretching from southwestern Siberia through eastern China to the north-western Pacific. During this stage, there was a slower average convergence rate of $\sim 3.6 \pm 0.3$ cm/yr. The final stage had even slower convergence rates of $\sim 0.4-0.6$ cm/yr and resulted in the closing of the remnant palaeoceanic basin between Siberia and North China-Amuria.

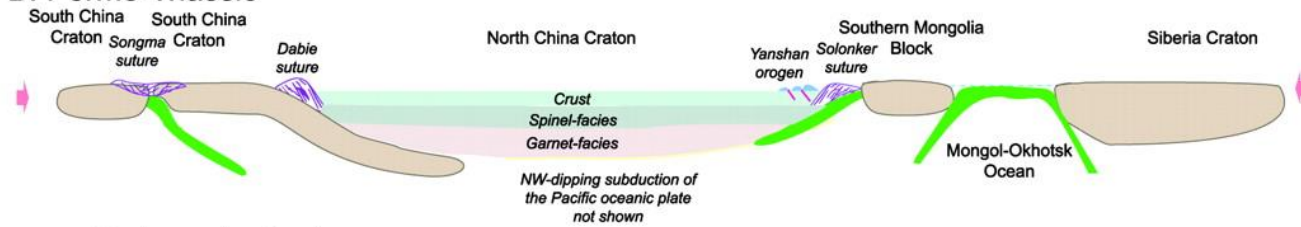
1.2.1 The Mongol-Okhotsk slab and seismic tomography

Modelling by Wu et al. (2017) suggests that more than 90% of the subducted slabs associated with the Mongol-Okhotsk Ocean were formed between 250-150 Ma by intraoceanic convergence and ocean-continent subduction. Seismic tomography models indicate a positive seismic anomaly under Siberia located between 1500 (mid-mantle) and 2980 km (core-mantle boundary); this feature has been interpreted as the Mongol-Okhotsk

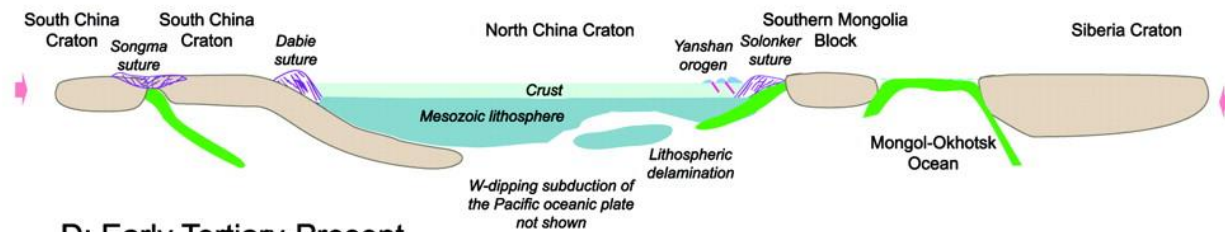
A: Paleozoic



B: Permo-Triassic



C: Jurassic-Cretaceous



D: Early Tertiary-Present

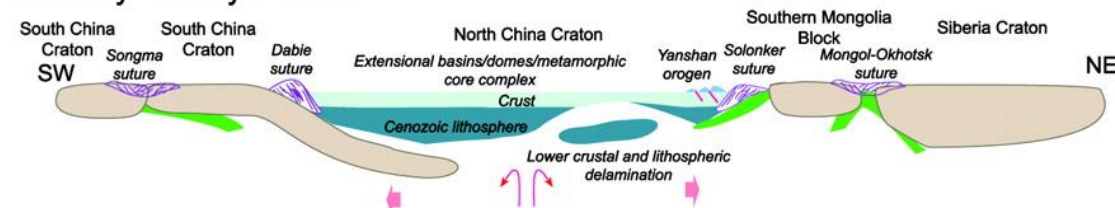


Figure 1.8: Sequential diagrams from Windley et al. (2010) showing the geodynamic processes and the mantle-crustal interactions during the development of the North China Craton and adjacent regions.

slab (e.g., van der Voo et al., 1998; van der Meer et al., 2010; Fritzell et al., 2016, and references therein). However, Shephard et al. (2014) performed mantle convection models to try and track subducting slabs through time and suggested that the Mongol-Okhotsk slab might be further west (albeit, no further east than 35°) and that the previously interpreted Mongol-Okhotsk slab may be related to subduction along the NW Panthalassa margin, including the Izanagi Plate. A numerical study by Fritzell et al. (2016) concluded that the predicted present-day location of the Mongol-Okhotsk slab remnant is west of ~40°E at 50°N. As a rough estimate, this equates to about ~3000 km away from the most westerly point of the Mongol-Okhotsk suture (**Fig. 1.5**).

1.3 The Palaeo-Pacific (Izanagi) Plate

“Activity associated with the Palaeo-Pacific plate had a strong influence on the late-stage development of the CAOB. It appears to have extended a considerable distance westward, accounting for Jurassic and Cretaceous magmatism at least as far inland as the Great Xing’an Range” (Wilde, 2015). One of the main pieces of evidence for this interpretation is the presence of Jurassic I-type granitoids which are interpreted to be the result of the collision of the Palaeo-Pacific plate with the CAOB (e.g., Wu et al. 2002, 2011; Wilde, 2015). Nevertheless, Meng, (2003) emphasised that the granitoid magmatism might reflect a far-field effect of the closure of the Mongol-Okhotsk Ocean.

The development of extensional basins in the Late Jurassic and Early Cretaceous, in the North China-Mongolia Tract (NCMT), could possibly reflect subductive roll-back of the Palaeo-Pacific plate (e.g., Watson et al., 1987; Traynor; Sladen, 1995, Meng, 2003 and references therein). However, several thermo-mechanical models have also been proposed such as transtensional faulting related to collision-extrusion tectonics (Kimura et al., 1990), magmatic underplating (Shao et al., 2000) and gravitational collapse of tectonically thickened crust (Graham et al., 2001). The widespread distribution of shallow-crustal extensional basins is a common feature of the NCMT (Meng, 2003 and references therein). Individual basins (and associated sub-basins) such as the East Gobi, Erlian and Yingen basin make up this shallow-crustal extensional basin system (**Fig. 1.5 & 1.14**).

The hypothesis that the Palaeo-Pacific plate extended so far westward and then underwent slab roll-back may be supported by a general eastward younging of basaltic magmatism

from the Jurassic through to the Cretaceous (e.g., Wu et al., 2011; Bars et al., 2018). This model will be discussed in greater detail later in this chapter.

Seismic images of the mantle beneath East Russia were presented by Zhao et al. (2010). The mantle tomography images are interpreted to show a stagnant Pacific slab in the

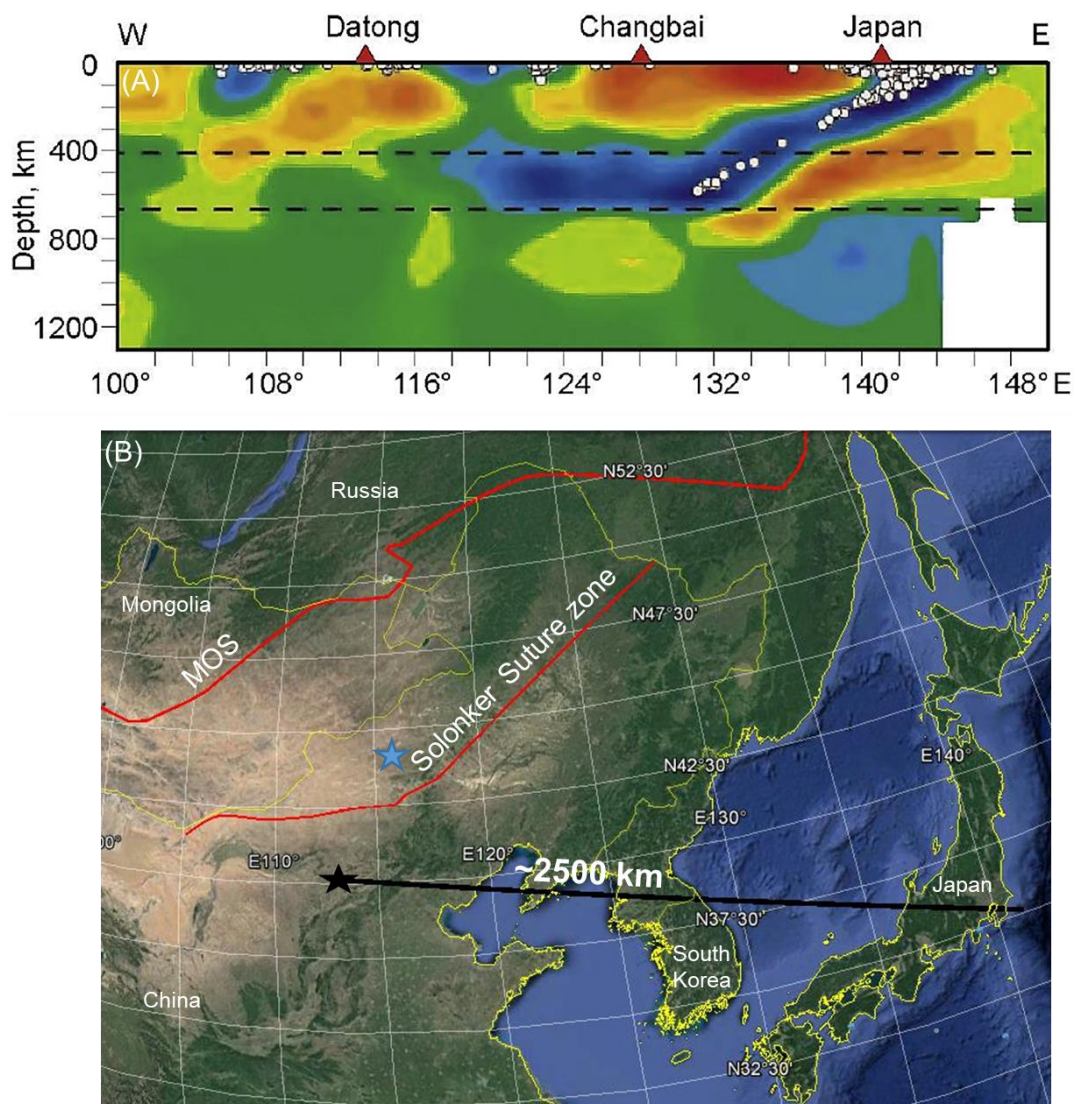


Figure 1.9: (A) East-west vertical cross-section of whole-mantle P-wave regional tomography. The red and blue colours denote low and high velocities, respectively (image from Zhao et al. 2010). (B) a Google Earth sketch image showing the approximate location of the Mongol-Okhotsk Suture (MOS) and Solonker Suture Zone (Data from Tomurtogoo et al., 2005; Chen et al., 2009; Eizenhöfer et al., 2014). The black star represents the Datong locality. The blue star represents Xilinhot metamorphic complex.

mantle beneath Western Alaska, Bering Sea, Sea of Okhotsk, Japan Sea and Northeast Asia (Zhao et al., 2010). Thus, present day seismic images do not show a Pacific plate beneath Eastern Mongolia or the North China Craton (**Fig. 1.9A**).

Overall, the extent at which the Palaeo-Pacific plate extended westwards during the Mesozoic is highly debated. This question is further complicated by the tectonic history of the CAOB.

1.4 The Solonker Suture

The Solonker Suture Zone (**Fig. 1.9B**; represents the final closure of the Palaeo-Asian Ocean) in northern Inner Mongolia (North China) separates the North China Craton from the South Mongolian microcontinent (e.g., Chen et al., 2009; Windley et al., 2010). The suture zone consists of two main magmatic belts: the Baolidao arc rocks represent a subduction-related magmatic belt, and the younger Halatu granites represent a collision-related belt (e.g., Chen et al., 2009). There is a debate about when the North China Craton and South Mongolian microcontinent started suturing, with suggestions ranging from late Devonian, early Carboniferous or late Permian (e.g., Kedong and Zhuyan, 1993, Chen et al., 2009 and references therein). Zircon $^{206}\text{Pb}/^{238}\text{U}$ data constrain the final closure between 296 and 234 Ma (Chen et al., 2009).

Whether the subduction occurred southwards (e.g., Windley et al., 2010), beneath the North China Craton (**Fig. 1.8**), or northwards, beneath the southern margin of the South Mongolian microcontinent (Sengör and Natal'in, 1996; Chen et al., 2000) is debated. Thrusted ophiolitic mélange and arc complexes were interpreted to be the result of a north-dipping subduction of the Palaeo-Asian oceanic slab under the southern margin of the South Mongolian microcontinent (Sengör and Natal'in, 1996; Chen et al., 2000). However, Windley et al. (2007) and Jian et al. (2008) interpreted these arc magmas as a product of ridge-trench interaction and the Xilinhote metamorphic core complex (**Fig. 1.9**) being the result of ridge subduction (Chen et al., 2009 and references therein). Chen et al. (2009) present a model of bi-modal subduction based on evidence of Palaeozoic arc rocks south of Sonidzuoqi reflecting north-dipping subduction while the south-dipping subduction is preserved in a Carboniferous-Early Permian continental arc on the northern margin of the North China Craton.

1.5 REGIONAL MAGMATISM

1.5.1 Triassic Magmatism

Triassic magmatism across the CAOB is commonly felsic (plutonic) or intermediate in composition (Table 1.2).

Table 1.2: Triassic magmatism across the CAOB.

Magmatism	Age (Ma)	Location
Granitoid, felsic metavolcanics and syenite; from metamorphic complexes (Donskaya et al. 2008)	265-211 U-Pb (Zircon)	Transbaikalia and northern Mongolia
Granitic batholith (Yarmolyuk et al. 2008)	260-242 U-Pb (Zircon)	Khangai batholith Mongolia
Granite and granodiorite (Jahn et al. 2004)	250-230 Sm-Nd (model ages)	Bayanhongor-Ulaanbaatar transect (Mongolia)
Granitoid (Orolmaa et al., 2008)	241-238 U-Pb Ar-Ar	Hangayon area (Central Mongolia)
I-type & A-type granites (Liu et al., 2018)	241-216 U-Pb (zircon)	Erguna and Xing'an massifs (NE China)
Cu-Mo porphyry deposit (Watanabe and Stein, 2000)	240 Re-Os on molybdenite	Erdenet deposit; North (central) Mongolia
Syenite and granite pegmatite (Reichow et al., 2010)	230-219 Rb-Sr	Mongolia-Transbaikalian Belt (Kharitonovo Complex and Malo-Kunalei pluton)
Granitoid (Wang et al., 2004)	228 U-Pb (Zircon)	Sino-Mongolian border (North China close to the Mongolian border)
Monzodiorite (Berzina et al., 2009)	236-214 Ar-Ar	Erdenetiyn-Ovoo magmatic center (northern Mongolia)
Rhyolite and granite (Donskaya et al., 2012)	226-223 U-Pb (zircon)	Kataev volcanoplutonic association (western Transbaikalia)
Granitic batholith (Yarmolyuk et al., 2002)	225-195 U-Pb	Hentiy-Daurian batholith
Trachybasaltic andesite, trachybasalt, trachyrhyodacite and pantellerite (Vorontsov et al., 2007A; and references therein)	236-209 K-Ar	Western Transbaikalia Rift Zone

Trachyandesite (Van Hinsbergen et al., 2015)	218 Ar-Ar	Dulaan Bogd; Gobi Altai (Mongolia)
Syenite and granite plutons (Yang and Wu, 2009)	215-205 Ar-Ar U-Pb (zircon)	Eastern North China Craton (Jiazishan & Chashan plutons)

Russian literature, at least with English translation, focuses on the Northern Mongolia-Western Transbaikalia rift zone which extends for more than 1200 km and is filled with peralkaline granite and bimodal volcanic associations (Yarmolyuk et al., 2002; Voronstov et al., 2007A). Geochemical data (Sr, Nd and Pb isotopes) is interpreted to reflect both crustal and mantle sources (e.g., Yarmolyuk et al., 2002; Voronstov et al. 2007A). The rift zone formed in a complex geodynamic setting which is interpreted to reflect collision in the Mongol-Okhotsk Suture with associated mantle plume activity (Voronstov et al. 2007A).

Mongolian Triassic magmatism is predominantly felsic (e.g., Jahn et al. 2004; Donskaya et al. 2008; Yarmolyuk et al., 2008; Reichow et al., 2010; Donskaya et al., 2012). However, towards the Late Triassic, more intermediate volcanism occurred too (e.g., Van Hinsbergen et al., 2015; Sheldrick et al., 2018). Granitic plutons are frequently interpreted to have their genesis linked to crustal thickening (e.g., from the closure of Mongol-Okhotsk Ocean) with melting being facilitated by mantle plume activity (e.g., Yarmolyuk et al., 2002; Berzina et al., 2009; Donskaya et al., 2008). More detailed discussion regarding the intermediate volcanism is a focus of later chapters in this study.

Plutons from the North China Craton are interpreted as resulting from delaminated, overthickened continental crust (Yang and Wu, 2009) reflecting extensive fractional crystallisation of hybrid coeval mantle – and crust-derived melts (Zhang et al., 2009). I-type granites from Erguna and Xing'an massifs (NE China) are interpreted as lower (mafic) crustal melts, generated in an Andean-type arc setting while A-type granites formed in supra-subduction extensional settings (Liu et al., 2018). A two-stage model involving southward subduction of the Mongol-Okhotsk oceanic plate followed by Late Triassic-Jurassic slab-rollback and supra-subduction extension was proposed by Liu et al. (2018). Thus, Chinese Triassic granitic plutons likely reflect a variety of geological processes (e.g., Yang and Wu, 2009; Zhang et al., 2009; Liu et al., 2018).

1.5.2 Jurassic Magmatism

Magmatism throughout the Jurassic is dominantly of intermediate and felsic composition with some basic magmatism too (Table 1.3).

Table 1.3: Jurassic magmatism across the CAOB.

Magmatism	Age (Ma)	Location
Granitoid Wang et al. (2015)	200-145 U-Pb (zircon)	The Mongol-Okhotsk Belt (Baikal-NE Mongolia and Great Xing'an Range)
Trachydolerite (Berzina et al. 2009)	190 Ar-Ar	Erdenetiyn-Ovoo magmatic center (northern Mongolia)
Basalt, high-Mg basalt and syenite (Li et al. 2004)	175-150 Ar-Ar	Southern Hunan and eastern Guangxi (SE China)
A-type granite (Liu et al., 2018)	173 U-Pb (zircon)	Erguna and Xing'an massifs (NE China)
Basalt to basaltic andesite (Wang et al. 2006a)	162-140 Ar-Ar *Formation straddles late Cretaceous	Tamulan formation; North China Craton
Trachybasalt to pantellerites (Andryushchenko et al. 2010)	159-156 Rb-Sr K-Ar	Khambin volcanotectonic complex (western Transbaikalia)
Adakitic lavas (Gao et al. 2004)	159 U-Pb (Zircon) *It was the lower section rhyolites which were dated	Xinglonggou (eastern, North China Craton)
Trachybasalts to trachyrhyodacite (Voronstov et al. 2007B)	158-145 K-Ar Rb-Sr	Western Tranbaikalia Rift Area (Russia)
Trachyandesite and rhyolite (Li et al. 2010)	151-145 U-Pb (Zircon) via LA-ICPMS	Hailaer, north-eastern Inner Mongolia (North China)
Andesite (Ying et al. 2010)	150 SHRIMP U-Pb (Zircon)	Manzhouli; Inner Mongolia (North China)

Magmatism	Age (Ma)	Location
Andesite (Zhang et al. 2006)	150 Rb-Sr isochron	Balinyouqi; eastern Inner Mongolia (North China)
Granite-porphyry (Nie et al. 2011)	147 Re-Os isochron on molybdenite	Chalukou (SE China)

Russian Jurassic magmatism is predominant in the Transbaikalia Rift Area and consists of basic and alkaline rocks: trachybasalts, trachyandesite-basalts, trachytes, trachydacites and trachyrhyodacites; this magmatism is attributed to a mantle plume (Voronstov et al. 2007B).

Mongolian Jurassic granitoids were reported by Wang et al. (2015). The granitoids evolved compositionally with time (Jurassic to Cretaceous) coinciding with a tectonic transition from contractional crustal thickening to extensional thinning. The Jurassic granitoids are interpreted to reflect melting of a deep-seated, thickened, lower continental crust. Thus, the granitoids in the Okhotsk belt reflect a subduction/collision setting due to the closure of the Mongol-Okhotsk Ocean (Wang et al. 2015). Mongolian mafic-intermediate rocks are undescribed in the literature, but newly discovered samples will be introduced later in this study (chapter 3 & 4).

Chinese Jurassic mafic-intermediate magmatism appears across the North China Craton with volcanism also appearing along the east coast of China (Meng, 2003 and references therein). Many researchers (e.g., Wang et al., 2006; Bars et al., 2018) attribute the late Mesozoic magmatism in East Asia to the tectonic regime of the Palaeo-Pacific plate (i.e. from slab-rollback), however many other models have also been proposed for magmatism which will be discussed in greater detail later in this chapter. The Late Jurassic granitoids (lower crustal melts) in the Great Xing'an Range and in the North China Craton may have formed in a syn- or post-collisional setting superposed by far-field effects of subduction of the Palaeo-Pacific plate or related to the subduction of Mongol-Okhotsk oceanic plate (Wang et al., 2015 and references therein; Liu et al., 2018).

1.5.3 Cretaceous Magmatism

Early Cretaceous magmatism is generally more intermediate to felsic in composition compared to the Triassic and Jurassic volcanic rocks, with magmatism becoming more intermediate to mafic in composition by the Late Cretaceous (Table 1.4).

Table 1.4: Cretaceous magmatism across the CAOB.

Magmatism	Age (Ma)	Location
Granite (Xie et al., 2011)	143-135 U-Pb (Zircon) via La- ICPMS & isotope dilution	Aershan; NE Inner Mongolia (NE China)
Basalt to trachybasalt. Some phonolite and syenites. (Voronstov et al., 2007B)	143-72 K-Ar	Western Transbaikalia Rift Area (Russia)
Basaltic andesite, trachyte and rhyolite (Fan et al., 2003)	139-116 K-Ar	Northern Da Hinggan Mountains (NE China) – Tamulangou, Jixiangfeng and Shangkuli formations. Also Murui Farm and Qiyi Prairie
Granite-porphyry (Qin et al., 2008)	138 Re-Os on molybdenite	Xiaodonggou (within Liaoning); NE China
Granite-porphyry (Zhou et al., 2010)	137 U-Pb (Zircon) via La- ICPMS	Huanggang (SE China)
Granite (Ge et al., 2005)	136-124 U-Pb (Zircon) via La- ICPMS	Wulanhaote, Inner Mongolia (North China)
Granite and basaltic magmatism (Li, 2000; and references therein)	136-97 Isotope age data	SE China
Granitoid (Wang et al., 2004)	135 U-Pb (Zircon)	Sino-Mongolian border (North China close to the Mongolian border)
Dacite (Guo et al., 2009)	135 SHRIMP U-Pb (Zircon)	Huolinhe; Inner Mongolia (North China)
Granite-porphyry (Ma et al., 2009)	134 U-Pb (Zircon)	Aolunhua; Inner Mongolia (North China)
Granite (Wang et al., 2012)	133 U-Pb (Zircon) via La- ICPMS	Chaihe (within Heilongjiang); North China Craton
Granite (Zhang et al., 2008)	132-131 U-Pb (Zircon) via La- ICPMS	Xinlan (within Zhejiang); East China

Magmatism	Age (Ma)	Location
Dioritic adakitic melts (Chen et al., 2013)	130	Shandong; North China Craton
Granite-porphyry (Wu et al., 2009)	130-128 SHRIMP U-Pb (zircon)	Luoguhe; NE China
Trachybasalt to tephriphonolites (Andryushchenko et al., 2010)	127-112 K-Ar	Khambin volcanotectonic complex (western Transbaikalia)
Dolerite-porphyrines intrusions (Liu et al., 2009)	127-123 U-Pb (Zircon)	Beibo gold district, Shandong Province; North China Craton
Basalt to trachyandesite (Yarmolyuk et al., 2015)	127-94 K-Ar	Mushugai well area; south Mongolia
Granite-porphyry (Yan et al., 2011)	126 U-Pb (Zircon) via LA- ICPMS	Banlashan (within Liaoning); NE China
Trachybasalt to basaltic tracyandesite (Graham et al., 2001)	126-123 Ar-Ar	Har Hotol Mongolia (Gobi)
Basalt to basaltic andesite (Wang et al., 2006a)	126-106 Ar-Ar	Shangkuli and Yiliekedede formation; North China Craton
Trachybasalt (Gao et al., 2008)	125-124 K-Ar	Sihetun and Liaoning; North China Craton
Basalt (Zhou et al., 2003)	125-122	Yixian, Liaoning; North China Craton
Trachybasalt and trachyandesite (Van Hinsbergen et al., 2015)	125-118 Ar-Ar	Jaran Bogd and Bulgantiin Uul; Gobi Altai (Mongolia)
Basalt (Zhang et al., 2002)	125-116 K-Ar	Fangcheng Shandong; North China Craton
Andesite (Wu et al., 2008)	124-114 Ar-Ar	Tequan (East China)
Adakitic intrusives (Xu et al., 2002)	123-106 K-Ar	Ningzhen area (East China)
Granite (Jahn et al., 2004)	120 Sm-Nd (model ages)	Bayanhongor-Ulaanbaatar transect (Mongolia)

Magmatism	Age (Ma)	Location
Adakitic volcanics (Liu et al., 2008)	120-116 K-Ar	Shandong Province; eastern North China Craton
Basanite to shoshonite (Dash et al., 2015)	120-104 Ar-Ar	Central and eastern Mongolia
Trachybasalt to basaltic trachyandesite (Barry, 1999)	120-99 Ar-Ar	Tsagaan Tsav and Tsost Magmatic Field; Gobi Altai (Mongolia)
Picrite (Pei et al., 2004)	119 K-Ar	Feixian; North China Craton
Trachybasalt (Yarmolyuk et al., 2015)	119 K-Ar	Zuun-Bogd Range; south Mongolia
Trachybasalt to basaltic trachyandesite	117-113 K-Ar	Khara-Argalant and Dund- Argalant range; south Mongolia
Trachybasalt to trachyandesite (Yarmolyuk et al., 2015)	116-109 K-Ar	Bayan-Tsagan Range; south Mongolia
Granite (Liu et al., 2005)	111 U-Pb (zircon) via Isotope dilution	Linxi; eastern Inner Mongolia (North China)
Basalt to basaltic trachyandesite (Yarmolyuk et al., 2015)	108-105 K-Ar	Chandman; south Mongolia
Basalt (Zhang and Zheng, 2003)	100 K-Ar	Fuxin, Liaoning; North China Craton
Trachybasalt (Yarmolyuk et al., 2015)	94 K-Ar	Dush Uul; south Mongolia
Basanite (dyke) (Zhang et al., 2008)	86-78 K-Ar	Qingdao region; China
Basalt (Zhou et al., 1998)	85 Rb-Sr Whole-rock isochron	North China Craton
Basalt (Wang et al., 2006b)	82 K-Ar	Qujiatun, Liaoning; North China Craton

Magmatism	Age (Ma)	Location
Basanite to trachyandesite (Yarmolyuk et al., 2015)	75-63 K-Ar	Borzongiin-Govi depression; south Mongolia
Basalt (Yan et al., 2005)	73	Daxizhuang, Shandong; North China Craton

Abundant Cretaceous volcanism appears in the Western Transbaikalia Rift Area (Table 4; Fig. 1.11) which is more mafic-intermediate in composition compared to the Jurassic and Triassic magmatism (Voronstov et al., 2007A, B). This rift-related magmatism is interpreted as having formed from melting of a mantle plume (Voronstov et al., 2007A, B).

Mongolian and Chinese Mesozoic mafic-intermediate magmatism becomes more abundant in the Cretaceous (e.g., Dash et al., 2015; Yarmolyuk et al., 2015). How the chemistry/composition of these volcanic rocks change with time is discussed more fully in later chapters (chapter 2 and 4) and petrogenetic models are discussed more fully in proceeding sections.

1.5.4 Cenozoic magmatism

Cenozoic basaltic magmatism occurs in Russia (Johnson et al., 2005; Voronstov et al., 2007B) and intermittently across central Mongolia (Barry et al., 2003; Hunt et al., 2012) and is also common in south China and the North China Craton (Fig. 1.10).

Table 1.5: Cenozoic magmatism across the CAOB.

Magmatism	Age (Ma)	Location
Trachybasalt to basaltic trachyandesite (Yarmolyuk et al., 2015)	62-38 K-Ar	Gurvan-Saikhan Range; south Mongolia
Basalt (Wang et al. 2006b)	58 K-Ar	Launshishanzi, Liaoning; North China Craton
Basalt to dolerite (Okamura et al., 1998)	54-5 K-Ar	East Russia (Sikhote-Alin and Sakhalin)
Basanite to sub-alkaline basalt (Voronstov et al., 2007B)	41-25 K-Ar	Western Transbaikalia Rift Area (Russia)
Basalt (Wang et al., 2007)	39-36 K-Ar	Caiyuan, Liaoning; North China Craton

Magmatism	Age (Ma)	Location
Basalt to phonotephrite (Barry et al., 2003)	33-6 Ar-Ar	Gobi Altai and Hangai; central Mongolia
Basalt (Liu et al., 1992)	23 K-Ar	Zhouba, Hebei; North China Craton
Basanite and basalt (Johnson et al., 2005)	16-6 K-Ar	Vitim volcanic field, Siberia
Basalt to trachybasalt (Liu et al., 1992)	10 K-Ar	Xiaogushan (Yitong), Jilin; North China Craton
Basalt (Liu et al., 1992)	9 K-Ar	Fangshan (Liuhe), Jiangsu; North China Craton
Basalt (Liu et al., 1992)	8-6 K-Ar	Qixia, Shandong; North China Craton
Basaltic volcanic cones (Fan et al., 2012)	2 K-Ar	Nuomin river, Great Xing'an Range
Basalt (Liu et al., 1992)	1 K-Ar	Jianshan, Anhui; North China Craton

Cenozoic basalts in eastern Russia (e.g., Okamura et al. 1998; Johnson et al., 2005; Voronstov et al., 2007B; Martynov and Khanchuk, 2012) are derived from asthenospheric mantle with various contributions from subcontinental lithospheric mantle. Source components may have been influenced by the Pacific Slab which has been identified by seismic images beneath East Russia and adjacent regions (Zhao et al. 2010). Teleseismic images also revealed a low-velocity zone (extending down to 660 km depth) beneath the Baikal rift zone which may represent a mantle plume (Zhao et al., 2010). How the chemistry/composition of these volcanic rocks change with time is discussed more fully in chapter 4.

Mongolian Cenozoic volcanism is diffuse and basalts from the Gobi Altai, southern Mongolia (~33 Ma) and Hangai, central Mongolia (<6 Ma) have geochemical similarities to the basalts in the North China Craton (Barry et al. 2003). These basalts are LREE-enriched, resembling ocean island basalt (OIB), and lack the negative Nb, Ta and Ti anomalies like Mesozoic lavas from the North China Craton and Mongolia (Sheldrick et al. 2018). However, the Mongolian Cenozoic basalts have isotopic characteristics advocating multiple source

components (lithospheric and enriched mantle domains). Olivine phenocryst helium isotope data (from Hamar Deban, Siberia and Hangai, central Mongolia) was used to investigate whether upwelling lower mantle (i.e. a mantle plume) could explain the

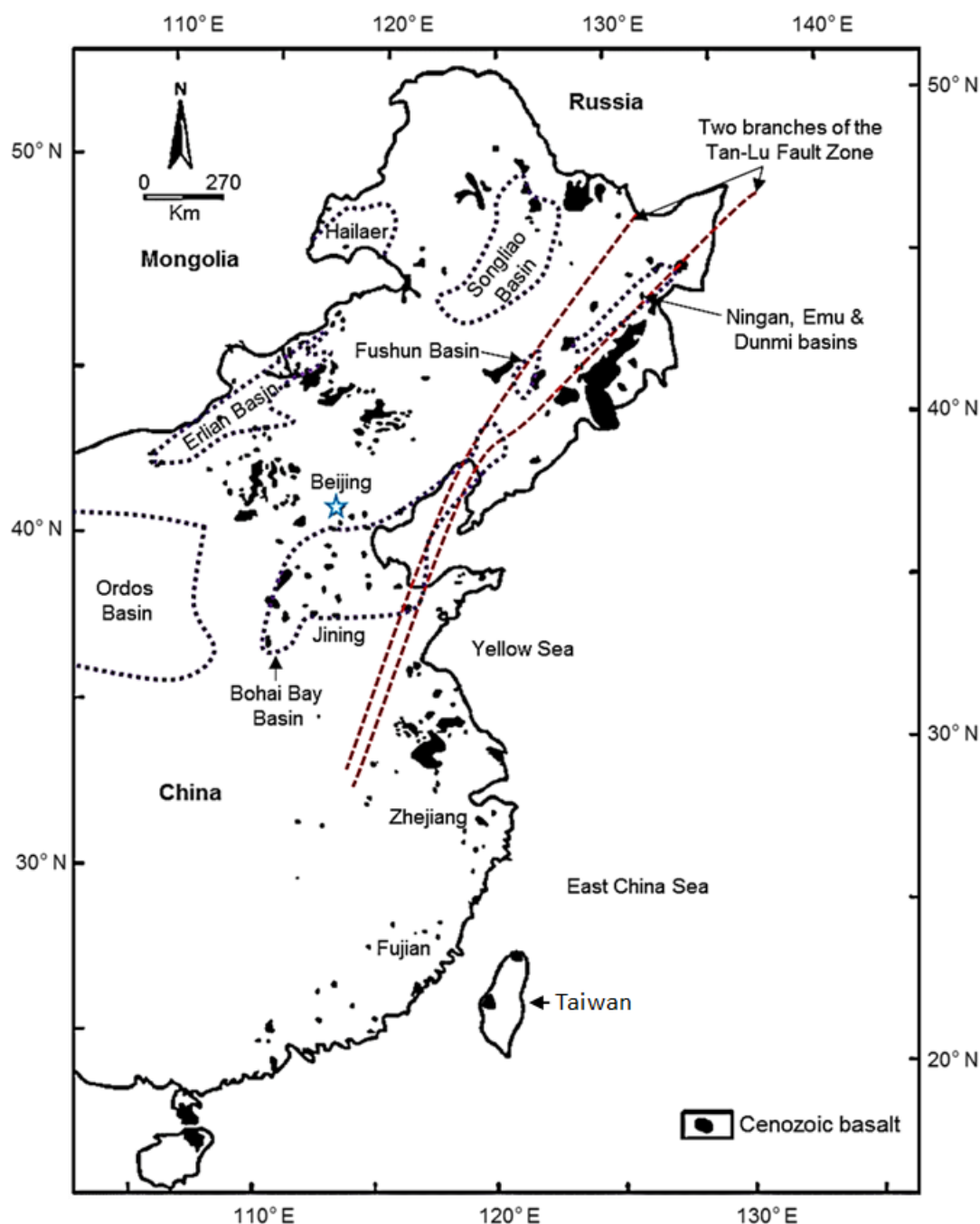


Figure 1.10: A map of North and South China showing the spatial distribution of Cenozoic volcanism; modified from Xu and Zheng (2017). Additional info from Hao et al. (2007) and Huang et al. (2015).

volcanism (Barry et al., 2007). However, the helium isotopic data indicated an asthenospheric mantle source and thus has similarities with the Cenozoic basalts from the North China Craton (e.g., Liu et al., 1995). The most abundant Cenozoic volcanism in Northeast and North China (**Fig. 1.10**) is continental rift basalts. Several subtypes have been

recognised according to age: Eocene basin-rift basalt, Neogene rift-valley basalt and continental lava basalts.

The Eocene basin-rift basalts are distributed in Cenozoic basins (e.g., Lower Liaohe-Bohai Basin). Rifting processes have been attributed to mantle diapirs from the Late Cretaceous to Eocene (Liu et al., 1995, and references therein). These basaltic magmas underwent varying degrees of partial melting of mantle material and frequently erupted along faults in the crust.

Several small Mesozoic and Cenozoic basins were also developed along the Tan-lu (Tancheng-Lujiang) Fault Zone (and the Fushun-Mishan Fault Zone in the Fushun Basin) forming a major rift valley (**Fig. 1.10**). The Neogene basaltic lavas erupted along graben and associated faults forming a volcanic zone running north-south throughout eastern China (Liu et al., 1995). Miocene alkali and tholeiitic continental basaltic lavas are also located around areas such as Jining, covering an area of more than 2500 km² (Liu et al., 1995); these basalts are also associated with rifting (**Fig. 1.10**).

From the Late Cretaceous to the Eocene, Southeast China was in a back-arc extensional environment (Liu et al., 1995, and references therein). Miocene basalts outcrop (>500 Km²) in the Zhejiang Province (**Fig. 1.10**) with thicknesses reaching up to 200 m, while Cenozoic basaltic lavas in the Fujian Province are found in parallel NE-striking trench fault zones and so are (Miocene) basalts in western Taiwan. Thus, Cenozoic basalts in Fujian, Zhejiang and western Taiwan are comparable to the North China Cenozoic basalts, in as such, that they formed in a rift-like environment. However, Quaternary calc-alkaline andesite formed in an island-arc environment in northern Taiwan while ophiolites and mid-ocean ridge basalt (MORB) in eastern Taiwan are representative of relic oceanic crust.

A large Sr-Nd-Pb isotope dataset (~400 data points) was used to assess the petrogenesis of the Cenozoic volcanism in China (Liu et al., 1995). To briefly summarise, this isotope data advocates mantle source variation geographically. Specifically, the mantle source under the

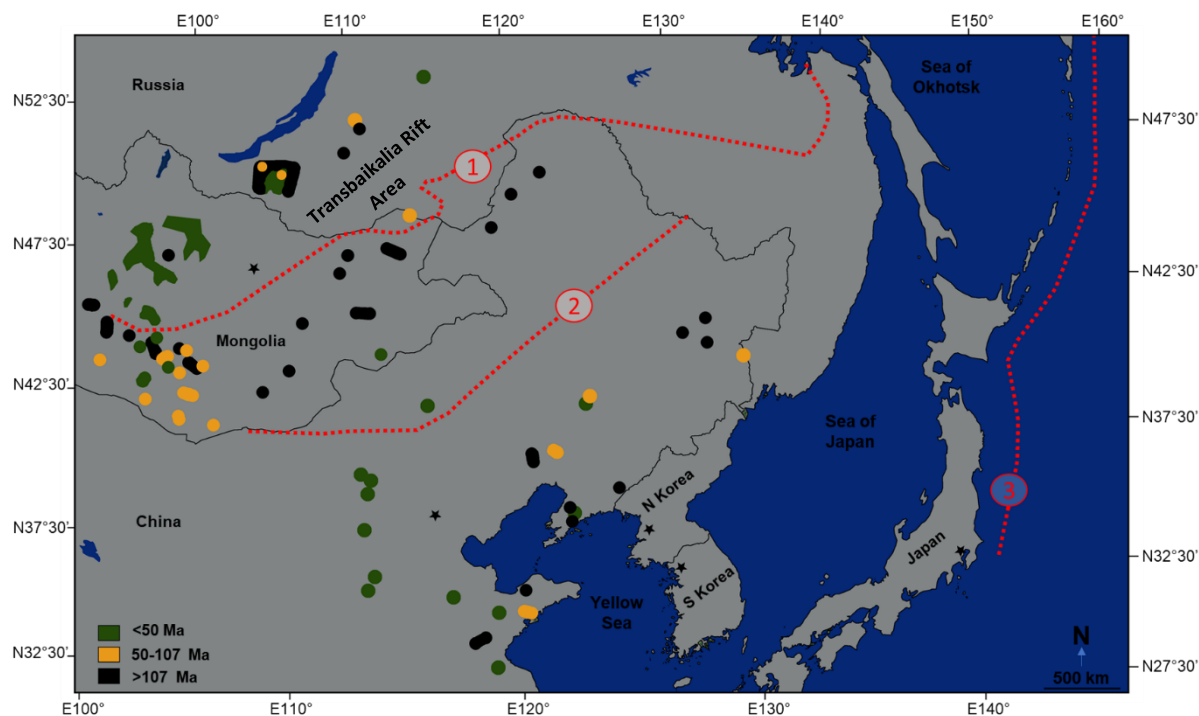


Figure 1.11: A map of Eastern Asia showing the distribution of radiogenic dated Mesozoic and Cenozoic basaltic samples in Eastern Russia, Mongolia, the NCC and north-east China. All data is included in the supplementary material (extended dataset 1; n=459 samples). Numbering: (1) Mongol-Okhotsk Suture; (2) Solonker Suture Zone; (3) Pacific Active Margin. Data sources: Barry et al. (1999, 2003), Graham et al. (2001), Zhang et al. (2003), Pei et al. (2004), Johnson et al. (2005), Yan et al. (2005), Tang et al. (2006), Weiqiang et al. (2007), Voronstov et al. (2007A & B), Liu et al. (2008), Gao et al. (2008), Yang et al. (2008), Andyushchenko et al. (2010); Ying et al. (2010), Ho et al. (2011), Pei et al. (2011), Wang et al. (2007), Wang et al. (2011), Kuang et al. (2012), Qicheng et al. (2012), Xu et al. (2012), Zhang et al. (2012), Chen et al. (2013), Ma et al. (2014), Dash et al. (2015), Wang et al. (2015), Yarmolyuk et al. (2015; and references therein), Li et al. (2017), Sheldrick et al. (2018). Additional Mongolian radiogenic data, for samples in central and eastern Mongolia is shown – these $^{40}\text{Ar}/^{39}\text{Ar}$ dating results are discussed in detail in chapters 3 and 4.

North and South China continents are most different while the area in between is transitional and hybrid. The South China mantle source is primarily depleted components whilst being rich in radiogenic Pb (OIB affinity). Northeast and North China mantle is described as having a more “primary mantle signature”.

1.6 MESOZOIC MAGMATIC MODELS

1.6.1 Slab roll-back and asthenospheric upwelling

Lithospheric delamination and asthenospheric upwelling induced by Palaeo-Pacific slab roll-back (**Fig. 1.12**) has been a popular model to explain Mesozoic magmatism across Mongolia, the North China Craton, Korea and Japan (e.g., Wang et al., 2006; Bars et al., 2018; Yang et al., 2018). Researchers (e.g., Wang et al., 2006; Bars et al., 2018) suggest that a younging of magmatism, from west to east, supports this theory.

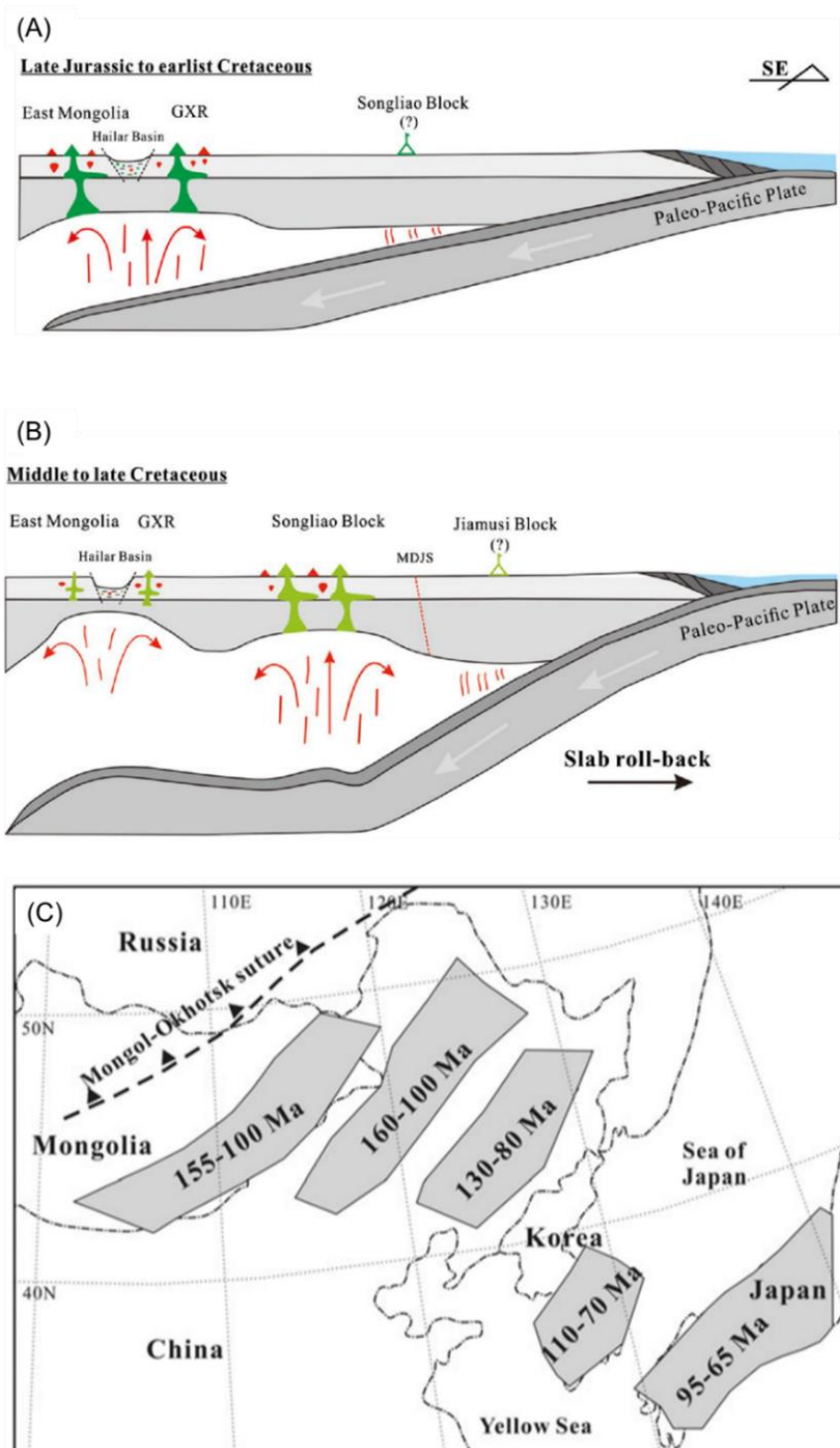


Figure 1.12: (A) Palaeo-Pacific plate subduction is accompanied by upwelling magmatism. (B) Palaeo-Pacific slab roll-back induces upwelling magmatism. (C) Sketch map showing the temporal and spatial Late Mesozoic volcanism in NE Asia. This map shows an apparent age progression. Images from Bars et al. (2018).

Furthermore, extensional basins, which are elongated in an NNE direction, are parallel to the Pacific subduction zone and have thus been used to support Palaeo-Pacific slab roll-back (e.g., Meng, 2003; Bars et al., 2018; **Fig 1.5**).

1.6.2 Convective mantle lithosphere removal

A model of convective mantle lithosphere removal was postulated by He (2014) to explain the Mesozoic magmatism in the North China Craton. In this model, a stagnating Palaeo-Pacific plate forms an extensive mantle wedge. Slab dehydration reduces the viscosity of the asthenosphere, resulting in small-scale upwellings within the upper mantle and convection of the mantle wedge. Ascending asthenosphere causes compression of the rheological boundary layer and increases the temperature gradient within this layer. This convection generates excess heat and causes lithospheric thinning and magmatism (He, 2014, 2015).

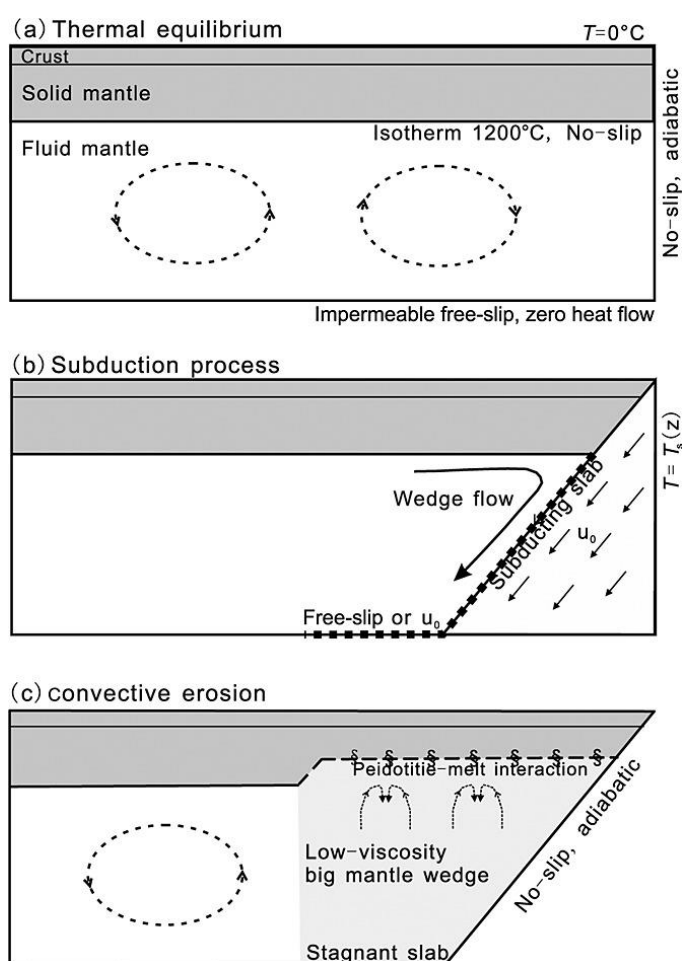


Figure 1.13 (from He, 2014):

(A) A thick stable craton.

(B) Subduction of the Palaeo-Pacific plate forms a big mantle wedge.

(C) The mantle viscosity is reduced by the big mantle wedge due to the dehydration of a stagnant slab, generating vigorous mantle convection and then causing thermal erosion of the lithosphere. Peridotite-melt interaction helps to lower the melting temperature.

1.6.3 Slab break-off in the Mongol-Okhotsk region

Slab break-off is the negative buoyancy-driven separation of attached dense lithosphere from adjoining less-dense lithosphere (e.g., Davies et al., 1995). A model invoking slab break-off (**Fig. 1.14**) due to crustal overthickening, from the collision of the amalgamated northern China-Mongolia tract with Siberia, was suggested by Meng (2003). This slab break-off resulted in lithospheric stretching of the adjacent northern China – Mongolia tract with subsequent ascent of hot asthenosphere and magmatic underplating. The extensional basins are explained by a combination of gravitational collapse and oceanic slab break-off.

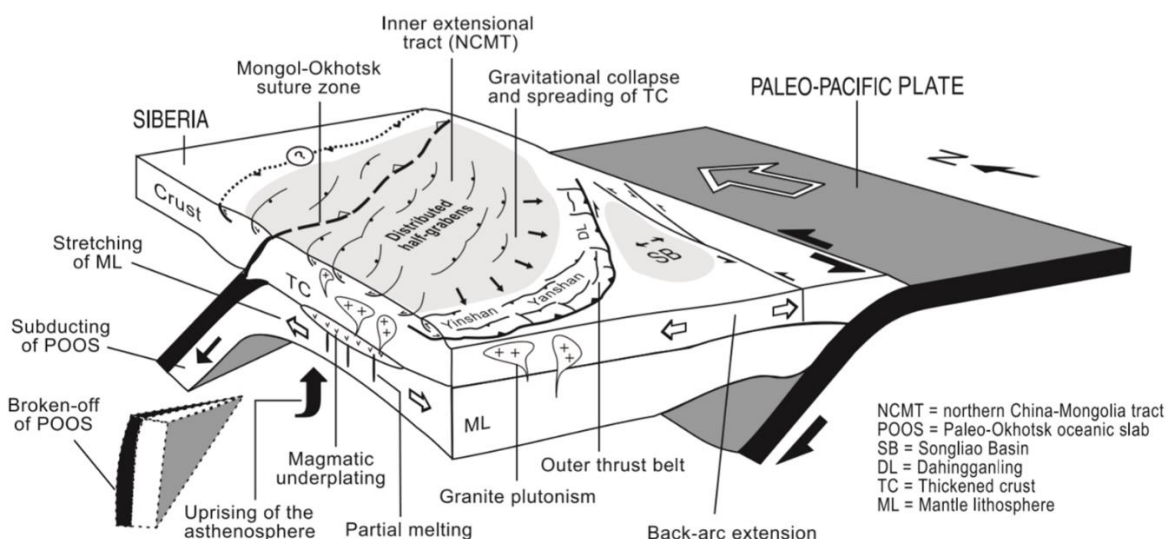


Figure 1.14: Oceanic slab break-off accompanied with gravitational collapse (image from Meng, 2003) causes the development of extensional basins, upwelling asthenosphere and magmatic underplating.

Thus, this model does not invoke Palaeo-Pacific plate involvement to drive magmatism, or extension, across Mongolia and the North China Craton.

1.6.4 Bi-directional delamination

A model of bi-directional partial delamination was suggested by Dash et al. (2015). In this model, thickened mantle lithosphere is formed during the closure of the Mongol-Okhotsk Ocean. Partial delamination of thickened mantle lithosphere occurred immediately after the ocean closure, to the west and to the east, leading to mantle upwelling and volcanism (**Fig. 1.15**). This bi-directional propagation of delamination caused progressive younging of the volcanic front to the west and to the east.

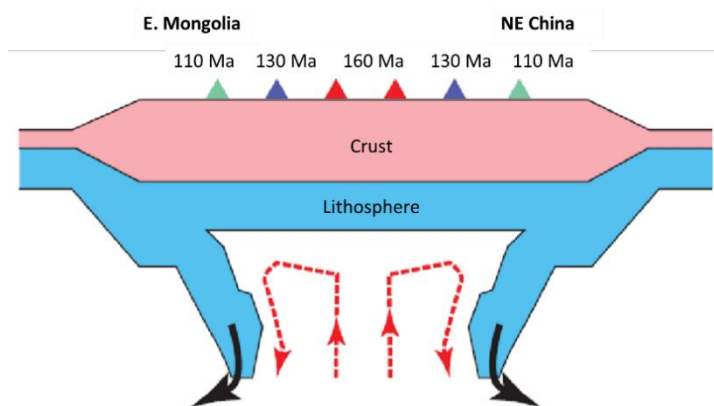


Figure 1.15: Thickened mantle lithosphere formed during the closure of the Mongol-Okhotsk Ocean undergoes partial bi-directional delamination. This forms a progressive younging of the volcanic front to the west and to the east. Figure and model from Dash et al. (2015).

1.6.5 Sinking of subducted oceanic slabs

Due to the closure of Palaeo-Asian oceans, thick piles of subducted oceanic slabs were postulated to be trapped at the top of an endothermic phase boundary at 670 km (Dash et al., 2015). The addition of subducted slabs in the upper mantle lowered the temperature; this lowering of temperature prevented the slab sinking through this endothermic phase boundary. Finally, the initiation of Palaeo-Pacific subduction may have caused a thermal perturbation, rising the temperature and reducing the viscosity of the upper mantle via upward mantle generated by the subduction.

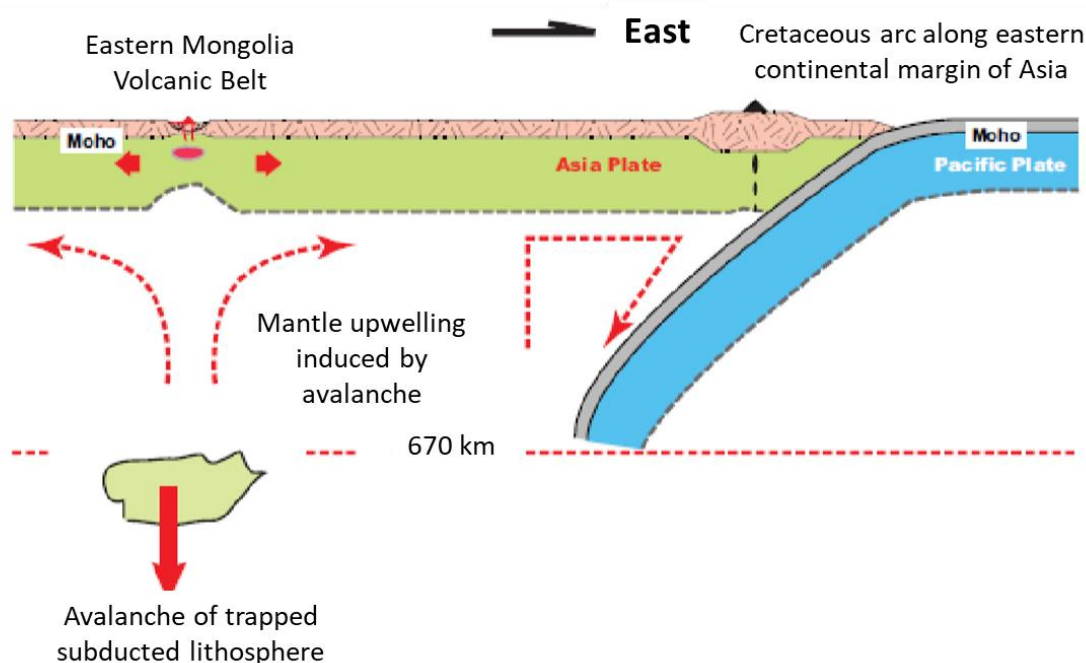


Figure 1.16: A model of trapped oceanic slabs sinking and causing mantle upwelling (Dash et al., 2015).

1.6.6 Mongol-Okhotsk slab window

A Mongol-Okhotsk mid-ocean ridge subduction model was proposed by Zhang (2014) to explain Mesozoic volcanism in the Great Xing'an Range. In this model, partial melting of

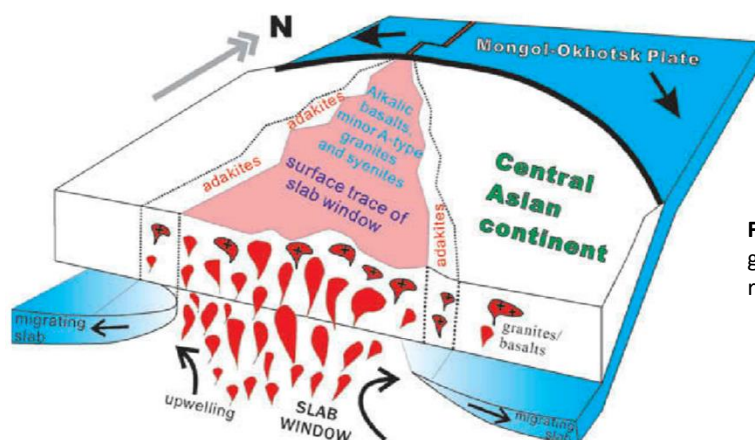


Figure 1.17: Slab window model for the genesis of the Great Xing'an Range igneous rocks (Zhang, 2014).

young, hot, subducting oceanic slabs close to the ridge formed adakitic rocks. Then, during ridge subduction, a slab window opened (**Fig. 1.17**), which triggered volcanism and basin formation.

1.6.7 Mantle plume

The “distribution of the Late Mesozoic-Cenozoic volcanism in Central Asia was controlled by a group of relatively small hot finger-type mantle plumes” (Yarmolyuk et al., 2015). The role of mantle plumes is also thought to have participated in the generation of the Baikal rift system (e.g., Voronstov et al., 2007 A, B; **Fig. 1.11**).

The argument for a mantle plume in this region of Mongolia was based on a combination of interpretations (Yarmolyuk et al., 2015):

- (1) Volcanism in the region was separated from other volcanic fields in Mongolia.
- (2) Volcanic migration over the region (**Fig. 1.18**; inset diagram) was controlled by a mantle hotspot.
- (3) Late Cenozoic magmatism in the region (**Fig. 1.18**) is associated with local asthenospheric uplift controlled by a low-velocity mantle anomaly.
- (4) Isotopic compositions of volcanic rocks correspond to sublithospheric sources, like recycled lithosphere.

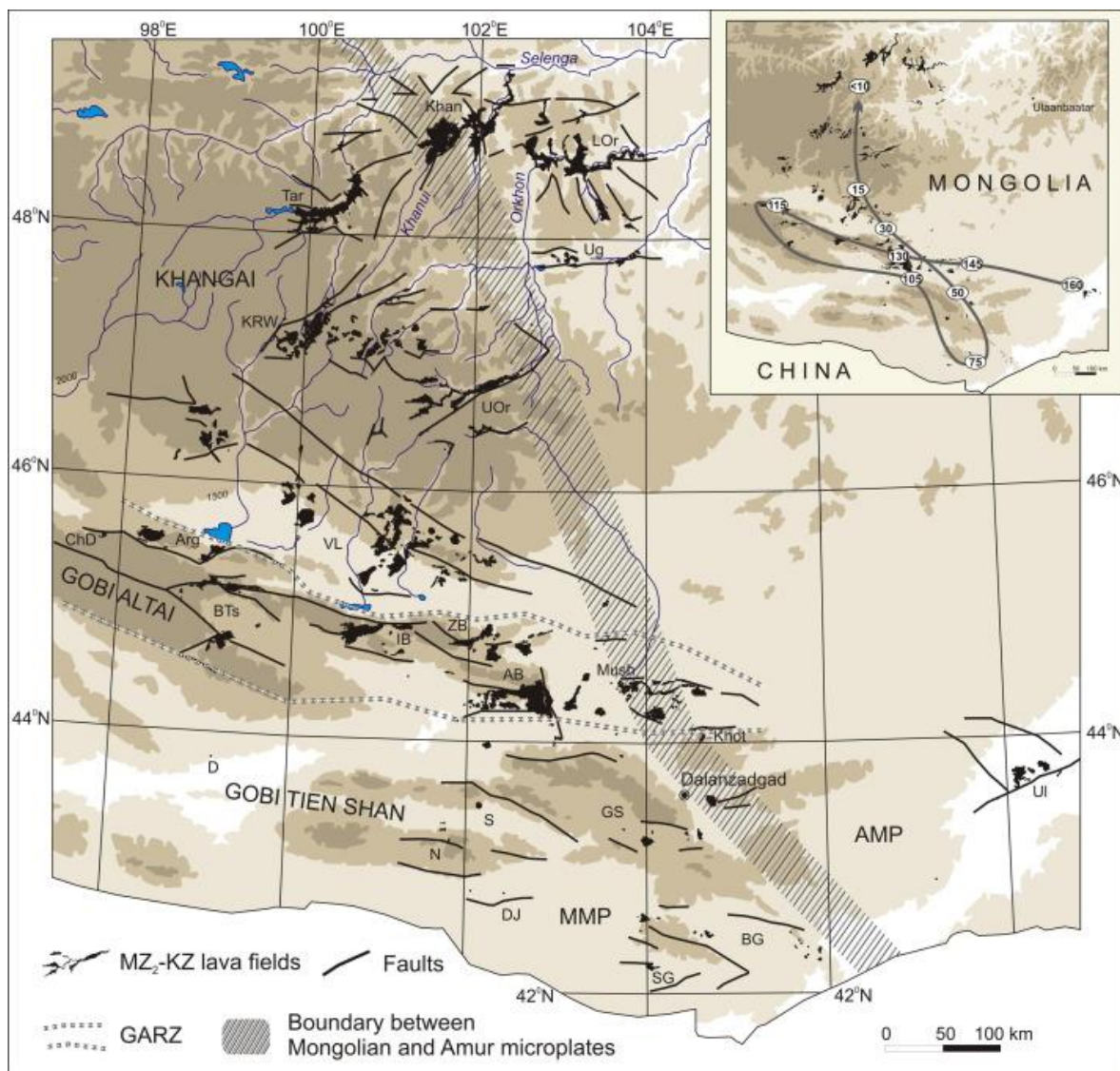


Figure 1.18: Sketch map from Yarmolyuk et al. (2015) of Mongolian volcanic fields; Inset diagram shows the temporal migration of volcanic centres.

1.7 SUMMARY

Numerous models have been proposed to explain the Mesozoic volcanism in Mongolia and the North China Craton (e.g., Meng, 2003; Yarmolyuk et al., 2015; Wang et al., 2006; Zhang, 2014; Dash et al., 2015; Bars et al., 2018). These models have either treated the volcanism in Mongolia and the North China Craton separately (e.g., Yarmolyuk et al., 2015) or as being connected (e.g., Wang et al., 2006; Dash et al., 2015). Furthermore, whether the volcanism was facilitated by the Palaeo-Pacific plate remains debated (e.g., Meng, 2003; Bars et al., 2018). Whether the Mongol-Okhotsk Oceanic plate influenced magmatism in Mongolia (e.g., from southern subduction or via slab break-off) is still uncertain (e.g., Meng, 2003;

Windley et al., 2010). Due to Mesozoic volcanism in Mongolia being comparatively understudied compared to neighbouring China (Yarmolyuk et al., 2005; Dash et al., 2015; Bars et al., 2018) much work can be done to improve our understanding of the volcanism.

CHAPTER 2

CONSTRAINING LITHOSPHERIC REMOVAL AND ASTHENOSPHERIC INPUT TO MELTS IN CENTRAL ASIA: A GEOCHEMICAL STUDY OF TRIASSIC TO CRETACEOUS MAGMATIC ROCKS IN THE GOBI ALTAI (MONGOLIA)

Throughout northeast China, eastern and southern Mongolia, and eastern Russia there is widespread Mesozoic intracontinental magmatism. Extensive studies on the Chinese magmatic rocks have suggested lithospheric mantle removal was a driver of the magmatism. The timing, distribution and potential diachroneity of such lithospheric mantle removal remains poorly constrained. This chapter examines successions of Mesozoic lavas and shallow intrusive volcanic plugs from the Gobi Altai in southern Mongolia that appear to be unrelated to regional, relatively small-scale deformation; at the time of magmatism, the area was ~200 km from any active margin, or, after its Late Jurassic-Early Cretaceous closure, from the suture of the Mongol-Okhotsk Ocean. $^{40}\text{Ar}/^{39}\text{Ar}$ radiometric age data place magmatic events in the Gobi Altai between ~220 to 99.2 Ma. This succession overlaps Chinese successions and therefore provides an opportunity to constrain whether Mesozoic lithosphere removal may provide an explanation for the magmatism here too, and if so, when.

Triassic to Lower Cretaceous lavas in the Gobi Altai (from Dulaan Bogd, Noyon Uul, Bulgantiin Uul, Jaran Bogd and Tsagaan Tsav) are all light rare-earth element (LREE) and large-ion lithophile element (LILE)-enriched, with negative Nb and Ta anomalies ($\frac{\text{Nb}}{\text{La}}$ and $\frac{\text{Ta}}{\text{La}} = <1$). Geochemical data suggest that these lavas formed by low degrees of partial melting of a metasomatised lithospheric mantle that may have been modified by melts derived from recycled rutile-bearing eclogite. A gradual reduction in the involvement of garnet in the source of these lavas points towards a shallowing of the depth of melting after ~125 Ma.

By contrast, geochemical and isotope data from the youngest magmatic rocks in the area — 107-99 Ma old volcanic plugs from Tsost Magmatic Field — have OIB-like trace element patterns and are interpreted to have formed by low degrees of partial melting of a garnet-bearing lherzolite mantle source. These rocks did not undergo significant crustal contamination and were derived from asthenospheric mantle. The evidence of a gradual shallowing of melting in the Gobi lava provinces, culminating in an asthenospheric source signature in the youngest magmatic rocks is similar to examples from neighbouring China, emphasising the wide-scale effect of a regional Mesozoic magmatic event during similar time periods. It is suggested that lithospheric thinning/delamination during the Mesozoic (between ~125 and ~107 Ma) enabled the generation of relatively small-scale asthenospheric-derived magmatism to predominate in the late Cretaceous.

*Sheldrick, T.C., Barry, T.L., Van Hinsbergen, D.J. and Kempton, P.D., 2018. Constraining lithospheric removal and asthenospheric input to melts in Central Asia: A geochemical study of Triassic to Cretaceous magmatic rocks in the Gobi Altai (Mongolia). *Lithos*, 296, pp.297-315.

2. INTRODUCTION & GEOLOGICAL BACKGROUND

To investigate the petrogenesis of the Mesozoic volcanism, the initial part of this study focusses on the distal limit of the Mesozoic volcanism, the Gobi Altai, located near the western end of the Mongol-Okhotsk Suture (**Fig. 2.1A**). In this area the volcanism occurred over a long-time frame (218.5-102.8 Ma), which included the closure of the Mongol-Okhotsk Ocean and events proceeding it, thus coinciding with key tectonic episodes. Samples were collected by previous researchers (Tiffany Barry, Douwe van Hinsbergen and Scott Dempsey) from 6 locations; Jaran Bogd in the west to Dulaan Bogd, Bulgantiin Uul, Noyon Uul, Tsost Magmatic Field and Tsagaan Tsav in the east (**Fig. 2.1B**). This study focuses on the Artsa-Bogd, Baga Bogd and Ih Bogd area of the Gobi Altai. Artsa-Bogd is an east-west graben with basaltic lavas overlying Cretaceous red beds. Ih Bogd and Baga Bogd are Cenozoic restraining bends that expose crystalline basement as well as Mesozoic to Cenozoic sedimentary rocks. Mafic lavas from the summit of Ih Bogd to the west of Baga Bogd and Artsa Bogd were dated at 198 ± 8 Ma and 193 ± 7 Ma and apatite fission track ages of rocks from the summit of Ih Bogd are Jurassic ~ 150 Ma or older, indicating minimal erosion of between 1 – 3 km since the Jurassic (^{40}Ar - ^{39}Ar ; Jolivet et al., 2007). Ih Bogd, Baga Bogd and Artsa Bogd crystalline basement is unconformably overlain by up to ≤ 1500 m of Cretaceous mafic volcanics which are interbedded with fluvial sandstones and lacustrine clay deposits (van Hinsbergen et al., 2008). The successions at Artsa Bogd are flat-lying or only slightly tilted, suggesting little post-Cretaceous tectonic deformation (Hankard et al., 2007) and where erosion has exposed volcanic plugs at Tsost Magmatic Field there is impressive columnar jointing (**Fig. 2.2**). A palaeolatitude position of 48.2°N has been given for the Gobi Altai between ~ 125 to 95 Ma (van Hinsbergen et al., 2008). From west to east, the lavas have been dated by ^{40}Ar - ^{39}Ar geochronology; the Jaran Bogd sequence gave ages ranging from ~ 125 to 118 Ma; Dulaan Bogd yielded an age of 218.5 ± 1.5 Ma; Bulgantiin Uul sequence yielded ages of 124.3 ± 0.9 and 122.7 ± 0.8 Ma (van Hinsbergen et al., 2008 and 2015) and those from Tsagaan Tsav yielded ages of 120.4 ± 1.1 and 117.7 ± 1.7 Ma (Barry, 1999). No age constraints are available for Noyon Uul in the south. The shallow intrusive plugs from Tsost Magmatic Field yield the youngest ages from the Gobi Altai region, with ages between 107.4 ± 0.9 and 99.3 ± 0.8 Ma (Barry, 1999).

The lavas and shallow plugs, other than those at Noyon Uul, overlie the Gobi Altai terrane which is a long narrow belt extending east into China and is composed of greenschist facies metamorphosed sandstone, mudstone, tuff and older volcanic rocks which are intruded by

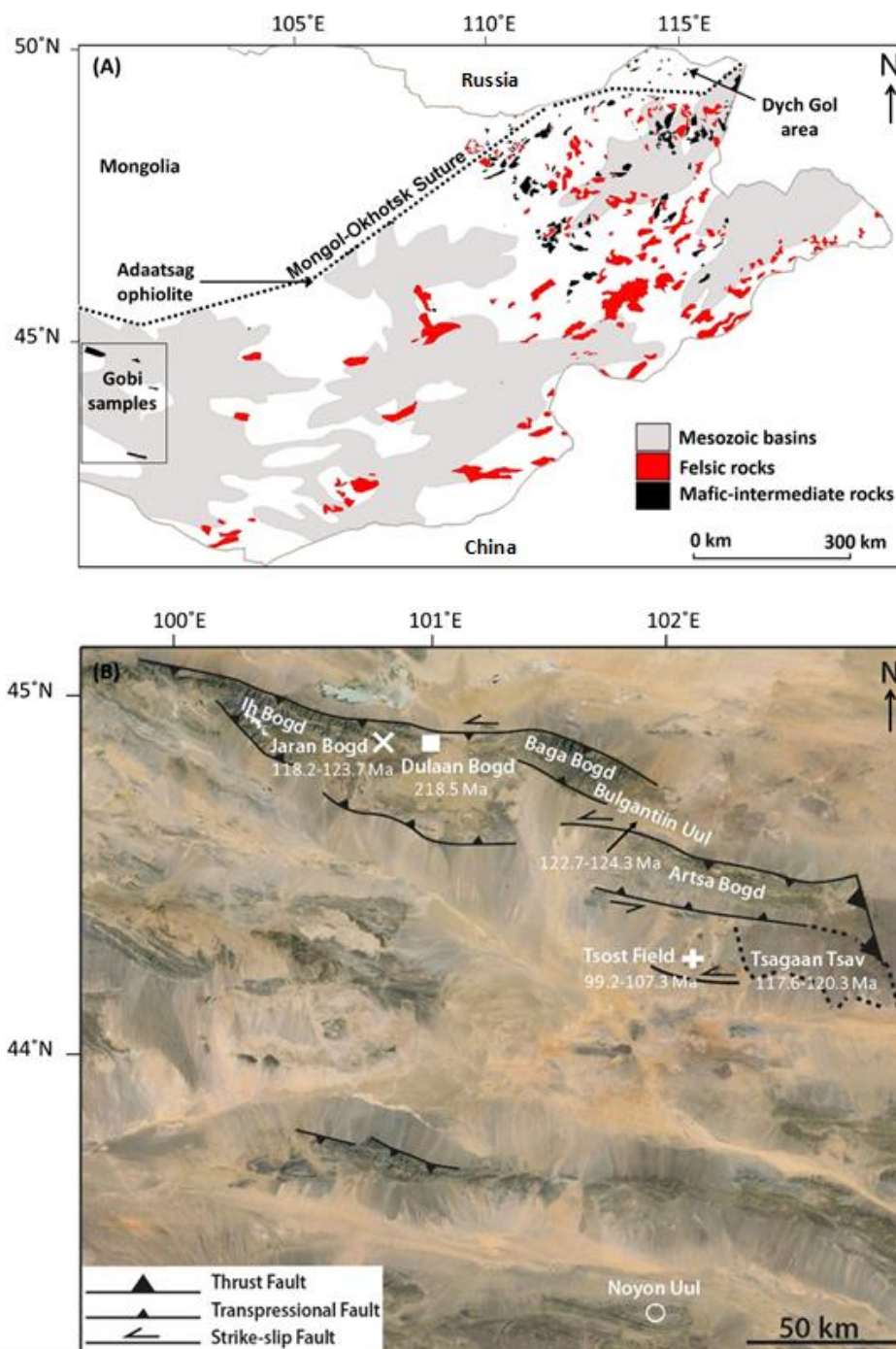


Figure 2.1: (A) A sketch map of Mongolia showing the sample area (boxed area) and the distribution of Mesozoic mafic to intermediate lavas. Felsic magmatism is also shown, but age relationships are often not established. The distribution of volcanism is based on Mongolian government geological maps and field observations. The distribution of Mesozoic sedimentary basins is from Johnson et al. (2003). (B) A portion of the Gobi Altai showing our field localities (Google Earth). Information on the distribution of faults is taken from van Hinsbergen et al. (2008).

Carboniferous and Permian granites. In the far south of the area, Noyon Uul (King Mountain) is on the Atasbogd terrane (backarc/forearc basin) consisting of Cambrian

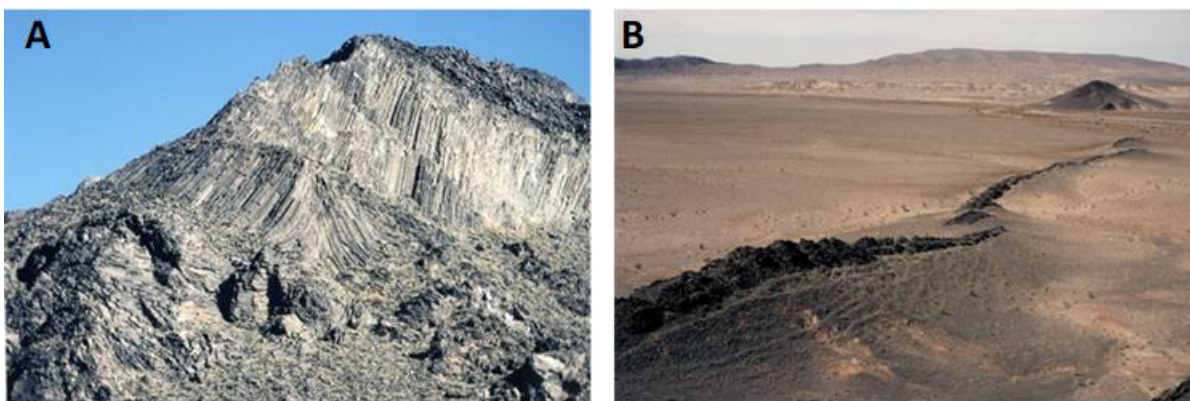


Figure 2.2: Photographs of Tsost Magmatic Field: (A) showing impressive columnar jointing and (B) an en echelon ending at a small volcanic plug in the distance.

greenschist facies, mudstone, limestone, Devonian pillow basalts, Cretaceous volcanic and sedimentary rocks and granite plutons (Badarch et al., 2002). Noyon Uul is a syncline and the dominant strata consist of fluvial and lacustrine facies. A Middle-Late Jurassic deformation phase was recognised based on a regional unconformity between Middle and Upper Jurassic rocks. The sedimentary attributes of the Noyon Uul strata were interpreted to be either foreland in origin or alternatively related to strike-slip faulting (Hendrix et al., 1996).

2.1 PETROGRAPHY

The Gobi lavas are porphyritic, vesicular and contain amygdales of carbonate and siliceous material (**Fig 2.4-2.7**). All Dulaan Bogd samples are holocrystalline while Bulgantiin Uul, Jaran Bogd and Tsagaan Tsav samples are holo- to hypocrySTALLINE. All the Noyon Uul samples are hypocrySTALLINE. There are phenocrysts of plagioclase, clinopyroxene and iddingsitised olivine. Glomerocrysts of altered olivine and clinopyroxene were identified in samples from Bulgantiin Uul, Jaran Bogd and Tsagaan Tsav. Rare xenocrysts of plagioclase crystals were identified in Bulgantiin Uul samples. The groundmass consists of iddingsitised olivine, clinopyroxene, plagioclase, opaque crystals and in some cases glass. There are samples from all magmatic provinces that have flow-aligned plagioclase crystals. Clinopyroxene subophitically encloses plagioclase in Jaran Bogd, Bulgantiin Uul and Tsagaan Tsav lavas. The Noyon Uul lavas also contain accessory apatite. In all samples olivine is fully or partially altered to iddingsite, whereas clinopyroxene and plagioclase are partially altered. Overall, Dulaan Bogd, Bulgantiin Uul and Jaran Bogd lavas are the least altered (approximately 2 to 32% altered), whereas Noyon Uul and Tsagaan Tsav lavas are

the most altered (approximately 10 to 40% altered). Most of this alteration is of specific phases; however, localised groundmass and glass alteration occurs in samples from all magmatic provinces.

Tsost Magmatic Field basalt samples (**Fig. 2.3**) are porphyritic, holocrystalline and hypocrySTALLINE, contain amygdales of zeolites and are generally fresher than the other sample localities (approximately 1 to 18% altered). There are phenocrysts of plagioclase, clinopyroxene and iddingsitised olivine (many only partially altered). Clinopyroxene and olivine crystals appear as glomeroporphyritic clusters. Skeletal hopper olivine crystals suggest quenching happened despite these basalts being intrusive. The groundmass consists of olivine, clinopyroxene, plagioclase feldspar, opaque crystals and, in some cases, glass.

Granulite crustal xenoliths were observed at Tsagaan Tsav and more rarely in Tsost Magmatic Field, but the latter also contains xenoliths consisting of plagioclase and pyroxene crystals.

Detailed sample specific descriptions are reported in Table 2.1.

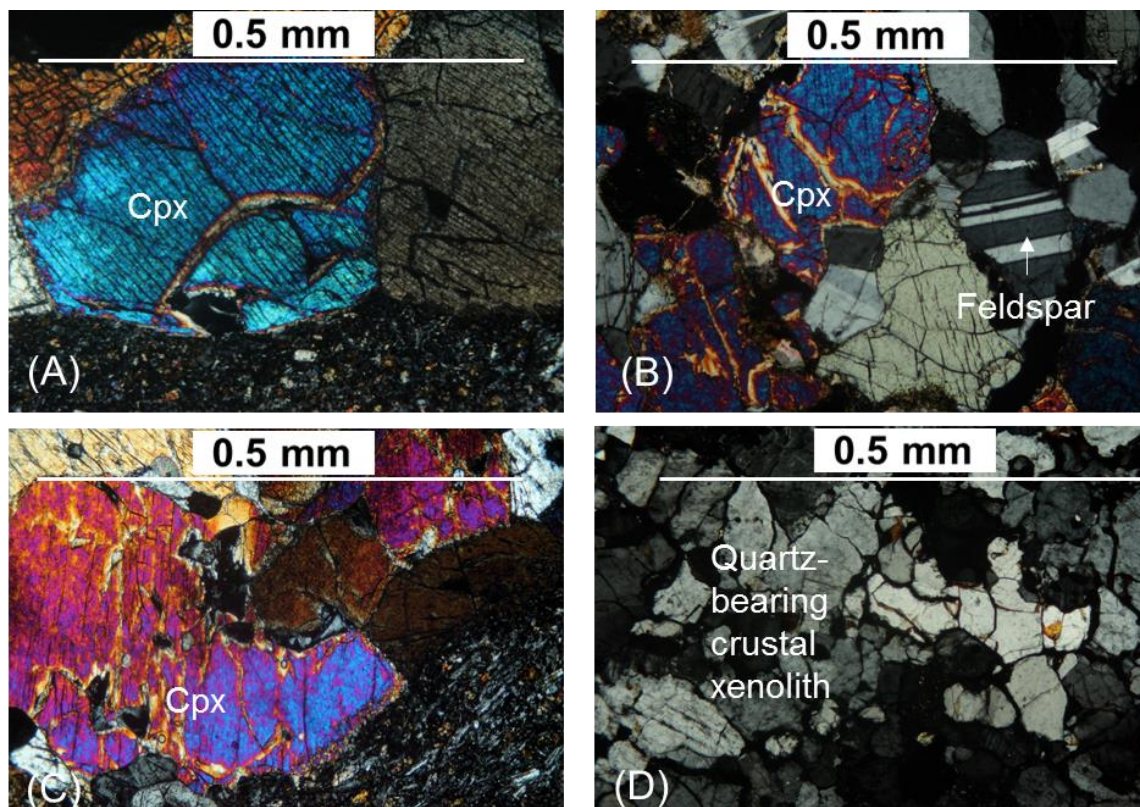


Figure 2.3: Photomicrographs of Tsost Magmatic Field basalts: (A) Pyroxene-rich xenolith; (B) pyroxene and feldspar bearing xenolith; (C) Pyroxene-rich xenolith and (D) Quartz-bearing crustal xenolith.

Table 2.1 – Petrology (thin section studies)

Sample	Phenocrysts %	Estimated groundmass modal composition:				Alteration %	Texture	Comments
		Ol	Cpx	Plag	Opq			
Tsost Magmatic Field:								
TB95-6.3	Ol (12%) + Cpx (17%)	-	-	65	6	1	Glom, seriate & amy	Glomeroporphyritic Ol. Flow banding of Plag. Zeolite infilling vesicle. Bowlingite alteration.
TB95-6.3.3	Ol (1%) + Cpx (1%)	19	20	57	2	1	Seriate	Skeletal Ol.
TB95-6.3.3i	Ol (20%)	-	30	46	4	-	Seriate	Flow banding of Plag. Sanidine xenocryst in disequilibrium.
TB95-6.3.4	Ol (21%) + Cpx (9%)	-	23	44	3	-	Seriate & amy	Zeolite infilling vesicles.
TB95-6.3.5	Ol (11%) + Cpx (2%)	-	7	48	15	-	Porh	Flow aligned Plag.
TB95-7.1.2	Ol (2%) + Plag (1%)	9	20	60	8	8	Glom & porh	Porphyritic Plag. Flow alignment of Plag. Glomeroporphyritic Cpx. Iddingsitised Ol.
TB95-7.1.6	Ol (3%)	9	19	65	4	6	Glom & amy	Flow aligned Plag. Glomeroporphyritic Cpx. Iddingsitised Ol. Zeolite infilling vesicle.
TB95-7.1.7	Ol (5%)	3	30	50	12	-	Glom & porh	Glomeroporphyritic Cpx.
TB95-9.1	Ol (5%) + Cpx (1%)	-	24	38	5	1	Hyp & porh	
TB95-9.4	Ol (6%)	13	17	60	4	18	Porh	Subophitic feldspars in Cpx. Skeletal Ol.
TB95-9.5.2	Plag (2%)	-	-	40	5	-	Seriate	Flow banding.

Sample	Phenocrysts %	Ol	Cpx	Plag	Opq	Alteration %	Texture	Comments
Tsagaan Tsav:								
TB95-8.1	Ol (8%)	20	-	72	1	40	Hyp & amy	Sericite and iddingsite alteration. Carbonate inclusions.
TB95-8.2	-	14	16	56	7	16	Hol	Sericite and iddingsite alteration. Flow-aligned Plag.
TB95-8.7	Cpx (5%)	17	9	65	4	16	Hol	Subophitic. Flow-aligned Plag.
TB95-11.6	Plag (22%)	12	6	58	2	11	Hyp & glom	Glomeroporphyritic Ol. Iddingsitised Ol.
Jaran Bogd:								
JB1	Cpx (2%)	4	23	70	1	10	Hol & porh	Some Cpx encloses Plag (subophitic). Iddingsitised Ol & Cpx partially altered.
JB3	Ol (5%)	15	20	58	2	10	Hol & porh	Microphenocrysts of Ol. Plag locally aligned. Iddingsitised Ol & Cpx partially altered.
JB7	-	15	23	60	2	15	Hol	Some Cpx encloses Plag (subophitic). Iddingsitised Ol & Cpx partially altered.
JB8	Cpx (5%) + Plag (5%)	5	22	60	3	5	Hol, glom & porh	Some Cpx encloses Plag (subophitic). Iddingsitised Ol & Cpx partially altered.
JB12	-	-	3	95	2	2	Hyp	
JB17	Ol (2%) + Plag (1%)	18	5	69	5	20	Hol & porh	Iddingsitised Ol.

Sample	Phenocrysts %	Ol	Cpx	Plag	Opq	Alteration %	Texture	Comments
JB26	-	13	35	45	2	13	Hol & amy	Amygdales filled with clay material. Cpx encloses Plag (subophitic). Convolute zoning in Plag. Iddingsitised Ol.
JB38	-	23	25	50	2	20	Hol	Some Cpx encloses Plag (subophitic). Iddingsitised Ol.
JB46	-	25	13	60	2	20	Hol	Some Cpx encloses Plag (subophitic). Iddingsitised Ol.
JB69	-	20	28	50	2	20	Hol	Some Cpx encloses Plag (subophitic). Iddingsitised Ol.
JB94	Plag (5 %)	15	8	69	3	15	Hol & porh	Cpx encloses Plag (subophitic). Convolute zoning in Plag phenocrysts. Iddingsitised Ol.
Bulgantiin Uul:								
BU3	Ol (30%) + Plag (10%)	-	5	35	20	32	Hol & porh	Cpx encloses Plag (subophitic). . Iddingsitised Ol & saussurization of Plag.
BU9	Ol (3%) + Plag (5%)	5	3	64	20	8	Hol & porh	Xenocryst of Plag crystals. Flow aligned Plag.
BU22	Plag (10%)	8	10	60	12	8	Hol & porh	Zoning in Plag phenocrysts. Iddingsitised Ol.
BU23	Plag (5%)	25	20	50	5	30	Hyp, porh & amy	Zoning in Plag phenocrysts. Amygdales of carbonate & clay material. Iddingsitised Ol, saussurization of Plag.
BU35	Ol (10%) + Plag (10%)	5	10	40	25	13	Hol, glom & porh	Glomerocrysts of Ol & Cpx. Zoning in Plag phenocrysts. Iddingsitised Ol, saussurization of Plag & accessory aegirine.
BU56	Plag (3%)	15	10	62	10	15	Hol, porh & amy	Amygdales of carbonate & clay material. Iddingsitised Ol.

Sample	Phenocrysts %	Ol	Cpx	Plag	Opq	Alteration %	Texture	Comments
BU119	-	20	3	60	17	20	Hol	Iddingsitised Ol.
BB2	Plag (5%)	20	7	65	3	24	Hyp & porh	Iddingsitised Ol & saussuritization of Plag. Some veins of carbonate material.
WB4	-	14	3	80	3	10	Hol	Iddingsitised Ol.
Noyon Uul:								
11-1	Plag (1%)	20	15	62	2	35	Hyp, porh & amy.	Plag phenocrysts show reabsorption features. Amygdales of clay material. Glass is altered in places. Iddingsitised Ol & alteration of Plag & Cpx. Accessory apatite.
11-2	-	12	8	70	10	20	Hyp & amy	Flow aligned Plag. Amygdales of quartz & carbonate. Accessory apatite.
11-4	-	17	21	60	2	30	Hyp	Iddingsitised Ol & alteration of Plag & Cpx.
11-5	-	6	4	75	15	25	Hyp & amy	Flow aligned Plag. Amygdales of quartz. Iddingsitised Ol, alteration of Plag & Cpx. Glass is altered in places.
11-6a	-	6	11	79	4	10	Hyp & amy	Flow aligned Plag. Amygdales of carbonate. Iddingsitised Ol, alteration of Plag & Cpx. Glass is altered in places.
11-6b	-	10	5	80	5	15	Hyp	Flow aligned Plag and zoned. Veins of carbonate. Iddingsitised Ol, alteration of Plag & Cpx.
Dulaan Bogd:								
DB4	-	13	5	80	2	13	Hol	Iddingsitised Ol.

Sample	Phenocrysts %	Ol	Cpx	Plag	Opq	Alteration %	Texture	Comments
DB5	Ol (3%) + Plag (2%)	5	2	80	8	10	Hol & porh	Carbonate inclusions. Iddingsitised Ol.
DB6	-	13	9	75	3	15	Hol	Flow aligned Plag. Iddingsitised Ol.
DB7	-	10	8	80	2	12	Hol	Iddingsitised Ol & minor alteration of Plag.
DB8	-	15	7	75	3	17	Hol	Iddingsitised Ol & minor alteration of Plag.
DB10	-	17	13	68	2	20	Hol	Iddingsitised Ol.
DB11	-	14	10	75	1	20	Hol	Iddingsitised Ol & minor alteration of Cpx & Plag.
DB12	-	15	8	75	2	18	Hol	Iddingsitised Ol & minor alteration of Plag.
DB13	-	16	14	68	2	18	Hol	Iddingsitised Ol & minor alteration of Cpx & Plag.
DB14	-	15	26	50	4	20	Hol	Iddingsitised Ol & minor alteration of Plag.

Ol, olivine; Cpx, clinopyroxene; Plag, plagioclase; Opq, opaques; Hol, holocrystalline; Hyp, Hypocrystalline; Porh, porphyritic; Amy, amygdaloidal; Glom, glomerophyritic.

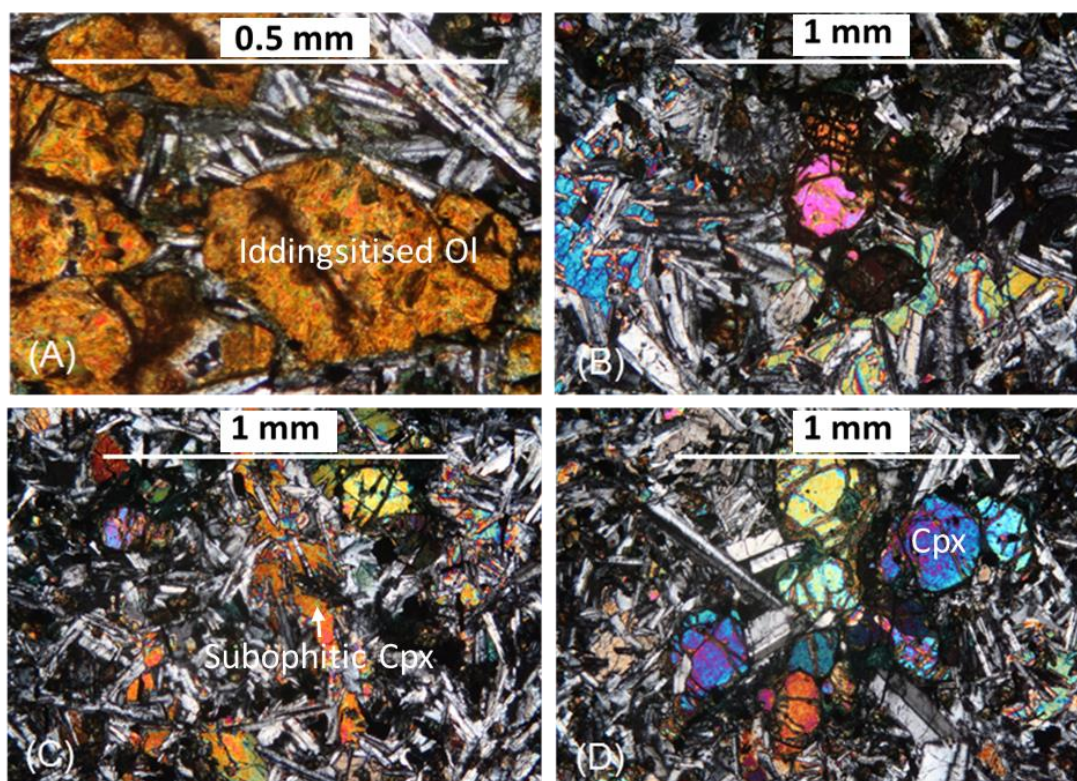


Figure 2.4: Photomicrographs of Jaran Bogd lavas: (A) Iddingsitised olivine phenocrysts; (B) iddingsitised olivine phenocrysts and subophitic clinopyroxene enclosing plagioclase; (C) subophitic clinopyroxene enclosing plagioclase and (D) glomerocrysts of clinopyroxene

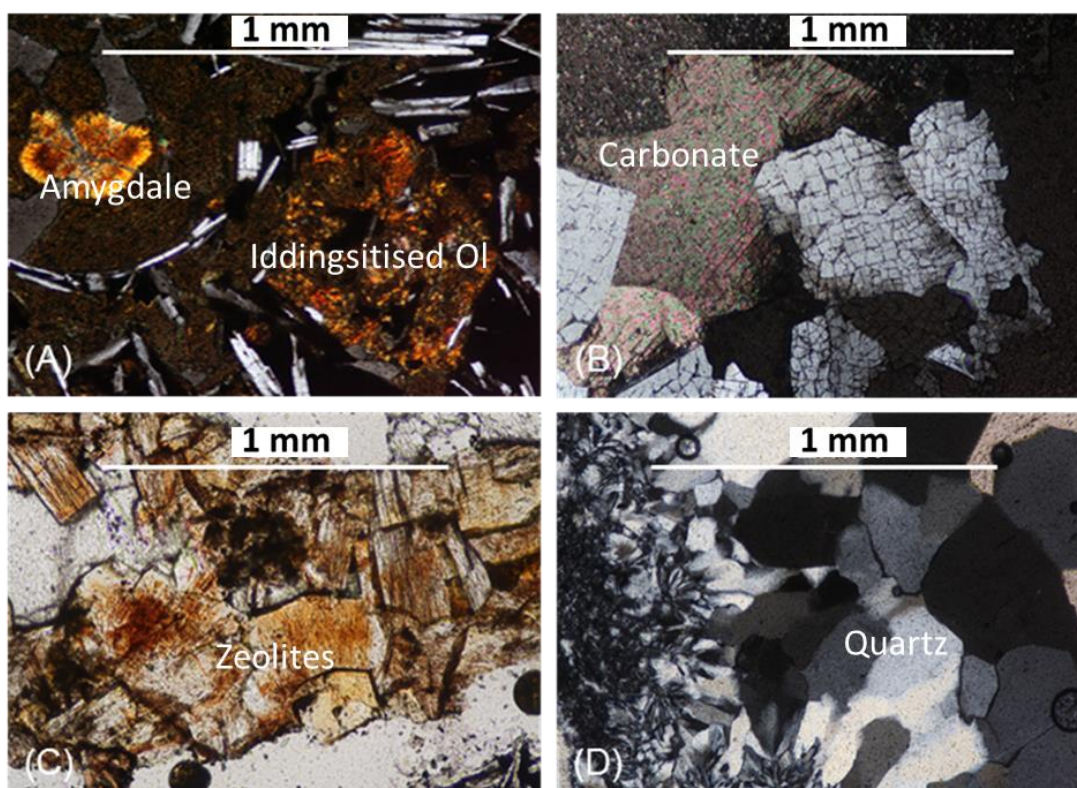


Figure 2.5: Photomicrographs of Noyon Uul lavas: (A) an amygdale filled with clay minerals with plagioclase laths around it. An iddingsitised olivine phenocryst is visible in right corner; (B) carbonate amygdale; (C) veins of altered zeolite minerals and (D) a quartz amygdale.

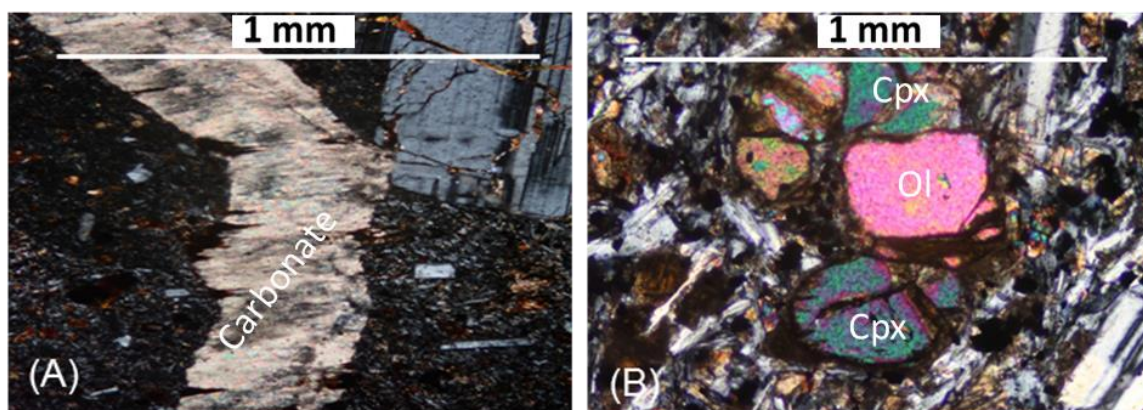


Figure 2.6: Photomicrographs of Bulgantiin Uul lavas: (A) part of a carbonate vein and (B) olivine and clinopyroxene phenocrysts.

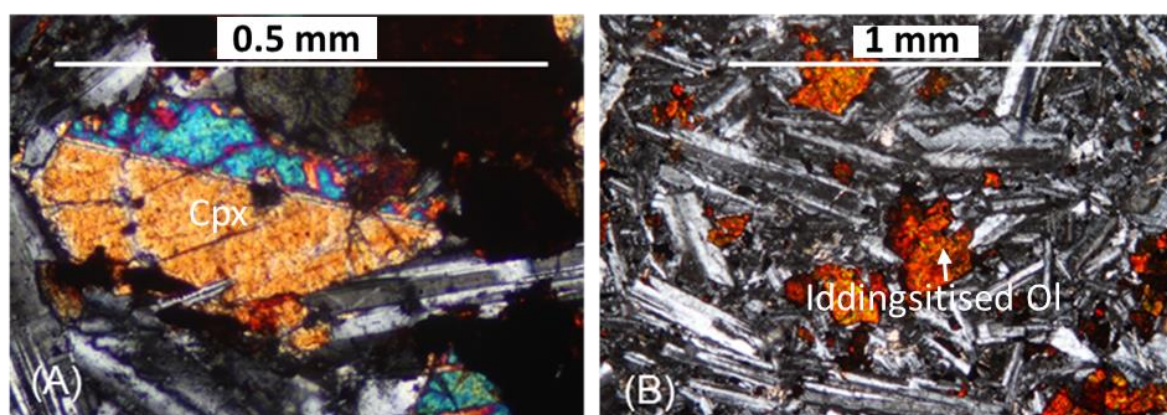


Figure 2.7: Photomicrographs of Dulaan Bogd lavas: (A) a altered twinned clinopyroxene phenocryst and (B) iddingsitised olivine and plagioclase laths.

2.2 GEOCHEMISTRY OF THE GOBI LAVAS AND INTRUSIVES

2.2.1 Major-element variations

Petrological observations reported above indicate that most phenocrysts and groundmass material had undergone at least some alteration. More than half the samples studied have <2 wt. % LOI (loss on ignition) values, suggesting they have not undergone extensive alteration. All of the Noyon Uul samples have LOI values >2 wt. %, whereas the other lava fields show evidence for more variable degrees of alteration. LOI versus trace-element plots show that many mobile elements (e.g. Rb, Ba, Pb, Na) have been affected by alteration (**Fig. 2.8**).

To classify the alkaline lavas and intrusive rocks a Total Alkali Silica (TAS) plot is used (**Fig. 2.9**). Although alteration will result in loss of some alkalis (**Fig. 2.8 D & E**) the lavas still plot in the alkaline fields (**Fig. 2.9**) and thus this classification is deemed suitable. Tsost Magmatic Field samples plot in the trachybasalt and basaltic trachyandesite fields. Most

of the localities exhibit a similar range in composition, with the majority of samples plotting in the basaltic trachyandesite field. Some samples from Noyon Uul, Bulgantiin

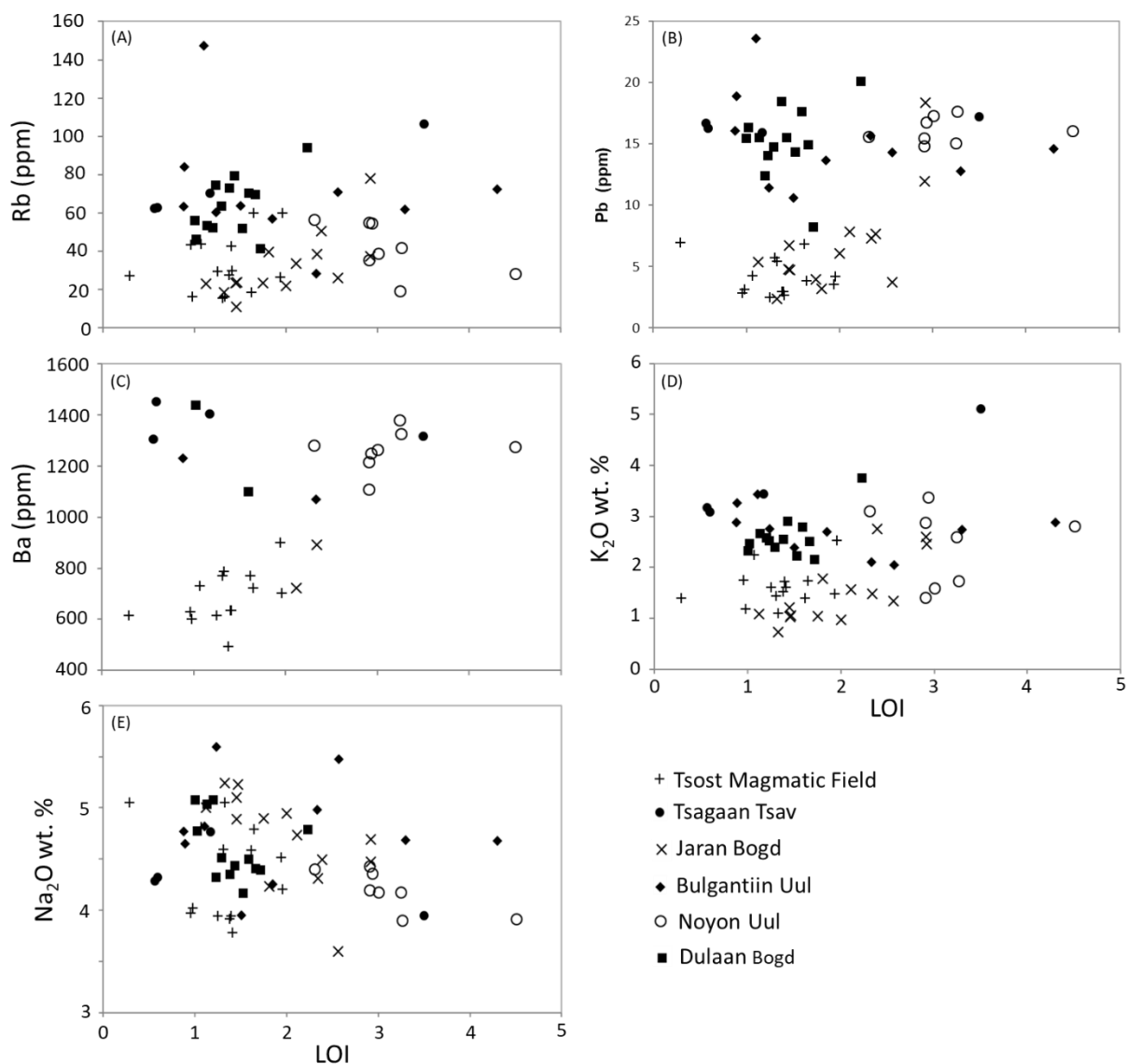


Figure 2.8: LOI vs. trace and major-elements plots for the Gobi Altai lavas and intrusives.

Uul and Tsagaan Tsav plot in the basanite (8 samples) or phonotephrite (2 samples) fields. On a normative Ne-Ol-Di-Hy-Qz diagram, most of the samples plot in the nepheline-normative and hypersthene-normative fields, but 12 samples plot in the quartz-normative field (**Fig. 2.10A**). However, the samples that plot in the quartz-normative field have low amounts of MgO (<3 wt. %) and a clear trend can be seen for some volcanic provinces (Tsost Magmatic Field, Jaran Bogd and Dulaan Bogd) going from nepheline-normative to quartz-normative as the melts become increasingly evolved (**Fig. 2.10B**).

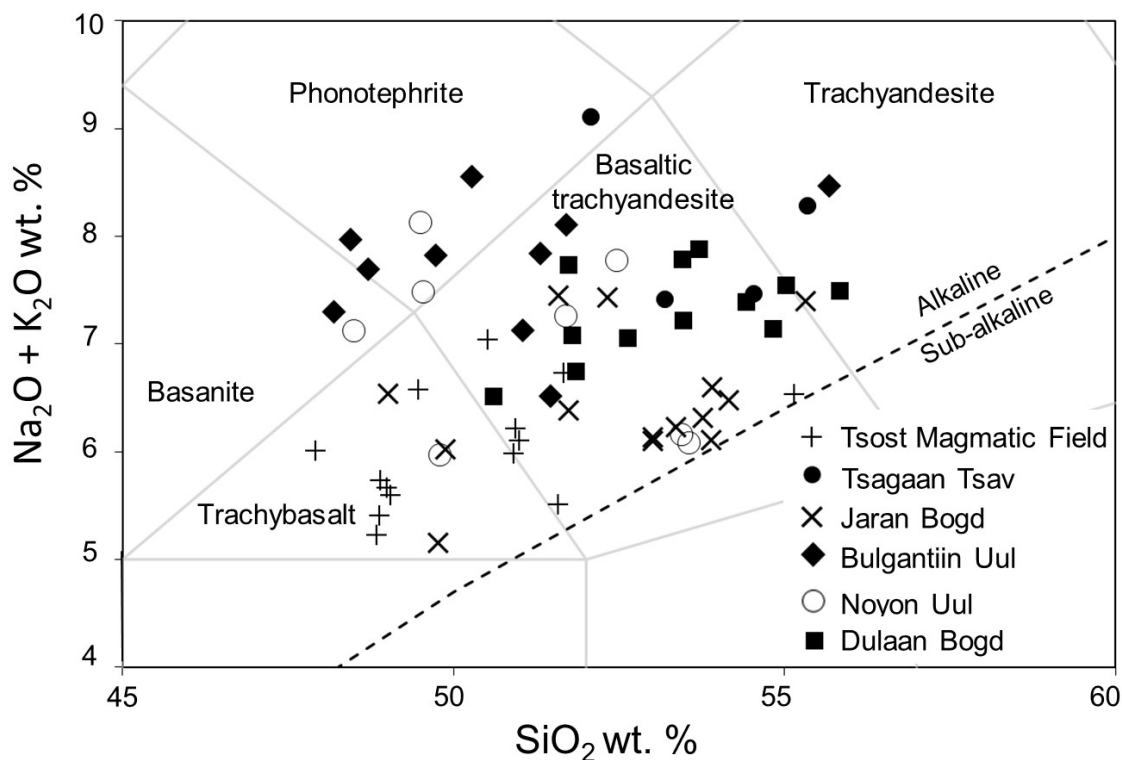


Figure 2.9: A Total Alkali Silica (TAS) diagram from LeBas et al. (1986) with the alkaline and sub-alkaline dividing line from Irvine and Baragar (1971) also shown.

Samples are variably evolved with MgO contents ranging from 0.44 to 8.25 wt. % depending on locality: Tsost Magmatic Field basalts have Mg-numbers (equation 1) between 43 and 68. Excluding Noyon Uul, the lavas have Mg-numbers between 27 and 56 (**Fig. 2.11**); Noyon Uul samples have Mg-numbers between 7 and 33. Generally Fe₂O₃ (T) does not vary as a function of Mg-number, except for Noyon Uul samples, which show a negative trend with increasing Mg-number (**Fig. 2.11C**). Samples from all locations show a positive trend between Mg-number and CaO contents, and CaO/Al₂O₃ ratios (**Fig. 2.11F & I**).

2.2.2 Trace-element and REE variations

Cr contents correlate positively with Mg-number (**Fig. 2.11H**). Tsost Magmatic Field basalts have the highest Cr concentrations with values ranging from 89 to 219 ppm, while Dulaan Bogd lavas have 47 to 177 ppm, Noyon Uul 6 to 110 ppm, Bulgantiin Uul 10 to 51 ppm, Jaran Bogd 17 to 187 ppm and Tsagaan Tsav 27 to 34 ppm.

Ni concentrations also increase with Mg-number (**Fig. 2.11G**). Tsost Magmatic Field basalts have Ni concentrations between 59 to 98 ppm, while Dulaan Bogd lavas have

values between 16 to 127 ppm, Noyon Uul 17 to 51 ppm, Bulgantiin Uul 10 to 50 ppm, Jaran Bogd 22 to 147 ppm and Tsagaan Tsav 34 to 45 ppm.

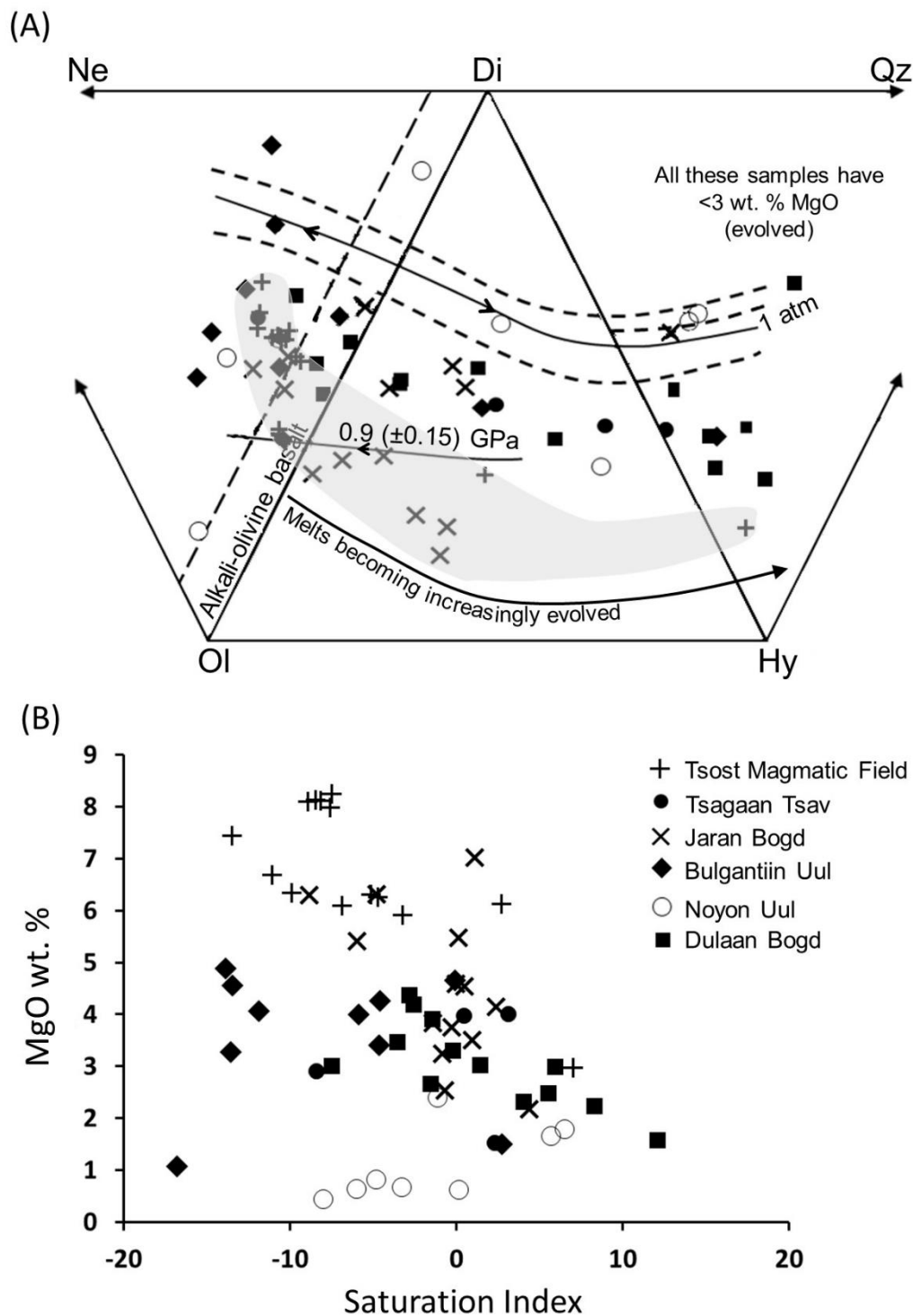


Figure 2.10: (A) a normative Ne-Ol-Di-Hy-Qz diagram using $\text{Fe}_2\text{O}_3/\text{FeO} = 0.2$. 1 atm and 0.9 GPa cotectics from Thompson et al. (2001); arrows point in the direction of decreasing temperature. Most samples plot below the 1 atm bar. The shaded area shows where the Tsost Magmatic Field basalts plot and highlights that many of the Jaran Bogd lavas show a similar distribution. (B) Saturation index (SI) versus MgO plot. $\text{SI} = 100(\text{Si} - (\text{Al} + \text{Fe}_2 + \text{Mg} + 3\text{Ca} + 11\text{Na} + 11\text{K} + \text{Mn} - \text{Fe}_3 - \text{Ti} - 4\text{P})/2)$ where Si, Al etc. are weight percent oxides divided by their respective molecular weights (Fitton et al., 1991). Fe_2O_3 wt. % was calculated from total Fe using $\text{Fe}_2\text{O}_3/(\text{Fe}_2\text{O}_3 + \text{FeO}) = 0.2$. Critically saturated basalts (neither hy- nor ne-normative) have $\text{SI} = 0$; under-saturated compositions (ne-normative) have $\text{SI} < 0$; saturated to over-saturated basalts have $\text{SI} > 0$.

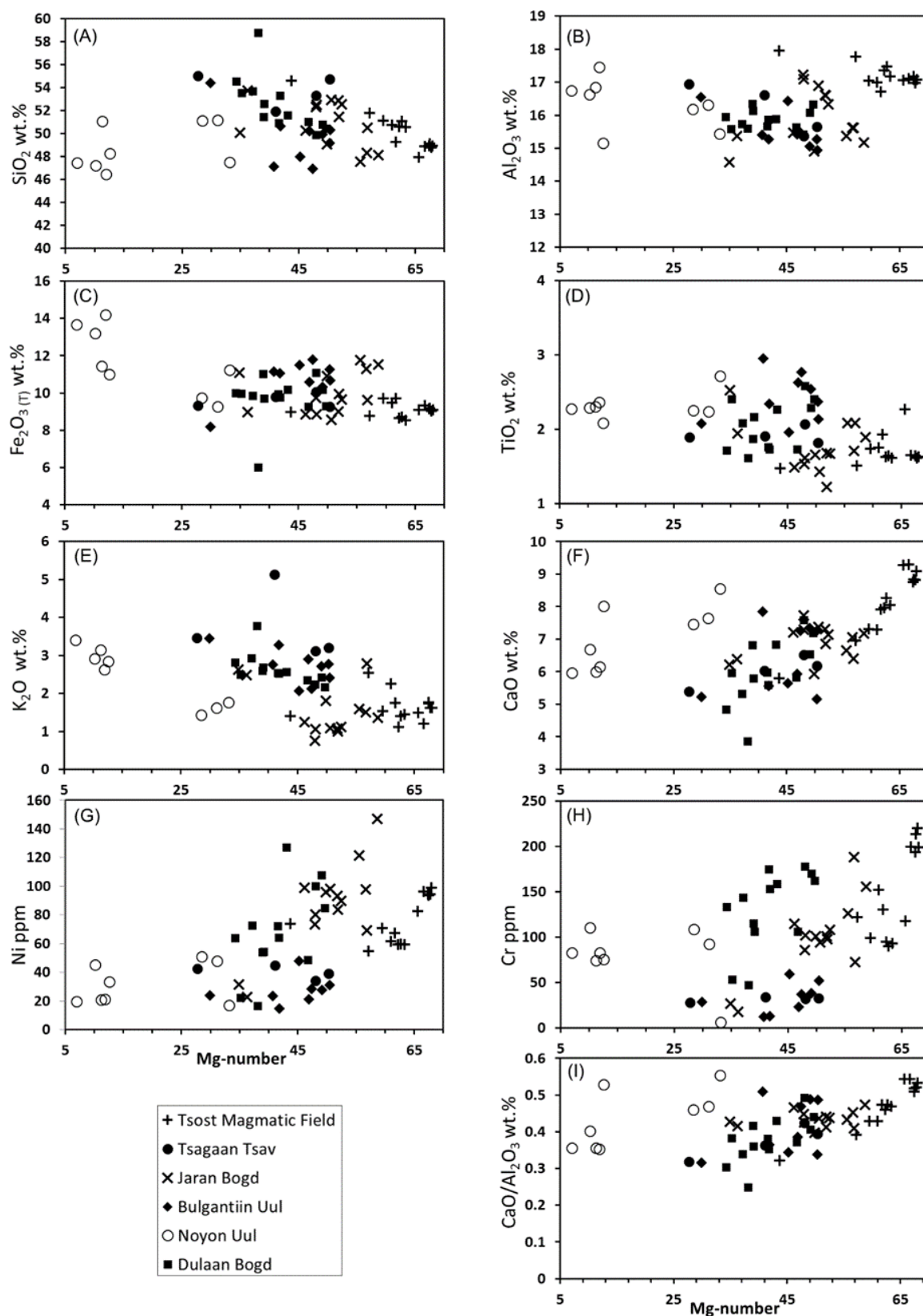


Figure 2.11: Variations in major-element oxides, compatible trace elements and CaO/Al₂O₃ with Mg-number (Mg-number $100 \times \left(\frac{\text{MgO}}{40.3}\right) / \left(\left(\frac{\text{MgO}}{40.3}\right) + \left(\frac{\text{FeO}}{71.85}\right)\right)$. FeO is calculated using a Fe₂O₃/FeO ratio of 0.2 ($\text{FeO} = \left(\frac{\text{Fe}_2\text{O}_3(\text{T})}{1 + \left(\frac{0.2}{1.111}\right)}\right) / 1.111$).

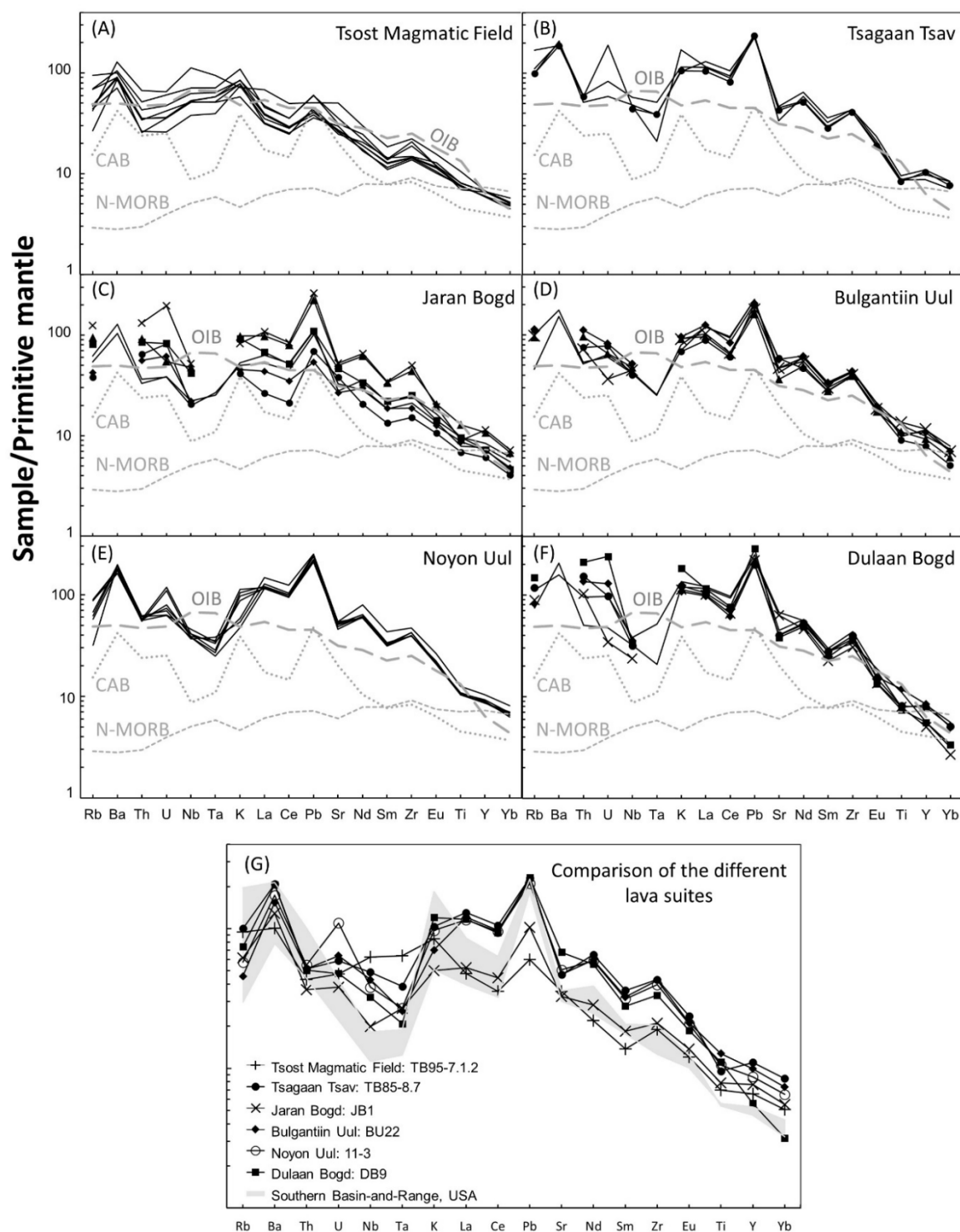


Figure 2.12: Primitive mantle-normalised trace element variation diagrams for the different lava suites. Normalization values for the primitive mantle from Sun and McDonough (1989) and the Pb normalization value used was 0.071. Data sources: average N-MORB: Gale et al. (2013); average OIB: Sun and McDonough (1989); average continental arc basalt (CAB): Kelemen et al. (2003); southern Basin-and-Range basaltic volcanism from Bradshaw et al. (1993).

All samples are enriched in the light rare earth elements (LREE) compared to normal mid-ocean ridge basalt (N-MORB) compositions and have elevated LREE relative to heavy rare earth elements (HREE).

Primitive mantle-normalised diagrams (**Fig. 2.12**) show that the samples are enriched in the high field strength elements (HFSE) and the large-ion lithophile elements (LILE) compared with N-MORB. However, the LILE are susceptible to alteration and given the degree of alteration of most samples (described above), original concentrations may have been changed. Except for Tsost Magmatic Field basalts, the lavas show prominent negative Nb and Ta anomalies, a feature commonly observed in island-arc volcanics, along with enrichment in the fluid-mobile incompatible trace elements such as the LILE (e.g., Rb, Ba, K). Throughout the sample suites, some samples have positive Ba, Pb and Zr anomalies, but these are less prominent in the Tsost Magmatic Field basalts. Some lavas also have negative Sr and Ti anomalies. However, unlike volcanic arc lavas, the Gobi samples are enriched in incompatible trace elements like Zr.

Similarities between an average continental arc basalt (CAB; **Fig 2.12 B-F**) and the Southern Basin-and-Range (USA; **Fig 2.12G**) lavas with the Gobi lavas are seen in the mirroring of positive and negative anomalies. This enrichment of Rb, Ba and K in the Basin-and-Range lavas has been attributed to melting of metasomatised lithospheric mantle (e.g., Fitton et al., 1991; Kempton et al., 1991). The lack of a negative Nb and Ta anomaly and a much weaker positive Pb anomaly for Tsost Magmatic Field basalts is comparable to ocean island basalt (OIB; **Fig. 2.12A**).

DATA INTERPRETATION

2.3 FRACTIONAL CRYSTALLISATION

The correlation of Cr and Ni with Mg-number likely reflects fractionation of olivine and Cr-spinel; in addition, fractionation of clinopyroxene is evident from decreasing CaO/Al₂O₃ ratios with Mg-number (**Fig. 2.11I**). Such a fractionation assemblage is supported by petrological observations which show olivine and clinopyroxene as the most common phenocryst phases. There does not seem to have been significant plagioclase fractionation for Tsost Magmatic Field basalts as shown by chondrite normalised Eu/Eu* numbers ($Eu/Eu^* = \frac{Eu_N}{Sm_N + Gd_N \cdot 0.5}$) ranging from 0.98-1.06. However, most of the other volcanic provinces exhibit negative Sr anomalies on primitive mantle plots and have Eu/Eu* numbers ranging from 0.72-0.83 for Dulaan Bogd, 0.76-0.81 for Noyon Uul, 0.78-0.87 for Bulgantiin Uul, 0.74-0.97 for Jaran Bogd and 0.80-0.87 for

Tsagaan Tsav, indicative of varying degrees of plagioclase fractionation. The presence of opaque minerals identified during petrological studies suggests fractionation of oxides.

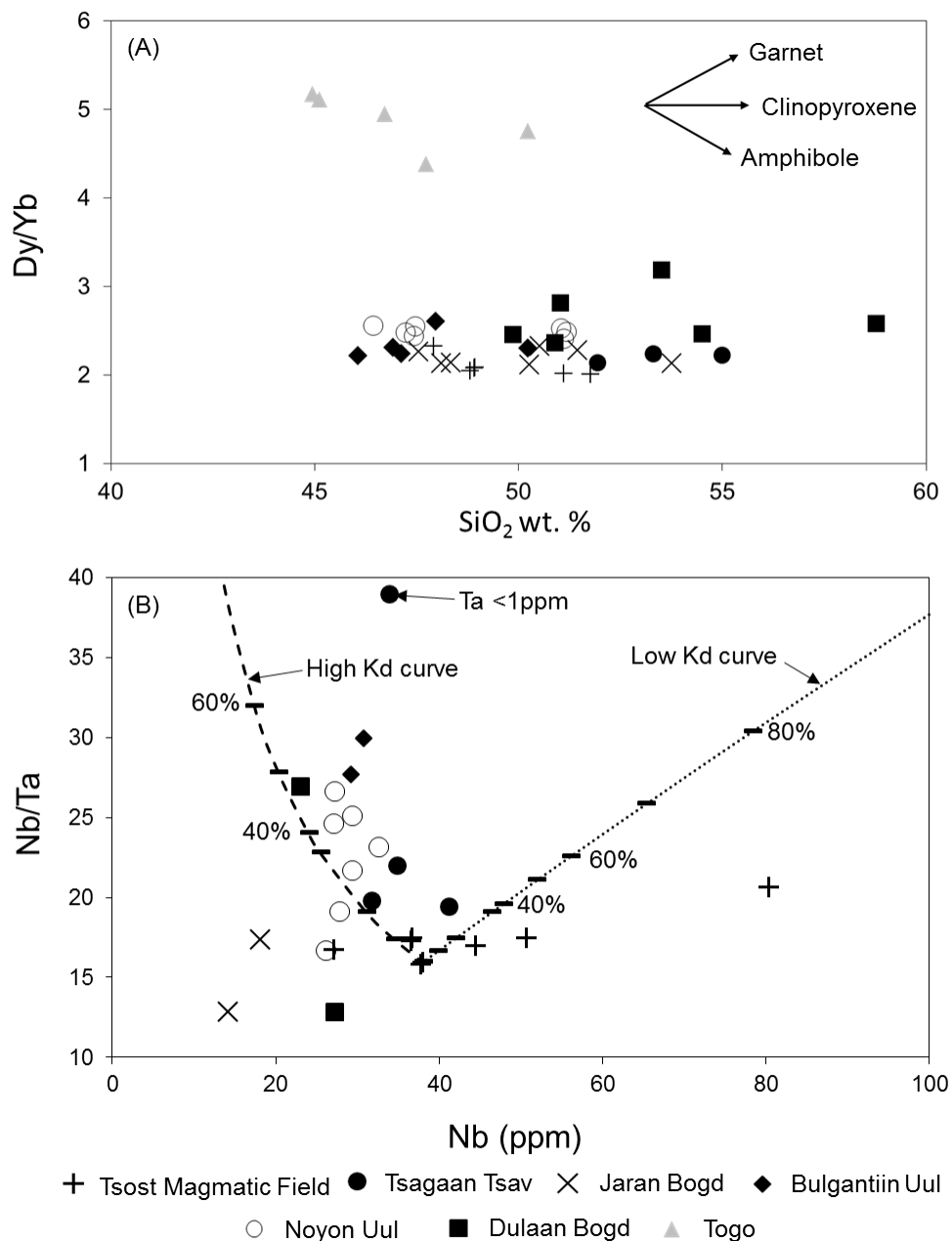


Figure 2.13: (A) Dy/Yb vs. SiO_2 wt. % plot with the Gobi samples and the Cenozoic Togo basalts from Mongolia plotted (Barry et al., 2003; Davidson et al., 2012) and shows mineral fractionation vectors. (B) A Nb/Ta vs. Nb plot showing results of Rayleigh fractional crystallisation modelling (equation 3) for ilmenite and spinel using sample TB95-6.3 from Tsost Magmatic Field as the starting composition. The partition coefficients used are those compiled from Klemme et al. (2006). Tick marks are in 10% fractionation intervals.

As the lavas and basalts from Dulaan Bogd, Jaran Bogd and Tsost Magmatic Field become increasingly evolved they move from the nepheline-normative to the quartz-normative fields (Fig. 2.10A & B). Because the Gobi samples are evolved (most samples <5 wt. % MgO), it is difficult to assess whether the trend from nepheline-normative to quartz-normative is because of fractionation processes at moderate pressures (5-10 kb), crustal

contamination, or simply because the normative mineralogy calculation for the evolved samples is not suitable (Chakraborty, 1980). However, it is interesting that many Jaran Bogd samples follow a similar trend to Tsost Magmatic Field samples, perhaps indicating similar fractionating conditions or some sort of mixing process.

Amphibole was not observed as a phenocryst or groundmass phase, and a Dy/Yb vs. SiO₂ wt. % plot (**Fig. 2.13A**) shows that each volcanic province has trends consistent with clinopyroxene fractionation, rather than amphibole involvement. For comparison, Cenozoic basalts from Mongolia (Togo) which have had a combination of garnet (high Dy/Yb ratios) and amphibole involvement in the source are also plotted (Barry et al., 2003; Hunt, 2011). Unlike the Gobi samples, the Togo basalts have decreasing Dy/Yb ratios with increasing SiO₂ wt. %, consistent with amphibole involvement.

The negative Nb, Ta and Ti anomalies on the primitive mantle-normalised plots (**Fig. 2.12**) suggest these lavas could have fractionated or interacted with residual rutile; alternatively, these geochemical attributes could be a source feature. If rutile was involved, then given that the minimum pressure stability of rutile is about 1.5 GPa, this would equate to a minimum depth of origin for the lavas of about 45-50 km (Xiong et al., 2005). Rutile fractionates Nb (Kd = ~28) from Ta (Kd = ~36), resulting in high Nb/Ta ratios in a melt derived from a rutile-bearing source; rutile dissolves when temperatures exceed 1250°C at 2-3 GPa (e.g., Foley et al., 2000; Bennett et al., 2004; Klemme et al., 2005; Xiong et al., 2005). If the source has high Nb/Ta ratios due to a fractionating phase like rutile, or because it has been modified by metasomatism, then any melt from such a source could also have high Nb/Ta ratios. Melts of rutile-free peridotite mantle, without recycled continental crust involvement, will be characterised by Nb/Ta ratios close to values for primitive mantle (17.39; Sun and McDonough, 1989). The Nb/Ta ratios for Tsost Magmatic Field basalts range from 15.8 to 20.6 (average of 17.3 ±1.4), similar to primitive mantle, whereas the Gobi lavas have more variable ratios (12.8 to 38.9; average of 22.6 ±6.5). Average continental crust has Nb/Ta ratios of 10.9 (Rudnick and Fountain, 1995) and therefore the ratios in the Gobi samples are unlikely to be explained by crustal contamination. Both Nb and Ta are also compatible in ilmenite and spinel, with Ta being more compatible than Nb; thus, fractionation of these oxides would also result in higher Nb/Ta ratios in the residual liquid.

To consider whether fractionation of these oxides can explain the ratios seen in the Gobi samples, a simple Rayleigh fractional crystallisation ($\frac{C_L}{C_O} = F^{D-1}$) model is considered (Fig. 2.13B; equation 3). To test whether the Gobi lavas are evolved versions of a melt similar to Tsost Magmatic Field basalts, but with Nb and Ta anomalies developed by fractionation of Fe-Ti oxides (ilmenite and spinel), the starting composition will use Nb = 38 ppm and Ta = 2.3 ppm based on sample TB95-6.3 (from Tsost Magmatic Field), as this sample has the most MgO and therefore is one of the least evolved. The partition coefficients (Kd) vary from 0.55 to 1.9 for Nb and 0.95 to 2.7 for Ta (Klemme et al., 2006). Two fractionation trends are considered, using the lowest and highest Kd values for Nb and Ta. To model the average Nb/Ta ratio of 22.6 using the smallest Kd values, ~58% fractionation of Fe-Ti oxides would be required, resulting in a positive correlation between Nb and Nb/Ta ratios. Alternatively, assuming the highest Kd values, ~36% fractionation would be required, resulting in a negative correlation between Nb and Nb/Ta. Therefore, both models require unreasonably large amounts of fractionation. Thus, fractionation of ilmenite/spinel may have helped elevate Nb/Ta ratios but can not be solely responsible for the high ratios in the lavas.

Considering that the high Nb/Ta ratios are unlikely to be explained by crustal contamination or fractionation of ilmenite/spinel, this leaves rutile fractionation or source controls as possible explanations.

It has been suggested by Klemme et al. (2002) that bulk TiO₂ in an eclogite protolith will need to be >1.6 wt. % for rutile saturation in the melt derived from the eclogite (at 3 GPa). Therefore, the protolith will need to contain sufficient bulk TiO₂ to stabilise rutile. Any interaction between a Ti-rich melt and mantle peridotite may lower the TiO₂ enough to prevent rutile fractionation, and it is argued in later sections that peridotite is the dominant source lithology. Mesozoic lavas (>110 Ma) from the North China Craton show similar negative Nb and Ta anomalies and high Nb/Ta ratios. Rutile fractionation was ruled out for these high MgO (>10 wt. %) lavas because there is a negative correlation between MgO and Nb and Ta (Liu et al., 2008b). This suggests that both Nb and Ta were incompatible during mantle melting. Instead, the geochemical features were attributed to source controls. Given the similar age of the Gobi lavas, they may have similar petrologic histories. Furthermore, none of the Gobi lava fields have decreasing Nb with

MgO (**Fig. 2.14**), consistent with the likelihood that there has not been rutile fractionation.

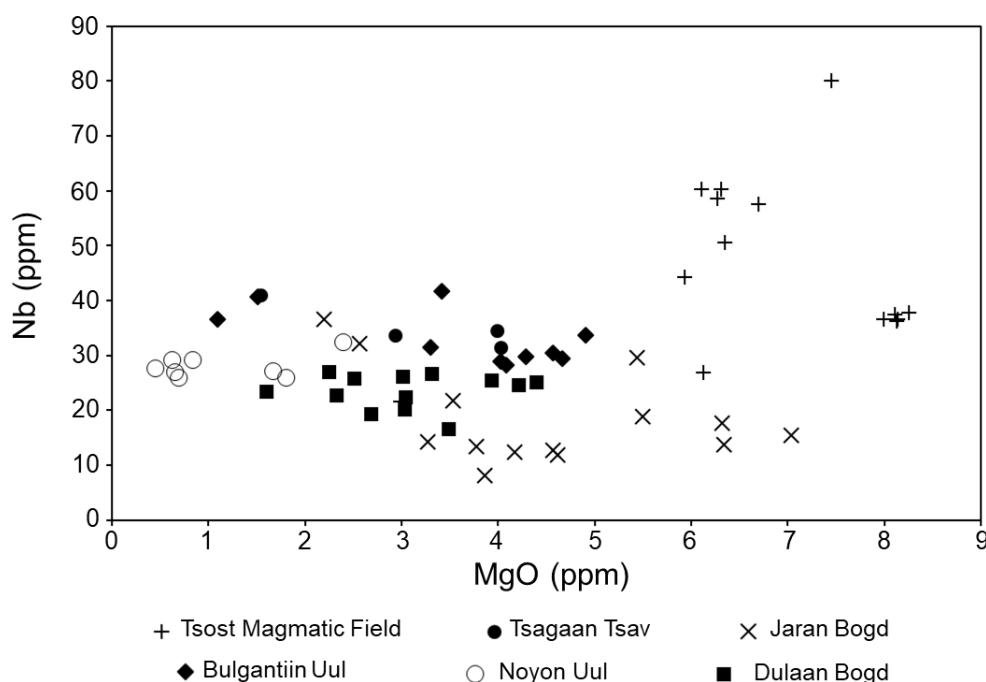


Figure 2.14: MgO vs. Nb plot for the Gobi samples.

If rutile is unlikely to have been a fractionating phase, then it is likely that the low Nb and Ta concentrations, and high Nb/Ta ratios are controlled by source characteristics. There are a number of ways this source could be generated for the Gobi lavas (or a combination of reasons): (1) interaction between mantle peridotite and a melt derived from a rutile-bearing, recycled eclogite (e.g., Liu et al., 2008b); (2) the involvement of previous subducted continental crust trapped in the lithospheric mantle (e.g., Fan et al., 2004) and (3) interaction between mantle peridotite and fluids with high concentrations of LREE but depleted in Nb and Ta. Peridotite xenoliths with melt pockets have been found in Cenozoic alkali basalts from Mongolia (Ionov et al., 1994). It was shown that the invading fluids were enriched in LREE, Th, U, Pb and Sr whilst also depleted in Nb and Ta, having high Nb/Ta ratios. Thus, considering xenoliths from Mongolia show a mantle enriched by metasomatism events, coupled with the similar age between the Gobi lavas and Chinese lavas (>110 Ma), it seems likely the negative Nb and Ta anomalies (**Fig. 2.12**) and high Nb/Ta ratios are a source characteristic, reflecting modified lithospheric mantle.

2.4 ISOTOPE VARIATIONS & CRUSTAL CONTAMINATION

Tsost Magmatic Field basalts have low $^{87}\text{Sr}/^{86}\text{Sr}_{(i)}$ isotopic ratios (0.7034-0.7041) and relatively high $^{143}\text{Nd}/^{144}\text{Nd}_{(i)}$ isotopic ratios (0.5126-0.5127; $\epsilon_{\text{Nd}(t)} = 3.3-4.88$). This is

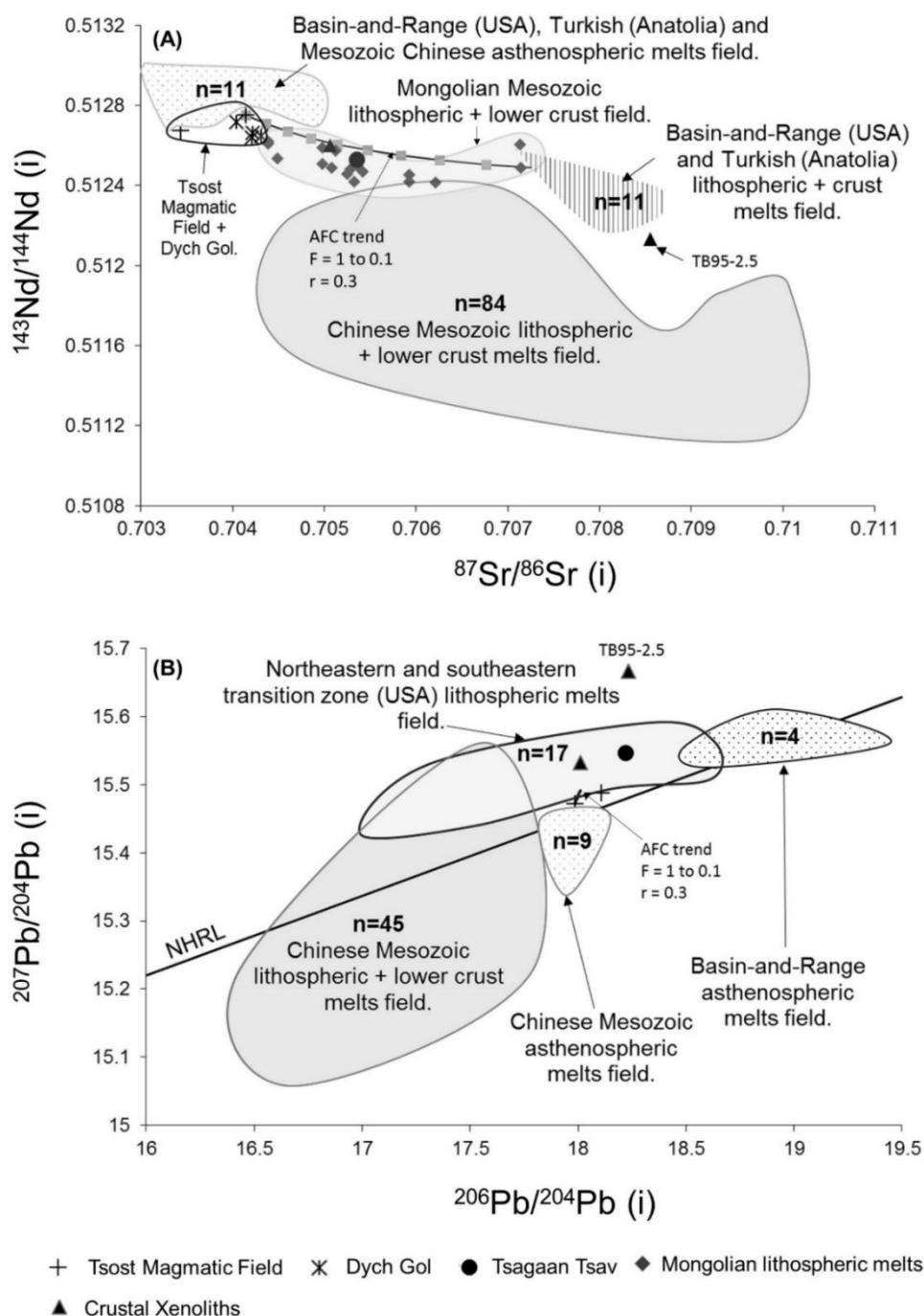


Figure 2.15: (A) Plot of $^{143}\text{Nd}/^{144}\text{Nd}_{(i)}$ vs. $^{87}\text{Sr}/^{86}\text{Sr}_{(i)}$ and (B) a $^{207}\text{Pb}/^{204}\text{Pb}_{(i)}$ vs. $^{206}\text{Pb}/^{204}\text{Pb}_{(i)}$ plot for the Gobi samples. Other Mongolian samples from Dash et al. (2015); Chinese lavas (Zhang et al., 2002; Fan et al., 2004; Hong-Fu et al., 2004 and Gao et al., 2008); Basin-and-Range, USA (Kempton et al., 1991 and Bradshaw et al., 1993; Pb isotope data non-age corrected) and Turkey, Anatolia (Aldanmaz et al., 2000). AFC trend uses a r value of 0.3 and a D value of 1.2 for Sr and 0.2 for Pb. The amount of F ranges from 1 to 0.1 and tick marks are in 10% intervals. The contaminant (TB95-2.5) and other granulite crustal xenoliths are from Barry et al. (2003) and are age corrected to 107 Ma.

similar to the Dych Gol lavas from Mongolia ($^{87}\text{Sr}/^{86}\text{Sr}_{(i)} = 0.704\text{--}0.7043$ and $^{143}\text{Nd}/^{144}\text{Nd}_{(i)} = 0.5126\text{--}0.5127$) which are also of a similar age to Tsost Magmatic Field basalts ($^{40}\text{Ar}/^{39}\text{Ar}$; $104.7 \text{ Ma} \pm 0.3 \text{ Ma}$) and were interpreted to be derived from a depleted asthenospheric mantle source (Dash et al., 2015). Chinese Jianguo basalts from Fuxin, Liaoning Province, are also of a similar age to Tsost Magmatic Field basalts and Dych Gol lavas (K/Ar ; $100.4 \text{ Ma} \pm 1.6 \text{ Ma}$), have similar isotopic signatures ($^{87}\text{Sr}/^{86}\text{Sr}_{(i)} = 0.7034\text{--}0.704$ and $^{143}\text{Nd}/^{144}\text{Nd}_{(i)} = 0.5127$) and have been interpreted to be derived from a depleted asthenospheric mantle source (Zhang and Zheng, 2003). Asthenospheric lavas from the Basin-and-Range (USA) and Turkey (Anatolia) also have compositions similar to Tsost Magmatic Field basalts (**Fig. 2.15A**). Thus, Tsost Magmatic Field basalts have Sr and Nd isotopic signatures that suggest derivation from a depleted asthenospheric mantle source.

In contrast, the Tsagaan Tsav sample (TB95-8.2) has a higher $^{87}\text{Sr}/^{86}\text{Sr}_{(i)}$ and lower $^{143}\text{Nd}/^{144}\text{Nd}_{(i)}$ isotopic value (0.7053 and 0.5125 respectively; $\epsilon_{\text{Nd}(t)} = 0.92$) than Tsost Magmatic Field samples, and plots within the field of the other Mongolian Mesozoic lavas that were analysed by Dash et al. (2015). These samples form an array that extends from the field of asthenosphere-derived melts towards lithosphere-derived lavas from China, Basin-and-Range (USA) and Turkey (**Fig. 2.15A**).

Tsost Magmatic Field basalts have $^{207}\text{Pb}/^{206}\text{Pb}_{(i)}$ vs. $^{206}\text{Pb}/^{204}\text{Pb}_{(i)}$ values that are close to the NHRL (Northern Hemisphere Reference Line) and are similar to the “Chinese Mesozoic asthenospheric melts field” (**Fig. 2.15B**). As discussed by Zhang and Zheng (2003), these Chinese Mesozoic basalts, and by extension the Tsost Magmatic Field basalts, have Pb isotopic values that are more similar to MORB rather than OIB. Tsost Magmatic Field samples therefore have Pb isotopic values that support a depleted asthenospheric mantle as the source. The Tsagaan Tsav sample plots above the NHRL, in the “north-eastern and south-eastern (USA) lithospheric melts transition zone” field; thus, Tsagaan Tsav has Pb isotopic signatures consistent with a lithospheric mantle source. However, it’s difficult to rule out the possibility of crustal contamination on this data alone.

The lack of mantle xenoliths and the evolved nature of the lavas suggest magma ascent was unlikely to have been rapid. Instead, the magmas probably evolved in crustal

magma chambers, where there was opportunity for crustal assimilation. The presence of granulite crustal xenoliths in samples from Tsagaan Tsav and Tsost Magmatic Field, supports the idea that crustal contamination processes occurred to some extent.

To assess whether crustal contamination combined with fractionation of an asthenospheric melt like Tsost Magmatic Field could produce the isotopic lithospheric signature of the Tsagaan Tsav sample, AFC modelling results are presented (**Fig. 2.15A & B**), using the equations from DePaolo (1981):

$$\frac{C_m}{C_m^0} = F^{-z} + \left(\frac{r}{r-1}\right) \frac{C_a}{zC_m^0} (1 - F^{-z}) \quad [4]$$

$$\varepsilon_m = \frac{\left(\frac{r}{r-1} \frac{C_a}{z} (1-F^{-z}) \varepsilon_a + C_m^0 F^{-z} \varepsilon_m^0\right)}{\frac{r}{r-1} \frac{C_a}{z} (1-F^{-z}) + C_m^0 F^{-z}} \quad [5]$$

where C_m^0 is the element concentration of the initial magma prior to fractionation and assimilation, C_a is the element concentration of the contaminator and C_m is the concentration of the element in the magma after AFC. ε_a is the isotope ratio of the wallrock, ε_m^0 is the isotope ratio of the original magma and ε_m is the isotope ratio concentration after AFC. Where r represents assimilation/fractionation ratio and F = mass of magma/initial mass of magma.

Sample TB95-6.3.5 from Tsost Magmatic Field is used as the initial magma due to its high MgO content; at 7.98 wt. % it is one of the least evolved samples in the suite. A granulite crustal xenolith (TB95-2.5) from the Gobi Altai (Barry et al., 2003) is used as the contaminant, because of its low Nd, and high Sr and Pb isotopic values.

Assuming an r -value (" r " = assimilation/fractionation ratio) of 0.3, approximately 50% of the magma would have to crystallise (i.e. $F = 0.5$, where " F " = mass of magma/initial mass of magma) to get $Sr_{(i)}$ and $Nd_{(i)}$ values close to the Tsagaan Tsav sample. Furthermore, to explain some of the other Mongolian lavas analysed by Dash et al. (2015) with this contaminant would require F -values >0.8 (**Fig. 2.15A**; Mongolian Mesozoic lithospheric + lower crust field). Because the granulite contaminant is low in Pb (0.7 ppm), even when F -values >0.9 , AFC processes with this contaminant could not explain the Pb isotopic composition of the Tsagaan Tsav sample (**Fig. 2.15B**). Thus, it seems unlikely that AFC processes can account for the difference in isotopic signature

between Tsagaan Tsav and Tsost Magmatic Field samples based on known granulite compositions.

An alternative approach to assessing the role of crustal contamination is to consider Nb/La ratios. Given that the partition coefficients for Nb and La are not significantly different for olivine, pyroxene and plagioclase (McKenzie and O’Nions, 1991), the Nb/La ratios should not change significantly because of fractional crystallisation. We can, therefore use a relatively straightforward mass balance approach to consider crustal contamination. This calculation allows us to consider different theoretical parental magmas (and contaminants), to test whether increasing assimilation of the continental crust can explain the negative Nb/La anomaly observed in all the lavas (**Fig. 2.16**). Using the equation:

$$C_a = \frac{(C_p \times 100) + (CC \times \% \text{ volume assimilated})}{(100 + \% \text{ volume of CC assimilated})} \quad [6]$$

where C_a is the composition of the lava after assimilation, C_p is the composition of the parental lava and CC is the composition of the contaminant. This equation shows that when 100% volume of CC is assimilated (a total volume increase to 200%) it would

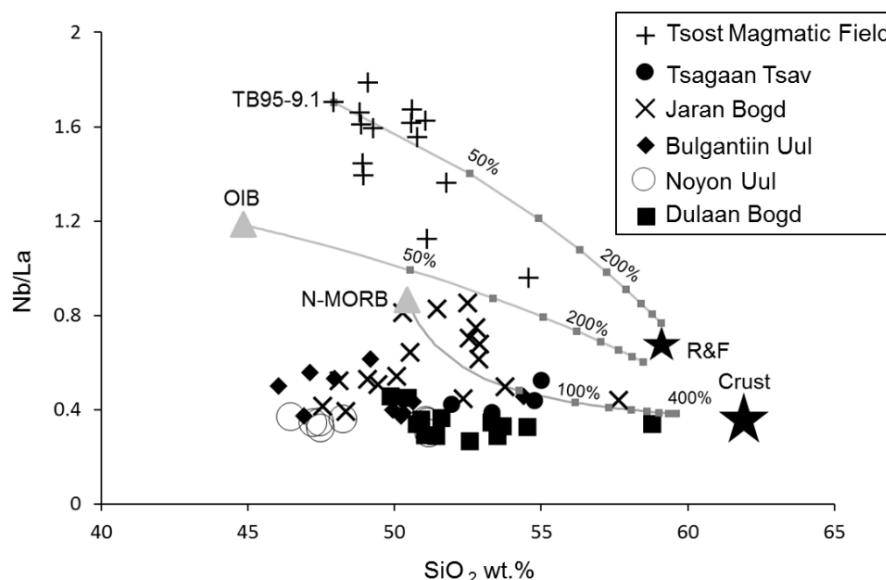


Figure 2.16: (A) A Nb/La vs. SiO_2 wt. % plot for the different magmatic fields showing different theoretical parental magmas which are undergoing assimilation of the crust. Parental magmas are; an average OIB (Fitton et al., 1991) and an N-MORB from Gale et al. (2013). Curves show assimilation; tick marks are shown on the curves which represent the amount of assimilation of the crust (CC) and are in 50% volume increments. The continental crust value was taken from Gao et al. (1998) and represents the interior of the North China Craton and was calculated on a carbonate rock-free basis. The average continental crust (RF) from Rudnick and Fountain (1995) is also plotted.

dilute/enrich C_p by 50%, or if 300% volume of CC is assimilated (a total volume increase

to 400%) it would dilute/enrich C_p by 75% with respect to CC , highlighting the amount of assimilation required to get compositions close to CC .

To calculate how much crustal contamination would be required to explain the negative Nb/La ratios, an average OIB composition from Fitton et al. (1991) is used to represent a Nb-rich parental magma. The crustal contaminant is a representative of the upper and lower crust from the interior of the North China Craton and was calculated on a carbonate rock-free basis (Gao et al., 1998). The average continental crust from Rudnick and Fountain (1995) is also plotted, but not used in the model due to the Nb/La ratios being higher than most of the lavas and as such could not explain the lavas' low ratios. The model suggests that to get low Nb/La concentrations purely by crustal contamination, using an OIB parental magma, would require significant amounts of assimilation. Even after 400% volume of the CC is assimilated the Nb/La ratios of the Ca are still higher (~ 0.6) than most of the Gobi lavas and it now has a SiO_2 content >58 wt. % (silica-saturated). In this model, the OIB parental magma would require lower starting SiO_2 compositions coupled with large amounts of assimilation to be able to explain the low Nb/La ratios of the Gobi lavas and thus seems unlikely.

In summary, although it seems unlikely that the Mongolian lavas could have traversed through the continental crust without undergoing some crustal contamination, based on the analysis above, it appears that consequences of that contamination are relatively small compared with the effects of compositional variation in the source.

2.5 SOURCE & MELTING CONDITIONS

2.5.1 A changing source

Since the negative Nb anomaly in the lavas likely reflects a source or mineral control, a Ta/Yb vs. Th/Yb diagram can be used to investigate source characteristics (Pearce, 1983). The ratios of these elements are largely unaffected by partial melting and fractional crystallisation when pyroxenes or feldspars are the dominant crystallising or residual phases (e.g., Irwin, 2006). The volcanic plugs from Tsost Magmatic Field plot within the mantle array (**Fig. 2.17**); melts that normally plot here are those from the asthenosphere, non-plume or plume-related asthenosphere, or from mantle lithosphere that has been enriched by melts from the asthenosphere. Enrichment in Th,

with respect to Ta, will displace samples vertically on this diagram. Such an enrichment may result from source region metasomatism caused by subduction components preferentially carrying Th, over Ta and Yb. Crustal contamination may also displace samples vertically if the contaminant has abundant Th. The average upper and lower

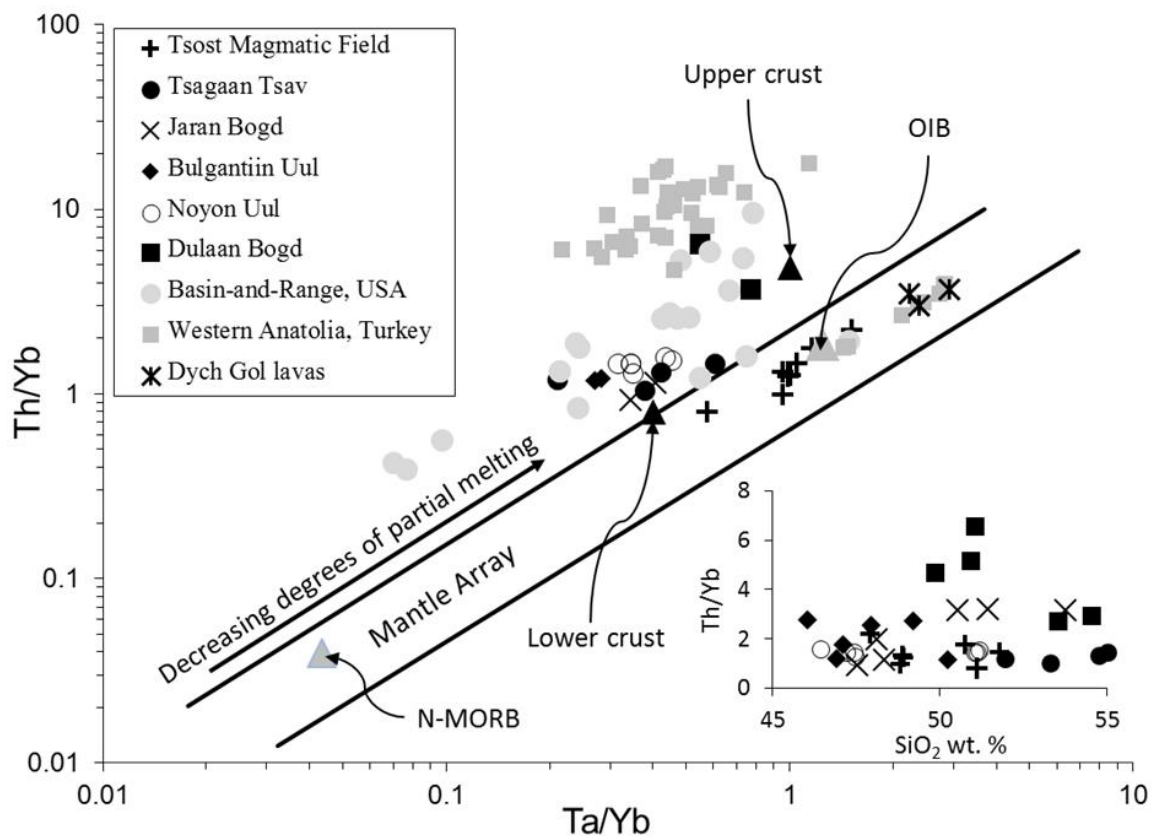


Figure 2.17: Ta/Yb vs. Th/Yb diagram of Pearce (1983) showing Gobi samples, Dych Gol lavas, lavas from the Basin-and-Range USA and from Western Anatolia, Turkey (Bradshaw et al., 1993; Aldanmaz et al., 2000 and Dash et al., 2015). Also plotted is an OIB from Sun and McDonough (1989) and average N-MORB from Gale et al. (2013).

crust from Rudnick and Fountain (1995) plot outside the mantle array. The lower crust has notably lower Th/Yb ratios due to being dominantly granulite facies. This plot therefore supports the interpretation that Tsost Magmatic Field basalts have not undergone significant crustal contamination and suggests they have not come from a mantle source that has undergone significant subduction modification processes. The melts also have higher Ta/Yb and Th/Yb ratios than N-MORB, closer to OIB, suggesting the melts originated from either a garnet-bearing source, with low degrees of partial melting, or from mantle that has been enriched by asthenospheric melts, or a combination of the two. The Gobi lavas are displaced vertically from the mantle array towards higher Th/Yb ratios, suggesting there may be a subduction component involved in their source. The Th/Yb ratios do not show a relationship with SiO₂, other than

perhaps melts from Jaran Bogd, indicating that these ratios have not been influenced by substantial late stage crustal contamination or fractionation (see inset diagram on Figure 2.17), and even samples with low SiO_2 , such as those from Noyon Uul and Bulgantiin Uul (~46 wt. %), do not plot within the Ta/Yb – Th/Yb mantle array. The low comparative Ta abundances in the lavas, as shown on primitive mantle normalisation diagrams (**Fig. 2.12**), is largely responsible for these lavas not plotting in the mantle array. The mantle source was therefore relatively depleted in Ta (and Nb). Metasomatism of the lithosphere, caused by the release of fluids during previous subduction events could have formed lithospheric pockets which are enriched in the LILE whilst also being relatively depleted in Nb and Ta. Therefore, the depletion in Nb, Ta and enrichment of the LILE indicates a source which has been conditioned by previous subduction inputs.

Basanite lavas from the Dych Gol area of eastern Mongolia (Dash et al., 2015) are also plotted, as these plot in the mantle array and are similar in age to the Tsost Magmatic Field basalts. For comparison with areas that have undergone thickening and then extension, lavas from the southern Basin-and-Range, USA (Bradshaw et al., 1993) and from western Anatolia, Turkey (Aldanmaz et al., 2000) are also plotted on the Ta/Yb vs. Th/Yb diagram (**Fig. 2.17**). The oldest lavas from both areas have lithospheric mantle signatures that plot outside the mantle array, while the younger lavas plot within the mantle array; similar to the Mesozoic melts from the Gobi.

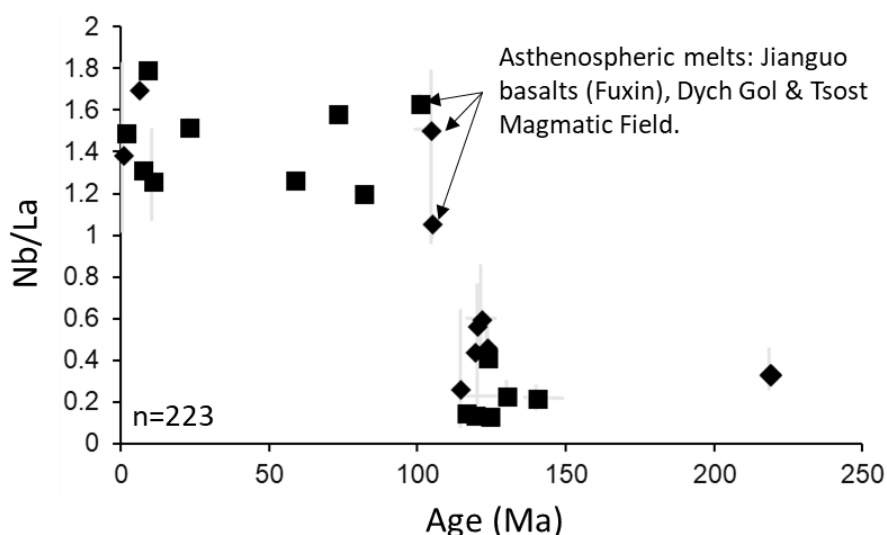


Figure 2.18: Nb/La vs. Time (Ma) plot, showing the average values for different volcanic provinces across Mongolia ($n=113$ samples: Barry et al., 2013; Dash et al., 2015 and this study) and China ($n=110$ samples; Zhang et al., 2002; Zhang and Zheng, 2003; Liu et al., 2008b and reference therein); bars show the minimum and maximum values for each volcanic province.

Interestingly, the switch from lithospheric-dominated magmatism to asthenospheric-dominated magmatism seems to have happened at a similar time in both Mongolia and China, as shown in Figure 2.18. Rocks older than 107 Ma have relatively low Nb/La values (average of 0.34 ± 0.17), whereas younger basalts have significantly higher ratios (average of 1.42 ± 0.23). These younger basalts are either interpreted to be asthenospheric melts or newly replaced lithospheric melts. However, the locations of the asthenospheric-dominated magmatism occur large distances from each other. For example, the Mesozoic Jianguo basalts from Fuxin, Liaoning Province (China), despite being a similar age to Tsost Magmatic Field basalts, are approximately ~1600 km away from the Gobi Altai. Similarly, the asthenospheric Mongolian Dych Gol lavas are approximately ~1150 km away from Tsost Magmatic Field. This would imply that the magmatism is linked to some large-scale process.

To further consider magmatic/metasomatic processes that may have affected the lithospheric mantle source, a Zn/Fe ratio plot is utilised to consider source characteristics (**Fig. 2.19A**). High Zn/Fe ratios have been used to identify pyroxenite source lithology, or garnet-pyroxene-rich sources that generate high Zn/Fe ratios by fractionation during partial melting (Le Roux et al., 2010; a pyroxenite source can generate Zn/Fe values as high as ~14, at 12 MgO wt. %, or even higher values if the source is garnet-rich). This is because Zn and Fe partition equally between olivine and orthopyroxene under mantle conditions ($K_D^{Fe}(\frac{ol}{melt}) \sim K_D^{Fe}(\frac{Opx}{melt})$ is $\sim 0.9 - 1$), whereas Zn

is more incompatible than Fe in garnet and clinopyroxene ($K_D^{Fe}(\frac{cpx}{melt}) \sim K_D^{Fe}(\frac{gt}{melt})$ is < 1).

However, high Zn/Fe melts can be produced from a peridotite source if metasomatism has enriched it in Zn (Le Roux et al., 2011). Therefore Zn/Fe ratios are not necessarily a sensitive indicator of non-peridotite source lithology (Davis et al., 2013), but may be an indication of source region metasomatism; thus Figure 2.19 shows source variation rather than source rock identification.

Although all the Gobi volcanic provinces have undergone clinopyroxene fractionation which will mask some aspects of source geochemistry and metasomatic processes, the plot clearly shows that Tsost Magmatic Field basalts have lower Zn/Fe ratios than the

the Gobi Altai lavas. The higher Zn/Fe ratios for the Gobi lavas relative to Tsost Magmatic Field is consistent with a composition reflecting fractionation processes and/or source metasomatism and potentially a different source lithology.

Interestingly, average Zn/Fe ratios from each magmatic field decreases with decreasing age: 21.77 for Dulaan Bogd; 20.53 for Bulgantiin Uul; 17.60 for Jaran Bogd, 12.64 for

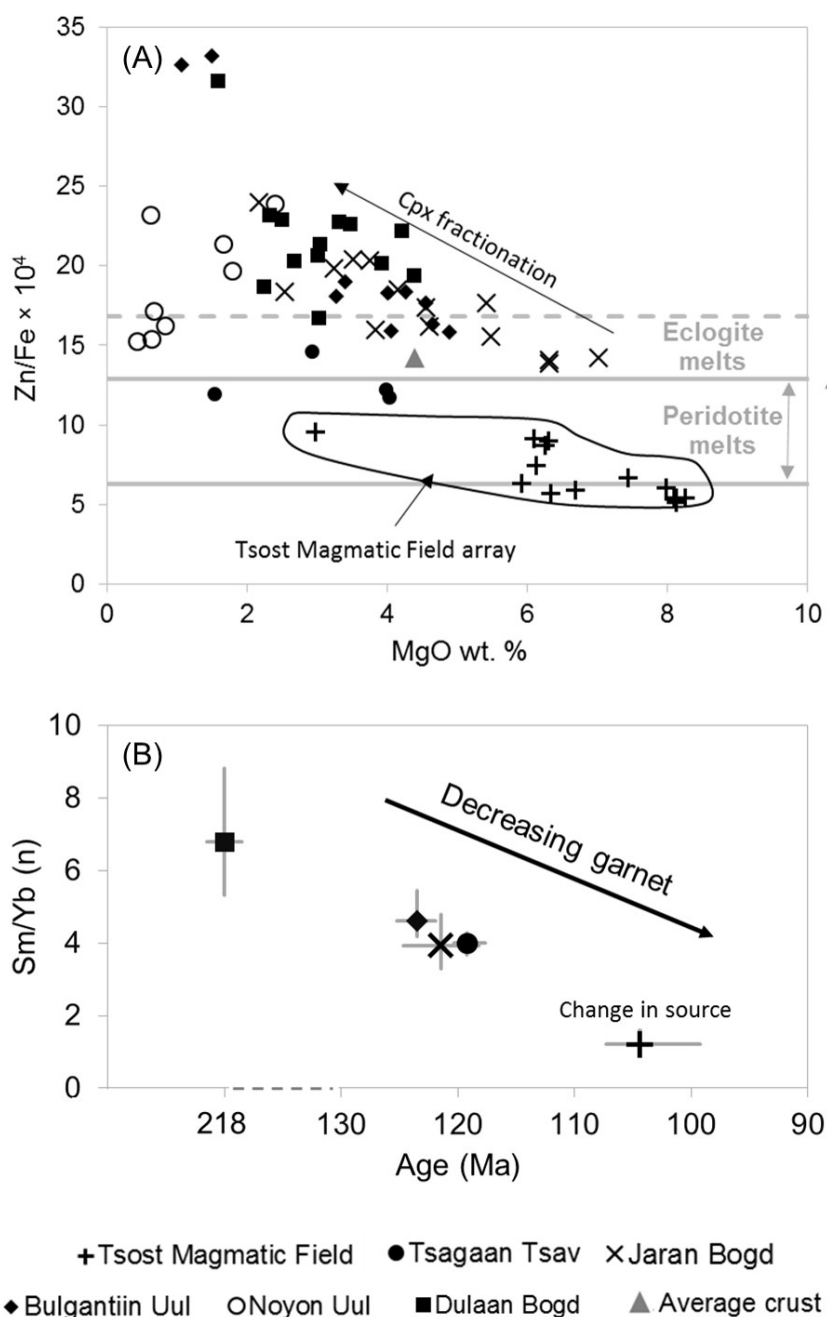


Figure 2.19: (A) Zn/Fe ($\times 10^4$) ratios vs. MgO wt. % plot ($\text{FeO} = \frac{\text{Fe}_2\text{O}_3(\text{T})}{(1 + \frac{0.2}{1.111})}$). The peridotite melts field and the upper eclogite field is based on information in Le Roux et al. (2010), however evolved samples which have undergone clinopyroxene fractionation will plot outside this field. Average crust value was taken from Rudnick and Fountain (1995). (B) Average primitive mantle-normalised Sm/Yb ratios (Sun and McDonough, 1989) vs. age for each magmatic field. Bars show the minimum and maximum range for each magmatic field.

Tsagaan Tsav and 5.79 for Tsost Magmatic Field. Furthermore, if we only consider averages from samples with between 4 to 5 wt. % MgO (most volcanic provinces have <5 wt. % MgO) to try and remove fractionation bias, average Zn/Fe ratios still generally decrease with age: 20.81 for Dulaan Bogd; 17.03 for Bulgantiin Uul; 17.36 for Jaran Bogd and 11.79 for Tsagaan Tsav. The highest Zn/Fe ratio from Tsost Magmatic field is 9.57 and that is from a sample (TB95-9.5.2) with 2.98 wt. % MgO; thus Tsost Magmatic Field rocks must have the lowest Zn/Fe ratios for a given MgO. This could suggest that any involvement from a metasomatised source could have had decreasing input with time and/or perhaps there was less involvement from garnet in the source too. Alternatively, there could have been less involvement from a hybridised source, such as peridotite + eclogite/pyroxenite.

To further evaluate geochemical changes with time, for the Gobi magmatic provinces, consideration is now given to garnet controls. Low chondrite-normalised $D_{Yn/Ybn}$ ratios (often <1.8) characterise melts which are derived from a spinel lherzolite source (e.g., Blundy et al., 1998) but all the Gobi samples have ratios greater than 2, suggesting that garnet was involved. I consider the change in garnet signature through time using Sm/Yb ratios. I use this ratio because Yb is highly compatible in garnet but not clinopyroxene. Primitive mantle-normalised Sm_n/Yb_n ratios are compared for each of the Gobi magmatic fields (**Fig. 2.19B**); the decreasing Sm_n/Yb_n ratios with time suggest diminishing garnet involvement for magmatic fields on the Gobi Altai terrane. One explanation for this reduced garnet signature is that there was less involvement from a garnet-bearing source and/or increased decompression melting in the spinel peridotite facies with time.

To further investigate partial melting and the role of garnet, a non-modal batch melting equation from Shaw (1970) is used to construct partial melt models, firstly for the basalts from Tsost Magmatic Field (**Fig. 2.20**) and then for the Gobi lavas (**Fig. 2.21**):

$$\frac{C_l}{C_o} = \frac{1}{(D_o + F(1-P))} \quad [7]$$

where C_l is the concentration in the liquid, C_o is the concentration in the solid, D_o is the bulk partition coefficient at the onset of melting, F is the weight fraction of melt formed and P is the bulk partition coefficient of phases entering the melt. The partition

coefficients used are those compiled from McKenzie and O’Nions (1991). To try and define a mantle array for Tsost Magmatic Field lavas two reference values are utilised in a similar method to Aldanmaz et al. (2000): (1) a depleted MORB mantle (DMM) source

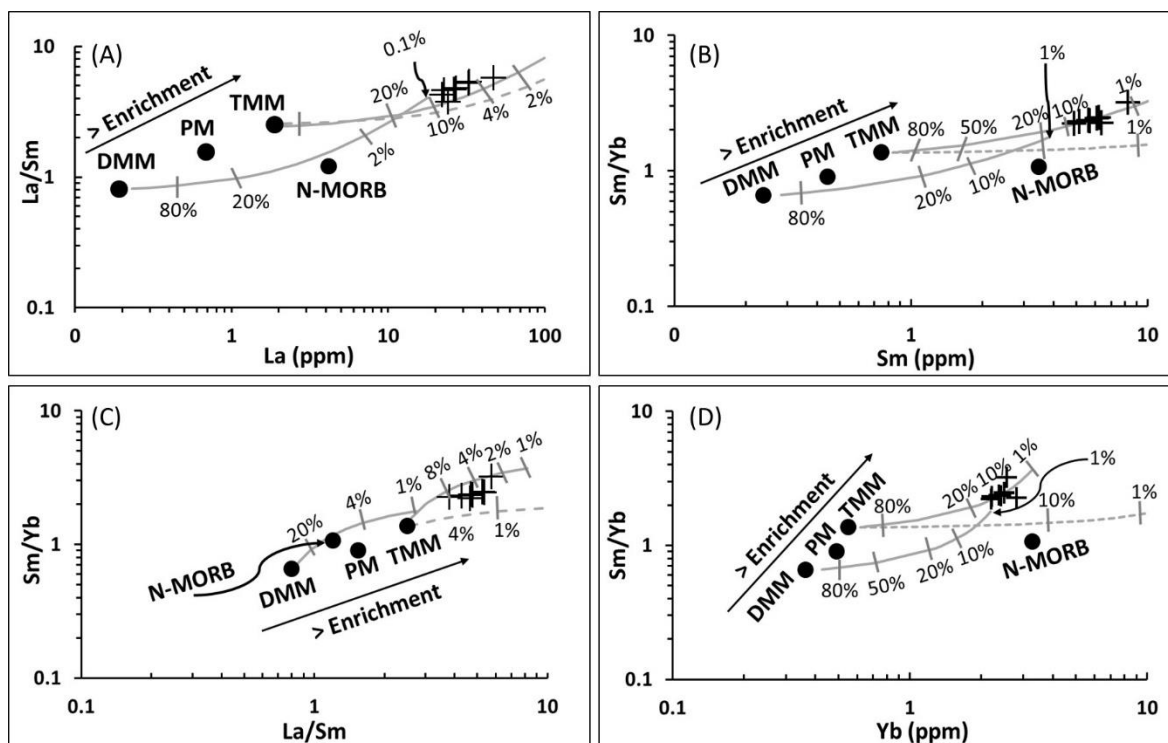


Figure 2.20: Non-modal batch melting plots with the basalts from Tsost Magmatic Field (crosses) plotted. The amount of partial melting is displayed (tick marks) where necessary. The solid lines represent melting of a garnet lherzolite and the dashed line represents a spinel lherzolite.

proposed by Workman and Hart (2005); and (2) primitive mantle (PM) from Sun and McDonough (1989). The DMM source is used to represent the convecting asthenospheric mantle and the PM is used to represent the initial mantle composition prior to MORB extraction. Using these two reference points, a theoretical mantle (TMM; Tsost Magmatic Mantle) has been projected. The dashed curve is used to represent a spinel lherzolite lithology of a TMM source, while the solid lines represent a garnet lherzolite source (specifics about the source mineralogy and chemistry are in Table 2.2). The elements La and Sm are used because they are not very compatible and because they are not affected significantly by garnet or spinel thus provide bulk information on the source. This model highlights that the basalts have La and La/Sm ratios that could not easily be explained by melting of a DMM source (even when the degrees of melting are very small 0.1%). Sm/Yb ratios are used because Yb is highly compatible in garnet

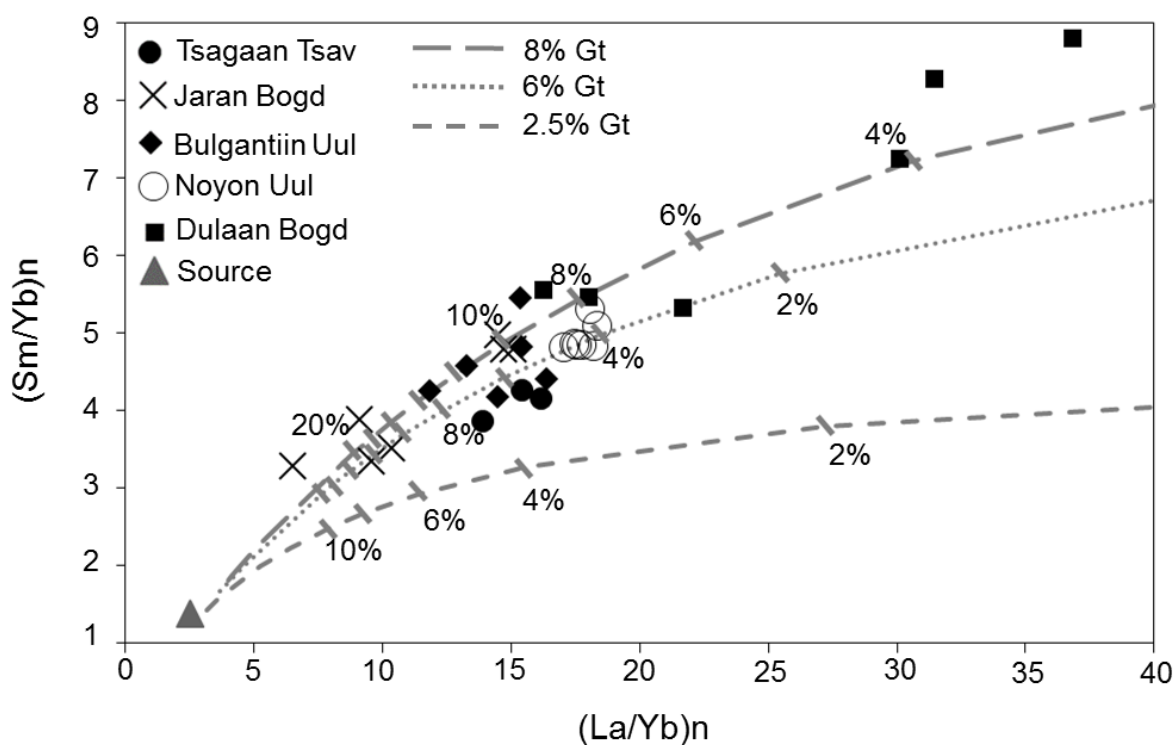


Figure 2.21: Primitive mantle-normalised (Sun and McDonough, 1989) La/Yb vs. Sm/Yb non-modal batch melting plot for Gobi Mongolian Mesozoic lavas. Tick marks denote 2% melting intervals and the amount of garnet (Gt) in the source is represented by various curves. Source composition is based on a spinel peridotite xenolith from the Shavaryn-Tsaram volcano, Tariat depression, central Mongolia ((Stosch et al., 1986).

Table 2.2 – non-modal batch melting parameters

	Source:	Source:	Mineral	Source:	Source:	Entering	Spinel	Entering
	MOZ1	TMM		(MOZ1)	(TMM)	melt	source	melt
Yb	0.48	0.55	Olivine	0.6	0.6	0.1	0.6	0.1
Sm	0.6	0.75	Orthopyroxene	0.235	0.2	0.1	0.25	0.1
La	2.34	1.88	Clinopyroxene	0.14	0.175	0.78	0.1	0.5
			Garnet	0.025	0.025	0.02	0	0
			Spinel				0.05	0.3

and not clinopyroxene and can therefore assess the role of garnet. These plots show that samples plot above the spinel lherzolite melting curves and are much better explained by the garnet lherzolite melting curve, indicating a link between residual garnet and their genesis. The amount of partial melting of the garnet lherzolite TMM

source required to explain the basalts varies from between 2-12%, but frequently the samples plot around 4-8%. The enriched nature of the TMM source compared to the DMM suggests that the asthenospheric mantle domain under Mongolia is more enriched than typical DMM or PM. Alternatively, the basalts from Tsost Magmatic Field may be enriched due to small degree partial melting processes of an asthenospheric mantle that then underwent further melting events in a more enriched mantle.

Further non-modal batch melting modelling is undertaken to consider melting regimes on the Gobi lavas (**Fig.2.21**). The source composition is based on a spinel peridotite lithospheric mantle xenolith (Mo-Z1) from the Shavaryn-Tsaram volcano, Tariat depression, central Mongolia (Stosch et al., 1986). The advantage of using this xenolith is the absence

of melt pockets which are present in other xenoliths from Mongolia (e.g. Ionov et al. 1994). The proportion of source minerals used in the model is based on descriptions from Preß et al. (1986). The xenolith consists of olivine, orthopyroxene, clinopyroxene and spinel only. Although the xenolith did not include garnet it is included in the model at the expense of clinopyroxene. By changing the wt. % garnet in the source, the model suggests that the lavas from Tsagaan Tsav are best approximated from a source containing around 3 to 4 % garnet; lavas from Jaran Bogd, Bulgantiin Uul and Dulaan Bogd exhibit a wider range of La_n/Yb_n ratios, requiring ~6-8 % garnet.

The amount of partial melting required for each grouping is approximately 3 to 7 % for Tsagaan Tsav; 6 to 20 % for Jaran Bogd; 4 to 14 % for Bulgantiin Uul; 2 to 6 % for Noyon Uul and 2 to 8 % for Dulaan Bogd. Because Jaran Bogd samples are likely hybrid melts (discussed in greater detail in the following sections), the amount of partial melting that this model estimates for these lavas is probably incorrect, as this model does not correct for mixing processes.

2.5.2 Peridotite vs. pyroxenite source: geochemical indicators

From a petrological perspective, peridotite and pyroxenite are distinguished lithologically based on mineral proportions of pyroxene versus olivine: peridotite, by definition, consists of >40% olivine whilst pyroxenite has <40% olivine. Factors such as

temperature, pressure and other mineral phases (e.g., spinel, garnet, Fe-Ti oxides) will influence the relative proportions of olivine and pyroxene.

Distinguishing peridotite from pyroxenite sources on the basis of lava composition can thus be difficult. Furthermore, processes such as magma mixing, fractional crystallisation and metasomatism can affect the final lava composition and, hence, obscure geochemical signals indicative of different source types. However, the involvement of pyroxenite as either a source rock, or as an addition (e.g., pyroxenite veins in the source rock), in magma genesis makes for an interesting debate (e.g., Yang and Zhou, 2013; Yang et al., 2016). Pyroxenite has been suggested as the source rock for Chinese Cenozoic basalts, while pyroxenite veins hosted in a peridotite source have been suggested for Mesozoic Chinese lavas (Liu et al., 2008b; Yang et al., 2016).

Whole-rock CaO-MgO relationships have been used to distinguish peridotite from pyroxenite sources (Herzberg, 2006), because melts derived from peridotite should theoretically have higher CaO contents at a given MgO wt. %. However, as emphasised in the appendix of Herzberg (2006), for alkali melts, peridotite melting can produce low-CaO melts. Furthermore, studies have shown that metasomatised garnet peridotite and small degree melts derived from a MORB-eclogite source that has interacted with peridotite on its way to the surface, can produce low-CaO basaltic melts at garnet-stable pressures (Mallik and Dasgupta, 2012). Therefore, as peridotite sources are capable of producing both low and high CaO melts, this scheme is unsuitable for determining source characteristics for the Mongolian lavas and thus not considered further.

Olivine phenocryst composition has been used to distinguish peridotite from pyroxenite source lithology (e.g., Herzberg et al., 2014). Olivine in basalts, which has low Ca and Mn, with high Ni and high Fe/Mn ratios at a given Fo content are features associated with a pyroxenite source. However, recognising whether olivine phenocrysts are xenocrysts can be difficult. Furthermore, olivine commonly exhibits chemical zoning; these zones can exhibit geochemical variance, which may lead to wrong interpretations. This is particularly important when considering the Gobi samples, as olivine is nearly always altered partially or completely to iddingsite. Therefore, finding and probing exposed areas of fresh olivine phenocryst can be difficult and may not truly represent the original mineral. Furthermore, it has been shown that temperature can have a

significant influence on how Ni partitions between olivine and the melt (e.g., Matzen et al., 2013), and therefore source/melt composition is not always the only control.

Based on melting experiments on peridotite and pyroxenite, a FC3MS ($\text{FeO}_T/\text{CaO}-3 \times \text{MgO}/\text{SiO}_2$ wt. %; equation 8) parameter was generated to distinguish peridotite from pyroxenite sources (Yang and Zhou, 2013). This parameter is primarily controlled by source composition and melting degree, while pressure and temperature have little effect. Fractionation controls also occur, with clinopyroxene fractionation increasing FC3MS values.

High FC3MS results are typically attributed to a pyroxenite source. To try and account for fractionation of the evolved Gobi melts, corrections have been applied to the oxides. However, the uncorrected data are plotted for comparison (**Fig. 2.22**). The correction on the oxides utilises the equation given in the appendix of Niu and O'Hara (2007). All the Gobi data are corrected to a Mg-number of 72. However, correcting a highly evolved melt back to a Mg-number of 72 is difficult and prone to error. Lavas with <1.5% MgO wt. % were not included in the correction procedure. Although alteration may have affected the major elements, LOI values are mostly <2 wt. % (although samples from Noyon Uul range from 2.29-4.49 wt. %) and the clear relationship between FC3MS values and MgO suggests that fractionation is the dominant control on these values.

A polynomial equation was utilised on MORB (Niu et al., 1999) to determine the polynomial coefficients (m_n). Using these polynomial coefficients the Gobi data have been corrected using the equation:

$$Y^{72} = Y_{Data} + \sum_{n=1}^N M_n (X_{72}^n - X_{Data}^n) \quad [9]$$

Where n refers to the n^{th} term of the polynomial equation.

For comparison purposes, experimental peridotite and pyroxenite melts are plotted. Also plotted are Cenozoic basalts from China that have been interpreted as pyroxenite melts (uncorrected for fractionation) and are discussed in detail by Yang et al. (2016). Cenozoic basalts from the Tariat-Chuloot Formation are plotted (as both uncorrected

values and values corrected for fractionation); these rocks have been interpreted as peridotite melts (Barry et al., 2003), or possibly garnet-pyroxenite melts (Hunt, 2011).

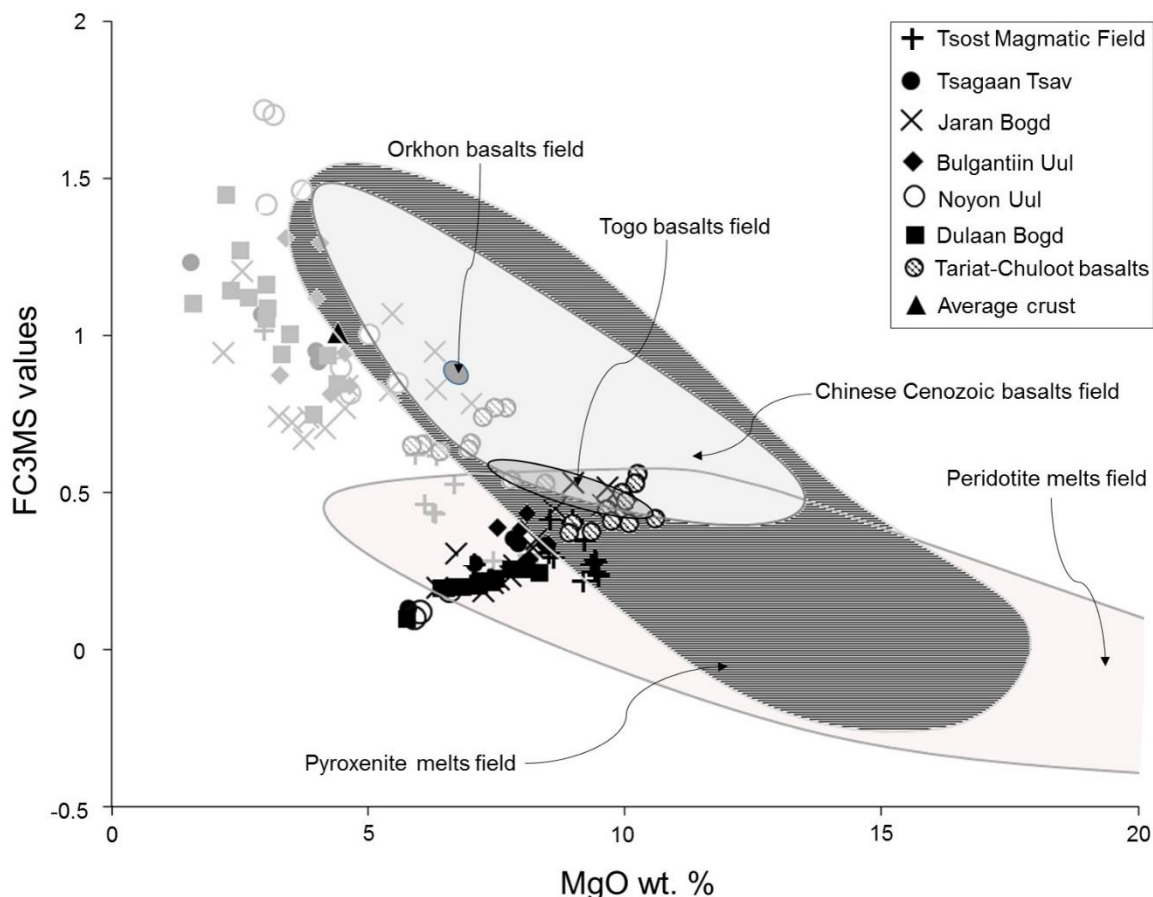


Figure 2.22: FC3MS ($\text{FeO}_T/\text{CaO}-3 \times \text{MgO}/\text{SiO}_2$ wt. %) values vs. MgO wt. %. FeO_T was calculated from $\text{Fe}_2\text{O}_{3(T)}$ ($\text{FeO}_T = \frac{\text{Fe}_2\text{O}_{3(T)}}{(1 + \frac{0.2}{1.111})} / 1.111$) for all Mongolian samples. The Chinese Cenozoic basalts are believed to be pyroxenite melts (Yang et al., 2016 and references therein). Pyroxenite and peridotite melting field is constructed from melting experiments and is from Yang et al. (2016). Orkhon and Togo Mongolian Cenozoic lavas from Barry et al. (2003). Average crust from Rudnick and Fountain (1995). The uncorrected Mongolian samples are the grey symbols. Fractionation-corrected (Mg-number of 72) FCSMS and MgO wt. % values are the black symbols.

Pleistocene and Quaternary Mongolian basalts from Orkhon and Togo (Hunt et al., 2012) are also plotted (uncorrected for fractionation) and previous trace-element interpretations define these as originating from a pyroxenite source, with the Togo basalts also being derived from amphibole-rich regions of the mantle (Barry et al., 2003; Hunt, 2011).

The Chinese Cenozoic basalts have high FC3MS values at a given MgO wt. %, consistent with their pyroxenite source interpretation. The Orkhon and Togo basalts have high FC3MS values (0.87-0.89 and 0.45-0.62, respectively), plotting with the Chinese Cenozoic basalts, suggesting that the Orkhon basalts originated or interacted with a pyroxenite source while the Togo basalts are more ambiguous. Modelling done by Yang

et al. (2013) indicates that the highest FC3MS value that can be produced from peridotite melting is 0.65 when MgO is > 7.5 wt. %. Two Togo samples have 7.4 wt. % MgO and have a FC3MS value of 0.61-0.62, which is very close to the upper limit achievable by peridotite melting. Therefore, FC3MS values for the Togo basalts are likely consistent with trace-element interpretations by Hunt (2011). The Cenozoic Tariat-Chuloot lavas have FC3MS values that are generally higher than the Mesozoic Gobi samples at comparable MgO wt. %, but display a range of FC3MS values.

Many of the Cenozoic Mongolian basalts have high LREE/HREE and MREE/HREE ratios, which have been used to infer depth of melting (Barry et al., 2003). These ratios are often higher than those in the Mongolian Mesozoic samples, which could be interpreted to reflect melting at greater depth. However, if the Cenozoic basalts are primarily pyroxenite-derived products, the typical garnet signature implied by the LREE/HREE and MREE/HREE ratios might not be indicative of a high-pressure garnet source, because garnet can be stable at lower pressures in pyroxenite (e.g., Lambart et al., 2013; Yang et al., 2016 and references therein).

The Gobi samples have high FC3MS values at low MgO wt. % (uncorrected for fractionation) likely due to clinopyroxene fractionation, although values are mostly lower than the Orkhon and Togo basalts. Many Gobi samples also have FC3MS values lower than the experimental pyroxenite melts and Chinese Cenozoic basalts at comparable MgO wt. %. Jaran Bogd lavas display a range of FC3MS values between samples with comparable MgO wt. %, perhaps indicating source variation or magma mixing. When the Gobi samples are corrected for fractionation, they plot with the peridotite experimental melts (FC3MS = 0.1-0.57); although there is much uncertainty in the correction procedure. Because so many of the Gobi samples have fractionation uncorrected FC3MS values that do not plot in the pyroxenite field, this probably reflects peridotite as the dominant source lithology (but it could be a combined peridotite + pyroxenite source).

2.5.3 Mixing between lithospheric and asthenospheric mantle melts

If the lithosphere was thinned or removed under Mongolia in the Mesozoic, as suggested for Archaean lithosphere under the North China Craton at this time (e.g.,

Menzies et al., 1993), and as suggested by the dramatic change in Nb/La ratio at about 107 Ma (**Fig. 2.18**), it is possible that the asthenospheric mantle had greater input to magma genesis over time. This might have been accentuated if melting happened at the base of the lithosphere, triggered in part by localised asthenospheric upwelling.

The lavas from Jaran Bogd show the greatest variation on the geochemical plots within any given province and therefore provide us with the best chance to test whether there could have been a transitional shift from a lithospheric to an asthenospheric source. Additionally, petrological studies identified sub-ophitic clinopyroxene enclosing plagioclase feldspar and convolute zoning in feldspar phenocrysts which might be indicative of magma mixing. Furthermore, because the exposures at Jaran Bogd provide a stratigraphic sequence of lava flows, there is an opportunity to investigate changes in the amount of asthenospheric input with time, as you move up sequence (JB1 towards the base while JB94 is towards the top of the sequence).

Using a combination of the oxides (FC3MS values; uncorrected for fractionation) and HFSE (Nb/La and Zr), geochemical trends are used to recognise asthenospheric vs. lithospheric inputs (**Fig. 2.23**). Using the sample with the lowest SiO₂ (47.5 wt. %) and high MgO (6.3 wt. %) from Jaran Bogd (JB8), two trends can be recognised. Some of the lavas from Jaran Bogd have geochemical signatures more similar to the older lithospheric melts (JB1 to JB17). However, as the SiO₂ content or Nb/La ratios increase, many of the Jaran Bogd lavas trend toward Tsost Magmatic Field compositions. Interestingly, Jaran Bogd lavas have lower Zr concentrations than the other Gobi lavas, on average, and are comparable to the asthenospheric basalts from Tsost Magmatic Field. Jaran Bogd and Tsost Magmatic Field samples both have decreasing Zr with increasing SiO₂ content, perhaps indicating a mineral fractionation control, too. This suggests Jaran Bogd lavas may represent a melt from a lithospheric source with variable amounts of evolved asthenospheric input, explaining the geochemical variation observed in the lavas.

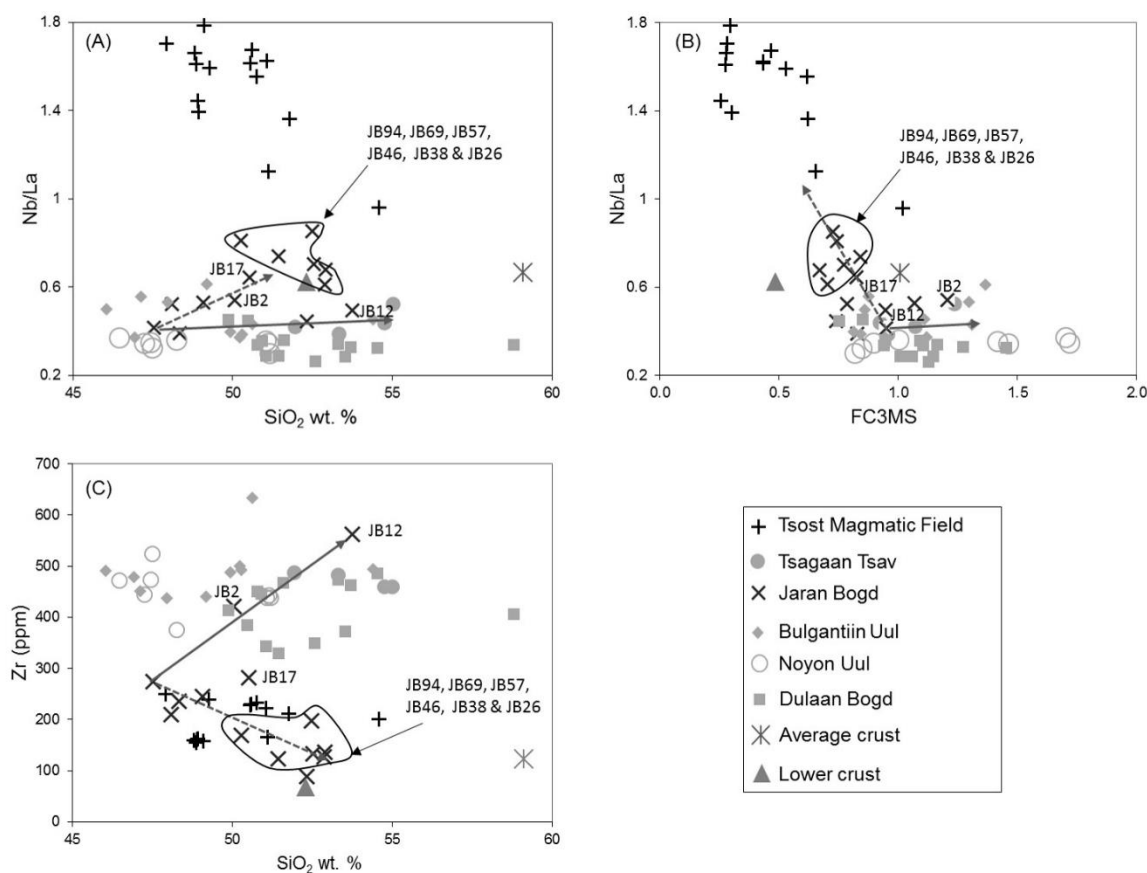


Figure 2.23: Variation diagrams for the Gobi lavas showing: (A) Nb/La vs. SiO₂ wt. %; (B) Nb/La vs. FC3MS (FeO₇/CaO-3 × MgO/SiO₂ wt. %) values and (C) Zr vs. SiO₂ wt. %. The arrows commence from sample JB8 and point in the general direction of two trends for the Jaran Bogd lavas.

The Tsagaan Tsav lavas show a strong lithospheric mantle geochemical signature despite overlapping the dated Jaran Bogd lavas in age, i.e. 120.3 to 117.6 ± 0.3 Ma for Tsagaan Tsav lavas vs. 124.7 to 118.2 ± 1.4 Ma for Jaran Bogd. This implies that the Jaran Bogd melts may have been triggered during a greater input of asthenospheric activity or maybe some of the Jaran Bogd lavas are actually younger than the Tsagaan Tsav lavas. The youngest dated sample from Jaran Bogd (JB26) has relatively low Zr concentrations whilst also having a high Nb/La ratio >0.73 compared to the other Gobi lavas. Samples JB38, JB46, JB57, JB69 and JB94 all appear stratigraphically higher in the sequence than the dated JB26 sample and show some of the greatest affinities to asthenospheric melts (relatively low Zr and Nb/La ratios ranging from 0.67 to 0.85).

2.6 DISCUSSION

The Gobi lavas are depleted in some HFSE (Nb, Ta and Ti) but are enriched in Zr, the LREEs and LILEs (**Fig. 2.12**). The Tsagaan Tsav sample (**Fig. 2.15**) has relatively high

$^{87}\text{Sr}/^{86}\text{Sr}_{(i)}$ and low isotopic $^{143}\text{Nd}/^{144}\text{Nd}_{(i)}$ values that are similar to other Mongolian Mesozoic subcontinental lithospheric mantle (SCLM) derived melts (Dash et al., 2015). The Tsagaan Tsav $\text{Pb}_{(i)}$ isotope ratios are higher than the NHRL, but similar to basalts from the transition zone between the Basin-and-Range and the Colorado Plateau (USA). The Gobi lavas plot outside the mantle array on a Th/Yb vs. Ta/Yb plot and have higher Zn/Fe ratios than Tsoist Magmatic Field basalts (**Fig. 2.17 & 2.19A**). Therefore, taken together, these data are interpreted as evidence that the Gobi lavas were derived from a metasomatised lithospheric mantle that may have been modified by melts derived from recycled rutile-bearing eclogite.

Tsoist Magmatic Field basalts have low $^{87}\text{Sr}/^{86}\text{Sr}_{(i)}$, relatively high isotopic $^{143}\text{Nd}/^{144}\text{Nd}_{(i)}$ values, and $\text{Pb}_{(i)}$ isotope ratios that are close to the NHRL. Furthermore, these basalts are not depleted in the HFSE (Nb, Ta, Ti), are less enriched in Zr compared to most of the Gobi lavas (**Fig. 2.23C**), but are enriched in the LREEs and LILEs. The basalts show geochemical parallels (**Fig. 2.15, 2.17 & 2.18**) to similar age Mesozoic basalts from Dych Gol, Mongolia (**Fig. 2.1**) and Chinese Jianguo basalts (Fuxin, Liaoning Province). The geochemical data suggest that Tsoist Magmatic Field basalts were derived from asthenospheric mantle.

Combining all this evidence (e.g. the decrease in garnet signature (Sm/Yb ratios) and magmatic/metasomatic input (Zn/Fe ratios) with time (**Fig. 2.19**), the gradual increase in asthenospheric input (**Fig. 2.23**) and a switch from lithospheric to asthenospheric magmatism) suggests that lithospheric mantle was stripped away under the Gobi. This event appears to have occurred after the Tsagaan Tsav magmatism (~118 Ma) but prior to the Tsoist Magmatic Field magmatism (~107 Ma).

At the time of their eruption, the oldest dated Gobi lavas from Dulaan Bogd (~218.5 Ma), were ~150-200 km south of a subduction plate boundary associated with the closing Mongol-Okhotsk Ocean, and likely in an overriding plate position (e.g., van der Voo et al., 2015). The Dulaan Bogd lavas are thought to have been deposited in a half-graben (van Hinsbergen et al., 2015), and contemporaneous extensional basins were also recognised elsewhere in the Gobi Altai region (Johnson et al., 2015b). Samples from all the magmatic fields are alkaline and enriched in the incompatible elements, such as Zr (88-633 ppm); thus, these volcanic rocks are not thought to be volcanic arc related.

Earlier, in the Palaeozoic, Northeast China and Mongolia amalgamated during the subduction of the Palaeo-Asian Oceans and the formation of the Central Asian Orogenic Belt (Xiao et al., 2015). It is therefore likely that the lithospheric mantle beneath the region had been enriched, by subduction-derived fluids and partial melts long prior to formation of the magmatic rocks studied in this chapter. The presence of small amounts of water and carbon dioxide in the lithospheric mantle may have assisted partial melting by reducing the mantle potential temperature required to initiate melting.

What triggered the magmatism in the Gobi Altai region is enigmatic (e.g., Yarmolyuk and Kovalenko, 2001; Fan et al., 2003; Meng, 2003; Wang et al., 2006; Dash et al., 2015; He, 2015). Although the Mesozoic magmatism occurred over a large area, no evidence of a mantle plume has been documented. Therefore, many studies have proposed a form of delamination to account for the magmatism across the CAOB. However, the suggestion by Wang et al. (2006) that eastward delamination of an earlier thickened lithospheric mantle formed by the latest Jurassic-earliest Cretaceous closure of the Mongol-Okhotsk Ocean does not seem an appropriate mechanism for the genesis of the Gobi magmatic provinces due to the spread of ages within the same region and across China (**Fig. 2.1B & 2.18**).

A model of convective mantle lithosphere removal was postulated by He (2014) to explain the Mesozoic magmatism in the North China Craton. In this model, to explain the most abundant volcanism (135-115 Ma), the formation of an extensive mantle wedge is required, due to a stagnating Pacific plate beneath the North China Craton. Slab dehydration would then reduce the viscosity of the asthenosphere and may result in small-scale upwellings within the upper mantle and convection of the mantle wedge. As the asthenosphere ascends, it may cause compression of the rheological boundary layer and consequently increases the temperature gradient within this layer. This convection and excess heat causes lithospheric thinning. The lowering of melting temperature by peridotite-melt interaction can help accelerate lithospheric thinning and, when combined with convective erosion, can result in significant thinning of a cratonic lithosphere (e.g., with a mantle viscosity of 10^{18} - 10^{19} Pa s and a peridotite melting temperature of 1000-1100°C a lithosphere could be thinned over tens of millions of years but at normal asthenospheric temperatures). In such a model, a

combination of vigorous upper mantle convection, peridotite-melt interaction and local delamination results in abundant magmatism and lithospheric thinning (He, 2014, 2015).

Apart from Dulaan Bogd (and possibly Noyon Uul), the Gobi lavas erupted between 124-117 Ma. Thus, they were erupted over a similar time interval to the magmatism in the North China Craton. Furthermore, when we consider that asthenospheric melts appear in Mongolia and China at similar times, it suggests that the Mesozoic magmatism in the North China Craton and Mongolia are linked to a large-scale event(s) affecting the east Asian mantle lithosphere.

Given their >2000 km separation, it's not feasible that the Pacific Plate extended horizontally all the way under the Gobi region during the Mesozoic. A southward subducting Mongol-Okhotsk slab may have extended far enough southwards to form an extensive mantle wedge below the Gobi region. It is also unclear how asthenospheric upwelling would be triggered over such a vast area so as to result in convective thinning under the Gobi region at the same time as that under the North China Craton. Therefore, we suggest that the convective model by He (2014, 2015), involving just the Pacific Plate, may not fully account for the extensive volcanism observed.

Interpreting this period of Gobi volcanism as the product of delamination, as suggested for similar age volcanism in the North China Craton (e.g., Windley et al., 2010), faces similar challenges in terms of the density contrasts between lithospheric keel and the asthenosphere (e.g., Menzies et al., 2007). That is, if a thick lithospheric keel (lower crust) was converted to eclogite, then a density contrast between the lower crust and lithospheric mantle may have assisted delamination. However, the absence of crustal eclogite xenoliths in the Gobi lavas makes it difficult to confirm this scenario.

Without further investigation into the magmatism across Mongolia it is difficult to assess whether the volcanism as a whole was a prolonged, gradual event or a relatively rapid one. If it was a rapid delamination model, it is unclear why so many places delaminated at the same time to give the asthenospheric signal, like that from Tsost Magmatic Field. Further investigation into asthenosphere input and Mesozoic magmatism will be explored in greater detail in Chapter 4 of this thesis.

The following model is proposed to explain the Gobi volcanism:

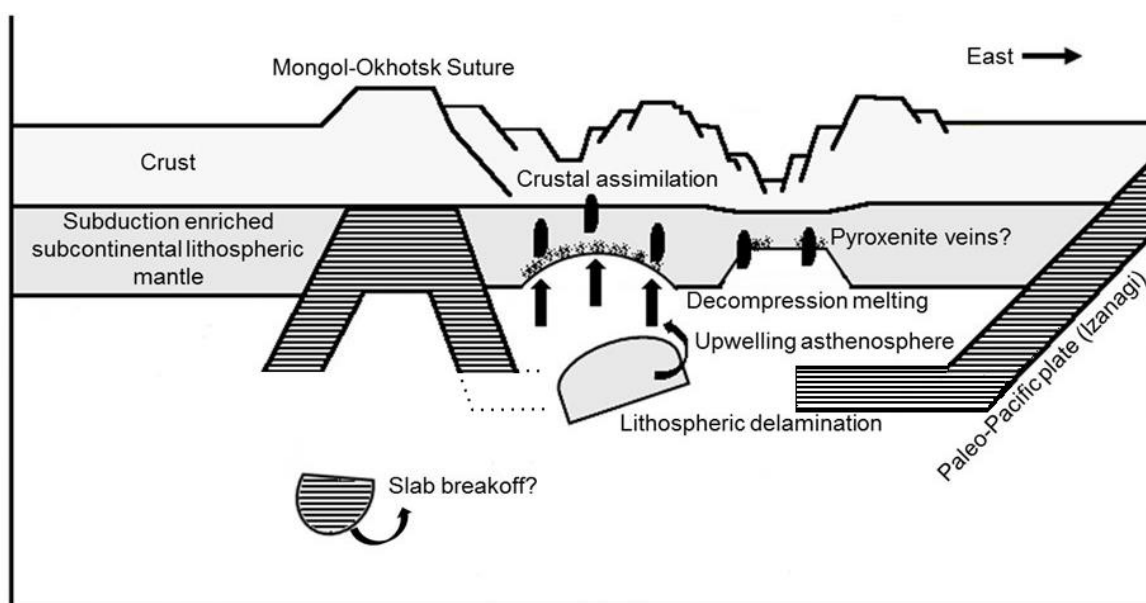


Figure 2.24: An illustration showing piecemeal lithospheric delamination and decompression melting of a subduction preconditioned lithosphere after the closure of the Mongol-Okhotsk Ocean. Slab breakoff may have also aided extensional events and facilitated rising asthenospheric melts.

(1) The lithosphere under the Gobi Altai was modified by previous metasomatic events and possibly by melts derived from recycled rutile-bearing eclogite. The oldest dated lavas (218.5 Ma), from Dulaan Bogd, erupted onto a thick lithosphere. Because the lithosphere was thick it could have provided a barrier to magma reaching the surface. It is thus difficult to assess whether Dulaan Bogd magmatism is evidence of a gradual lithospheric removal processes under the Gobi region, or whether this magmatism is just unrelated to later postulated delamination processes.

(2) Because the rest of the dated Gobi lithospheric mantle melts are a similar age (~124-118 Ma) to much of the volcanism in the North China Craton (~135-115 Ma) and eastern Mongolian lithospheric mantle melts (120-114 Ma), it is possible that the whole region underwent rapid delamination model (**Fig. 2.24**). The closure of the Mongol-Okhotsk Ocean may have helped provide the necessary conditions for delamination in the Gobi.

(3) As the lithosphere was gradually stripped away, younger Mesozoic asthenospheric melts (~107 Ma) were able to erupt. However, because asthenospheric melts appear elsewhere in Mongolia and the North China Craton at a very similar time,

it suggests that a period of large-scale (possibly localised) asthenospheric upwelling occurred.

2.7. SUMMARY

(1) The Gobi lavas are LREE and LILE-enriched whilst being depleted in some HFSE (Nb, Ta and Ti). The Tsagaan Tsav sample has relatively high $^{87}\text{Sr}/^{86}\text{Sr}_{(i)}$ and low $\epsilon\text{Nd}_{(i)}$ values and are comparable to other Mongolian Mesozoic lavas. $\text{Pb}_{(i)}$ isotope ratios plot above the NHRL, but are similar to basalts from the transition zone between the Basin-and-Range and Colorado Plateau (USA), consistent with an interpretation as subcontinental lithospheric mantle melts. The Gobi lavas represent melts from a subduction-preconditioned lithospheric mantle that was likely modified from recycled rutile-bearing eclogite melts and metasomatism. What triggered the melting is unclear, but delamination is a potential mechanism.

(2) The volcanic plugs from Tsost Magmatic Field are LREE- and LILE-enriched and are not depleted in the HFSE. These melts have low $^{87}\text{Sr}/^{86}\text{Sr}_{(i)}$ and relatively high $\epsilon\text{Nd}_{(i)}$ values; $\text{Pb}_{(i)}$ isotope ratios plot close to the NHRL. The geochemical data suggest that Tsost Magmatic Field basalts were derived from the asthenospheric mantle.

(3) FC3MS values suggest that pyroxenite is not the dominant source lithology under the Gobi region. However, some of the Cenozoic lavas from Mongolia may be pyroxenite-derived melts.

(4) The decrease in garnet signature (Sm/Yb ratios), and magmatic/metasomatic input (Zn/Fe ratios) with time, the gradual increase in asthenospheric input and a switch from lithospheric to asthenospheric magmatism suggests that the lithospheric mantle was stripped away under the Gobi, with its removal by ~ 107 Ma.

(5) Asthenospheric melts appear in Mongolia at a similar time interval to those in China. This suggests some large-scale process was responsible for asthenospheric upwelling because distances between this asthenospheric magmatism is up to ~ 1600 km.

CHAPTER 3

EVIDENCE FOR SOUTHWARD SUBDUCTION OF THE MONGOL-OKHOTSK OCEANIC PLATE: IMPLICATIONS FROM MESOZOIC ADAKITIC LAVAS FROM MONGOLIA

The existence of the Palaeozoic and Mesozoic Mongol-Okhotsk Ocean is evident from the Mongol-Okhotsk suture, which stretches from central Mongolia to the Sea of Okhotsk. There is uncertainty whether this ocean closed in a bi-modal fashion, or whether there was subduction along the northern, or southern, margin only. This lack in understanding leads to difficulties in reconstructing the history and geometry of this penultimate ocean closure event which united the Asian continent.

Low-silica adakite-like (LSA) and high-silica adakite (HSA) samples from eastern and south-central Mongolia, on the southern side of the Mongol-Okhotsk suture, provide constraints on the closure style of the Mongol-Okhotsk Ocean in the Mesozoic. New $^{40}\text{Ar}/^{39}\text{Ar}$ dating results indicate the LSA samples are Cretaceous, around ~138 Ma, while the HSA samples are Triassic, at ~230 Ma. Chemically, the LSA samples compare closely to 121 Ma old trachyandesite lavas from across eastern Mongolia (Group 1 lavas). A combination of major- and trace-element data, plus Sr-Nd-Pb-Hf isotope data, are used to investigate the petrogenesis of this magmatism. All samples are light rare-earth element and large-ion lithophile element enriched but depleted in some high field strength elements (notably Nb, Ta and Ti).

The LSA samples are interpreted as melts derived from a lithospheric mantle wedge that was previously metasomatised by slab melts. The spatial distribution of these samples implies that metasomatism likely occurred due to a southward-subducting Mongol-Okhotsk slab associated with the closure of the Mongol-Okhotsk Ocean. Similarly, Group 1 lavas are interpreted as melts deriving from a subduction-enriched subcontinental lithospheric mantle.

Two alternative models are proposed to explain the petrogenesis of the HSA samples. (1) A southward-subducting Mongol-Okhotsk slab underwent partial melting in the Triassic during the closure of the Mongol-Okhotsk Ocean, with the resultant melts assimilating mantle and crustal material. Alternatively (2), a basaltic underplate of thickened (>50 km; >1.5 GPa), eclogitic lower crust foundered into the underlying mantle, and underwent partial melting with minor contamination from mantle material and some shallow-level crustal contamination. What caused either of these processes in the Triassic is uncertain.

Overall, the proximity of the adakites to the Mongol-Okhotsk suture is best explained by the involvement of a southward-subducting Mongol-Okhotsk slab. When this interpretation is combined with previous evidence for a northward-subducting Mongol-Okhotsk slab it suggests the Mongol-Okhotsk Ocean closed in a bi-modal fashion.

3. ADAKITE PETROGENESIS

3.1.1 What is an adakite?

Adakites were originally defined by Defant and Drummond (1990) as being volcanic or intrusive igneous rocks associated with the subduction of young oceanic lithosphere. The partial melting of subducted basalt which has been metamorphosed to eclogite or amphibolite was attributed to giving adakites their unique geochemical characteristics (Table 3.1).

Table 3.1: Geochemical characteristics for adakites derived from slab melting. Info from Castillo (2006).

Geochemical characteristics	Potential links to slab melting
<p>Low MgO (<3 wt. %)</p> <p>High Al₂O₃ (>15 wt. %)</p> <p>High SiO₂ (>56 wt. %)</p>	<p>If the melt is primary, then this is indicative that it was not derived from peridotite melting.</p> <p>When SiO₂ wt. % is high (>70%) this could be indicative of high-pressure partial melting of eclogite or amphibolite.</p> <p>High-pressure melting of eclogite or garnet amphibolite.</p>
<p>High Sr (> 300 ppm)</p> <p>High Sr/Y (>20)</p> <p>Low Yb (<1.9 ppm) and high La/Yb (>20)</p> <p>Low HFSE's (Nb and Ta)</p>	<p>Absence of plagioclase in the residue or melting of plagioclase.</p> <p>Indicative of garnet and/or amphibole as a residual or liquidus phase.</p> <p>HREE depleted indicative of garnet being a residual or liquidus phase. LREE enriched relative to HREE's is also indicative of garnet controls.</p> <p>A Ti-phase (e.g. rutile or hornblende) in the source.</p>
<p>Low ⁸⁷Sr/⁸⁶Sr (<0.704), low ²⁰⁶Pb/²⁰⁴Pb and high ¹⁴³Nd/¹⁴⁴Nd signatures.</p>	<p>N-MORB signature.</p>

The melting of slab-melt metasomatised peridotite within a mantle wedge setting has increasingly been suggested in adakite petrogenesis (e.g., Rapp et al., 1999; Martin et al., 2005). This had led to the term "low-Si" and "high-Si" adakites; low-Si adakites are often more enriched in MgO, Sr, Cr and Ni than high-Si adakites. Low-Si adakites are regularly interpreted as melts from mantle peridotite that was metasomatised by slab-melts while high-Si adakites are more pristine slab-melts that have interacted with minor mantle peridotite (Castillo, 2006).

High-Nb basalts, which are often alkaline, HFSE-enriched and low in Si are often interpreted to be mantle-melts that have been metasomatised by slab-melts (e.g.,

Defant and Jackson, 1992; Sajona et al., 1994). Adakites and high-Nb basalts regularly coexist, and their appearance together is often used to support slab-melting (Casillo, 2006 and references therein). The reason for this thinking is based on interpretations that when a slab melts (producing an adakite melt) it ascends through mantle wedge and will fractionate amphibole. If the amphibole-bearing mantle then melted, it would release HFSE into adjacent mantle wedge peridotite which could become the source for high-Nb basalts (Castillo et al., 2006).

3.1.2 Adakitic melts

Adakite geochemistry can also be produced without slab-melting and these melts are referred to as being adakitic. Examples of how an adakitic melt could be generated include: underplated basaltic lower crust (Atherton et al., 1993), delamination of lower crust (Xu et al., 2002) and fractionation of late stage accessory minerals such as apatite (Richards and Kerrich, 2007).

Adakitic rocks can also be produced entirely from crustal-melts (e.g., Xiong et al., 2003) or from something interacting with mantle peridotite (for example, if the lower crust has delaminated into the underlying mantle; Xu et al., 2002, Gao et al., 2004). This variance between pure crustal-melts or crustal + mantle material further complicates distinguishing adakites from adakitic melts because of geochemical parallels.

Common criteria for distinguishing adakites from adakitic melts include:

- Establishing a fractionation trend for the melts. If any of the least evolved samples do not meet the criteria for an adakite, this can indicate that fractionation is the dominant control on the geochemistry rather than source rock (e.g. Richards and Kerrich 2007; Moyen, 2009).
- Consideration of the tectonic regime and geophysical evidence to establish the presence or absence of slab protoliths and non-arc environments.
- Isotope signatures; adakites derive abundant Sr and Nd elemental contents from subducted oceanic basalt and therefore should have oceanic crust-like isotopic signatures.

- Adakites are rarely associated/interbedded with basalt or basaltic-andesite. Adakite is associated with High-Nb basalt and basalts belonging to the alkali series (which are enriched in LILE).

*The author rejects classifying the new Mongolian samples as either adakite or adakitic, based on petrogenesis – In the following text the Mongolian rocks here will be termed adakite based on major and trace element abundances (Table 3.3) rather than their petrogenesis (until the source/mode of melting is constrained).

3.1.3 Melting models for adakite petrogenesis

Dehydration melting experiments by Sen and Dunn (1994) were done on a basaltic composition amphibolite at conditions appropriate to a hot slab geotherm (1.5 – 2 GPa, 850 – 1150 °C). Comparison of the major element compositions of the experimentally produced melts with compositions of presumed slab melts (an adakite) showed that the amphibolite partial melting experiments could produce melt compositions similar to andesitic- and dacitic-adakites, except for significant MgO and CaO depletions.

Trace element modelling of amphibolite dehydration melting using the 2 GPa melting reactions of Sen and Dunn (1994) produced REE abundances similar to adakites produced from 10 – 15% batch melting; but the models did not reproduce the high Sr/Y ratios characteristic of adakites. It was concluded that if adakites are partial melts of a subducted slab, they must undergo significant interaction with the mantle or crust to acquire several of their distinctive characteristics (e.g., high Mg, Ni and Cr). The effect of olivine assimilation vs. orthopyroxene precipitation could, for example, influence the Sr/Y ratios because Y is much more compatible in orthopyroxene than olivine (Nielsen et al. 1992; Adam and Green, 2006).

Laboratory experiments by Rapp et al. (1999) were performed to simulate melt and rock reactions at the slab-mantle wedge interface. In experiments at 3.8 GPa, assimilation of fertile and depleted peridotite by slab-melts (melt and rock ratio of ~2:1) produced Mg-rich, high-Si liquids with pyrope-rich garnet and low-Mg orthopyroxene, whilst olivine was fully consumed (no xl phases). At melt to rock ratios (~1:1) the slab-melts were fully replaced, along with the peridotitic olivine, and the formation of sodic amphibole and high-Mg orthopyroxene occurred. The hybridised melting investigations were compared

geochemically with a pure slab-melt experiment to recognise the effects of assimilation of the mantle wedge. It was shown that assimilation of peridotite decreased SiO_2 and Al_2O_3 with simultaneous increases in MgO , FeO , Na_2O , K_2O , and TiO_2 . However, although trace element abundances in the hybridised slab-melts increased, many of the trace element ratios remained similar.

3.1.4 Mongolian and Chinese rocks with adakite geochemistry

To understand the processes responsible for adakite genesis in Mongolia and China, this section summarises research on adakites across these localities. Emphasis is on Mesozoic adakites from China where research over the last two decades has helped improve understanding of adakite petrogenesis. Due to less extensive research in neighbouring Mongolia, no English publications report any Mesozoic adakites within Mongolia.

Adakites from the Carboniferous Shuteen Complex (isochron age of 321 ± 9 Ma for a pluton and 336 ± 24 Ma for associated andesites) are located (**Fig. 3.1**) on the Gurvansaikhan island arc terrane in South Mongolia (Batkishig et al., 2010). This volcanic-plutonic ring complex is associated with Cu-Au porphyry mineralisation. The complex is silica-saturated ($\text{SiO}_2 > 56$ wt. %), rich in Al_2O_3 (> 15 wt. %), low MgO (< 6 wt. %), low Y (< 18 ppm) and Yb (< 1.9 ppm) whilst also being rich in Sr (> 400 ppm) and $^{87}\text{Sr}/^{86}\text{Sr}_{(i)} < 0.7040$ (Batkishig et al., 2010). Partial melting was deemed to be the dominant process during the petrogenesis of this complex and the adakite composition was interpreted to have formed from partial melting of subducted oceanic crust, with minor interaction of mantle material. Modelling indicated that the subducted slab contained oceanic basalt and minor oceanic sediment, which together with a restite eclogite phase, formed the source of the Shuteen magma.

Carboniferous adakitic andesites and high-Mg andesites (HMAs) have been reported from the Sanchazi block of the Mian-Lue ophiolitic melange in the Qinling Mountains, central China (Xu et al., 2000). The adakitic andesites have a steep REE pattern, low Y, low Yb and high La/Yb values. The HMAs have adakite affinities but have lower La/Yb ratios (~ 10) and Al_2O_3 (< 15 wt. %). The adakitic andesites and HMAs are enriched in MgO , Ni and Cr compared to typical andesites and basalts (Xu et al., 2000). Age-

corrected (350 Ma) $\text{Nd}_{(i)}\text{-Pb}_{(i)}$ isotopic compositions are higher than typical MORB and this was interpreted to reflect addition of continental crust material or sediment. The adakitic andesites and HMAs were interpreted to be derived from partial melting of eclogitic oceanic crust (with possible addition of subducted sediments), which had then interacted with mantle wedge material and then finally undergone crustal contamination.

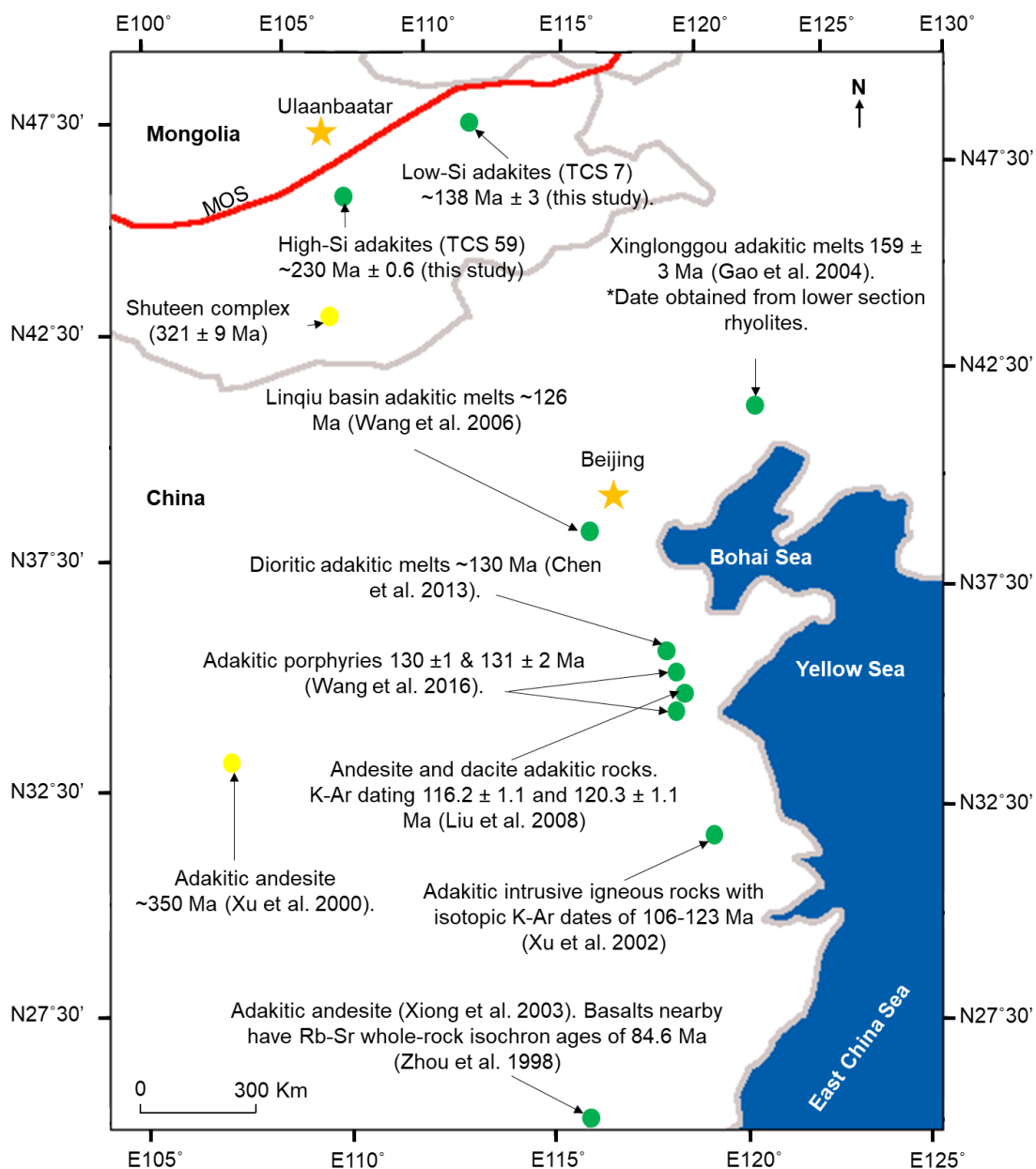


Figure 1.1: Sketch map of Mongolia and China showing the distribution of magmatism with adakitic geochemistry (Zhou et al., 1998; Xu et al., 2000; Xu et al., 2002; Gao et al., 2004; Wang et al., 2006; Liu et al., 2008b; Batkhisig et al., 2009; Chen et al., 2013 and Wang et al., 2016). The yellow dots show Palaeozoic adakite localities while the green dots show Mesozoic localities. The Mongol-Okhotsk Suture (MOS) is also shown to highlight the proximity to adakites from this study (TCS 7 and TCS 59). The LSA and HSA samples were dated in this study and are discussed more fully in section 3.4.

Early Cretaceous (K-Ar isotopic dates 106-123 Ma) Anjishan adakitic intrusive igneous rocks, from the Ningzhen area, east China, formed in a continental setting unrelated to subduction (Xu et al., 2002). Based on low $\epsilon\text{Nd}_{(i)}$ values (-6.8 to -9.7) and high $^{87}\text{Sr}/^{86}\text{Sr}_{(i)}$ values (0.7053-0.7066) it was argued that these melts were not a result of slab melting. Melting of mafic material, at the base of a thick (>40 Km) lower crust was suggested as the source. However, because of relatively high MgO values it was suggested that these melts had interacted with the underlying mantle rocks, through a model of lower crustal delamination into underlying mantle.

Andesites which were erupted in the Late Cretaceous Huichang Basin of SE China, have adakite affinities (high Al and Sr with low HREE) but have high $^{87}\text{Sr}/^{86}\text{Sr}_{(i)}$ ratios between 0.707-0.708 (Xiong et al., 2003). Basalts crop out to the north of the andesites and these were dated at 84.6 Ma by Rb-Sr whole-rock isochron methods (Zhou et al., 1998). The andesites are enriched in Na_2O (6.59-8.46 wt. %) and low in CaO (0.62-1.79 wt. %). These andesite adakite-like magmas were interpreted to be derived from underplated basaltic lower crust and to explain the high Na_2O and Low CaO, the protolith was considered an alkali-rich basaltic rock.

Adakitic granitoids (K-Ar and Ar-Ar; 125-130 Ma) from the Tietonggou pluton, in the west Shandong province (Luxi terrane), were briefly discussed by Chen and Zhou (2005). These granitoids have high SiO_2 (70.5-72.0 wt. %), high Na_2O (4.5-5.2 wt. %), $\text{Na}_2\text{O}/\text{K}_2\text{O} > 1$, high Sr (590-670 ppm) and are depleted in the HREE's (Yb < 0.3 ppm and Y < 4 ppm). Because these granitoids have geochemical similarities to other slab melts (Martin et al., 2005) it was suggested that their genesis was from partial melting of the subducted Palaeo-Pacific slab.

Lower crustal foundering and subsequent mantle peridotite interaction was proposed to explain adakitic melts (159 \pm 3 Ma from $^{206}\text{Pb}/^{238}\text{U}$ concordant ages were obtained from lower section rhyolites) from Xinglonggou, the western Liaoning Province (Gao et al., 2004). Based on high $^{87}\text{Sr}/^{86}\text{Sr}_{(i)}$ values (0.7055-0.7073) slab melting was not considered viable, especially since crustal contamination was considered minor. However, the melts have high Mg-numbers, and Ni, Cr values consistent with mantle peridotite assimilation.

Potassium-Ar dating (116.2 ± 1.1 and 120.3 ± 1.1 Ma) and a Sr-Nd isotope study was also done on western Shandong volcanic (andesite and dacite) adakitic rocks on the Luxi terrane, adjacent to Fangcheng, to decipher their petrogenesis (Liu et al., 2008b). Based on low $\epsilon\text{Nd}(t)$ values (-10.3 to -13.2) and high Sr isotope values (0.7089 to 0.7098) a model of dehydration melting of delaminated crust, with subsequent mantle peridotite interaction was proposed for melt genesis.

Mesozoic high-Mg dioritic rocks (130 Ma; Yang et al., 2006) in the North China Craton (Luxi terrane), from the JinLing-Tietonggou plutons, have adakitic geochemical affinities (Chen and Zhou 2005; Martin et al., 2005; Chen et al., 2013). Most adakitic rocks from the North China Craton have been interpreted to be partial melts of delaminated mafic crust (eclogite) with interaction of mantle peridotite (e.g. Xu et al., 2002; Gao et al., 2004; Wang et al., 2007; Xu et al., 2008). However, Chen et al. (2013) presented an alternative to the popular delamination model, on the basis of petrological observations and Os isotopic data. A model of magma mixing between siliceous crustal melts and basaltic magma from a metasomatised mantle in a post-kinematic setting was suggested to explain the chemistry of these melts. Due to high Mg-numbers they rejected a model of lower crustal melting (e.g. Liu et al., 2008b). Moreover, they suggest that the formation of the Mesozoic magmas and basins in the North China Craton is associated with Pacific plate rollback. This interpretation was based on the observation that most of the Mesozoic basins and magmas in the North China Craton are along NE-trending lineaments (Chen et al., 2004).

Therefore, three models have been suggested to explain adakitic rocks on the Luxi terrane alone: (1) partial melting of subducted Palaeo-Pacific slab (Chen and Zhou 2005); (2) partial melting of delaminated lower crust (Liu et al., 2008b) and (3) magma mixing between siliceous crustal melts and basaltic magma (Chen et al., 2013). However, Wang et al. (2016) also investigated adakitic porphyries (Mengyin 130 ± 1 Ma and Liujing 131 ± 2 Ma) on the Luxi terrane. Based on whole-rock geochemistry and Hf isotope analysis, two separate models are suggested. The Mengyin adakites petrogenesis was attributed to partial melting of subducted oceanic slab with input from lower crust components. The Liujing adakitic porphyry was interpreted to be a result of partial melting of delaminated underplated thick lower crust, which then interact with above

asthenospheric mantle peridotite. Slab rollback and ridge subduction of the Palaeo-Pacific slab was suggested as the geodynamic mechanism to trigger the magmatism. The variety of models to explain adakitic melts on just one terrane highlights the complexity in understanding petrological processes behind adakitic melt generation.

3.2. GEOLOGICAL SETTING

Low-silica adakite (LSA) samples (TCS 7.1 to TCS 7.7) were collected from a large outcrop on the border of the Adaatsag and Ereendavaa terrane (**Fig. 3.1 & 3.2**). The Adaatsag terrane, which extends into northeast Russia, is described as an accretionary wedge (Badarch et al., 2002) and represents part of the Mongol-Okhotsk Belt; a part of the Mongol-Okhotsk suture. As described by Kurichara et al. (2008), the Adaatsag terrane contains serpentised dunites and harzburgites associated with Carboniferous layered gabbro, sheeted mafic dykes, basalts overlain by red cherts and clastic sediments, suggesting an evolved oceanic crust existed until the Carboniferous. The Ereendavaa terrane extends into Russia and NE China and is a cratonic terrane that includes intrusions of Upper Triassic-Lower Jurassic granite plutons (Badarch et al., 2002). Samples TCS 7.1 to 7.7 represent different units through a sequence of lavas; where TCS 7.1 was at the top and TCS 7.7 at the base of the sequence. Trachyandesite and trachyte lavas (Group 1; TCS 2.1 to 13.1) were also collected along strike from the LSA outcrop (~15 to ~160 km from the LSA outcrop) and are included in this study for comparison.

High-silica adakite (HSA) samples were collected from a large outcrop ~45 km west of Choir, close to the Tsagandelger area (**Fig. 3.2**). These lavas are located on the Middle Gobi volcanic belt (Badarch et al., 2002). In the Tsagandelger area, Mesozoic volcanic rocks occur in calderas located within graben structures. As described by Dash et al. (2015) there are Mesozoic shoshonite lavas in the Tsagandelger area ($^{40}\text{Ar}/^{39}\text{Ar}$; 114 ± 0.7 Ma) and absarokite lavas which are close to the HSA outcrop and are included in this study (Group 2).

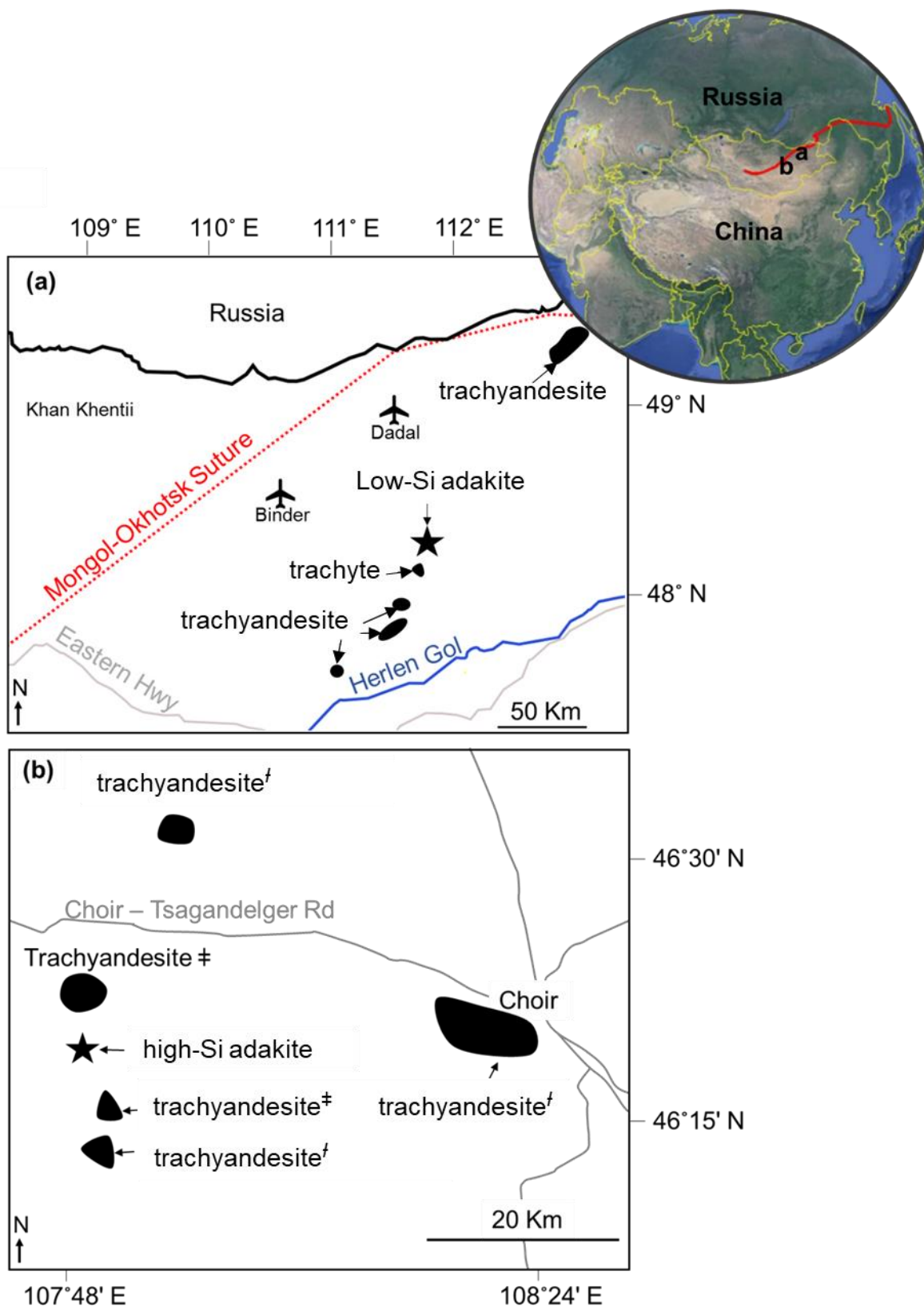


Figure 3.2: Sketch maps showing the field localities for (a) the low-silica adakites and (b) the high-silica adakites. Trachyandesite lavas (^f= Absarokite, [‡]= shoshonite attributes) for image “b” was taken from Dash et al. (2015). Also shown is an inset Google Earth image highlighting the Mongol-Okhotsk Suture in red. [‡]

3.3 PETROLOGY

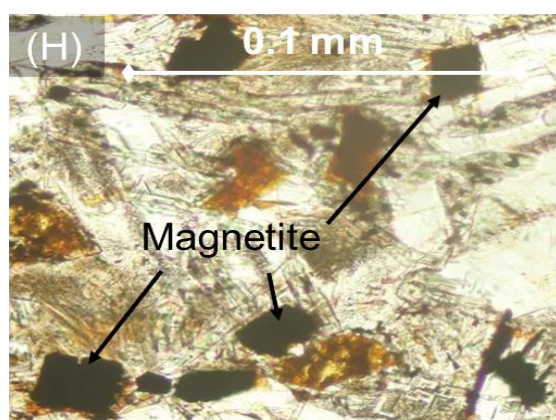
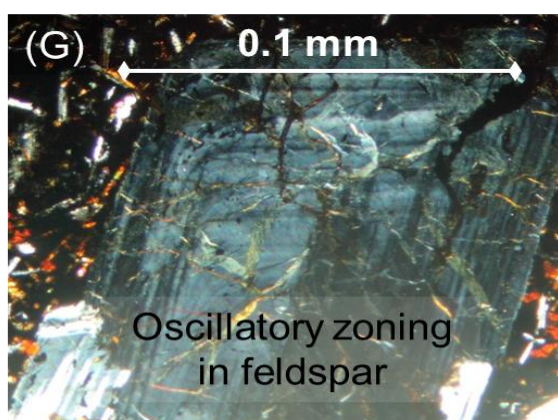
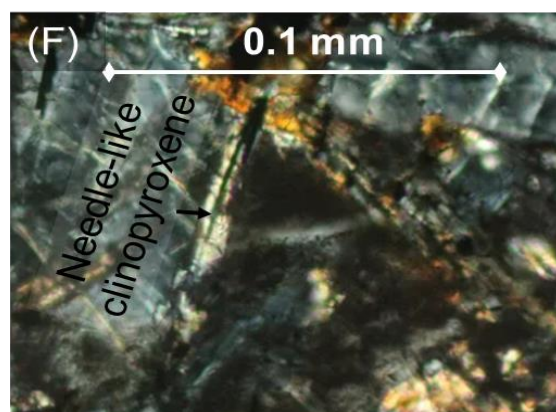
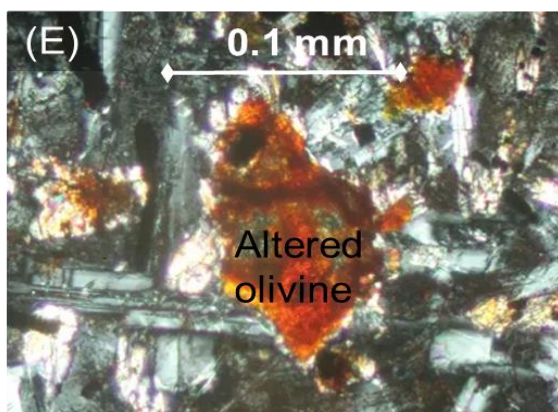
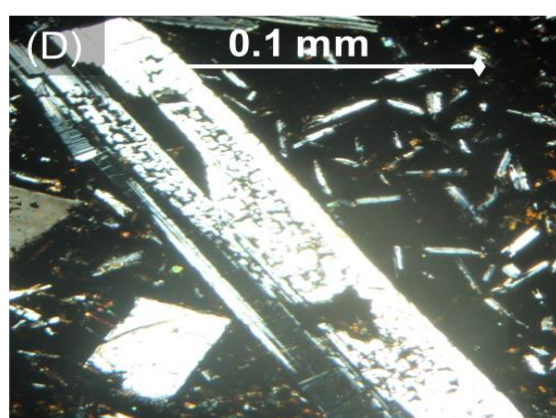
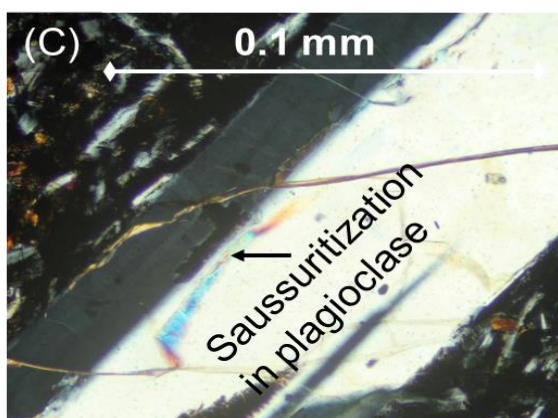
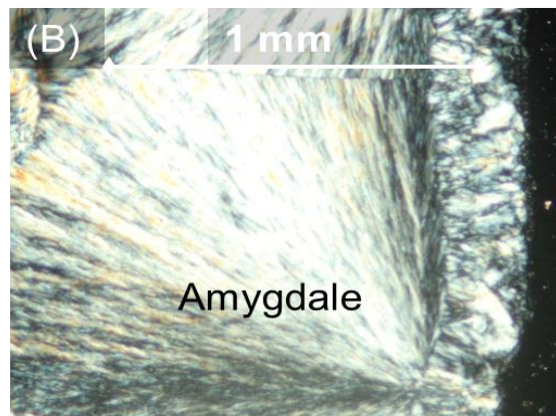
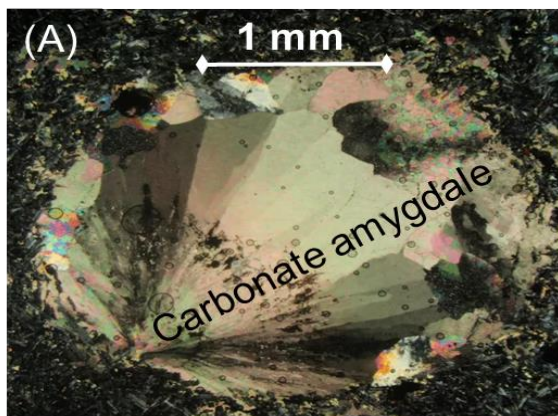
3.3.1 *Petrological observations*

Representative phenocryst abundances and sample specific information is reported in Table 3.2.

Group 1 trachyandesite outcrops have undergone weathering, are vesicular (commonly infilled with agate) and have FeO reaction tops. Trachyandesite lavas are hypocrySTALLINE and the groundmass contains abundant plagioclase, altered clinopyroxene and rare iddingsitised olivine. Some plagioclase crystals have undergone alteration and phenocrysts have sieve textures and oscillatory zoning (**Fig. 3.3 C, D**). Sample TCS 13.1 contains rosetta plagioclase phenocrysts. Some feldspar crystals, in the groundmass, contain apatite inclusions. Samples (TCS 2.1, 3.1 & 4.1) contain carbonate amygdales (**Fig. 3.3A**). The single trachyte sample (TCS 5.1) is hypocrySTALLINE, contains crustal xenoliths (**Fig. 3.3I**), megacrysts of alkali feldspar and abundant antecrysts of plagioclase which exhibit sieve textures and resorption features. This trachyte also contains altered clinopyroxene, alkali feldspar phenocrysts and aegirine phenocrysts which have FeO and magnetite-rich reaction coronas (**Fig. 3.3 J-N**).

The Group 2 trachyandesite lavas, next to the HSA outcrop, are described as having porphyritic textures with phenocrysts of hypersthene, augite, amphibole, mica and feldspar (Dash et al., 2015). The groundmass is dominantly glass and plagioclase.

The LSA lavas are hypocrySTALLINE and have a glomeroporphyritic texture (**Fig. 3.4**). The main glomerocrysts consist of plagioclase feldspar and augite. There are occasional sanidine phenocrysts and there is rare sericitisation of plagioclase. The groundmass makes up ~80% of the rock volume and is dominated by plagioclase feldspar (intermittently containing apatite inclusions; **Fig. 3.4 E-F**) and minor opaque minerals.



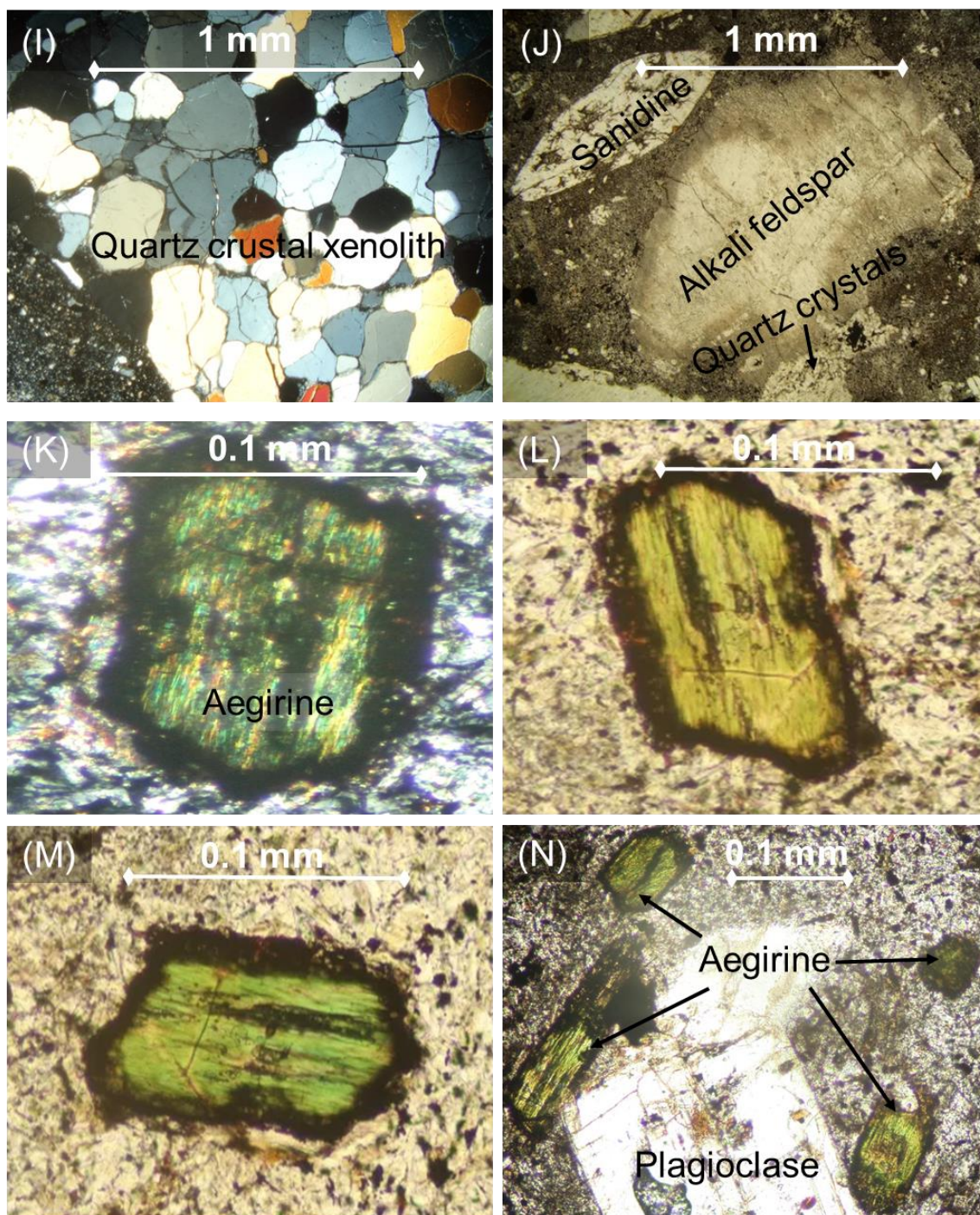


Figure 3.3: Photomicrographs of trachyandesite (A to H) and trachyte (I to N): (A) carbonate amygdale; (B) amygdale filled with radiating material; (C) saussuritization of plagioclase feldspar; (D) plagioclase crystal with a sieve texture; (E) olivine microphenocryst altered to iddingsite; (F) needle-like clinopyroxene in the groundmass; (G) oscillatory zoning in feldspar; (H) magnetite crystals with FeO reaction rims; (I) crustal xenolith consisting of quartz crystals; (J) altered alkali feldspar xenocryst partially enclosed by quartz crystals; (K, L & M) the same phenocryst of clinopyroxene which has been altered to aegirine displaying slight pleochroism; (N) aegirine with magnetite-rich coronas and a plagioclase phenocryst. Photomicrographs “A” to “G”, “I” and “K” are XPL view. Photomicrographs “H”, “J” and “L” to “N” is in PPL view.

The HSA samples are fresh, glomeroporphyritic, hypocrySTALLINE and contain more glass than the LSA lavas. The glomerocrysts contain clinopyroxene (augite and minor pigeonite) while there are separate phenocrysts of enstatite and plagioclase feldspar.

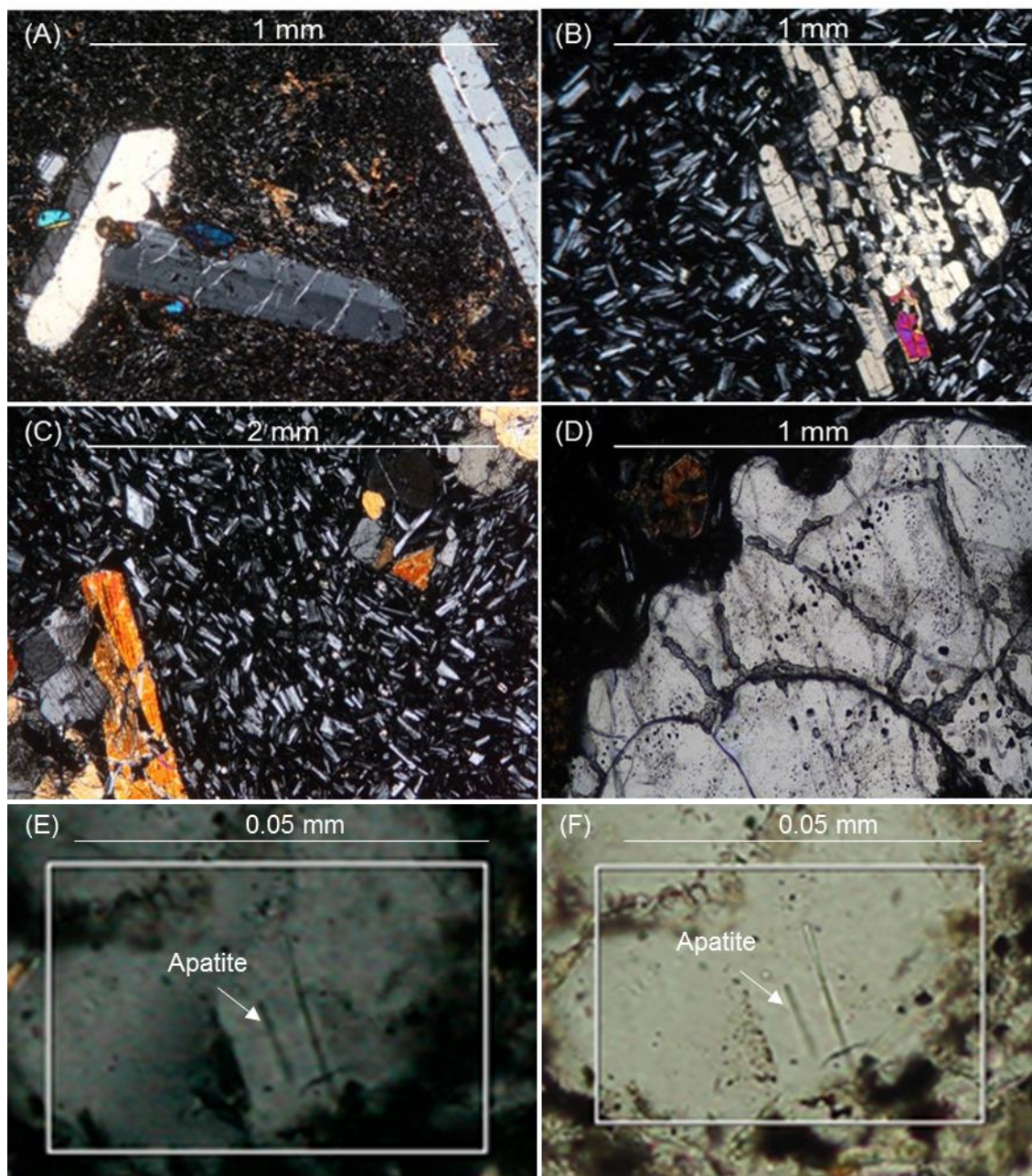


Figure 3.4: Representative photomicrographs of the low-silica adakite (A, E and F) and high-silica adakite (B, C and D) samples: (A) sanidine, plagioclase and augite phenocrysts; (B) an enstatite and augite phenocryst showing resorption features; (C) glomerocrysts of clinopyroxene phenocrysts; (D) a quartz crystal containing melt inclusions; (E & F) apatite inclusions in a feldspar phenocryst; however the camera has given these apatite crystals a false green tinge. Photomicrographs “A” to “E” are in XPL view while “F” is in PPL view.

Some of the pyroxene crystals show evidence of resorption and there are also clusters of quartz crystals with melted edges. The plagioclase compositions are predominantly andesine composition although there is also rare labradorite. The groundmass makes up ~90% of the rock volume and consists primarily of plagioclase feldspar.

3.3.2 Probe analysis

The LSA and HSA samples underwent electron-probe microanalysis at the University of Leicester using a JEOL JXA 8600-S with an advanced micro-beam control system. Prior to analysing the unknown samples a calibration of the instrument was performed using known standards. The unknown samples were analysed with a beam current of 30 keV and a beam size of 5 μm . Multiple analyses were taken on each phenocryst to check for consistency between the count number totals for the different oxides.

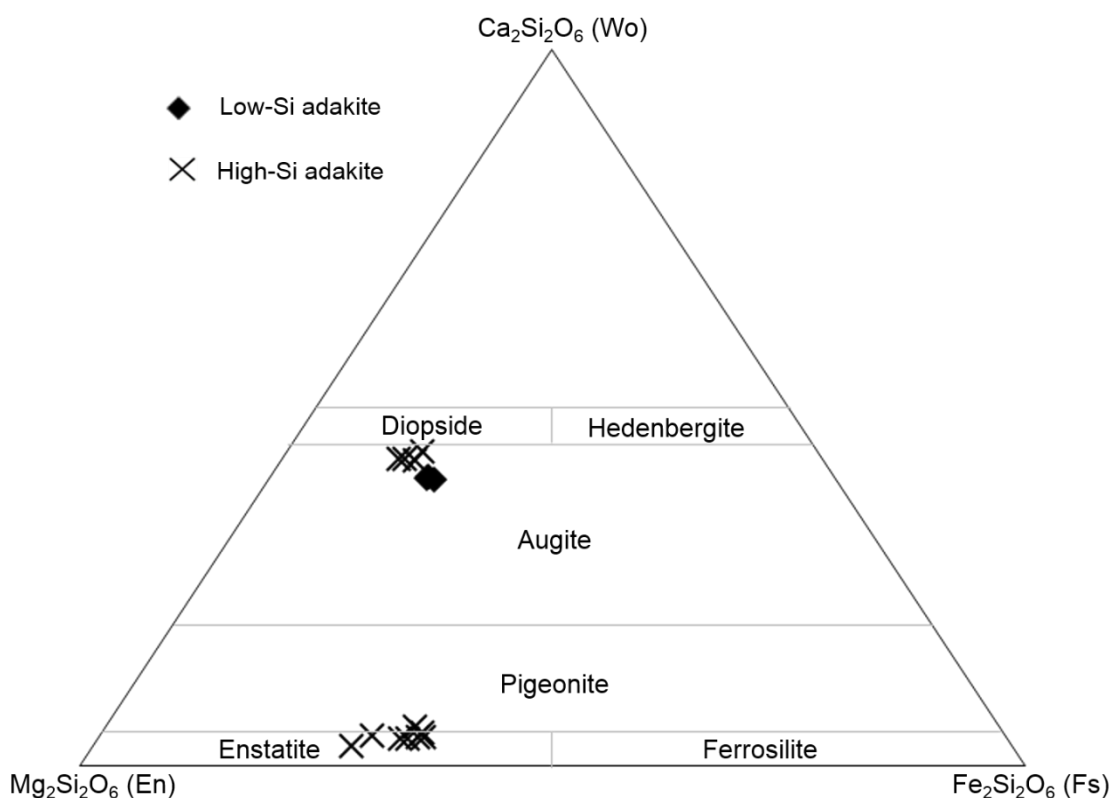


Figure 3.5 A pyroxene nomenclature plot (Wo-En-Fs) from Morimoto et al. (1988). The LSA samples contain augite phenocrysts while the HSA samples contain both augite and enstatite phenocrysts.

Pyroxene phenocrysts in both the LSA and HSA samples were analysed with the micro-probe. The major element data was entered into the program PX-NOM (Strum, 2002). Only when the major element total exceeded 97 % was this data used to classify the pyroxene phenocryst composition. The PX-NOM program uses the cation allocation rules of Morimoto et al. (1988) to determine the structural formula of the pyroxene phenocrysts and then this information was used to determine respective nomenclature.

The nomenclature is based on the scheme introduced by the International Mineralogical Association.

The calculated pyroxene parameters (enstatite, ferrosilite and wollastonite proportions) are plotted (**Fig. 3.5**) on the classification diagram from Morimoto et al. (1988). The LSAs

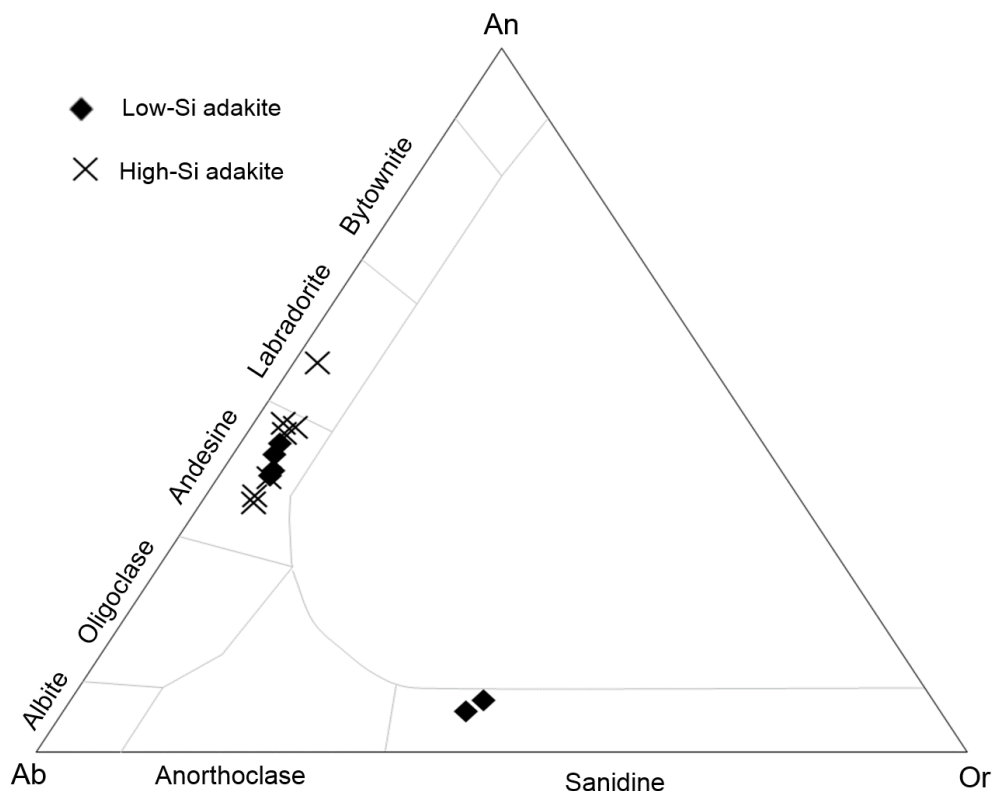


Figure 3.6: A feldspar discriminant plot (An-Ab-Or). The LSA samples contain andesine and sanidine whilst the HSA samples contain primarily andesine with rare labradorite.

are dominated by augite phenocrysts while the HSAs are dominated by enstatite, augite and minor pigeonite phenocrysts.

Plagioclase and sanidine phenocrysts were also analysed with the probe. An-Ab-Or compositions were calculated using normalised Ca, Na and K cations. In agreement with petrological observations the LSAs are dominated by andesine but also contain some sanidine suggesting the melt is potassium rich. The HSA samples are dominated by andesine and rare labradorite (**Fig. 3.6**).

Table 3.2: Petrological descriptions

Sample	CIPW- norm	Rock type	% estimated phenocryst population:						Groundmass %	Alteration %	Texture	Comments
			Ol	Cpx	Orth	Plag	Alk	Qtz				
TCS 2.1	Qtz- norm	TA	5	-	-	95	-	-	~95	20	Hyp & amy	Plag phenocrysts have undergone some sericitisation and saussuritization, Ol microphenocrysts are completely altered to iddingsite. There are carbonate amygdales. Groundmass dominated by Plag, occasional needle-like Cpx, rare Ol, glass (altered in places) and minor opaque crystals. Feldspar crystals contain small apatite crystals.
TCS 4.1	Qtz- norm	TA	-	5	-	95	-	-	~90	10	Hyp, porh & amy	Some of the Plag phenocrysts have oscillatory zoning. Some amygdales. Groundmass dominated by Plag, some altered Cpx, rare altered Ol, glass and minor opaque crytals. Feldspar crystals contain small apatite crystals.
TCS 5.1	Qtz- norm	TRC	-	-	-	80	20	-	~80	15	Hyp & trach	Phenocrysts of Plag, megacrysts of Alk and occasional sanidine. Sieve textures in some of the Plag. Crustal xenoliths. There is an altered green mineral (aegirine) with a third order green colour, slightly pleochroic, prismatic cleavage and high relief with magnetite-rich reaction coronas. Groundmass is dominated by Plag, some Cpx and minor opaque crystals.

% estimated phenocryst population:												
Sample	CIPW- norm	Rock type	% estimated phenocryst population:						Groundmass %	Alteration %	Texture	Comments
			Ol	Cpx	Orth	Plag	Alk	Qtz				
TCS 6.1	Qtz- norm	TA	-	1	-	99	-	-	~98	15	Hyp	Abundant fresh Plag in the groundmass and occasional Plag phenocrysts. Abundant Cpx, glass and rare Ol in the groundmass which is altered to clay minerals. There are minor opaque crystals.
TCS 7.1	Qtz- norm	LSA-TA	-	15	-	85	-	-	~80	5	Hyp & glom	Plag phenocrysts exhibit oscillatory zoning and the Cpx phenocrysts can exhibit simple twinning. The groundmass is dominated by Plag, glass and minor opaque crystals. Feldspar crystals contain small apatite crystals.
TCS 7.4	Qtz- norm	LSA-TA	-	20	-	80	-	-	~80	5	Hyp & glom	Accessory Qtz with undulose extinction. Some Plag phenocrysts exhibit oscillatory zoning. Cpx exhibits simple twinning. Accessory biotite. The groundmass is dominated by Plag, glass and minor opaque crystals. Feldspar crystals contain small apatite crystals.
TCS 7.7	Qtz- norm	LSA-TA	-	15	-	85	-	-	~85	10	Hyp & glom	Some Plag phenocrysts exhibit oscillatory zoning and have undergone some minor sericitism. Cpx can exhibit simple twinning. Accessory sanidine. The groundmass is dominated by Plag, glass and minor opaque minerals. Feldspar crystals contain small apatite crystals.

Sample	CIPW-norm	Rock type	% estimated phenocryst population:						Groundmass %	Alteration %	Texture	Comments
			OI	Cpx	Orth	Plag	Alk	Qtz				
TCS 10.1	Qtz-norm	TA	-	-	-	100	-	-	~90	10	Hyp & porh	Large phenocrysts of Plag with sieve textures. Groundmass dominated by Plag, glass and occasional altered Cpx and minor opaque crystals. Feldspar crystals contain small apatite crystals.
TCS 59.1	Qtz-norm	HSA-D	-	35	17	45	-	3	~90	1	Hyp & glom	Fresh. Some pyroxene phenocrysts have undergone resorption. Plag phenocrysts can exhibit oscillatory zoning. Groundmass is dominated by Plag, glass and minor opaque minerals.
TCS 59.4	Qtz-norm	HSA-D	-	64	10	20	-	6	~90	3	Hyp & glom	Plag phenocrysts can exhibit oscillatory zoning. Clusters of Qtz crystals which have melted edges and contain melt inclusions. The groundmass is dominated by Plag. Feldspar crystals contain small apatite crystals.

TA, trachyandesite; TRC, trachyte; LSA, low-silica adakite; HSA, high-silica adakite; D, dacite; Ol, olivine; Cpx, clinopyroxene; Orth, orthopyroxene; Plag, plagioclase; Alk, alkali feldspar; Qtz, quartz; Hyp, hypocrystalline; Amy, amygdaloidal; Porh, porphyritic; Trach, trachytic; Glom, glomeroporphyritic. CIPW-norm used $Fe_2O_{3T}/FeO = 0.2$.

3.4 ARGON DATING

Of the adakitic rocks, two samples from the LSA sequence (TCS 7.1 & 7.7) and one sample from the HSA outcrop (TCS 59.2) were selected for whole-rock $^{40}\text{Ar}/^{39}\text{Ar}$ dating. One additional trachyandesite sample from Group 1 (TCS 4.1) was also selected for whole-rock $^{40}\text{Ar}/^{39}\text{Ar}$ dating. Samples were selected based on high total alkali ($\text{K}_2\text{O} + \text{Na}_2\text{O}$) content and the freshness of feldspar phenocrysts and groundmass material. Samples were crushed, washed in H_2O , sieved to $600\ \mu\text{m}$ and then carefully picked under a binocular microscope to sample the freshest material. Whole-rock sample TCS 7.1 were then sent to The Open University (Milton Keynes, United Kingdom) while the other samples were sent to the SUERC (Scottish Universities Enterprise and Research Centre) labs. Age spectra and isochron ages ($^{40}\text{Ar}/^{36}\text{Ar}$ versus $^{39}\text{Ar}/^{36}\text{Ar}$) were calculated for incremental heating experiments and the analytical procedure is reported in appendix material. The $^{40}\text{Ar}/^{39}\text{Ar}$ plateau diagrams are presented below (Fig. 3.7):

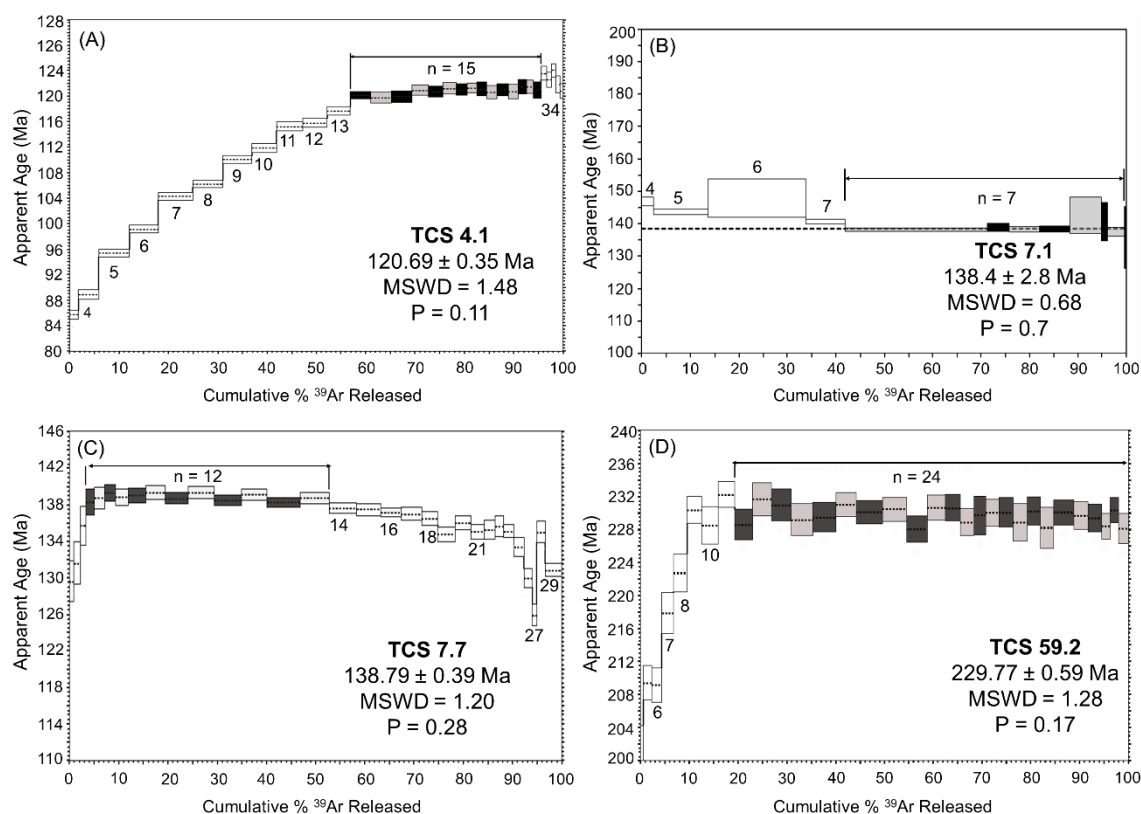


Figure 3.7: Whole-rock ^{40}Ar - ^{39}Ar age plateau diagrams for TCS 4.1 (A), the low-Si adakites (B-C) and high-silica adakite (D). Also shown on each plateau diagram is the MSWD (mean square weighted deviation) and P (Chi Square value).

The two LSA samples (TCS 7.1 and 7.7) have plateau ages of 138.4 ± 2.8 and 138.8 ± 0.39 Ma which is in good agreement with calculated isochron ages of 139.2 ± 6.1 and 138.8

± 7.6 respectively. The HSA sample (TCS 59.2) has a plateau age 229.7 ± 0.59 Ma and is in good agreement with the isochron age of 230.2 ± 1 Ma. Finally, the Group 1 sample (TCS 4.1) has a plateau age of 120.7 ± 0.35 Ma and an isochron age of 118.9 ± 2.3 Ma. As discussed by deVor et al. (1992), when P (Chi Square value) is <0.05 the plateau age should be rejected. Furthermore, a good plateau should contain at least three consecutive steps to calculate a meaningful age (Baksi, 2006). The high P values and number of consecutive steps on each plateau diagram suggest that these ^{40}Ar - ^{39}Ar plateaus are good representatives of their crystallisation age. Although sample TCS 4.1 has a plateau age (120.7 ± 0.35 Ma) made from only 39 % of the total ^{39}Ar released (**Fig. 3.7A**), the high number of consecutive steps ($n = 15$) and high P value (0.11) suggest that this plateau age is reliable. The two LSA samples (TCS 7.1 and 7.7) have plateaus made from 58 % and 49 % of the total ^{39}Ar released respectively (**Fig. 3.7B & C**). These two samples were analysed at different labs and the plateau ages are mutually supportive. Finally, the HSA sample (**Fig. 7D**) has a plateau age (230 ± 0.59 Ma) which utilises 81 % of the total ^{39}Ar released and thus likely reliable.

The LSA samples are a similar age to adakitic lavas in the North China Craton; these adakitic localities seem to align in a north-south direction (**Fig. 3.1**; Chen et al. 2013; Wang et al. 2016).

The HSA samples are older than the LSA and Chinese adakitic localities located further east (**Fig. 3.1**). Yet, the HSA are younger than the Carboniferous Shuteen Complex adakites which were interpreted to be melts from subducted oceanic crust. Consideration of the geochemical data in the following sections is used to assess the petrogenesis of the HSA samples and to discuss possible geodynamic scenarios.

3.5 GEOCHEMICAL RESULTS

3.5.1 Rock classification and major-element variations

Petrological observations reported above (Table 3.2) show that the HSA samples have undergone little alteration while the LSAs have experienced sericitisation (**Fig 3.4B**) and groundmass breakdown to clay minerals. Group 1 trachyandesite lavas have altered plagioclase feldspar and iddingsitised olivine. The trachyte sample (TCS 5.1) contains

altered aegirine. Other than sample TCS 7.5 which has a LOI value of 4.75 wt. %, all the HSA, LSA and Group 1 samples have LOI values <2 wt. % (**Fig. 3.8**). Due to the higher LOI value for sample TCS 7.5, this sample is omitted from further study.

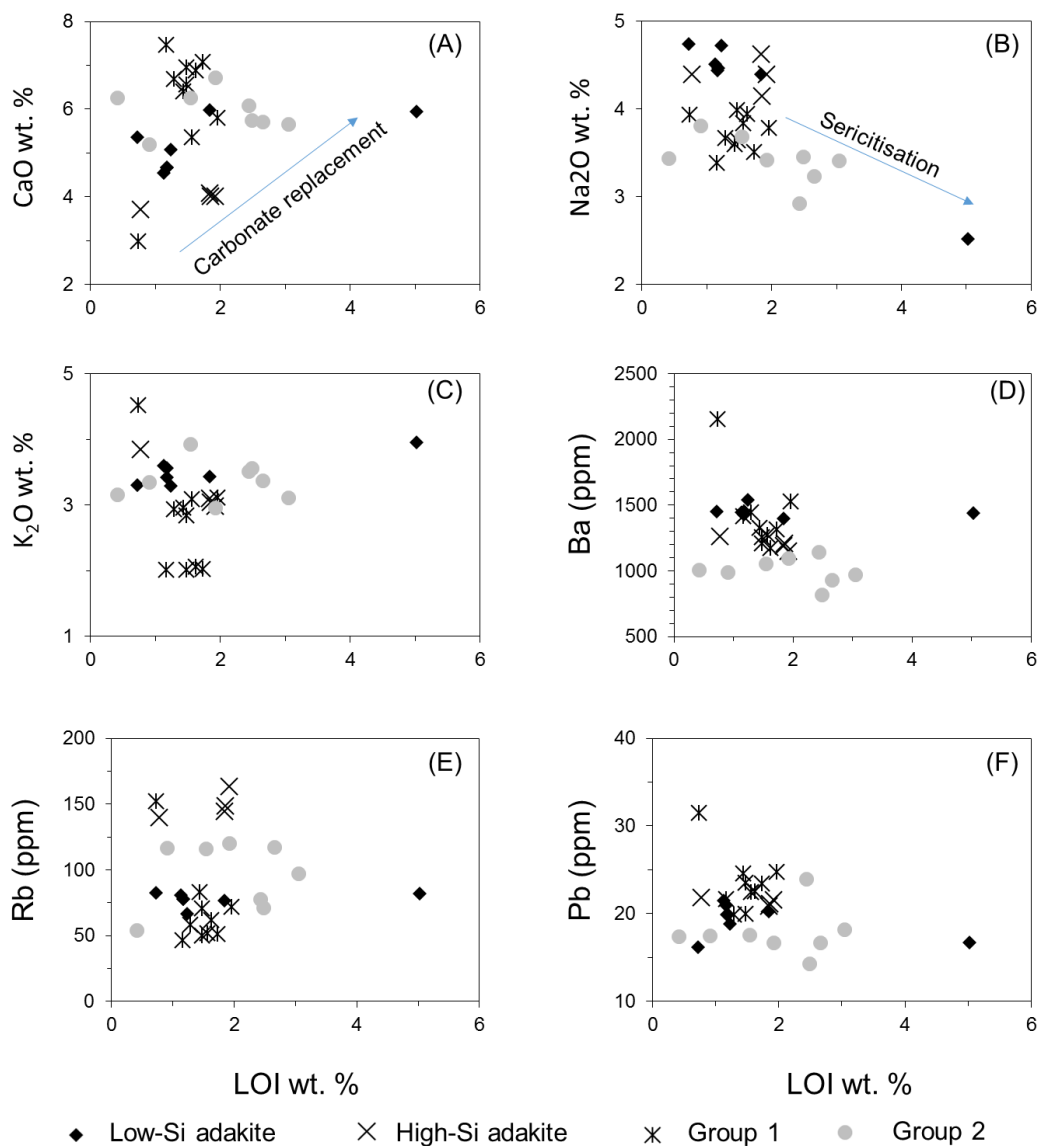


Figure 3.8: Loss on ignition (LOI) vs. oxides (A-C) and mobile trace-element (D-F) plots.

To classify the samples, a SiO₂ wt. % vs. Nb/Y (immobile elements) plot is used (**Fig. 3.9**). The LSA samples plot in the trachyandesite field while the HSA samples plot in the dacite field. Group 1 and 2 samples plot predominantly in the basaltic-trachyandesite/trachybasalt to trachyandesite field. Sample TCS 5.1 classifies as a trachyte. The Na₂O + K₂O vs. SiO₂ classification system from Irvine and Baragar (1971) discriminated the LSA samples as belonging to the alkaline series and the HSA samples

in the sub-alkaline series (**Fig. 3.10A**). Other than three samples (TCS 5.1, TCS 13.1 and 4/626), the Group 1 and 2 samples plot in the alkaline series. The discriminant scheme from Hastie et al. (2007) uses elements Th and Co to further classify sub-alkaline volcanic rocks. On this Th-Co classification diagram, the HSA samples plot in the high-K/shoshonite field (**Fig. 3.10B**).

On a Sr/Y vs. Y plot (**Fig. 3.11A**), the LSA samples form a trend which leaves the “mantle array” and trends into the “adakite array”. The HSA samples plot in the adakite field. Other than two samples (3/11 & 3/12) from Group 2, the Group 1 and 2 samples plot in the “mantle array”. The LSA and HSA samples have increasing La/Yb ratios with decreasing Yb (**Fig. 3.11B**). Fractionation of accessory minerals, such as zircon and

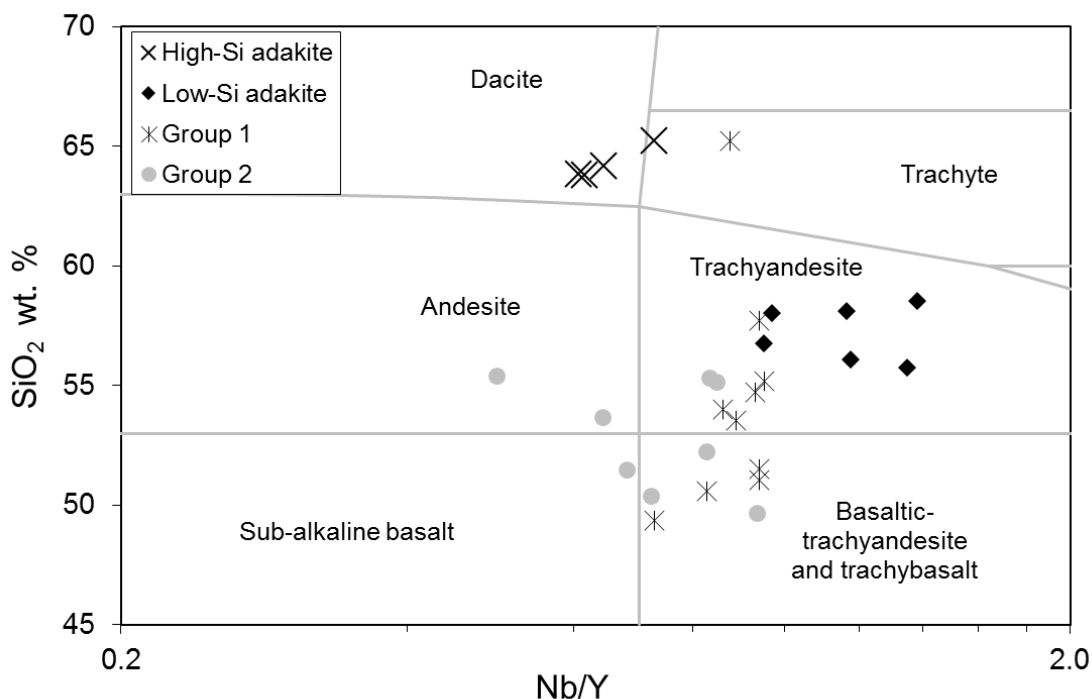


Figure 3.9: A Nb/Y vs. SiO₂ immobile element rock classification diagram (from Winchester and Floyd, 1977) for all samples.

apatite, can deplete HREE's from a melt and this is emphasised in the calculated Rayleigh fractionation curve (**Fig. 3.11B**).

The LSA and HSA samples have a low MgO content (**Fig. 3.12**); having 1.75 to 2.2 wt. % and 0.96 to 2.08 wt. % respectively. Group 1 and 2 samples typically have higher MgO contents; with 0.61 to 3.6 wt. % and 2.23 to 4.18 wt. % respectively.

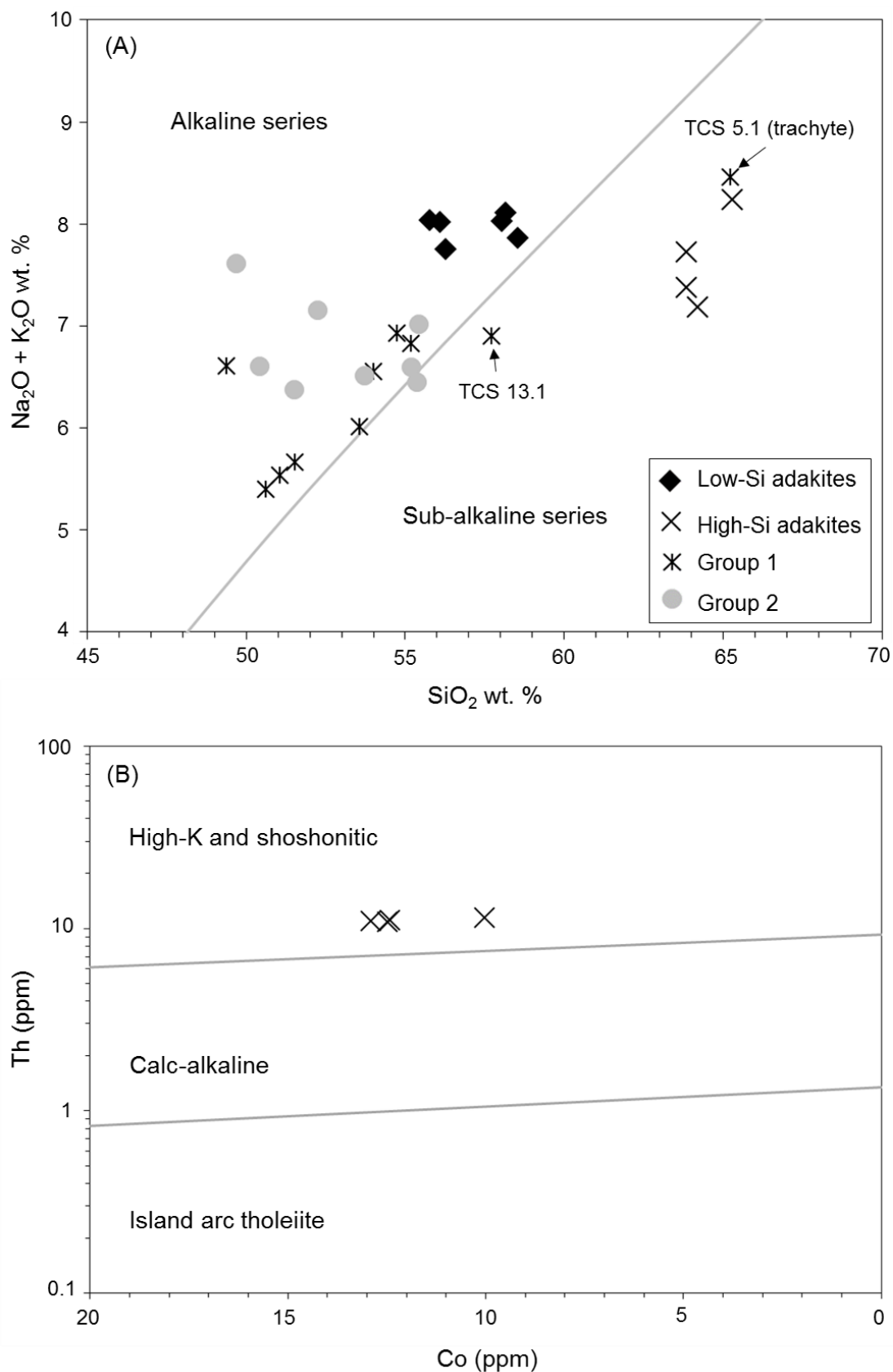


Figure 3.10: (A) SiO_2 vs. $\text{Na}_2\text{O} + \text{K}_2\text{O}$ plot (from Irvine and Baragar, 1971) for all samples. (B) A plot of Co vs. Th (from Hastie et al. 2007) for the HSA samples.

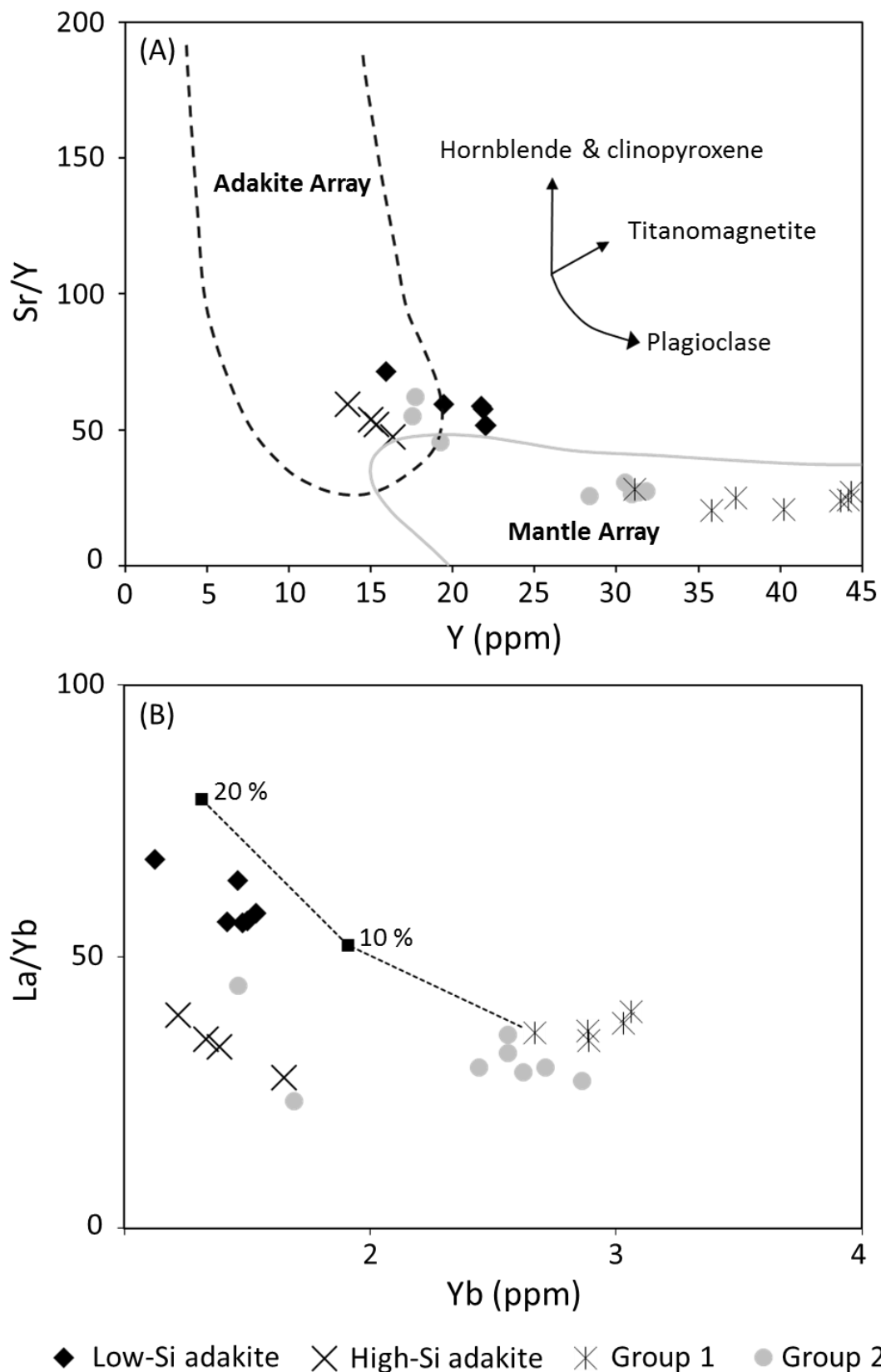


Figure 3.11: (A) Y vs. Sr/Y (after Hansen et al., 2002) and (B) Yb vs. La/Yb plots. A calculated Rayleigh fractional crystallisation curve (25 % clinopyroxene, 70% plagioclase, 3% zircon and 2% apatite) is shown on Figure B. The partition coefficients utilised were calculated from alkali basalt and trachyandesite compositions (Fujimaki et al. 1986 and Luhr et al. 1984) and the amount of fractionation is shown next to the curve (a maximum of 20% is shown).

There is a negative correlation between SiO_2 vs. MgO wt. % (**Fig. 3.12A**) and a positive correlation between $\text{Fe}_2\text{O}_{3(\text{T})}$, TiO_2 , CaO , and $\text{CaO}/\text{Al}_2\text{O}_3$ vs. MgO wt. % for all sample suites (**Fig. 3.12 C, D, F & I**). Other than Group 2 (which show no clear trend), the other sample suites have a negative correlation between Al_2O_3 , K_2O with MgO (**Fig. 3.12B & E**).

3.5.2 Trace-element and REE variations

There is a positive correlation between Ni and MgO for the LSA and HSA samples; Ni concentrations range from 22 to 36 ppm and 17 to 21 ppm respectively. Group 1 and 2 samples have <1 (TCS 5.1; trachyte) to 28.9 ppm Ni, and 53 to 122 ppm Ni respectively; there is no clear correlation with MgO for Group 1 but a positive correlation for Group 2 (**Fig. 3.12G**). Chromium concentrations range from 52 to 58 ppm for the LSA samples and 30 to 38 ppm for the HSA samples; there is a positive correlation with MgO (**Fig. 3.12H**). Group 1 samples have Cr concentrations ranging from <1 (TCS 5.1; trachyte) to 47 ppm and there is no clear correlation with MgO . Group 2 samples do not have Cr concentrations recorded for them (Dash et al., 2015). The LSA and Group 2 samples have decreasing Zr concentrations with increasing SiO_2 (**Fig. 3.13A**). The LSA, Group 1 and 2 samples have clear correlations for SiO_2 vs. P, Sm and Yb (**Fig. 3.13 B-G**).

Primitive mantle-normalised diagrams (**Fig. 3.14A**) show that the LSA, HSA, Group 1 and 2 samples are enriched in the LREE, HFSE and LILE compared to N-MORB. Furthermore, these samples are much more depleted in the HREE compared to N-MORB and have negative Nb and Ta anomalies. The LSA and HSA samples also have negative Y anomalies. In addition to all the samples having positive Pb anomalies they also have negative P, Sm and Ti anomalies. The LSA samples have positive Ba anomalies and are more enriched in the LREE and MREE compared to the HSA samples. The HSA samples are more enriched in Rb, Th and U but have much lower concentrations of Nb and Ta compared to the LSA samples. Group 1 and 2 samples often have positive Ba anomalies.

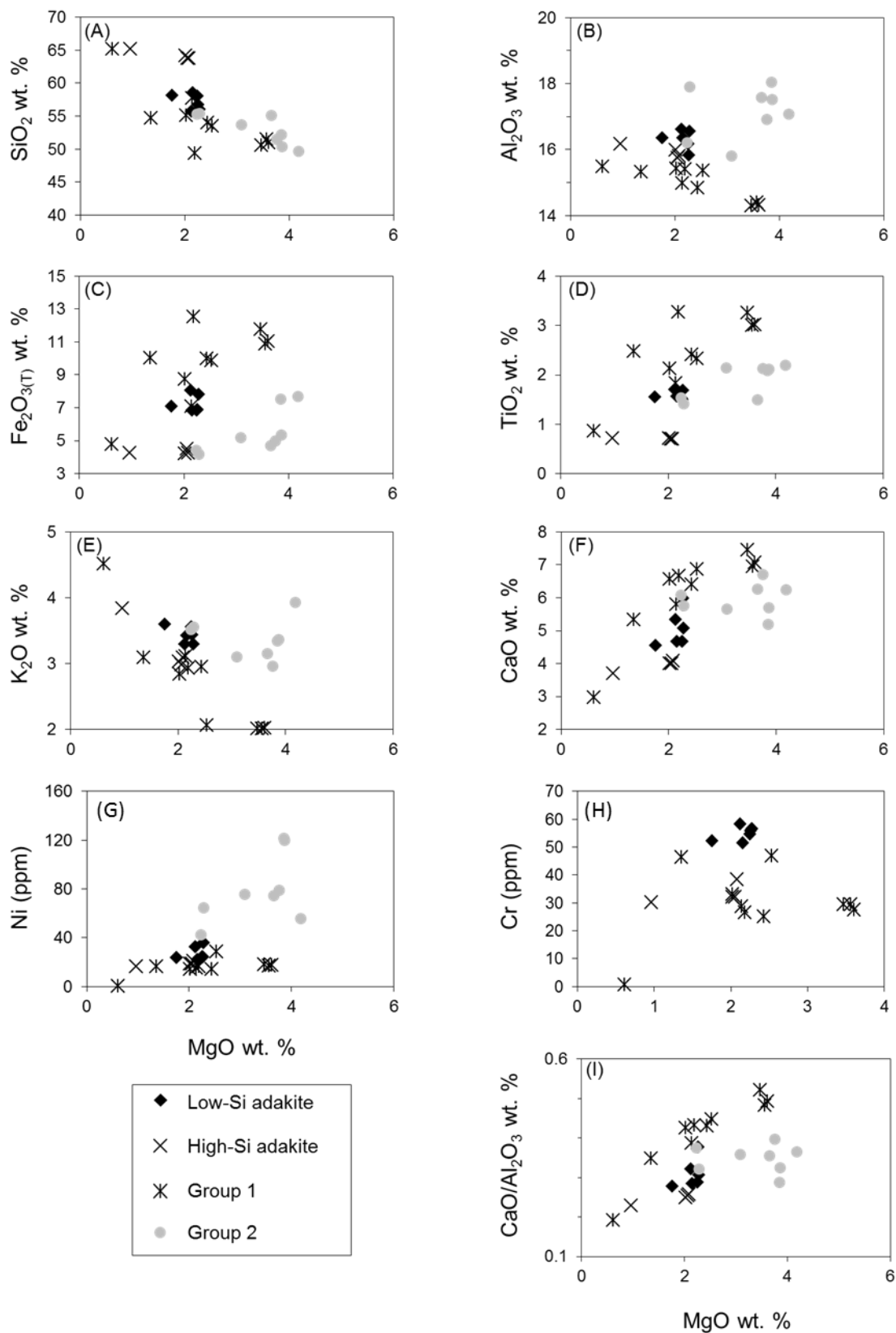


Figure 3.12: Variations in major-element oxides, compatible trace elements and CaO/Al₂O₃ with MgO wt. % for the low-Si adakites, high-Si adakites, Group 1 and 2 samples.

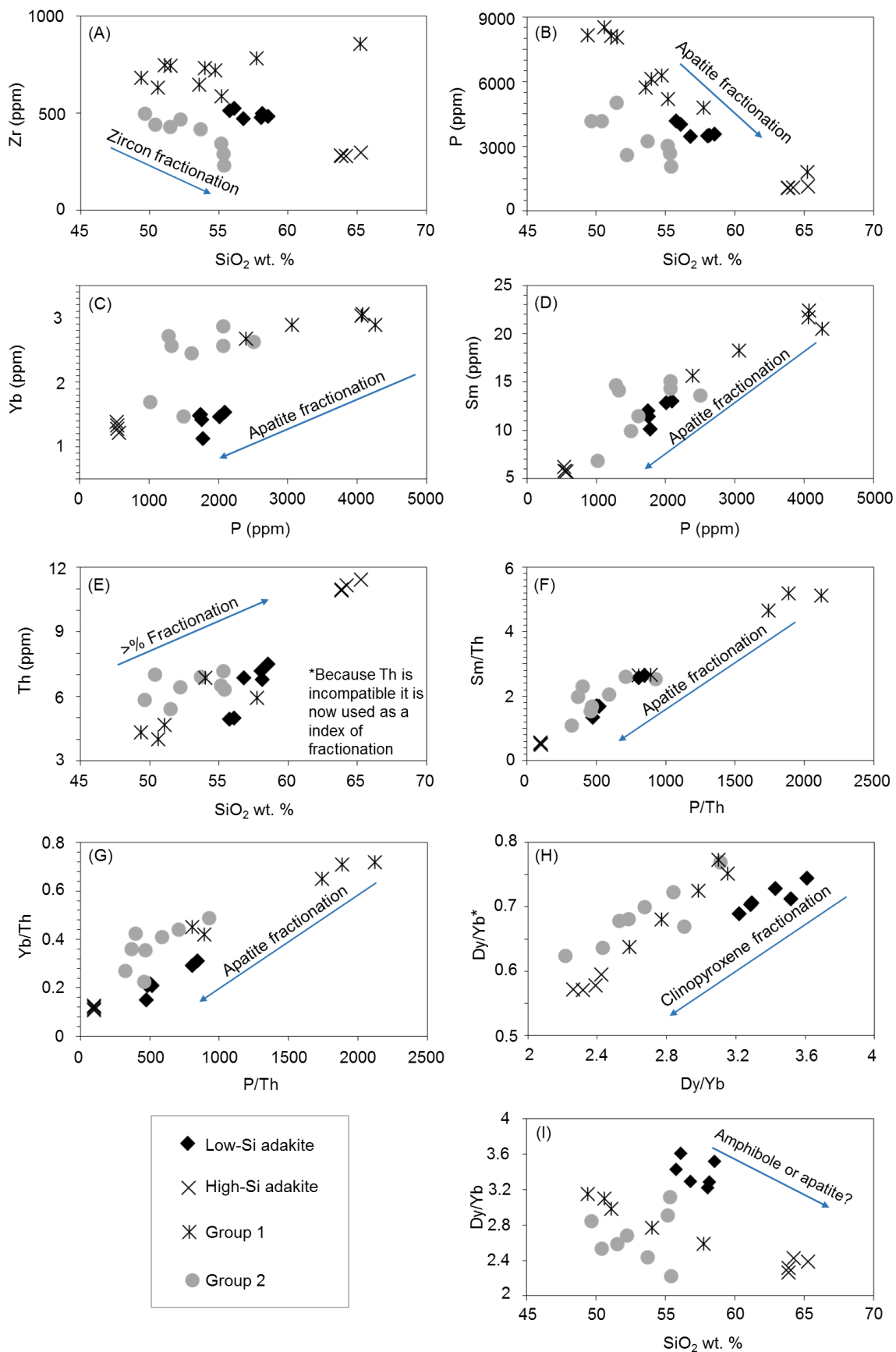


Figure 3.13: Variations in major-element oxides and trace elements for the low-Si adakites, high-Si adakites, Group 1 and 2 samples.

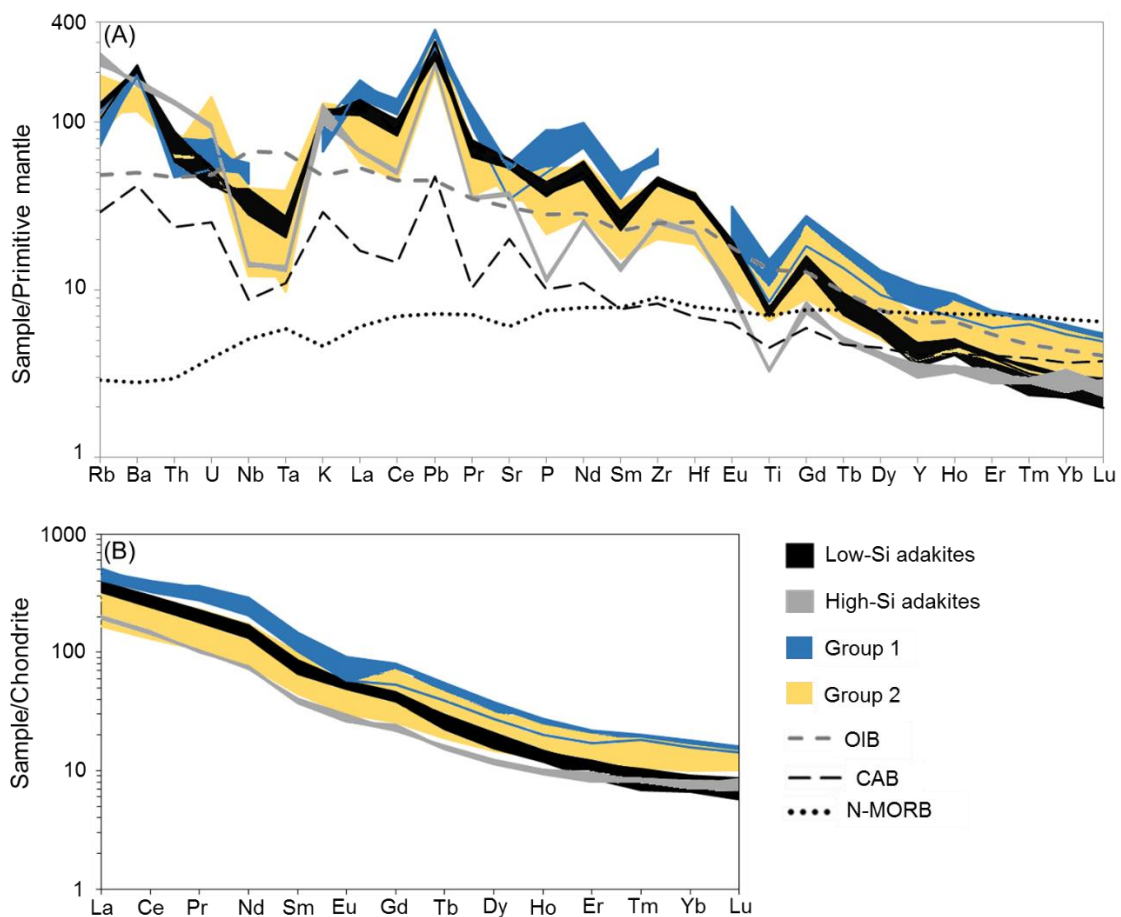


Figure 3.14: (A) Primitive mantle-normalised trace element variation diagram. (B) Chondrite-normalised REE diagram. The normalisation values for the primitive mantle and chondrite are from Sun and McDonough (1989) and the primitive mantle Pb normalisation value used was 0.071. Data sources: OIB: Sun and McDonough (1989); average CAB: Kelemen et al. (2003) and N-MORB: Gale et al. (2013).

All the samples are enriched in the fluid-mobile incompatible trace elements such as LILE (e.g., Rb, Ba, K) compared to OIB (Sun and McDonough, 1989) and average continental arc basalt (CAB; Kelemen et al. 2003). Similarities between the CAB and Mongolian samples are evident from the mirroring of many element anomalies. However, all the Mongolian samples are more enriched in LILE, HFSE and LREE than CAB. The LSA, HSA and some Group 2 samples are more depleted in HREE compared to CAB.

Chondrite-normalised REE patterns (**Fig. 3.14B**) show that the LSA samples are more enriched in LREE, and can be more depleted in the HREE, than the HSA samples. Chondrite-normalised La_n/Yb_n ratios are between 40.2-48.6 for the LSA samples and 23.6-27.3 for the HSA samples. Group 2 samples show a similar level of enrichment in the LREE to the LSA samples but are often more enriched in the MREE as well. Group 1 and 2 samples are more enriched in the HREE compared to the LSA and HSA samples.

Group 1 and 2 samples have chondrite-normalised La_n/Yb_n ratios between 24.8-28.6 and 16.8-32.1 respectively.

3.5.3 Comparative summary

A brief summary of the geochemical results is shown below:

Table 3.3 – Geochemical summary. Adakite geochemical characteristics according to Castillo (2006).

Adakite geochemical characteristics	Low-Si adakites	High-Si adakites	Group 1	Group 2
Low MgO (<3 wt. %)	1.7 – 2.2 ✓	0.9 – 2 ✓	0.6 – 3.6	2.2 – 4.1
High Al_2O_3 (>15 wt. %)	15.8 – 16.6 ✓	15.7 – 16.1 ✓	14.3 – 15.4	15.8 – 18 ✓
High SiO_2 (>56 wt. %)	55.7 – 58.5 ✓	63.8 – 65.2 ✓	50.7 – 57.7	49.6 – 55.4
High Sr (> 300 ppm)	1036 – 1273 ✓	776 – 809 ✓	645 – 1206 ✓	725 – 1102 ✓
Low Yb (<1.9 ppm)	1.1 – 1.5 ✓	1.2 – 1.3 ✓	2.6 – 3	1.4 – 2.8
High La/Yb (>20)	56 – 67 ✓	32 – 38 ✓	34.5 – 39.9 ✓	23 – 44 ✓
Low $^{87}\text{Sr}/^{86}\text{Sr}_{(i)}$ (<0.704)	0.705	0.705	0.705	0.705 – 0.707
Low $^{206}\text{Pb}/^{204}\text{Pb}_{(i)}$	18.41 – 18.42	18.33 – 18.34	18.31 – 18.49	No data
High $^{143}\text{Nd}/^{144}\text{Nd}_{(i)}$	0.5124 – 0.5125	0.5124 – 0.5125	0.5123-0.5125	0.5124 – 0.5125

DATA INTERPRETATION

3.6 FRACTIONAL CRYSTALLISATION

No olivine phenocrysts were identified in the LSA and HSA samples; this suggests that if there was any olivine fractionation, then this must have occurred in the parental magma at depth. Olivine fractionation is evidenced in Group 1 samples because iddingsitised olivine phenocrysts were identified during petrological studies reported above (**Fig. 3.3E**).

Petrological studies identified augite in the LSA, HSA and Group 1 samples; decreasing CaO/Al₂O₃ ratios with MgO emphasises this fractionating phase (**Fig. 3.12I**). Augite was identified in the Group 2 lavas by Dash et al. (2015), suggesting these lavas also had augite as a fractionating phase. Decreasing Dy/Dy* vs. Dy/Yb (**Fig. 3.13H**) trends for all sample suites further indicate clinopyroxene fractionation.

Plagioclase feldspar was identified in all samples and likely a fractionating phase (Table 3.2). Chondrite-normalised Eu/Eu* numbers $\left[\frac{Eu}{Eu^*} = \left(\frac{Eu_n}{((Sm_n+Gd_n)^{0.5})}\right)\right]$ range from 0.87 to 0.95 for the LSA samples and 0.83 to 0.95 for the HSA samples; this does not indicate significant plagioclase fractionation (or accumulation). Group 1 and 2 samples have Eu/Eu* numbers ranging from 0.74 to 0.84 and 0.66 to 0.86 respectively, which correlate positively with Sr, suggesting plagioclase fractionation was more significant (**Fig. 3.15**).

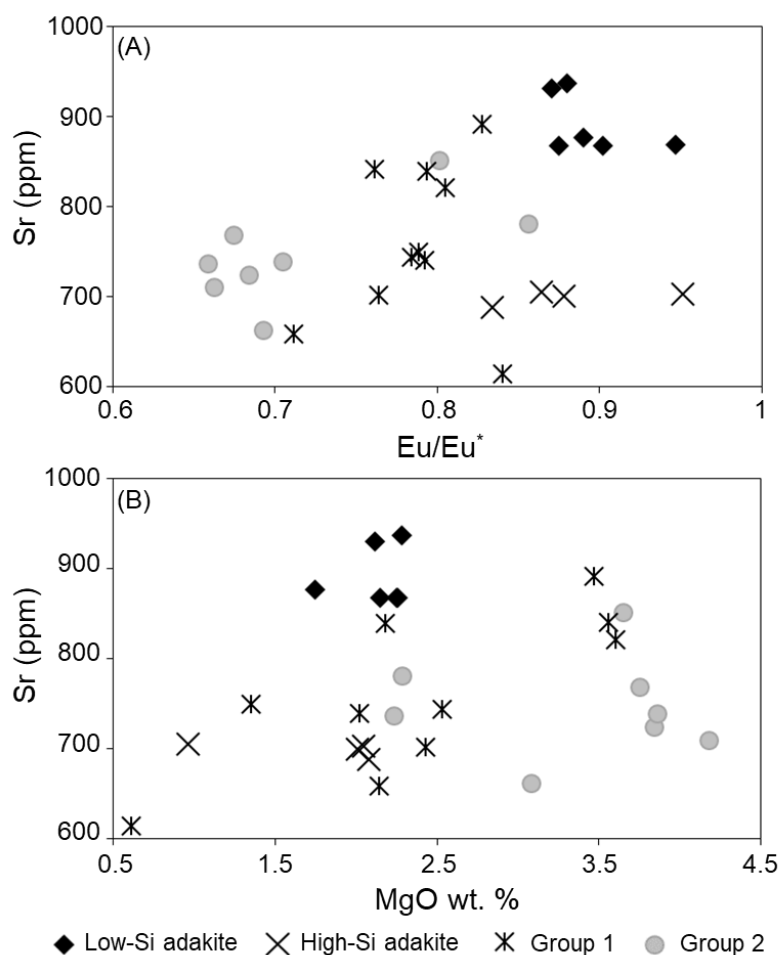


Figure 3.15: Chondrite-normalised $\frac{Eu}{Eu^*} \left[\frac{Eu}{Eu^*} = \left(\frac{Eu_n}{((Sm_n+Gd_n)^{0.5})} \right) \right]$ plot vs. Sr (ppm) for the low-Si adakites, high-Si adakites and Group 1 and Group 2 samples.

Zircon and apatite fractionation can deplete the HREE's (Luhr et al., 1984). The LSA and Group 2 samples have negative correlations between Zr and SiO₂ which suggests zircon fractionation (**Fig. 3.13A**). The primitive mantle-normalisation diagram shows samples from all groupings have negative P and Sm anomalies; this might indicate intrasuite apatite fractionation (**Fig. 3.14A**). Furthermore, other than for the HSA samples, clear trends for P vs. SiO₂, Yb and Sm supports apatite fractionation (**Fig. 3.13 B-G**). Finally, petrological observations identified small apatite inclusions within feldspar crystals, further indicating apatite fractionation processes in the LSA, HSA and Group 1 samples. The negative Y anomalies, on the primitive mantle plot (**Fig. 13.4A**), for the LSA and HSA samples might reflect residual garnet. Although Y is compatible in apatite, Ho is often more compatible (e.g., Bea et al., 1994; Dawson and Hinton, 2003 – partition coefficient values were taken from the same studies, on like-to-like rock compositions for better comparison, however, limited to carbonatite and granitic compositions due to availability (Geochemical Earth Reference Model database); and Y is more compatible than Ho in garnet (e.g., Green et al., 2000; Tuff and Gibson, 2007 – from studies on like-to-like rock compositions for better comparison; basalt to picrite).

Although no amphibole was identified in the LSA, HSA and Group 1 samples during petrological studies, it is difficult to completely rule out amphibole fractionation, or the involvement of cryptic amphibole. Melts which have undergone significant amphibole fractionation, or have been affected by residual amphibole, often have depletions in K on primitive mantle plots compared to neighbouring elements of similar compatibility (e.g., Mayer et al., 2013); this is not the case for any of the Mongolian sample suites. However, the LSA and Group 1 samples have a negative correlation between Dy/Yb ratios and SiO₂ (**Fig. 3.13I**) which could indicate that the magma for these lavas interacted with cryptic amphibole rather than necessarily fractionating the mineral phase (Smith, 2014). However, partition coefficients for Dy and Yb in apatite suggests that Dy is more compatible. For example, in a trachyandesite composition, the partition coefficient reported for Dy is ~24 while it's ~12 for Yb (Luhr et al., 1984). Therefore, on balance, there is not much independent evidence to support amphibole involvement.

3.7 MAJOR-ELEMENT, TRACE-ELEMENT AND REE COMPARISONS

The aim of the following comparisons is to evaluate broad variations between adakitic melts of different origins.

3.7.1 Mg# numbers and their significance

High-magnesium andesites (HMAs), such as those from the western Aleutians (Bryant et al., 2011) and the Qinling Mountains in central China (Xu et al., 2000) are thought to be oceanic eclogitic melts that have interacted with mantle wedge material (**Fig. 3.16**) and share many geochemical affinities with adakites. Because the high Mg# (where $Mg\# = \{\text{molar Mg}/(\text{Mg} + \text{Fe}^{2+})\}$) of the HMAs is inconsistent with pure slab melting experiments (e.g. Sen and Dunn, 1994; Rapp et al., 1999) it is suggested that interaction with the overlying mantle wedge (peridotite) has given the HMAs their high Mg#.

Carboniferous adakites from the Shuteen Complex in Mongolia have lower Mg# numbers than the HMAs and are interpreted to be melts of subducting oceanic crust with minor mantle interaction (Batkishig et al., 2010). Their Mg# is comparable to the “slab + peridotite” melting experiments of Rapp et al. (1999) where 10 to 15% peridotite was added to the slab melt. Note how these adakites plot above the “slab melts” field but below the HMAs (**Fig. 3.16**).

Intrusive adakitic rocks from the Ningzhen area in east China (Xu et al., 2002) show a steep gradient of decreasing SiO₂ with increasing Mg# and some of these adakitic rocks plot in the HMAs field (**Fig. 3.16**). These rocks have been interpreted to be a product of delamination of the lower crust with subsequent sinking into the underlying mantle. These melts are therefore a product of lower crust and mantle mixing and therefore their high Mg# is consistent with this homogenisation process.

Adakitic lavas from the Huichang Basin in SE China (Xing et al., 2003) and Lingqiu Basin in north China (Wang et al., 2006) are interpreted to be products of an underplated basaltic lower crust. Thus, these melts have had no interaction with mantle material and generally have low Mg#. Yet, if this is correct, then evidently, there can still be a range in Mg# for crustal derived melts (**Fig. 3.16**). Unpublished data on the Yungay adakitic ignimbrites (Peru), collected by B. Coldwell, is also presented henceforth (**Fig. 3.16**). Coldwell

modelled, and proposed, that these adakitic ignimbrites were crustal melts (garnet amphibolite). The low Mg# of the Yungay ignimbrites is consistent with a crustal protolith.

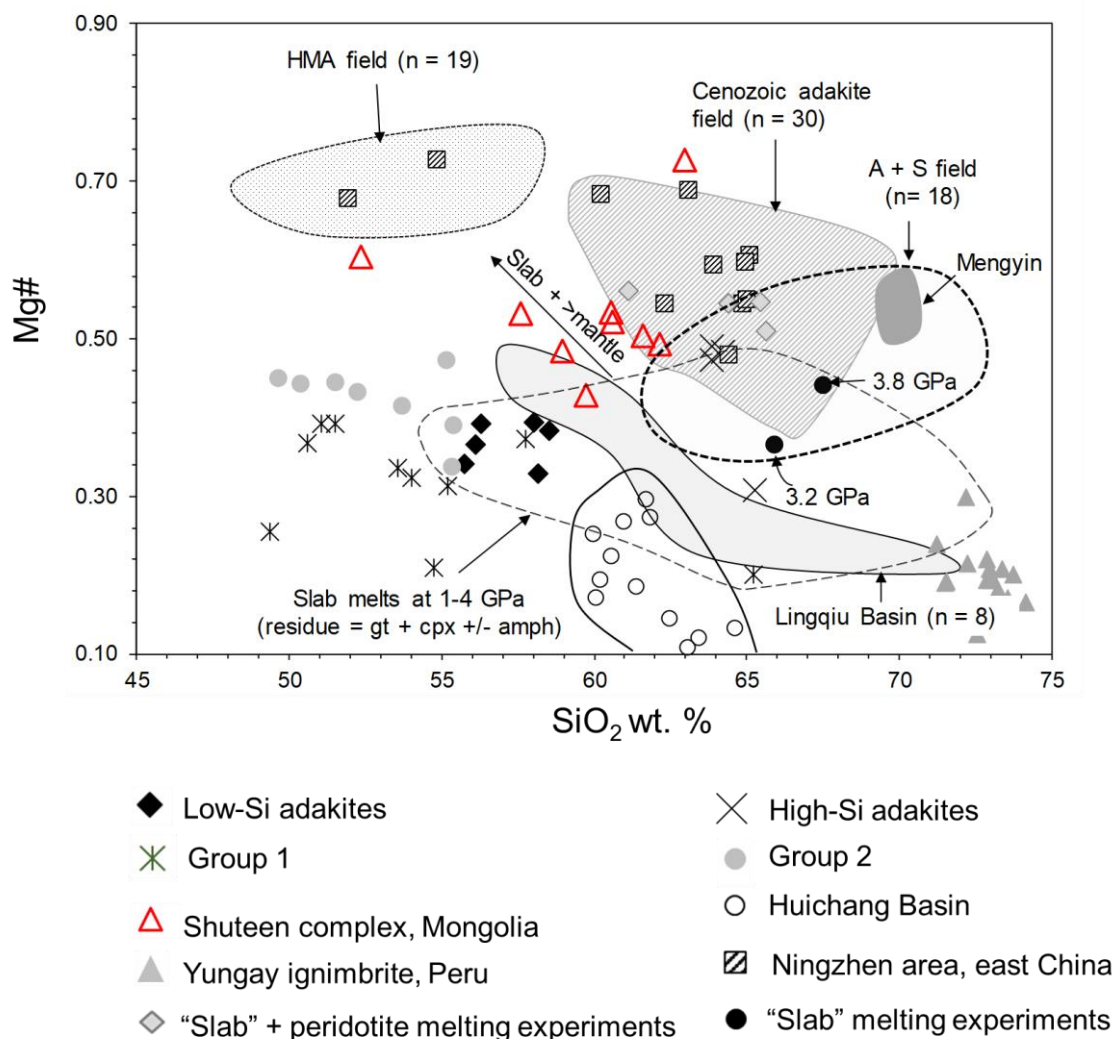


Figure 3.16: A Mg# (where $Mg\# = \{molar\ Mg / (Mg + Fe^2)\}$) vs. SiO₂ wt. % plot. The "high-Mg andesite field" (HMA) represent oceanic eclogitic melts that have interacted with the mantle wedge (Xu et al., 2000; Bryant et al., 2011). Previously interpreted slab melts from Mongolia and China are coloured red. The volcanic adakites from the Shuteen complex, Mongolia (Batkhishig et al., 2010) represent melts of subducting oceanic crust with minor mantle interaction. The Mengyin adakites were interpreted as subducted palaeo-Pacific oceanic slab melts (Wang et al., 2016). The intrusive adakitic rocks from the Ningzhen area, east China (Xu et al., 2002) represent lower-crustal delaminated melts that have interacted with mantle rocks. The adakitic lavas from the Huichang Basin, SE China (Xiong et al., 2003) and Lingqiu Basin, North China (Wang et al., 2006) represent melts of an underplated basaltic lower crust. The "A + S" field represent Awulae and Sanchakou (Xinjiang Tianshan region, China) adakitic rocks and were interpreted as a product of basaltic underplating at the base of the lower crust (Zhao et al., 2008). The "slab" melting and "slab" + peridotite (mantle) melting experiments are from Rapp et al. (1999) and the 1-4 GPa "slab melts" field was from Sen and Dunn (1994) and Rap and Watson (1995) in Rapp et al. (1999). The Cenozoic adakite field generated from data within Aguillón-Robles et al. (2001) and Stern and Kilian (1996); Vizcaino Peninsula, Mexico; Lautaro; Viedma, Aguilera, Reclus; Mt Burney and Cook Island.

Adakitic rocks (Awulae and Sanchakou) from Xinjiang Tianshan (China) were interpreted to be the product of basaltic underplating at the base of the lower crust (Zhao et al. 2008); and thus have minor mantle interaction. However, it is interesting to note that these have

quite high Mg# (A + S Field; **Fig. 3.16**), comparable to interpreted slab melts, or to adakitic lavas that have foundered into mantle material.

The LSAs from Mongolia typically have lower Mg# numbers (from 0.33-0.39) than the HSAs because they are more enriched in $\text{Fe}_2\text{O}_{3(\text{T})}$. The samples plot within the “slab melting” field. It is surprising that the LSAs have lower Mg# than the HSAs and this is not consistent with a simple model invoking slab + more mantle peridotite. Furthermore, the LSAs samples have Mg# numbers comparable to Group 1 lavas, which have Mg# numbers between 0.21 and 0.39.

The Mongolian HSA samples have Mg# numbers ranging from 0.31 to 0.49. Most of these lavas plot in the “slab melting” field, or just above it, next to the “slab + peridotite melting experiments” suggesting only minor mantle assimilation, or extensive fractional crystallisation processes. Most of the samples sit comfortably in the Cenozoic adakite field, close to the Shuteen Complex adakites. Three of the samples have Mg# numbers ranging from 0.47 to 0.49 at >63 wt. % SiO_2 and is comparable to the slab + peridotite melting experiments (Rapp et al., 1999). However, these Mg# are also comparable to the Awulae and Sanchakou adakitic rocks and to the Lingqiu Basin adakitic lavas, albeit the HSAs have a higher Mg# at a comparable SiO_2 content. Thus, the HSA samples are more ambiguous than the crustal melts from the Huichang Basin (China) or the Yungay ignimbrites (Peru). The HSA have Mg# that are most comparable to slab + minor mantle material or, alternatively, to the Awulae and Sanchakou adakitic rocks.

3.7.2 Na_2O abundances in slab and lower crust melts: melt reactions within the mantle

Experimental basalt partial melts, produced under 1.5-3 GPa conditions to mimic scenarios relevant to adakite genesis (e.g. Rapp et al., 1999) have high Na_2O abundances. However, most adakites have lower Na_2O than those produced from melting experiments. This Na_2O deficiency has been explained by these lavas interacting with overlying mantle material resulting in a dilution of the Na_2O whilst enriching the mantle by metasomatism processes. However, lower crustal adakitic melts often have high Na_2O contents because these melts have not interacted with mantle material (Xiong et al., 2003).

Because HMAs are believed to have interacted with mantle material, these lavas should have low Na_2O compared to pure slab or lower crustal melts. Furthermore, the Na_2O concentration should decrease with decreasing SiO_2 ; to reflect increasing assimilation of

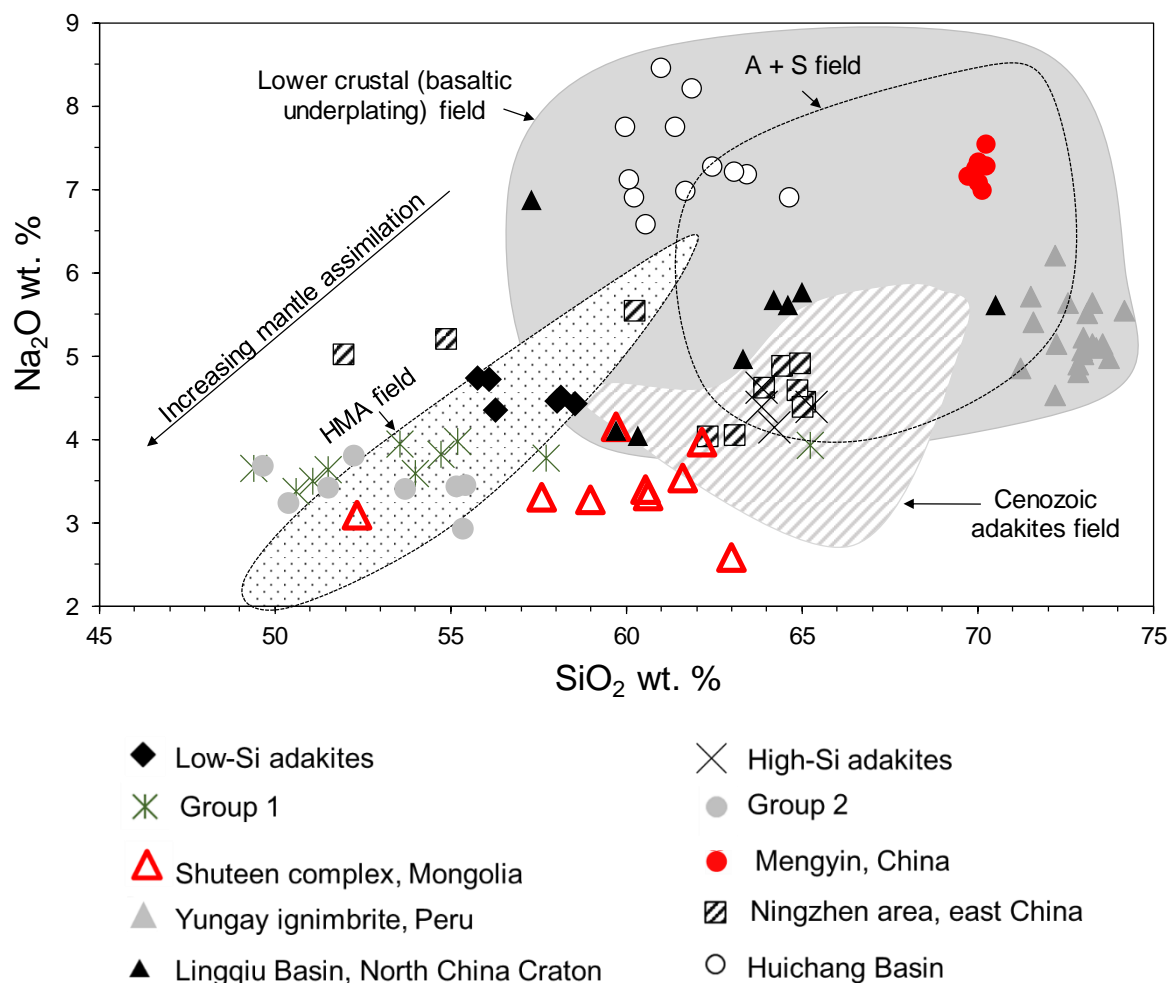


Figure 3.17: A Na_2O vs. SiO_2 wt. % plot. The “high-Mg andesite field” (HMA) represent oceanic eclogitic melts that have interacted with the mantle wedge (Xu et al. 2000; Bryant et al. 2011). Previously interpreted slab melts from Mongolia and China are coloured red. The volcanic adakites from the Shuteen complex, Mongolia (Batkhisig et al., 2010) represent melts of subducting oceanic crust with minor mantle interaction. The Mengyin adakites were interpreted as subducted palaeo-Pacific oceanic slab melts (Wang et al., 2016). The intrusive adakitic rocks from the Ningzhen area, east China (Xu et al., 2002) represent lower-crustal delaminated melts that have interacted with mantle rocks. The adakitic lavas from the Huichang Basin, SE China (Xiong et al., 2003) and Lingqiu Basin, North China (Wang et al., 2006) represent melts of an underplated basaltic lower crust. The “A + S” field represent Awulake and Sanchakou (Xinjiang Tianshan region, China) adakitic rocks and were interpreted as a product of basaltic underplating at the base of the lower crust (Zhao et al. 2008). The Cenozoic adakite field generated from data within Aguillón-Robles et al. (2001) and Stern and Kilian (1996).

mantle peridotite. The HMAs from the western Aleutians (Bryant et al., 2011) and the Qinling Mountains in central China (Xu et al., 2000) have some of the lowest Na_2O concentrations and also show a positive trend between Na_2O and SiO_2 (Fig. 3.17) in agreement with their proposed genesis.

The Mongolian Shuteen Complex adakites have Na_2O concentrations (2.6 – 4 wt. %) lower than the “lower crustal melts field” and often have lower Na_2O than the comparative

Cenozoic adakites. Their Na_2O concentrations could therefore reflect slab + mantle material assimilation processes. The Mengyin adakites have high Na_2O values (similar to the lower crustal basaltic underplated adakitic melts) which is uncharacteristic of the other adakites used in this comparison.

The LSAs have Na_2O concentrations (4.4 – 4.7 wt. %) that are higher than the Group 1 lavas (3.4 – 4 wt. %) and Shuteen Complex adakites. This could be because of assimilation processes or be because the source was more alkali enriched (or a combination of both); distinguishing between the two scenarios is difficult, nevertheless, because there is no correlation between SiO_2 and Na_2O , it suggests the latter. However, the LSA have also undergone sericitisation which will reduce the Na_2O content and perhaps mask fractionation processes (**Fig. 3.8B**). Overall, the LSAs have lower Na than the adakitic melts interpreted to be from basaltic underplating of the lower crust but similar to the crust + mantle samples from the Ningzhen area.

The HSA samples have higher Na_2O concentrations (4.15 to 4.39 wt. %) than the Shuteen complex adakites but plot comfortably in the Cenozoic adakite field. However, the Na_2O concentrations are also similar to some of the adakitic samples (A + S field; Lingqui Basin and Ningzhen area). This makes it difficult to sway in favour of a slab (+ mantle?) or a lower crustal melting model for the HSA samples.

3.7.3 Th/U and $\text{K}_2\text{O}/\text{Na}_2\text{O}$ ratios

Magmas derived from the partial melting of basaltic oceanic crust are commonly enriched in Na, with $\text{K}_2\text{O}/\text{Na}_2\text{O}$ ratios of ~ 0.4 and Th/U ratios of ~ 3 (Defant and Drummond, 1990; Martin, 1999). While, lower continental crust-derived adakitic rocks often have higher $\text{K}_2\text{O}/\text{Na}_2\text{O}$ and Th/U ratios (e.g. Wang et al., 2007; Ling et al., 2011). This criterion is often applied to recognise the source of adakitic rocks (e.g. Wang et al., 2016). Despite the mobility of these elements, for comparative purposes, these ratios are now used to consider potential source characteristics of the LSA and HSA samples (**Fig. 3.18**).

The HMAs from the western Aleutians and the Qinling Mountains have $\text{K}_2\text{O}/\text{Na}_2\text{O}$ ratios between 0.3 to 0.45 and 0.02 to 1.08 respectively. The Th/U ratios range between 1.7 to 2.2 and 2.5 to 7.5 respectively. As demonstrated by the HMAs from the Qinling Mountains,

these oceanic eclogitic and mantle melts can have a broad range in K_2O/Na_2O and Th/U ratios.

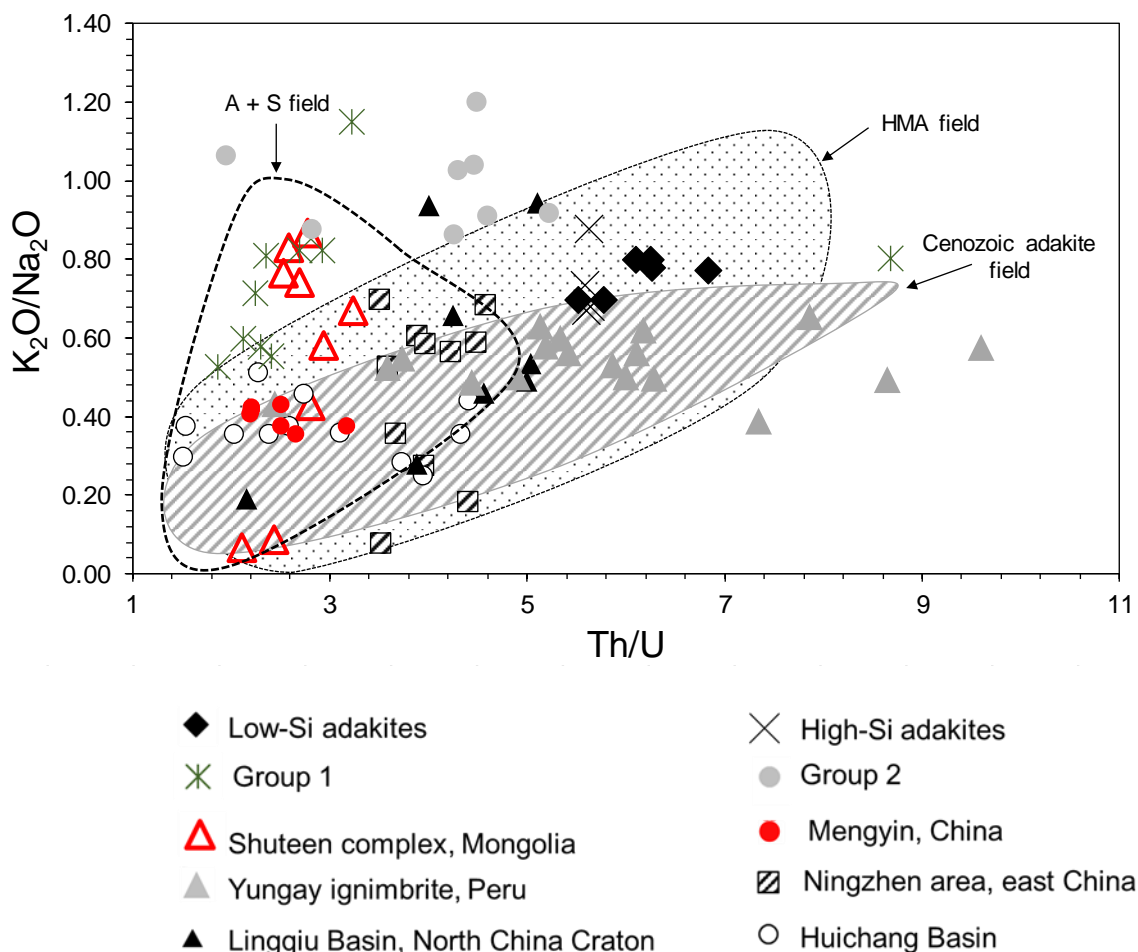


Figure 3.18: Th/U vs. K_2O/Na_2O plot. The “high-Mg andesite field” (HMA) represent oceanic eclogitic melts that have interacted with the mantle wedge (Xu et al. 2000; Bryant et al. 2011). Previously interpreted slab melts from Mongolia and China are coloured red. The volcanic adakites from the Shuteen complex, Mongolia (Batkishig et al., 2010) represent melts of subducting oceanic crust with minor mantle interaction. The Mengyin adakites were interpreted as subducted palaeo-Pacific oceanic slab melts (Wang et al. 2016). The intrusive adakitic rocks from the Ningzhen area, east China (Xu et al., 2002) represent lower-crustal delaminated melts that have interacted with mantle rocks. The adakitic lavas from the Huichang Basin, SE China (Xiong et al., 2003) and Lingqiu Basin, North China (Wang et al., 2006) represent melts of an underplated basaltic lower crust. The “A + S” field represent Awulake and Sanchakou (Xinjiang Tianshan region, China) adakitic rocks and were interpreted as a product of basaltic underplating at the base of the lower crust (Zhao et al. 2008). The Cenozoic adakite field generated from data within Aguillón-Robles et al. (2001) and Stern and Kilian (1996).

The Shuteen complex adakites, which were interpreted to have a subducted oceanic crust (oceanic basalt and sediments + minor mantle assimilation) source, have K_2O/Na_2O ratios between 0.06 to 0.86 and Th/U ratios between 2.1 and 3.2. Therefore, although these adakites have high K_2O/Na_2O ratios, the Th/U ratios support their proposed genesis.

The intrusive adakitic rocks, from the Ningzhen area (interpreted as delaminated lower crust and mantle material), have K_2O/Na_2O ratios between 0.18 to 0.69 and Th/U ratios between 3.5 and 5.5.

The Yungay adakitic ignimbrites have K_2O/Na_2O ratios between 0.39 and 0.65 and Th/U ratios between 2.4 to 9.6. The adakitic samples from the Huichang Basin (SE China) have K_2O/Na_2O ratios between 0.25 to 0.51 and Th/U ratios ranging from 1.5 to 4.4. Interestingly, most of these Huichang Basin samples (**Fig. 3.18**) have K_2O/Na_2O and Th/U ratios similar to true adakites (i.e. slab melts of subducted basaltic oceanic crust). However, the Huichang adakitic samples were interpreted to be the product of underplating of an alkali-rich basaltic protolith. Finally, the Lingqui Basin (North China Craton) adakitic samples (interpreted as lower crustal basaltic underplated rocks) have K_2O/Na_2O ratios between 0.19 to 0.94 and Th/U ratios between 2.2 and 5.1.

The LSA and HSA samples have K_2O/Na_2O ratios between 0.7 to 0.8 and 0.67 to 0.87 respectively. The Th/U ratios range between 5.52 to 6.83 and 5.58 to 5.63 respectively. Therefore, for both the LSA and HSA samples, the K_2O/Na_2O and Th/U ratios are higher than what might be expected for a basaltic oceanic crust source. However, if there was crustal assimilation, this may be one way of increasing these ratios.

Group 1 and 2 samples have K_2O/Na_2O ratios between 0.52 to 1.15 and 0.87 to 1.2 respectively. The Th/U ratios range between 1.85 to 8.67 and 1.94 to 5.2 respectively.

Based on the above comparisons, K_2O/Na_2O and Th/U ratios frequently show great variation (e.g., Cenozoic adakite field). Therefore, using these ratios to determine the source, or mechanism of melting, needs to be applied with caution. Due to the great variation in these ratios, this criteria is not applied to understand the petrogenesis of the samples in this study.

3.7.4 Cr and Ni abundances

Melting of eclogite should produce melts with low Cr and Ni concentrations. Thus, melts of an eclogite lower crust, which have undergone minor/no mantle interaction should have

low Cr and Ni. However, because slab melts must pass through the mantle, the melts should become enriched due to mantle (i.e. peridotite) assimilation processes.

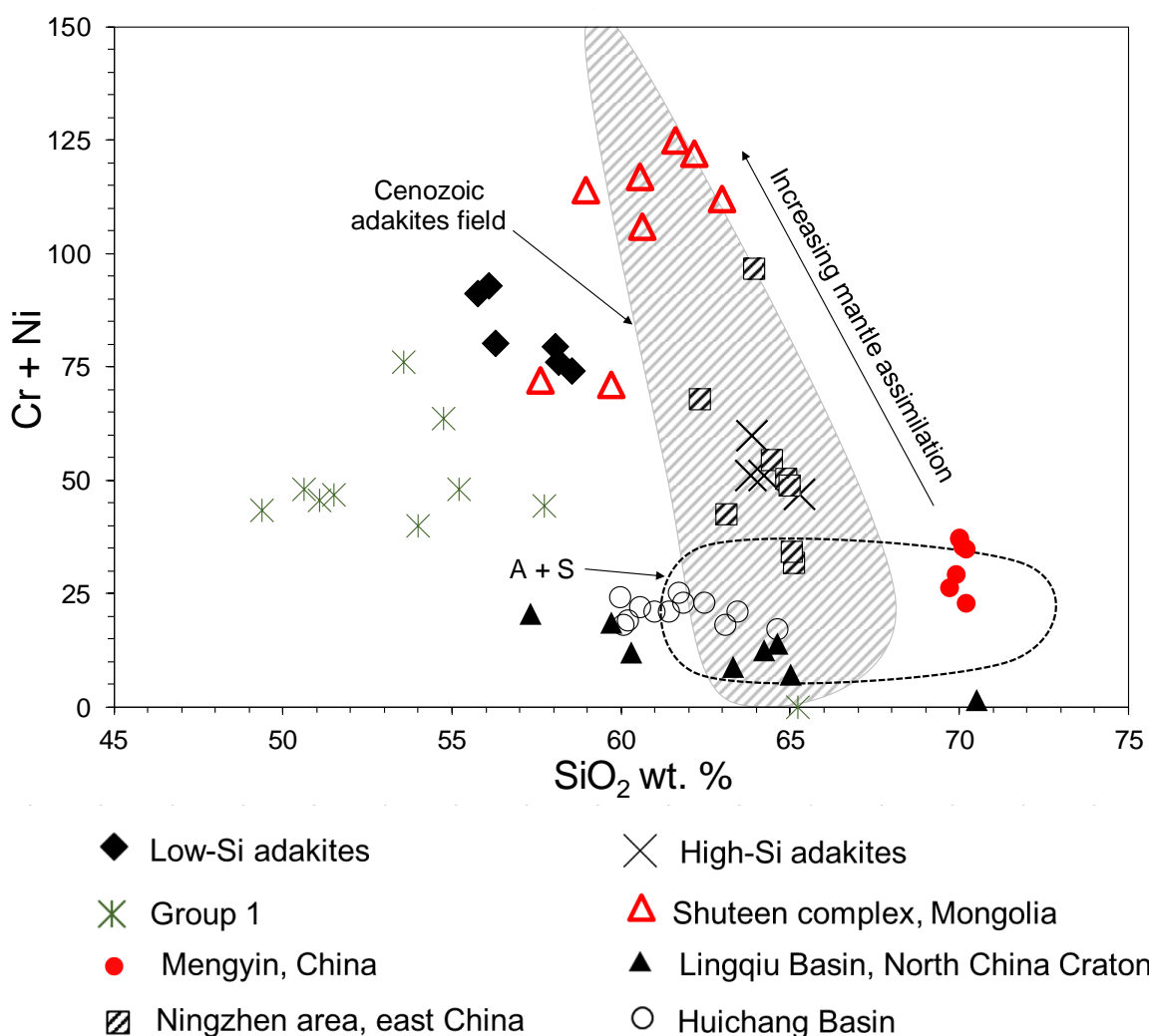


Figure 3.19: SiO_2 vs. $\text{Cr} + \text{Ni}$ plot. Previously interpreted slab melts from Mongolia and China are coloured red. The volcanic adakites from the Shuteen complex, Mongolia (Batkhishig et al., 2010) represent melts of subducting oceanic crust with minor mantle interaction. The Mengyin adakites were interpreted as subducted palaeo-Pacific oceanic slab melts (Wang et al. 2016). The intrusive adakitic rocks from the Ningzhen area, east China (Xu et al., 2002) represent lower-crustal delaminated melts that have interacted with mantle rocks. The adakitic lavas from the Huichang Basin, SE China (Xiong et al., 2003) and Lingqiu Basin, North China (Wang et al., 2006) represent melts of an underplated basaltic lower crust. The "A + S" field represent Awulae and Sanchakou (Xinjiang Tianshan region, China) adakitic rocks and were interpreted as a product of basaltic underplating at the base of the lower crust (Zhao et al. 2008). The Cenozoic adakite field generated from data within Aguilón-Robles et al. (2001) and Stern and Kilian (1996).

The HMAs from the western Aleutians and the Qinling Mountains have very high $\text{Cr} + \text{Ni}$ concentrations (332–1123 ppm; not plotted on Figure 3.19 due to scale). This is consistent with the interpretation of oceanic eclogite + mantle wedge.

The adakitic rocks from the Huichang Basin, Lingqiu Basin and Xinjiang (Awulae and Sanchakou) have low $\text{Cr} + \text{Ni}$ abundances (Fig. 3.19), consistent with a crustal source that

has undergone minor mantle assimilation. The Yungay adakitic ignimbrites have Ni concentrations below detection (<2 ppm). The Ningzhen area adakitic samples were interpreted to be crust that have foundered into the mantle – thus the sharp trend of increasing Cr + Ni with decreasing SiO₂ could be evidence of mantle assimilation processes.

The Shuteen Complex adakites have relatively high Cr + Ni concentrations (**Fig. 3.19**), consistent with a slab melt that has assimilated some mantle material. However, the Mengyin adakites are not as enriched in Cr + Ni, possibly reflecting less mantle assimilation.

The LSA samples have Cr + Ni concentrations higher than the crustal melts which have undergone minor mantle assimilation (**Fig. 3.19**). The Cr + Ni concentrations are also higher than the Group 1 lavas and the negative correlation with SiO₂ likely reflects fractionation processes, or possibly, mantle assimilation.

The HSA samples have higher Cr + Ni concentrations than the adakitic melts that have undergone minor mantle assimilation and also the Mengyin adakites. The HSA samples plot in the Cenozoic adakites field and close to some Ningzhen adakitic samples. Thus, the HSA samples have Ni + Cr concentrations likely reflecting slab + mantle, or crust + mantle.

3.7.5 Nb/Ta and Zr/Hf ratios

A combination of Nb/Ta and Zr/Hf ratios are now used to consider potential source characteristics (**Fig. 3.20 & 3.21**).

3.7.5.1 Nb/Ta ratios

The continental crust has low average Nb/Ta ratios (10.9-13; Rudnick and Fountain, 1995; Rudnick and Gao, 2003) compared to MORB (16.7 ± 1.8 ; Kamber and Collerson, 2000) and primitive mantle (17.5 ± 2 ; McDonough and Sun, 1995). However, rutile partitions Nb and Ta, but fractionates them from one another (Foley et al., 2000; Liang et al., 2009; Xiong et al., 2011). Therefore, melts in equilibrium with residual rutile should be characterised by high Nb/Ta ratios (e.g., Gao et al., 2004; Xiong et al., 2005). A mantle that has been metasomatised by small degree (partial melting) eclogite melts may also have high Nb/Ta ratios (e.g., Foley et al., 2002; Sheldrick et al. 2018). In summary, initial melts of rutile-bearing eclogite should have relatively high Nb/Ta ratios. However, progressive melting of

this eclogite would exhaust rutile, therefore resulting in melts with low Nb/Ta ratios inherited from earlier melt depletion (e.g., Liu et al. 2008A).

Based partly on low Nb/Ta ratios, Condie (2005) determined that adakitic tonalite-trondhjemite-granodiorite may be produced from partial melting of hydrous mafic rocks in the lower crust (Nb/Ta ratios have averages as low as 5) and are thus not slab melts. As discussed by Condie (2005), most Nb data from XRF must be rejected and only high precision ICP-MS Nb and Ta should be used; hence the data is plotted on the same diagram as Condie (2005) using ICP-MS data for these elements.

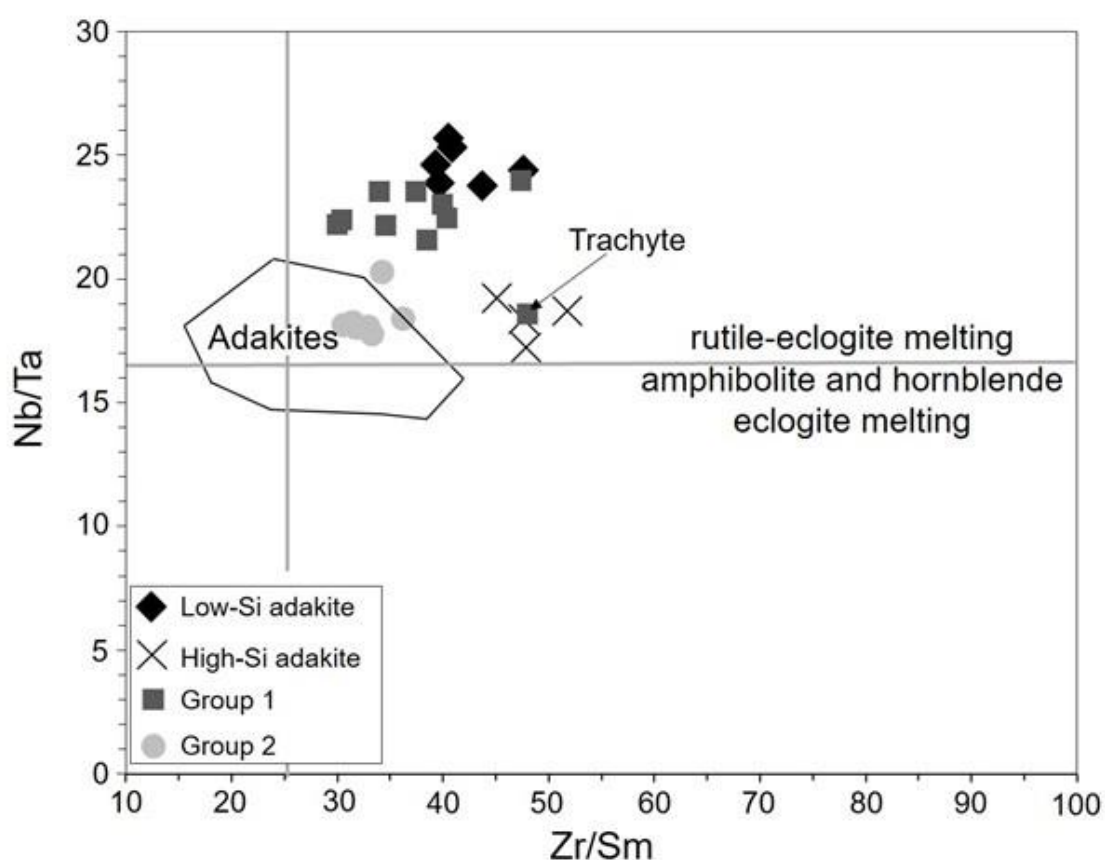


Figure 3.20 Zr/Sm vs. Nb/Ta plot. The vertical line represents the average Zr/Sm value for primitive mantle (25.2; Sun and McDonough, 1989) and melting fields from Foley et al. (2002). The adakite field is from Condie (2005).

The LSA and HSA samples have an average Nb/Ta ratio of 24.6 (± 0.77) and 18.38 (± 0.85) respectively. Therefore, the LSA samples have high Nb/Ta ratios consistent with a source that contained residual rutile or underwent metasomatic processes (e.g., by melts from a rutile-bearing protolith). The HSA samples have lower Nb/Ta ratios which are close to average MORB and primitive mantle, consistent with the experimental melt comparisons. Thus, the HSA samples have Nb/Ta ratios consistent with rutile-eclogite melting, albeit,

they plot out of the adakite field defined in Condie (2005). The Group 1 samples (excluding the single trachyte sample – TCS 5.1) have an average Nb/Ta ratio of $22.78 (\pm 0.79)$, whereas the Group 2 samples have an average Nb/Ta ratio of $18.4 (\pm 0.84)$. Therefore, the Group 1 and 2 samples have Nb/Ta ratios higher than average continental crust and likely reflect melting from a source which underwent metasomatism possesses. The lower Nb/Ta ratios in the Group 2 samples might reflect melting from a less metasomatized source, and/or increased crustal involvement.

3.7.5.2 Zr/Hf ratios

Zirconium/hafnium ratios are considered to remain largely unaffected by magmatic processes due to their similar ionic radii and isovalent state (4^+ ; e.g. Taylor and McLennan, 1985; Dostal and Chatterjee, 2000). In most igneous rocks, the Zr/Hf ratio is in the narrow

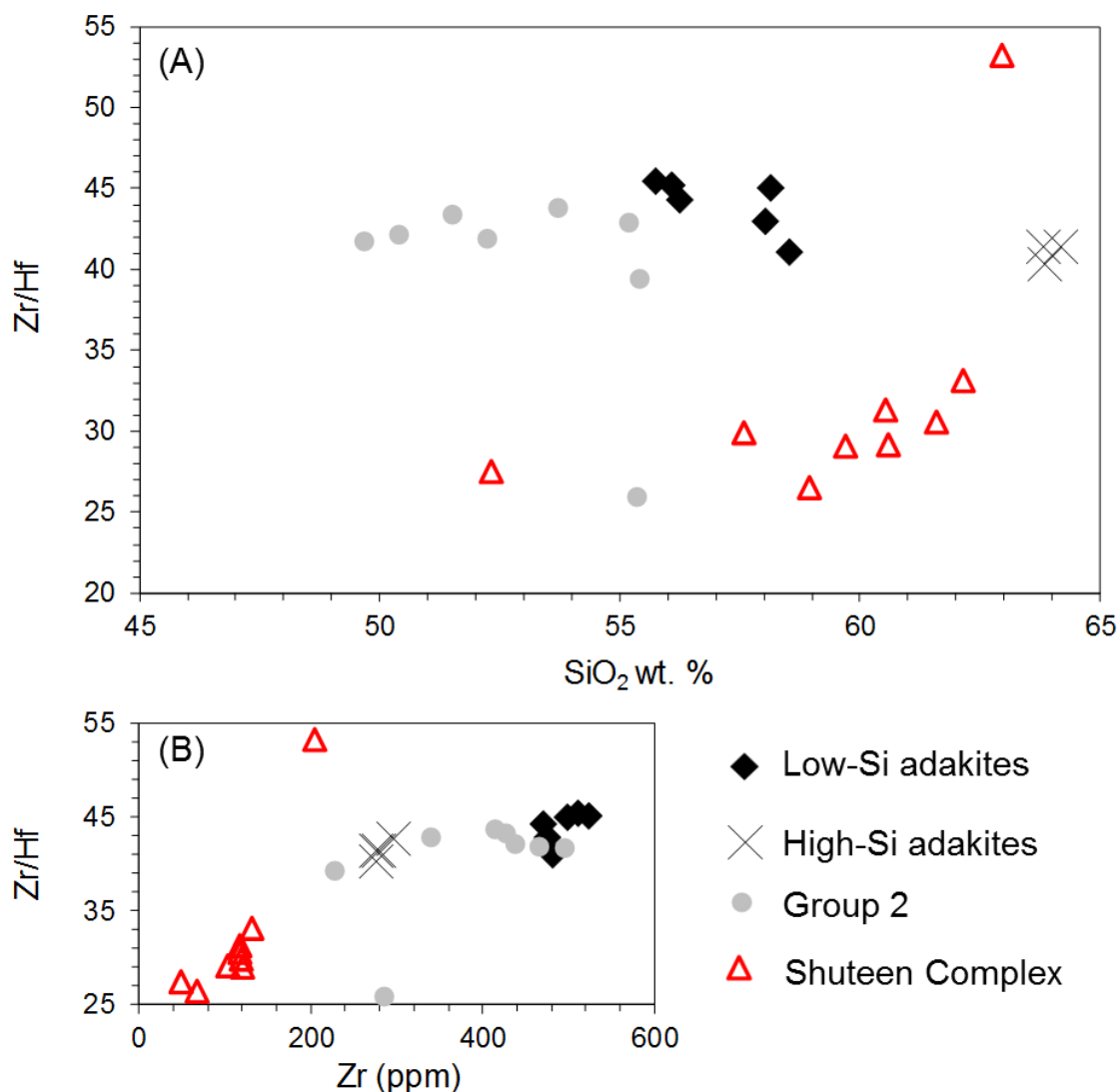


Figure 3.21: (A) SiO₂ vs. Zr/Hf and (B) Zr vs. Zr/Hf.

range of 33 to 40; this includes the value for crust and chondrites (e.g. Jochum et al., 1986; Dostal and Chatterjee, 2000). Deviation of this ratio is rare and frequently attributed to carbonate metasomatism (e.g. Rudnick et al. 1993; Dupuy et al., 1992) or to crystal fractionation involving accessory phases such as rutile (e.g. Linnen, 1998).

The LSA and HSA samples have high Zr/Hf values ranging from 40.3-45.5 (**Fig. 3.21**). Although there is no Hf data available for the Group 1 lavas, the Group 2 lavas show values (25-43.8 \pm 5.8, with an average of 40.2) similar to the LSA and HSA samples.

The negative correlation between SiO₂ wt. % and Zr for the LSA samples (**Fig. 3.13A**) suggests Zr fractionation and therefore may explain the trend on Figure 3.21A. Therefore, the least fractionated LSA samples (i.e. those with the least SiO₂ wt. %) have the highest Zr/Hf ratio. Such a high Zr/Hf ratio is uncharacteristic of a crustal source and could be due to derivation from a carbonate metasomatised lithospheric mantle source (e.g. Dupuy et al., 1992).

Although the HSA samples have high Zr/Hf ratios, the ratio increases with increasing degrees of fractionation, possibly because Zr is more incompatible than Hf (**Fig 3.21A**). Thus, this ratio might just reflect late-stage fractionation processes rather than indicating original source values. Such an interpretation is valid when one considers that the Shuteen Complex adakites also have very high Hf/Zr ratios at high SiO₂ wt.% (**Fig. 3.21A**); albeit, the few HSA samples cluster together which makes it difficult to confirm.

3.7.6 Major-element comparisons with high-pressure basalt partial melts

Diagnostic trace-element characteristics for adakites are high Sr/Y and La/Yb ratios from a depletion in the HREE's. Therefore, garnet is often necessary as a residual phase during partial melting - while plagioclase enriched in Sr is minor in the residue (e.g., Rapp and Watson, 1995). The partial melting of hydrated basaltic rocks at low pressures (\leq 8 kbar; Beard and Lofgren, 1991; Rushmer, 1991) does not produce liquids in equilibrium with garnet. However, garnet + clinopyroxene \pm amphibole \pm plagioclase is often present in melting experiments at pressures \geq 10 kbar and temperatures of 850-1150°C (e.g., Rapp et al., 1991; Winther and Newton, 1991; Sen and Dunn, 1994; Wolf and Wyllie, 1994; Rapp, 1995; Rapp and Watson, 1995). Adakitic melts are produced at 10-40 kbar (Rapp et al., 1999).

Following the method used by Xiong et al. (2003), geochemical fields are generated for adakitic liquids produced from partial melts of basaltic compositions with pressures greater than 10 kbar (**Fig. 21**);

- The R₁ grouping (n = 13 samples) corresponds to melting experiments done between 12-38 kbar (Rapp et al. 1991, 1999; Rapp, 1995; Rapp and Watson 1995). The starting material was an alkali-rich basalt with high total alkalis (Na₂O + K₂O) and low CaO, FeO, MgO and TiO₂.
- The R₂₋₄ SW grouping (n = 59 samples) used data from Rapp and Watson (1995) at 16-32 kbar, Sen and Dunn (1994) at 15-20 kbar, and Winther (1996) at 10-30 kbar. The starting material utilised a composition close to N-MORB. However, some of the starting compositions (R₂) have slightly higher Na₂O and K₂O (S) than average N-MORB (Hofmann, 1988).
- The WW grouping (n = 14 samples) utilised data from Wolf and Wyllie (1994) at 10 kbar. The starting material was a low-K and low-Na, high-Mg and high-Ca amphibolite.

Also included on these plots is the adakite field from Xiong et al. (2003, and references therein). This adakite field was generated from 11 global Cenozoic adakite localities: Aleutian Arc, Alaska; Cook Island, Chile; Baja of California, Mexico; Sierra Madre, Mexico; Skagway, Alaska; Mindanao, Philippines; Southwest Japan; Austral Andes and Quimsacocha, Ecuador.

The LSA samples have major-element characteristics where some (or all) of the samples do not plot in any of the high-pressure basalt partial melts or adakite fields (**Fig. 3.22 A, B, C, E & F**). They have significantly less Al₂O₃, less CaO and more K₂O than the basaltic melts produced from the low-K, -Na and high-Na, -Mg amphibolite (WW) and thus it seems unlikely that this would be an appropriate protolith. Furthermore, the LSA samples have less Al₂O₂, Na₂O and more CaO than the experimental partial melts on alkali-rich basalt (R₁). Other than for Na₂O, the LSA samples do not plot in the R₂₋₄SW field (e.g., for Al₂O₃, FeO and K₂O; **Fig. 3.22 A, C & F**). On those plots where the LSA locality does have some samples plotting in the R₂₋₄SW field (**Fig. 3.22 B & E**) it appears to be a trend into this field; such a trend likely reflects late-stage fractionating phases. On all plots (**Fig. 3.22**), the LSA

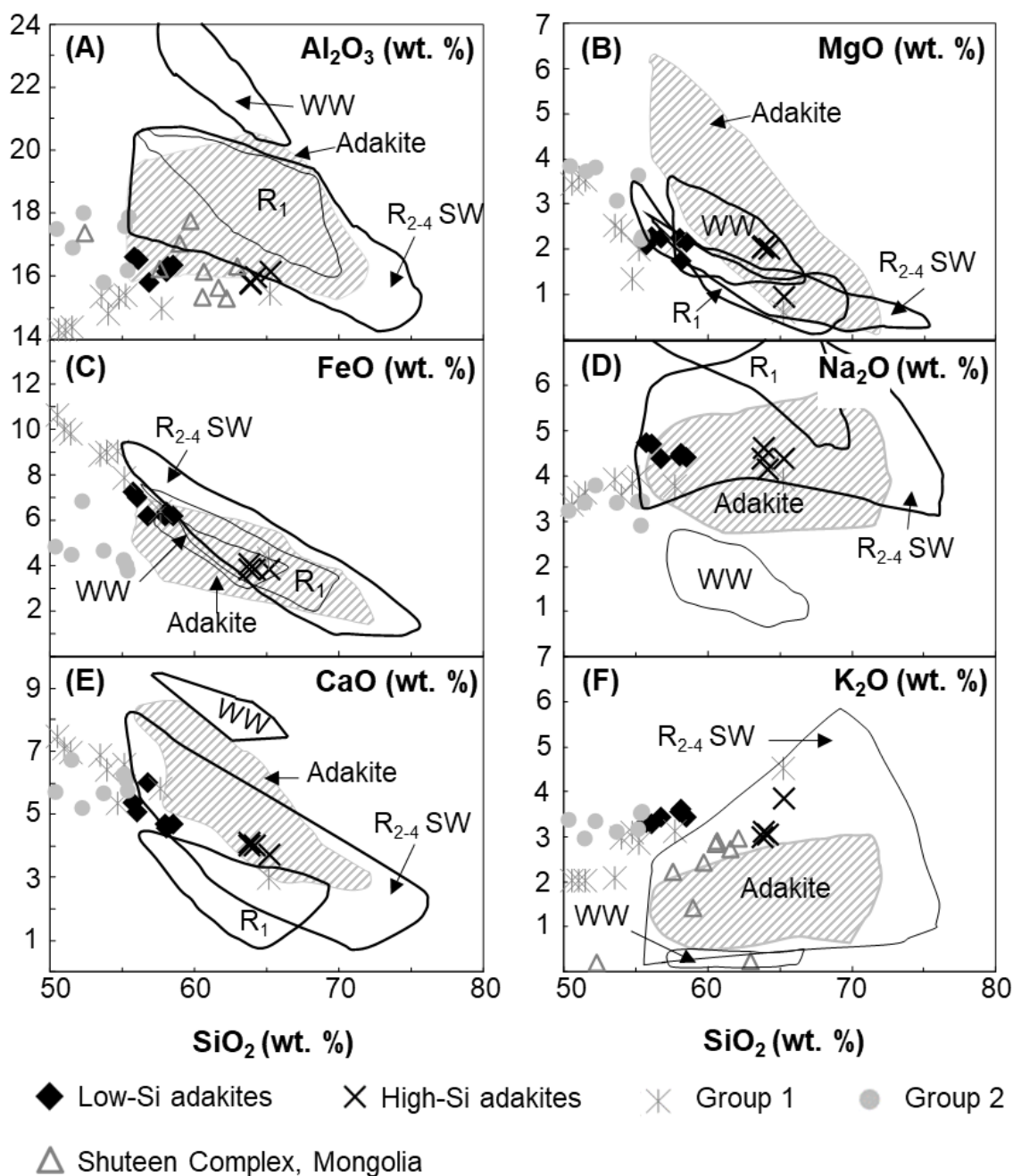


Figure 3.22: Compositional comparison of the different sample suites with adakites and high pressure (≥ 10 kbar) partial melts of basalt (Xiong et al. 2003, and references therein). Also included are the Carboniferous adakites from the Shuteen Complex, Mongolia (Batkishig et al., 2010). The different fields correspond to: R_1 = partial melts of alkali basalt at 12-38 kbar; R_{2-4} SW = partial melts of basalts compositionally close to N-MORB at 10-32 kbar; WW = partial melts of a low-K, low-Na, high-Mg, high-Ca basalt at 10 kbar. This adakite field was generated from 11 Cenozoic adakite localities: Aleutian Arc, Alaska; Cook Island, Chile; Baja of California, Mexico; Sierra Madre, Mexico; Skagway, Alaska; Mindanao, Philippines; Southwest Japan; Austral Andes and Quimsacocha, Ecuador.

locality has some (or all) samples not plotting in the adakite field. If these melts assimilated mantle material, then it might explain why frequently they do not plot in the high-pressure basalt/adakite partial melt fields. However, the low Ni and Cr concentrations and high Na_2O does not support significant late-stage mantle assimilation processes. Furthermore, the

LSAs have lower Mg# numbers at a given SiO₂ wt. % compared to sample localities that have incorporated mantle material (**Fig. 3.16**). The LSAs often have trends similar to the Group 1 lavas. Therefore, the LSA samples might have a source similar to the Group 1 lavas (albeit, this source may contain more garnet) and the adakitic characteristics may be from late-stage fractionation processes. Further consideration to source characteristics is discussed later.

The HSA samples have significantly less Al₂O₃ (**Fig. 3.22A**) and CaO (**Fig. 3.22E**) whilst being more enriched in Na₂O and K₂O (**Fig. 3.22 D & F**) than the 10 kbar amphibolite partial melts (WW) and thus arguably precludes this protolith composition. Furthermore, the HSA samples have less Al₂O₃ (**Fig. 3.22A**), Na₂O (**Fig. 3.22D**) and more CaO (**Fig. 3.22E**) than the alkali-rich basalt partial melts (R₁; these experiments were also done at a range of pressures between 12-38 kbar) suggesting this may also be an unsuitable protolith. Most HSA samples plot in the R₂₋₄SW field. However, some HSA samples do not plot in the R₂₋₄SW field for Al₂O₃ (**Fig. 3.22A**) and only one of the samples plots in this field for MgO (**Fig. 3.22B**). Other than for Al₂O₃ and K₂O (**Fig. 3.22 A & F**) the HSA samples frequently plot in the adakite field. Although enrichment in K₂O has been used to suggest that Mesozoic adakites from China are crustal melts (e.g., Wang et al. 2006) this criterion alone is insufficient. For example, the Carboniferous Shuteen Complex adakites are often more enriched in K₂O than other adakites and depleted in Al₂O₃ (**Fig. 3.22 A & F**) yet have ⁸⁷Sr/⁸⁶Sr_i <0.704. Therefore, the HSA samples have geochemical parallels with other adakites and high-pressure melting experiments on compositions close to N-MORB.

The low Ni (17-21 ppm) and Cr (30-39 ppm), low MgO and high Na₂O (**Fig. 3.12 & 3.22B**) suggests that the HSA samples have not incorporated significant mantle material. The HSA samples are sub-alkaline (**Fig. 3.10A**), unlike the nearby Group 2 lavas, and thus unlikely to be evolved melts from a similar protolith. Furthermore, the HSA samples often plot away from the Group 2 lavas despite some of these Group 2 lavas being just as depleted in MgO (**Fig. 3.22B**). Therefore, the HSA samples could be a product of basaltic underplating/foundering (with minor mantle assimilation to account for slight enrichment in MgO and Cr + Ni) or melting of subducted oceanic basalt/crust.

3.7.7 Summary

Despite having less SiO₂, the LSA samples have lower Mg# numbers and higher Na₂O than the Shuteen Complex samples which were interpreted to be slab (oceanic basalt and crust) + mantle material (**Fig. 3.16 & 3.17**). If the LSA samples were also slab melt + mantle material, it might be expected that the samples would have incorporated more mantle material than the Shuteen Complex samples (to account for the lower SiO₂ concentrations). Yet, the lower Mg# numbers and higher Na₂O do not support this scenario. Furthermore, the LSA samples have low Ni and Cr concentrations which are uncharacteristic of late-stage significant mantle assimilation processes (e.g., Xu et al., 2000; Bryant et al., 2011). The LSA samples do not share many major-element characteristics with other adakites and high-pressure basalt melting experiments. However, the LSA samples are more comparable to the Group 1 lavas (e.g., **Fig. 3.22**). Furthermore, the high Zr/Hf ratios (**Fig. 3.21**) might reflect derivation from a carbonate metasomatised lithospheric mantle source (e.g. Dupuy et al., 1992). The LSAs also have Nb/Ta ratios which are much higher than average continental crust and N-MORB (**Fig. 3.20**).

The HSA samples are sub-alkaline (**Fig. 3.10A**), unlike the nearby Group 2 lavas, and thus unlikely to be evolved melts from a similar protolith. Furthermore, the HSA samples often plot away from the Group 2 lavas despite some of these Group 2 lavas being just as depleted in MgO (**Fig. 3.22B**). The low Ni (17-21 ppm) and Cr (30-39 ppm), low MgO and high Na₂O (**Fig. 3.12 & 3.22**) suggest that the HSA samples have not incorporated significant mantle material. The HSA samples have Nb/Ta ratios that are more similar to N-MORB rather than average continental crust (**Fig. 20**) and share many major-element characteristics with Cenozoic adakites and high-pressure basalt partial melts (**Fig. 3.22**).

3.8 ISOTOPE VARIATIONS AND CRUSTAL INPUT

Petrological studies did not reveal any crustal xenoliths in the LSA samples, but accessory quartz crystals were identified. The HSA samples contain cumulates of melted quartz crystals indicative of crustal assimilation processes.

Although there is not abundant isotopic data, the data that does exist suggests that both the low-Si and high-Si adakites have undergone crustal assimilation processes (**Fig. 3.23**).

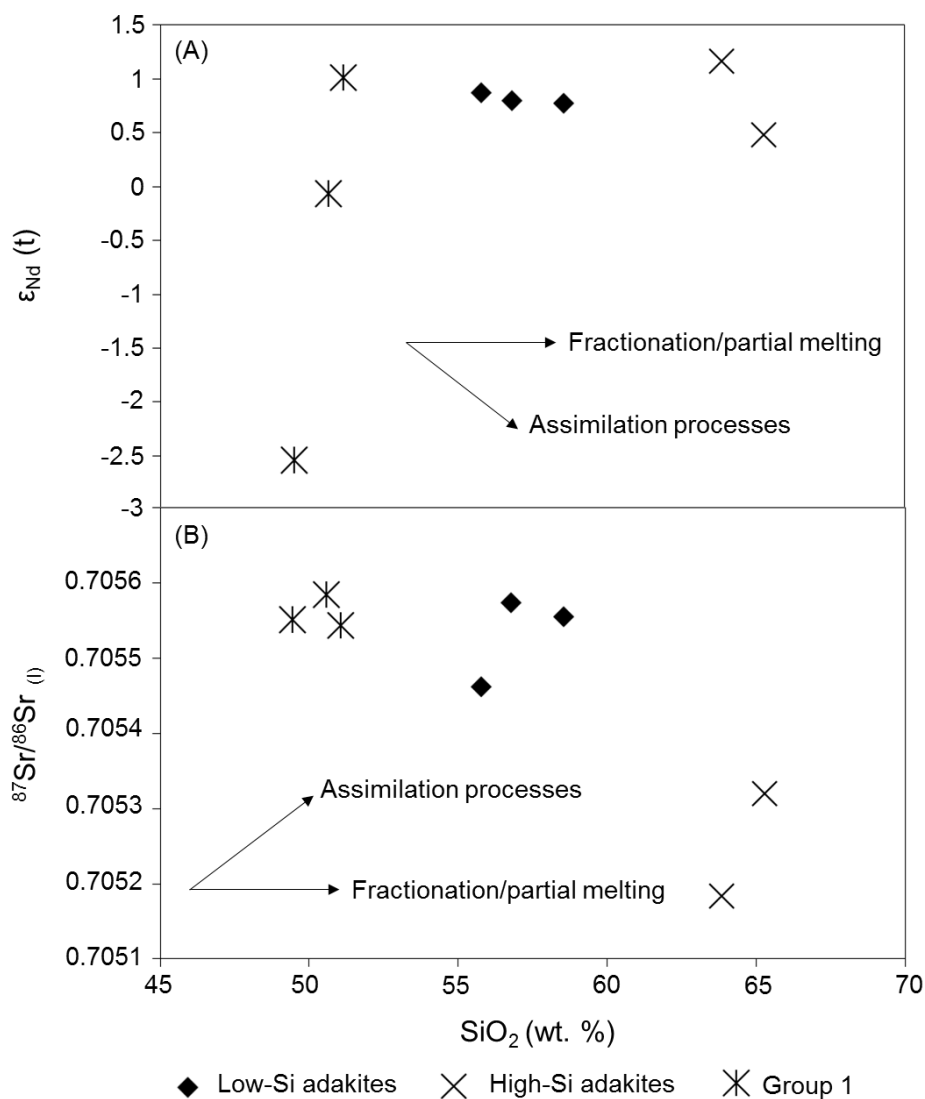


Figure 3.23: (A). SiO_2 vs. $\epsilon_{\text{Nd}}(t)$ and (B) SiO_2 vs. $^{87}\text{Sr}/^{86}\text{Sr}(t)$ plots. All Group 1 lavas had isotopic values age corrected to 121 Ma.

It is more difficult to use the isotopic data to assess crustal contamination of the Group 1 lavas due to potential source variation (i.e. samples were collected from different localities) and because there is insufficient data; however, a more complete isotope dataset will be used to assess regional assimilation processes in the following chapter (Chapter 4). Considering all the volcanism occurred during/ or shortly after a regional compressional event, associated with the closure of the Mongol-Okhotsk Ocean, the magma may have traversed through a thickened crust. The low MgO of all samples (**Fig. 3.22B**) and the fractionation of late-stage accessory minerals (e.g., apatite and zircon; **Fig. 3.13**) suggests

that the samples are evolved and thus likely had opportunity to assimilate crustal material. Due to not knowing the primary magma or exact contaminant compositions, it is not possible to constrain accurately the amount of crustal contamination. Nevertheless, AFC processes are further considered below to try and assess potential sources.

The $^{207}\text{Pb}/^{204}\text{Pb}_{(i)}$ vs. $^{206}\text{Pb}/^{204}\text{Pb}_{(i)}$ and $^{208}\text{Pb}/^{204}\text{Pb}_{(i)}$ vs. $^{206}\text{Pb}/^{204}\text{Pb}_{(i)}$ values (**Fig. 3.24**) for the LSA, HSA and Group 1 samples show a high range in values that are all very similar. These samples plot above the NHRL and P-MORB field. The Group 1 samples have similar Pb isotopic abundances to the LSA and HSA despite not having adakite-like major and trace element abundances. When combined with previous geochemical interpretations, this could support the interpretation that the LSA and Group 1 samples came from a similar source. All the Mongolian samples are most similar to the global Cenozoic and Chinese Mengyin adakites and are not as enriched in radiogenic Pb as the Peruvian Yungay adakitic ignimbrites or, Chinese Liujing and Ningzhen area adakitic samples. However, despite being slightly more enriched in radiogenic Pb, the Mongolian samples are also comparable to the Awulale adakitic samples, which were interpreted as the product of basaltic underplating of amphibole-eclogite facies (Zhao et al., 2008). Thus, overall, it is difficult to sway in favour of a slab + crust or lower crust source for the HSA from Pb isotopic values.

The $^{87}\text{Sr}/^{86}\text{Sr}_{(i)}$ vs $\epsilon\text{Nd}_{(t)}$ values for the LSA, HSA and Group 1 samples are also very similar to one another (**Fig. 3.25A**). All the samples plot in the mantle array and are similar to the Mesozoic Mongolian subcontinental lithospheric mantle derived melts (Sheldrick et al. 2018). The HSA have positive $\epsilon\text{Nd}_{(t)}$ values (0.48 – 1.17) unlike most of the crustal adakitic rocks from China and the Yungay adakitic ignimbrites. Furthermore, the $^{87}\text{Sr}/^{86}\text{Sr}_{(i)}$ values (0.7051– 0.7053) are frequently lower than the crustal derived adakitic rocks from China (**Fig. 3.25A**). Nevertheless, the isotopic values are also similar to the Awulale adakitic rocks. The samples have isotopic values close to some Cenozoic adakites (**Fig. 3.25A**). Using the equation from DePaolo (1981), AFC modelling is undertaken to see how much crustal contamination would be required to change the Shuteen Complex isotopic values to values close to the HSA samples. The crustal contaminant was a granulite crustal xenolith from southern Mongolia (Barry et al. 2003) and a r-value of 0.5 is used. This contaminant is not as enriched in Sr, or as depleted in ϵNd as the North China Basin lower crust which has $^{87}\text{Sr}/^{86}\text{Sr}_{(i)}$ values \sim 0.706– 0.714 and $\epsilon\text{Nd}_{(t)}$ values -28 to -40 (Wang et al. 2016). However,

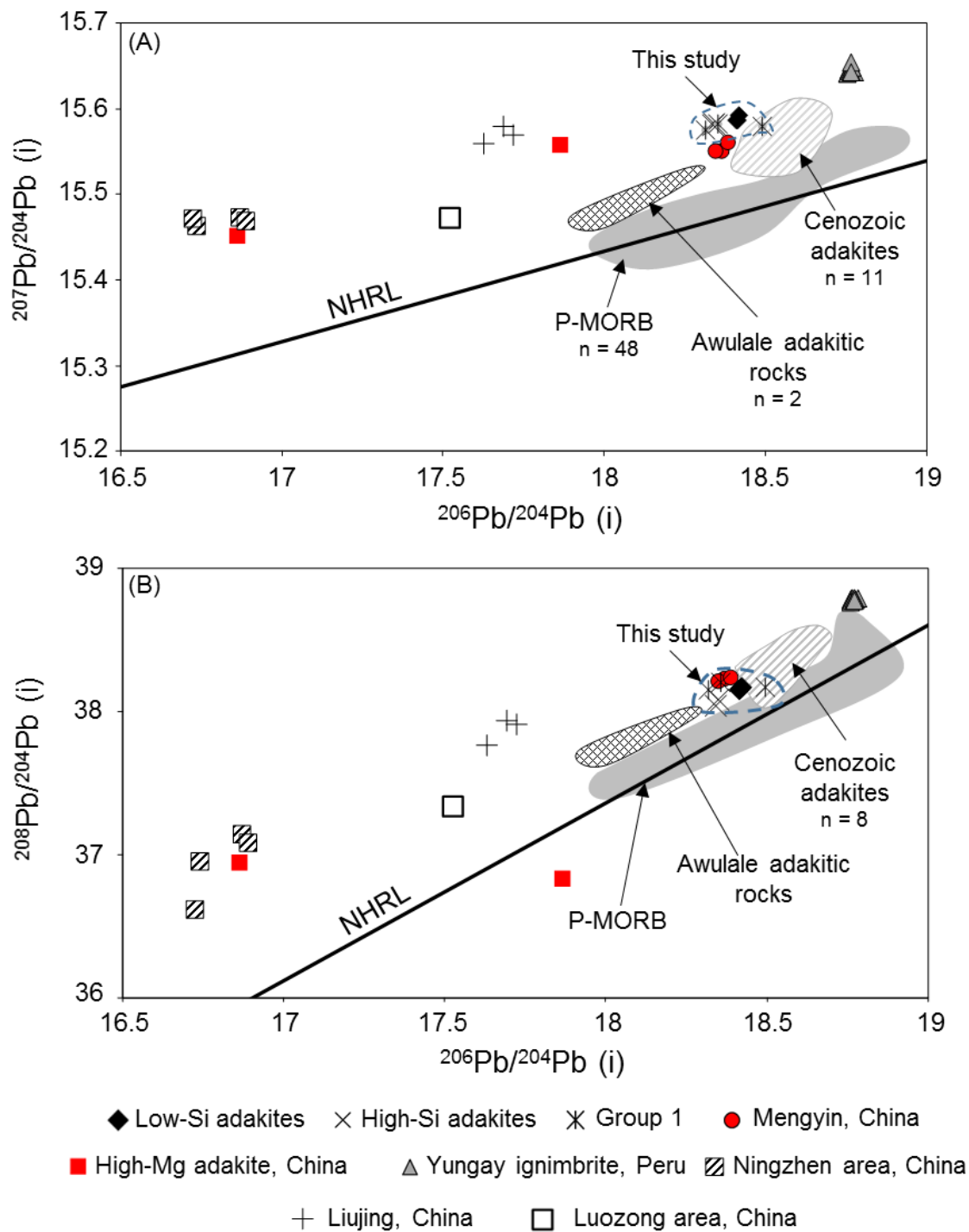


Figure 3.24: (A) Plot of $^{207}\text{Pb}/^{204}\text{Pb}$ vs. $^{206}\text{Pb}/^{204}\text{Pb}$ and (B) a plot of $^{208}\text{Pb}/^{204}\text{Pb}$ vs. $^{206}\text{Pb}/^{204}\text{Pb}$. All Group 1 samples were age corrected to 121 Ma. The adakites from Mengyin (China) and adakitic rocks from Liujing (China) were age corrected to 131 Ma (Wang et al. 2016). The high-Mg adakites (China) were age corrected to 350 Ma (Xu et al. 2000). The Ningzhen area (China) adakitic samples were age corrected to 123 Ma (Xu et al. 2002). The Luozong area (China) adakitic samples were age corrected to 136 Ma (Wang et al. 2006). The Awulale adakitic rocks were age corrected to 260 Ma (Zhao et al. 2008; $n = 2$). The Cenozoic adakites field generated from: the Andean-Austral volcanic zone (Stern and Kilian, 1996; Lautaro, Viedma, Reclus and Mt. Burney); Cerro Pampa, South southern America (Kay et al. 1993) and Vizcaino Peninsula, Mexico (Aguillón-Robles et al. 2001.). The Pacific MORB field generated from: Juan de Fuca; Gorda; and East Pacific Rise (White et al. 1987; $n = 48$).

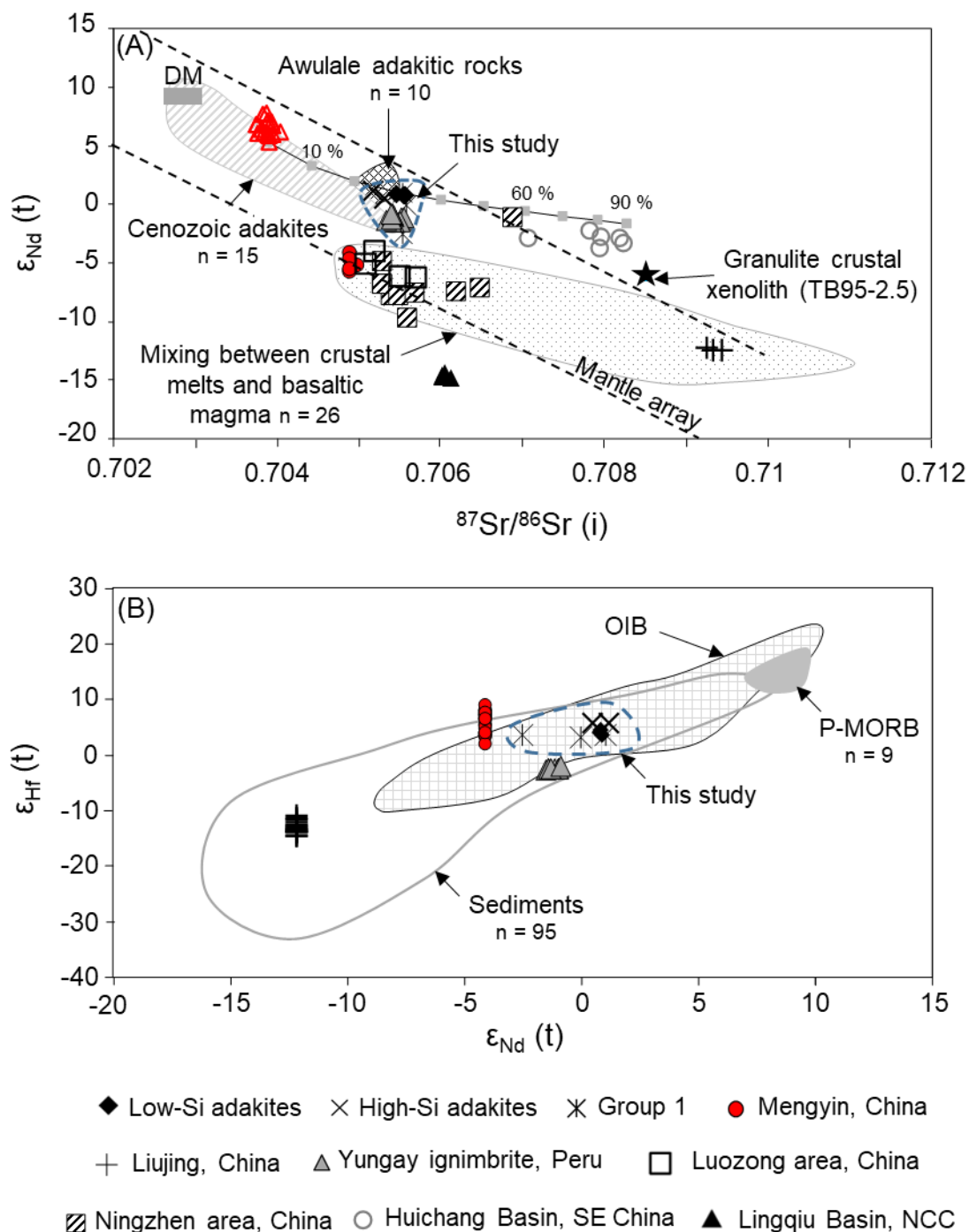


Figure 3.25: (A) Plot of $^{87}Sr/^{86}Sr(i)$ vs. $\epsilon_{Nd}(t)$ and (B) a plot of $\epsilon_{Nd}(t)$ vs. $\epsilon_{Hf}(t)$. The adakites from Mengyin and adakitic rocks from Liujing are from Wang et al. (2016) and Hf data from zircons. The Ningzhen area adakitic samples from Xu et al. (2002). The Luozong area adakitic samples were from Wang et al. (2006). The Awulale adakitic rocks from Zhao et al. (2008). The mixing of crustal and basaltic melts field from Chen et al. (2013). The Cenozoic adakites field generated from: the Andean-Austral volcanic zone (Stern and Kilian, 1996; Lautaro, Viedma, Reclus and Mt. Burney); Cerro Pampa, South America (Kay et al. 1993); La Yeguada Volcanic Complex, Panama (Defant et al. 1991) and Vizcaino Peninsula, Mexico (Aguillón-Robles et al. 2001.). The P-MORB field generated from: Alexander Island, Antarctica; SW & NW Pacific crust and Venezuela (Barry et al. 2017 and references therein). The depleted mantle (DM) is from Zindler and Hart (1986); mantle array is from Zhang et al. (2005); OIB field from Wang et al. (2016; and references therein) and sediment field from Vervoort et al. (1999) but excluded the Archean shales. The AFC modelling (equations from DePaolo, 1981) utilises a r value 0.5 and the starting composition used sample SH-18. The amount of F ranges from 1 to 0.1 and tick marks are in 10% intervals. The granulite contaminant (TB95-2.5) is from Barry et al. (2003) and isotopic values are age adjusted to 230 Ma.

even with this contaminant, the modelling indicates that the HSA could be from an oceanic slab with ~20% crustal assimilation of the granulite (**Fig. 3.25A**).

The $\epsilon_{\text{Hf}(t)}$ values for the LSA, HSA and Group 1 samples are also very similar (2.94-5.59). Despite these values being lower than P-MORB (**Fig. 3.25B**), they are similar to the Mengyin adakite zircons and higher than adakitic Yungay ignimbrites and Liujing zircons.

3.9 DISCUSSION

Palaeomagnetic data (e.g., Kravchinsky et al., 2002; Cognè et al. 2005; Van der Voo et al., 2015) advocates that the closure of the Mongol-Okhotsk Ocean occurred between the Late Jurassic (~155 Ma) and the beginning of the Early Cretaceous (~120 Ma). Modelling by Wu et al. (2017) suggests the Mongol-Okhotsk Ocean closed in three major stages; between 250-200 Ma, 200-150 Ma and finally 150-120 Ma. Their modelling proposes, that during the first stage, approximately 62.5-76.1% of the Mongol-Okhotsk Ocean lithosphere subducted beneath Siberia and North China-Amuria with an average convergence rate of $\sim 8.8 \pm 0.6$ cm/yr. Therefore, the HSA magmatism corresponds with when the Mongol-Okhotsk Ocean was closing fastest. It is debated whether the Mongol-Okhotsk Ocean was subducting northwards, southwards or in a bimodal fashion (e.g., Fritzell et al., 2016). However, if the HSAs are slab melts from a subducting Mongol-Okhotsk Ocean then this would suggest that there was southward and/or bimodal subduction. Alternatively, the crust could have been thickened during the closure of the Mongol-Okhotsk Ocean and the HSA samples could reflect basaltic underplating/lower crustal foundering. However, the depletion in Nb, Ta (high Nb/Ta ratios) and Ti suggests the involvement of residual rutile, while the depletion in HREE's suggests the involvement of residual garnet. For both garnet and rutile to be stable together requires pressures >1.5 GPa, with depths >50 km (e.g., Zhao et al., 2008 and references therein) and therefore would have required significant crustal thickening.

The HSA samples are close in composition to the younger (~120 Ma; Dash et al. 2015) Group 2 lavas which were interpreted to derive from metasomatised lithospheric mantle. Whether this lithospheric mantle underwent metasomatism via subduction derived fluids

and/or melts from a southward subducting Mongol-Okhotsk slab is unclear. It is interesting that no high-Nb basalts have been identified close to the HSAs which are often used to support slab melting (e.g., see Zhao et al., 2008).

Overall, the geochemistry of the HSA samples is ambiguous. These samples generally have higher $^{87}\text{Sr}/^{86}\text{Sr}_{(i)}$ and lower $\epsilon\text{Nd}_{(t)}$ values than other adakites globally (**Fig. 3.25**). However, many of the adakitic rocks from China have similarly much higher $^{87}\text{Sr}/^{86}\text{Sr}_{(i)}$ and lower $\epsilon\text{Nd}_{(t)}$ values. However, the HSA samples have isotopic values similar to the Awulale adakitic melts which were interpreted to be a product of basaltic underplating of an eclogitised lower crust. The HSA samples have Mg# and MgO wt. % concentrations which suggest some mantle assimilation (**Fig. 3.16 & 3.22B**). Furthermore, the relatively low Na_2O and high Ni + Cr concentrations compared to crustal melts also supports that the HSAs have undergone some mantle assimilation (**Fig. 3.17 & 3.19**). Two models are proposed to explain the petrogenesis of the HSA samples:

(1) A southward subducting Mongol-Okhotsk oceanic slab underwent eclogitisation during the closure of the Mongol-Okhotsk Ocean. This rutile-bearing eclogite subsequently underwent melting. Ascending slab melts then interacted and became hybridised with the mantle, and metasomatised it, and during ascent through the crust underwent crustal contamination.

(2) The closure of the Mongol-Okhotsk Ocean helped to thicken the crust (>50 km) enhancing basaltic underplating and promoting eclogitisation. This lower crust later foundered into the underlying mantle. Secondary mantle interaction and crustal contamination then followed (**Fig. 3.26**).

Because the HSA petrogenesis corresponds with the closure of the Mongol-Okhotsk Ocean and contains clear petrological evidence for crustal contamination, I favour model 1.

The LSA samples have Sr/Y vs. Y values that trend into the adakite field (**Fig. 3.11A**) but plot with major and trace element concentrations unlike adakites (**Fig. 3.22**). The LSA samples frequently have geochemical attributes more similar to the Group 1 samples (e.g., **Fig. 3.16, 3.22, 3.24 & 3.25**). Thus, much of the HREE depletion in the LSA samples likely reflects late-stage fractionation of accessory minerals such as zircon and apatite (**Fig. 3.13**). However, the

LSA lavas are still more depleted in the HREEs at a given MgO/SiO₂ wt. % than the Group 1 lavas (e.g., **Fig 3.13C**). Furthermore, the LSA samples are more enriched in Na₂O than the Group 1 and 2 lavas and have high Nb/Ta ratios (**Fig. 3.20**). Thus, in all likelihood, the LSA

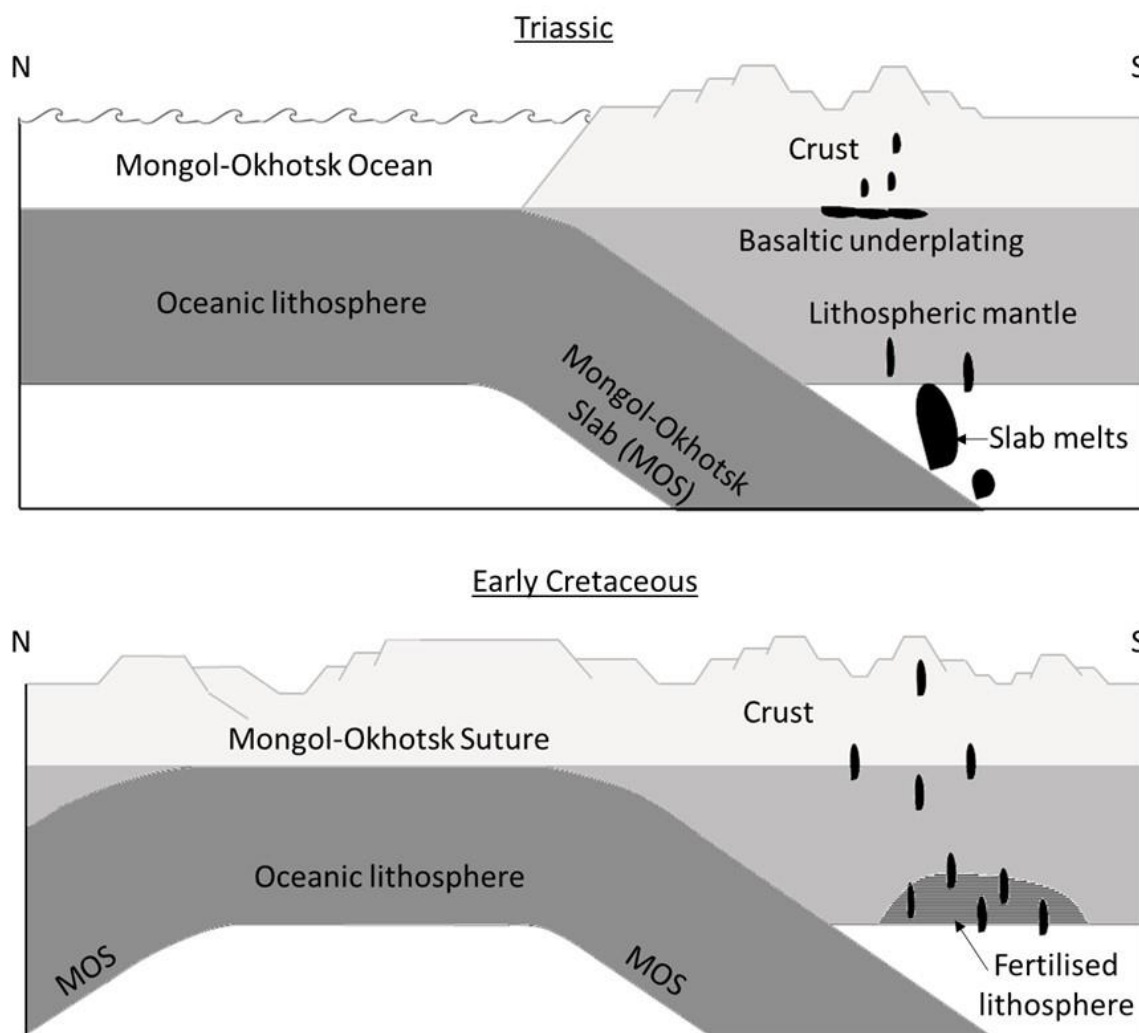


Figure 3.26: A sketch showing bimodal closure (Triassic) of the Mongol-Okhotsk Ocean and the petrogenesis of the HSA (either as slab melts or from basaltic underplating). Early Cretaceous shows a fertilised lithosphere which underwent melting generating the Low-Si adakites.

source was more depleted in the HREEs or contained more residual garnet than the Group 1 and 2 lavas. One way of getting both higher Na₂O and high Nb/Ta ratios is to have a source modified by small-degree partial melts of a rutile-bearing eclogite. Such a source could also help explain the HREE depletion. The following model is proposed to explain the petrogenesis of the LSA lavas:

During the final stages of closure of the Mongol-Okhotsk Ocean, a southward subducting Mongol-Okhotsk rutile-bearing slab underwent small degrees of partial melting causing metasomatism of the overlying mantle wedge/lithospheric mantle. This enriched mantle

then underwent partial melting, potentially from a similar delamination process suggested for the Mesozoic melts in the Gobi Altai (Sheldrick et al. 2018). Melts from this process then underwent fractional crystallisation and crustal contamination.

The Group 2 lavas share many geochemical similarities to lithospheric melts from the Gobi Altai and eastern Mongolia (Dash et al. 2015; Sheldrick et al. 2018). A much larger comparative study of all these melts is included in the following chapter, which will introduce a new extensive dataset across eastern and southern Mongolia. The Group 2 lavas will be included in this study for greater comparison.

CHAPTER 4

EVALUATING THE WIDER SCALE CONTEXT OF MAGMATISM ACROSS EAST ASIA: A REGIONAL COMPARISON WITH DATA FROM RUSSIA, MONGOLIA, THE NORTH CHINA CRATON AND KOREA.

Major and trace-element data, Sr-Nd-Pb-Hf isotopes and $^{40}\text{Ar}/^{39}\text{Ar}$ radiometric dating results on volcanism from central and east Mongolia are combined with data from the literature. Volcanism from Mongolia and the North China Craton share similar geochemical characteristics through time – with Mesozoic magmatism >107 Ma being predominantly derived from subcontinental lithospheric mantle and has lower ΔNb , $\epsilon\text{Nd}_{(i)}$, $\epsilon\text{Hf}_{(i)}$ and higher $^{87}\text{Sr}/^{86}\text{Sr}_{(i)}$ values than volcanism between ~50-107 Ma from the asthenospheric mantle. Mongolian volcanism trends to negative $\epsilon\text{Nd}_{(i)}$ values from ~50 to 30 Ma and then $\epsilon\text{Nd}_{(i)}$ values finally increase again; some of the volcanism from the North China Craton also trends to negative $\epsilon\text{Nd}_{(i)}$ values, over the same time period. Russian lavas have geochemical parallels to the Mongolian and North China Craton volcanism, with samples >107 Ma having geochemical signatures consistent with a subcontinental lithospheric mantle source. However, the limited Russian data does not suggest a switch to asthenospheric volcanism at ~107 Ma, like Mongolia and China; Russian asthenospheric magmatism does not appear until the Cenozoic. Korean magmatism does not have an asthenospheric geochemical signature until the Cenozoic.

The whole-rock geochemical data and radiometric dating results from Mongolia are used to test a previously proposed model which advocates a temporal migration of volcanic centres associated with a mantle plume. The age distribution and geochemical parallels between the Mongolian and North China Craton volcanism does not agree with this model.

A model of convective erosion and local (piecemeal) delamination is proposed to explain Mesozoic volcanism in Mongolia and the North China Craton. In this model, a combination of subducted dehydrating slabs from the Mongol-Okhotsk Ocean, Palaeo-Asian and Palaeo-Pacific plates control asthenospheric dispersal and lithospheric destruction.

4.1. INTRODUCTION

The aim of this chapter is to introduce new data from across eastern and southern Mongolia and compare with existing data from Russia, Mongolia the North China Craton and Korea. To achieve the best spatial and temporal view of magmatic processes, new samples were collected from traverses parallel and perpendicular to, the Mongol-Okhotsk Suture (**Fig. 4.1**). A combination of XRF, ICP-MS, Sr-Nd-Pb-Hf isotope analysis and $^{40}\text{Ar}/^{39}\text{Ar}$ data collection has been undertaken.

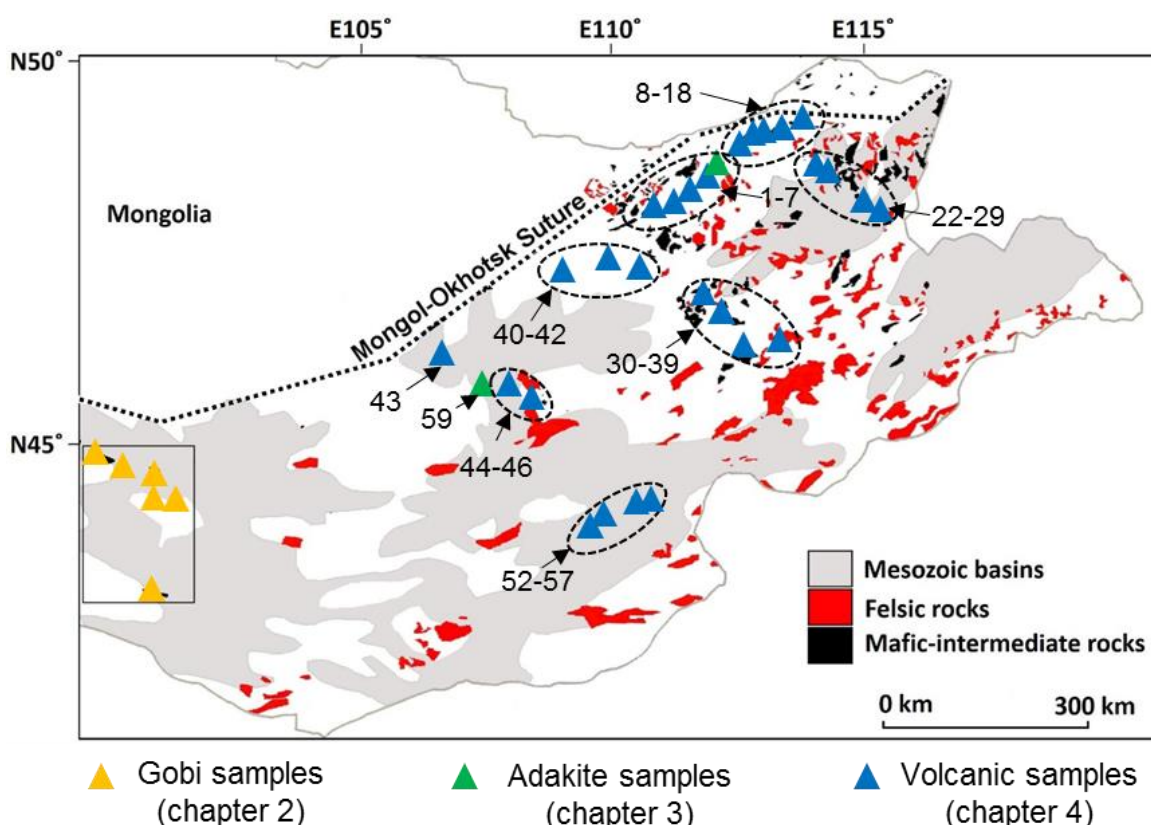


Figure 4.1: A map of Mongolia showing the distribution of samples collected for this study (corresponding sample numbers shown). The distribution of volcanism is based on Mongolian government geological maps and field observations. The distribution of Mesozoic sedimentary basins is from Johnson et al. (2003).

4.2. PETROLOGY

Volcanic rocks from the different sample localities showed variation in their freshness with some areas having relatively unaltered samples with good exposure. However, more commonly, volcanic rocks were poorly exposed, weathered and exhibited epidote/chlorite alteration (e.g., **Fig. 4.2A**). Samples were often vesicular (e.g., **Fig. 4.2B**) and siliceous

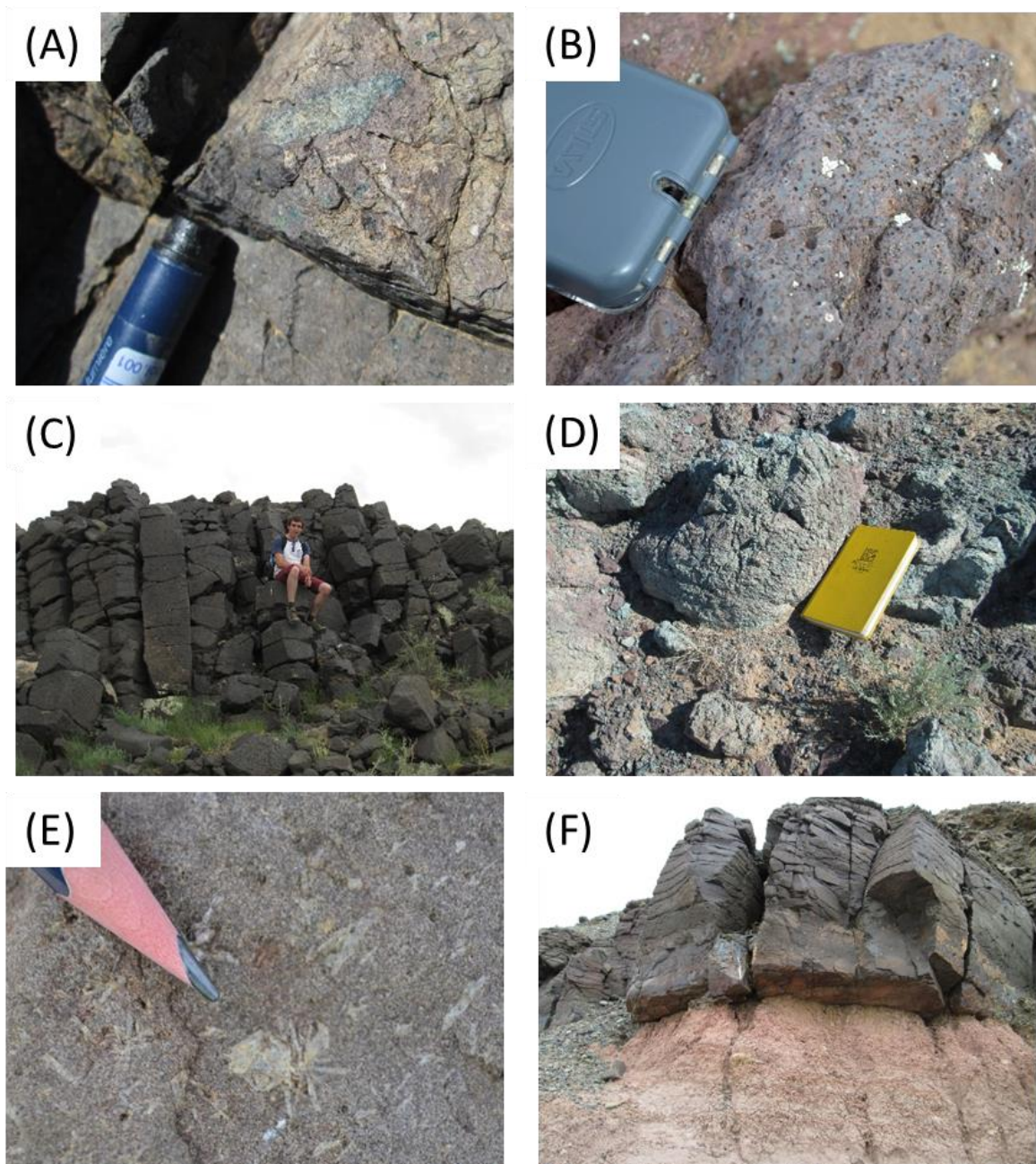


Figure 4.2: (A) epidote alteration in a basaltic sample; (B) typical vesicular basaltic sample; (C) fresh basaltic lavas exhibiting columnar jointing; (D) Onion skin weathering in altered basaltic volcanics (near TCS. 57); (E) rosetta plagioclase and nepheline phenocrysts indicative of late-stage fractional crystallisation processes or incorporation of cumulate assemblage (sample locality TCS. 13); (F) fresh basaltic lavas at Har HotoI (near TCS. 56).

amygdales were common. Columnar jointing (e.g., **Fig. 4.2C**) and onion skin weathering (e.g., **Fig. 4.2D**) was also observed at some localities.

Thin section investigations show that the trachyandesite lavas are hypocrySTALLINE (**Fig. 4.3A & B; 4.6**) with groundmass material consisting of plagioclase feldspar (sometimes flow-aligned), iddingsitised olivine and altered clinopyroxene. Sometimes clinopyroxene encloses plagioclase crystals (poikilitic) and there are nepheline microphenocrysts. Carbonate and clay amygdales occur.

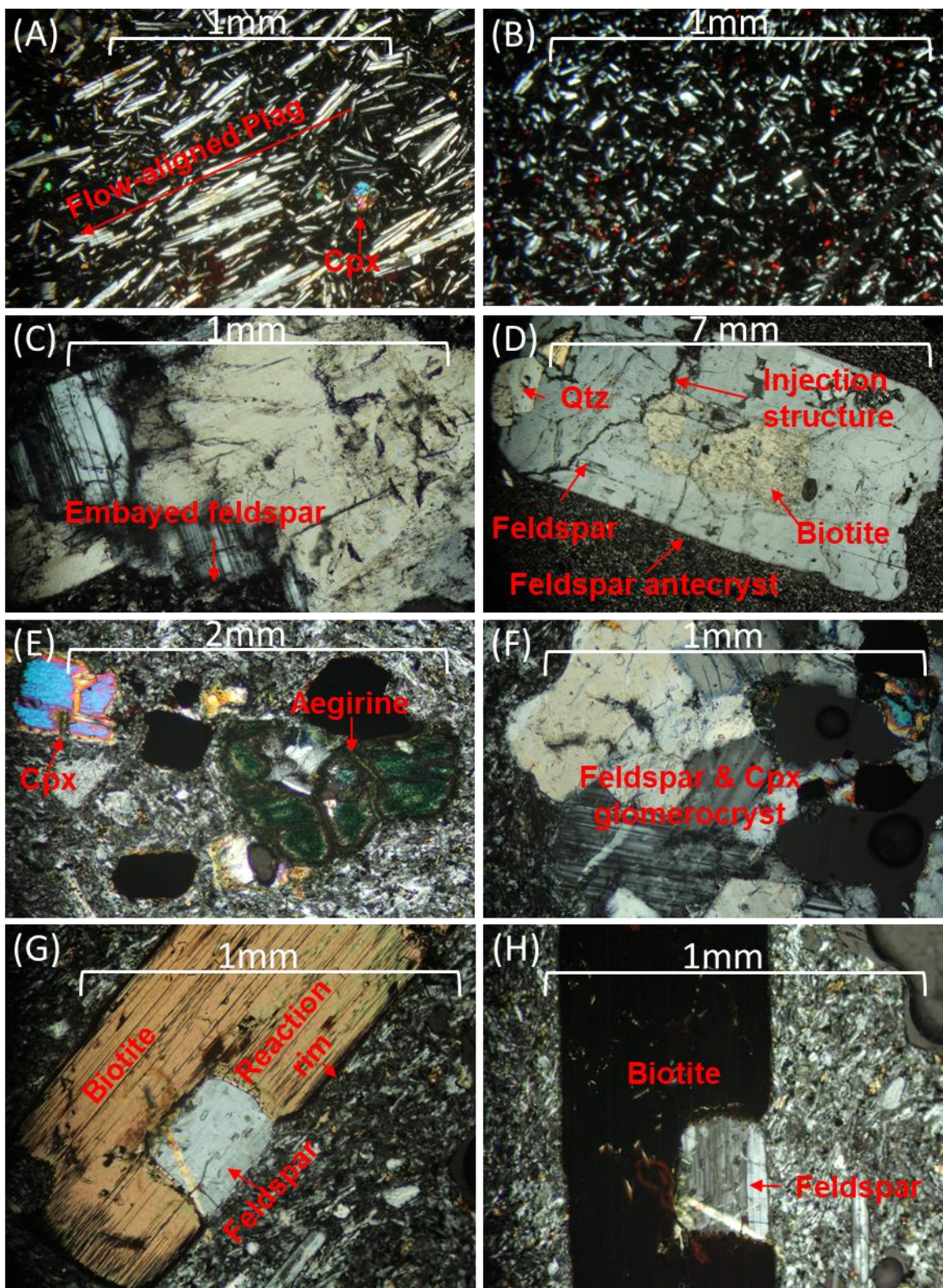


Figure 4.3: (A) Flow-aligned plagioclase feldspar and intermittent clinopyroxene crystals (TCS. 35.1); (B) plagioclase laths and iddingsitised olivine (TCS. 40.1); (C) glomerocryst of feldspar crystals with embayed edges (TCS. 51.1); (D) Antecryst of feldspar containing injection structures, a reabsorbed biotite crystal and inclusions of feldspar and quartz (TCS. 51.1); (E) clinopyroxene and aegirine phenocrysts in a groundmass of feldspar crystals (TCS. 58.1); (F) feldspar and clinopyroxene glomerocryst (TCS. 58.1); (G) biotite phenocryst containing an ingrown feldspar crystal and (H) the same biotite crystal as shown in Image G but now with straight extinction and feldspar showing the characteristic twinning (TCS. 58.1).

Trachyte samples contain glomerocrysts of alkali feldspar (**Fig. 4.3C & F; 4.6**) with oscillatory zoning, antecrysts of feldspar (**Fig. 4.3D**), clinopyroxene phenocrysts which are sometimes altered to aegirine (**Fig. 4.3E**), biotite and quartz phenocrysts (**Fig. 4.3G & H**). There are also microphenocrysts of nepheline. The embayment of feldspar glomerocrysts (**Fig. 4.3C**), replacement of biotite, injection structures and reaction rims (**Fig. 4.3D, G, H**) indicate incorporation of antecrysts which were unstable and melted.

Representative phenocryst abundances and sample specific information is reported in Table 4.1.

Table 4.1: Petrological descriptions

Sample	Phenocrysts %	Estimated groundmass modal composition:					Alteration %	Texture	Comments
		Ol	Cpx	Plag	Alk	Opq			
TCS. 25.1 Trachyandesite	-	15	20	60	-	5	30	Hypocrystalline & Amy	Ol is fully altered to iddingsite and Cpx is commonly altered. Carbonate amygdales.
TCS. 35.1 Trachyandesite	-	10	23	60	-	2	30	Hypocrystalline & Amy	Ol is fully altered to iddingsite and Cpx is commonly altered. Glass is altered (murky brown colour). Carbonate amygdales.
TCS. 40.1 Alkali basalt	-	10	10	78	-	2	15	Hypocrystalline	Ol is fully altered to iddingsite and Cpx is commonly altered.
TCS. 44.1 Trachyandesite	-	8	15	76	-	1	15	Hypocrystalline	Ol is fully altered to iddingsite and Cpx is commonly altered.
TCS. 44.2 Trachyandesite	-	7	17	75	-	1	15	Hypocrystalline	Ol is fully altered to iddingsite and Cpx is commonly altered.
TCS. 45.1 Trachyandesite	-	8	12	78	-	2	15	Hypocrystalline & Amy	Ol is fully altered to iddingsite and Cpx is commonly altered. Carbonate amygdales.
TCS. 51.1 Trachyte	Quartz (5 %). Disintegrated feldspars (3%).	-	20	78	-	4	20	Hypocrystalline & glomeroporphyritic	Antecryst of feldspar with biotite, feldspar and Qtz inclusions. Disintegrated glomeroporphyritic clusters of feldspar crystals. Cpx is commonly altered.

Sample	Phenocrysts %	Ol	Cpx	Plag	Alk	Opq	Alteration %	Texture	Comments
TCS. 53.1 Basaltic- trachyandesite	Microphenocrysts of nepheline (1 %)	10	13	75		2	20	Hypocrystalline & Amy	Ol is fully altered to iddingsite and Cpx is commonly altered. Clay amygdales.
TCS. 55.1 Basaltic- trachyandesite	-	10	38	50	-	2	35	Hypocrystalline	Plag appears as thin, needle-like laths and often enclosed by Cpx (poikilitic). Ol is fully altered to iddingsite and Cpx is commonly altered. The glass is altered in places.
TCS. 58.1 Trachyte	Cpx (10 %), Plag (3 %) Alk (10 %) Biotite (1 %). Nepheline (1 %),	-	8	62	3	2	30	Hypocrystalline & glomeroporphyritic	Microphenocrysts of glomeroporphyritic Cpx with some alteration to aegirine. Alkali feldspar crystals have oscillatory zoning. Biotite phenocrysts with intergrown feldspar perhaps indicating that the two crystals crystallised in an epitaxial fashion.

Cpx, clinopyroxene; Plag, plagioclase; Alk, alkali feldspar; Qtz, quartz; amy, amygdaloidal; porh, porphyritic; trach, trachytic; glom, glomeroporphyritic.

4.3. ARGON DATING

To try and test for an age progression away from the Mongol-Okhotsk Suture, 5 samples were selected for whole-rock $^{40}\text{Ar}/^{39}\text{Ar}$ dating (**Fig. 4.4**). This data will be combined with previous $^{40}\text{Ar}/^{39}\text{Ar}$ dating results (Chapter three) and with existing $^{40}\text{Ar}/^{39}\text{Ar}$ data from Mongolia (Graham et al., 2001; Dash et al., 2015; Sheldrick et al., 2018). The analytical procedure is reported in Appendix A.

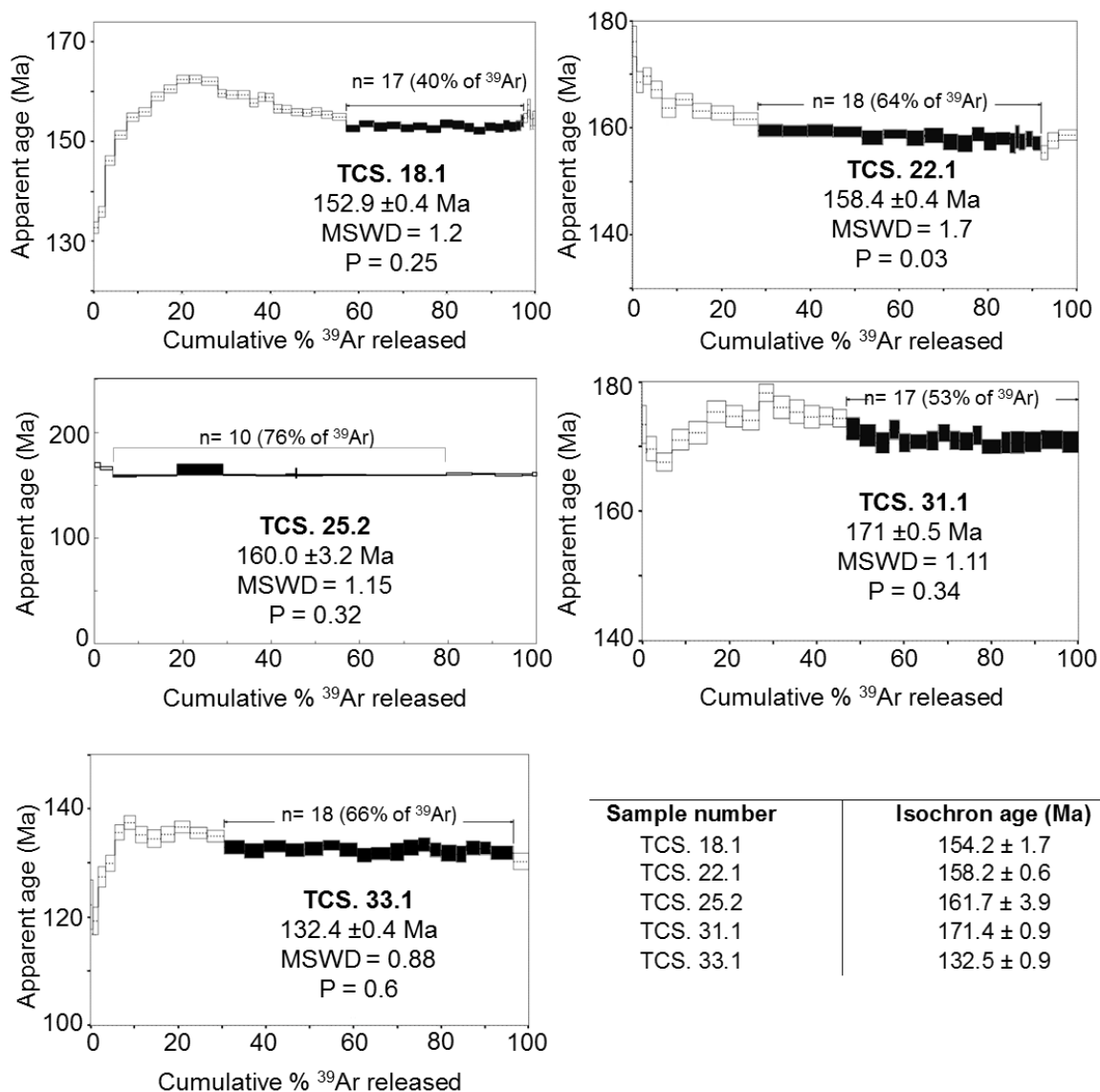


Figure 4.4: Whole-rock ^{40}Ar - ^{39}Ar age plateau diagrams and corresponding calculated isochron ages.

Other than sample TCS. 18.1, the plateaus are developed from >50% of the released ^{39}Ar (**Fig. 4.4**). The plateaus were constructed from a large number of consecutive steps ($n = \geq 10$) and have high MSWD values (>0.8). Calculated isochron ages are however in good agreement with the plateau ages.

The dated Mesozoic samples (**Fig. 4.5**) show no obvious age progression, parallel or perpendicular to, the Mongol-Okhotsk Suture. However, the large spatial distribution and age range provides an excellent opportunity to consider spatial and temporal geochemical changes.

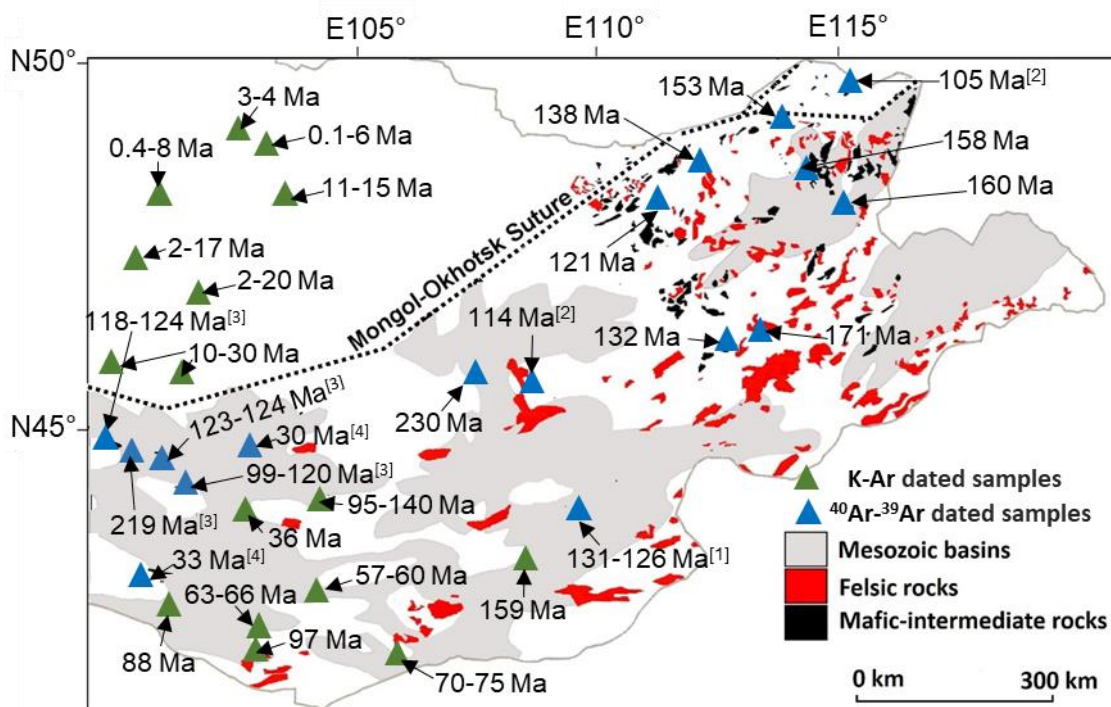


Figure 4.5: A sketch map of Mongolia showing the distribution of Mesozoic and Cenozoic mafic-intermediate volcanism that have undergone ⁴⁰Ar-³⁹Ar and K-Ar dating. The distribution of volcanism is based on Mongolian government geological maps and field observations. The distribution of Mesozoic sedimentary basins is from Johnson et al. (2003). Previously dated samples: [1] Graham et al. (2001); [2] Dash et al. (2015); [3] Sheldrick et al. (2018); [4] Barry et al. (2003). The K-Ar dates were from the appendix of Yarmolyuk et al. (2015) and references therein.

4.4. GEOCHEMICAL RESULTS

4.4.1 Rock classification and *major-element variations*

To classify the new samples in this study, a SiO₂ wt. % vs. Nb/Y (immobile elements) plot is used (**Fig. 4.6A**). The samples plot predominantly in the basaltic-trachyandesite/trachybasalt to trachyandesite field. Two samples plot in the trachyte field (TCS. 5.1 & 33.1) and two samples plot in the dacite field (TCS. 18.1 & TCS 57.3). Although eleven samples plot in the andesite field and one in the sub-alkaline field, these samples plot in the trachybasalt to trachyandesite field on a TAS diagram (included in Appendix B). The vast majority of samples have high-K (n=39), or are shoshonitic (n=20), and only one sample (TCS. 28.1) straddles into the medium-K field (**Fig. 4.6B**).

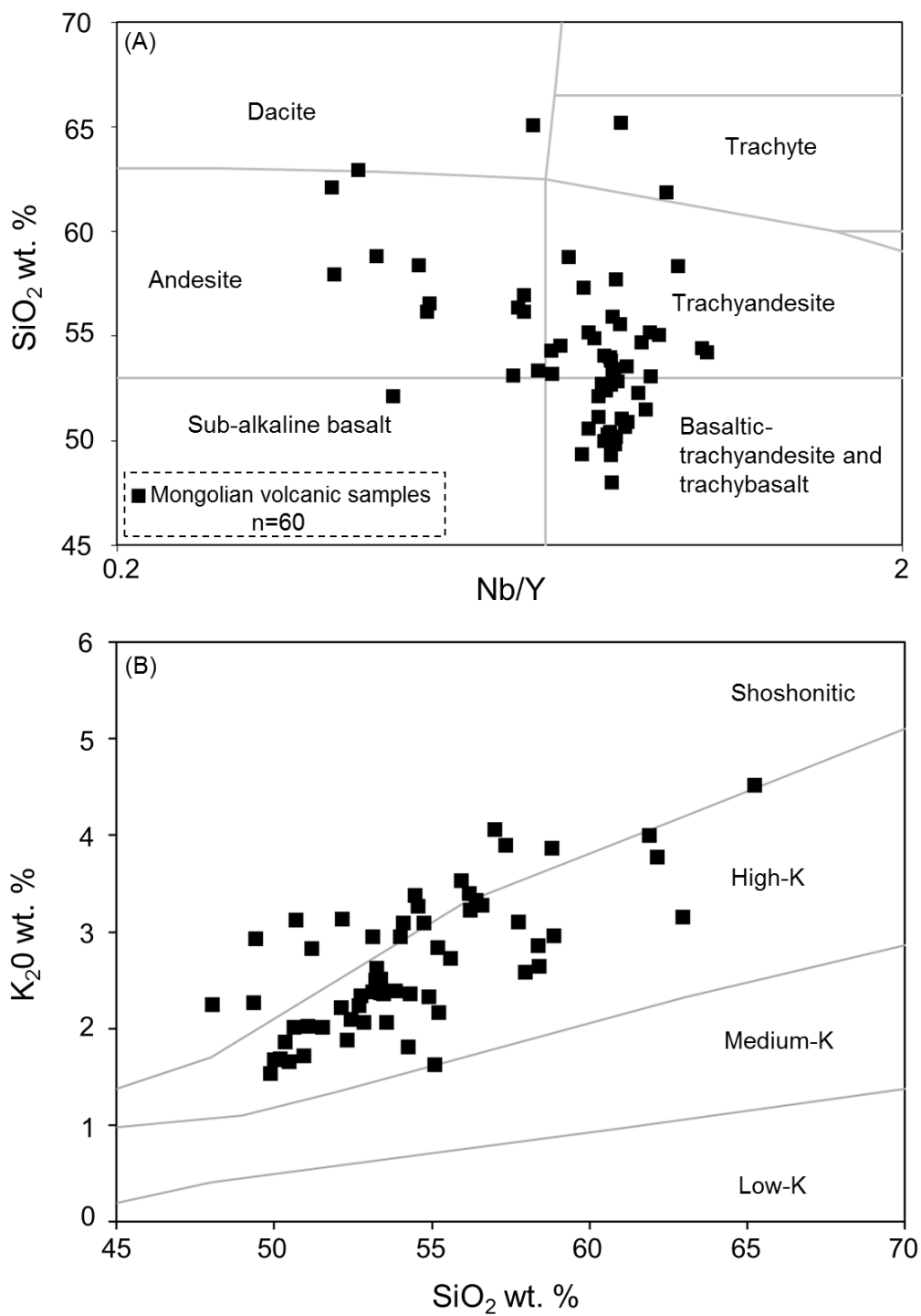


Figure 4.6: (A) SiO₂ vs. Nb/Y immobile element rock classification diagram from Winchester and Floyd. (1977) and (B) a SiO₂ vs. K₂O wt. % plot based on Ewart (1982) for the Mongolian samples (excluding the adakites discussed in chapter 3, the Gobi samples from chapter 2 and also TCS. 18.1 on Figure B due to high K₂O).

DATA INTERPRETATION

4.5 GEOCHEMICAL VARIATIONS

The aim of this section is to test for changes in geochemistry both spatially and with time.

4.5.1 *K/La ratios through time and space*

It has been suggested that the Mongolian “shoshonite series were derived from the most metasomatised source” (Dash et al. 2015). Although K is mobile during alteration

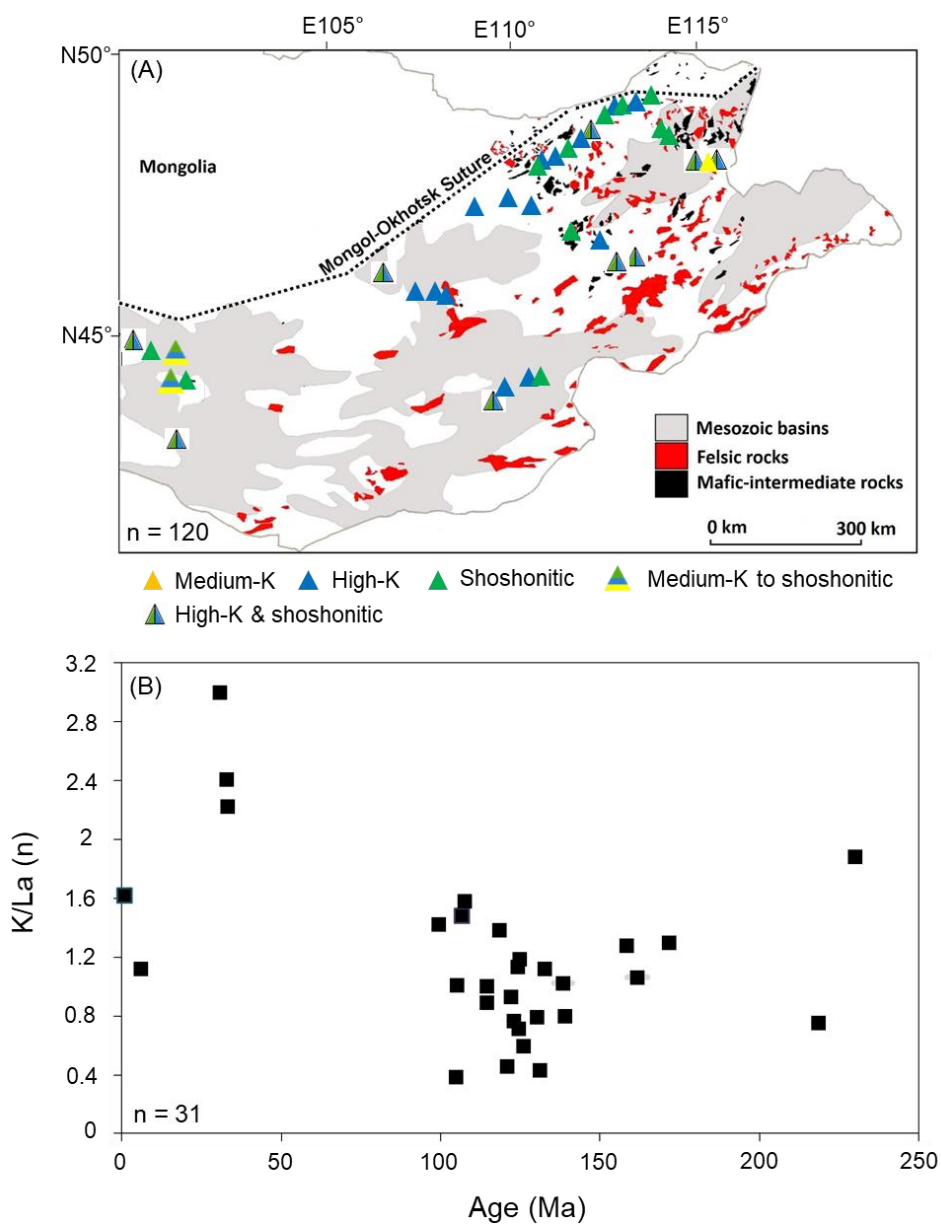


Figure 4.7: (A) Distribution map showing samples with medium-K to shoshonitic compositions which used the classification criteria from Ewart (1982). (B) Primitive mantle-normalised (Sun and McDonough, 1989) K/La vs. Age; all age data from ^{40}Ar - ^{39}Ar dating. Additional ^{40}Ar - ^{39}Ar data taken from: Graham et al. (2001); Dash et al. (2015) and Sheldrick et al. (2018). Sample TCS. 18.1 omitted (dacite) due to high K (K/La ratio = 5.5).

processes, this element is used to help test for source metasomatism because it is fluid mobile, such as in slab fluids (Fig. 4.7). Although most samples are high-K or shoshonitic (Fig. 4.6 & 4.7), there is no obvious spatial distribution (Fig. 4.7A), with the distribution of medium-K to shoshonitic samples showing no obvious trends, parallel or perpendicular to, the Mongol-Okhotsk Suture (Fig. 4.7A). Furthermore, samples show a range of compositions, with medium-K to shoshonitic samples appearing at the same localities (Fig. 4.7A). Primitive mantle-normalised K/La vs. Age results (Fig. 4.7B; only using $^{40}\text{Ar}/^{39}\text{Ar}$ dating) initially show no obvious correlation. However, trends become more apparent when the data is compared on a terrane-basis (Fig. 4.8; terranes based on info from Badarch et al. 2002). Nevertheless, more data is required to assess for changes on some of the terranes (e.g., Gurvansayhan and Idermeg terranes). The trends on the Gobi Altai terrane (Fig. 4.8A), and Middle Gobi Belt and Ereendavaa Terrane (Fig. 4.8B), could reflect a progressive change in source composition through time. Further consideration will be given to this in the following sections.

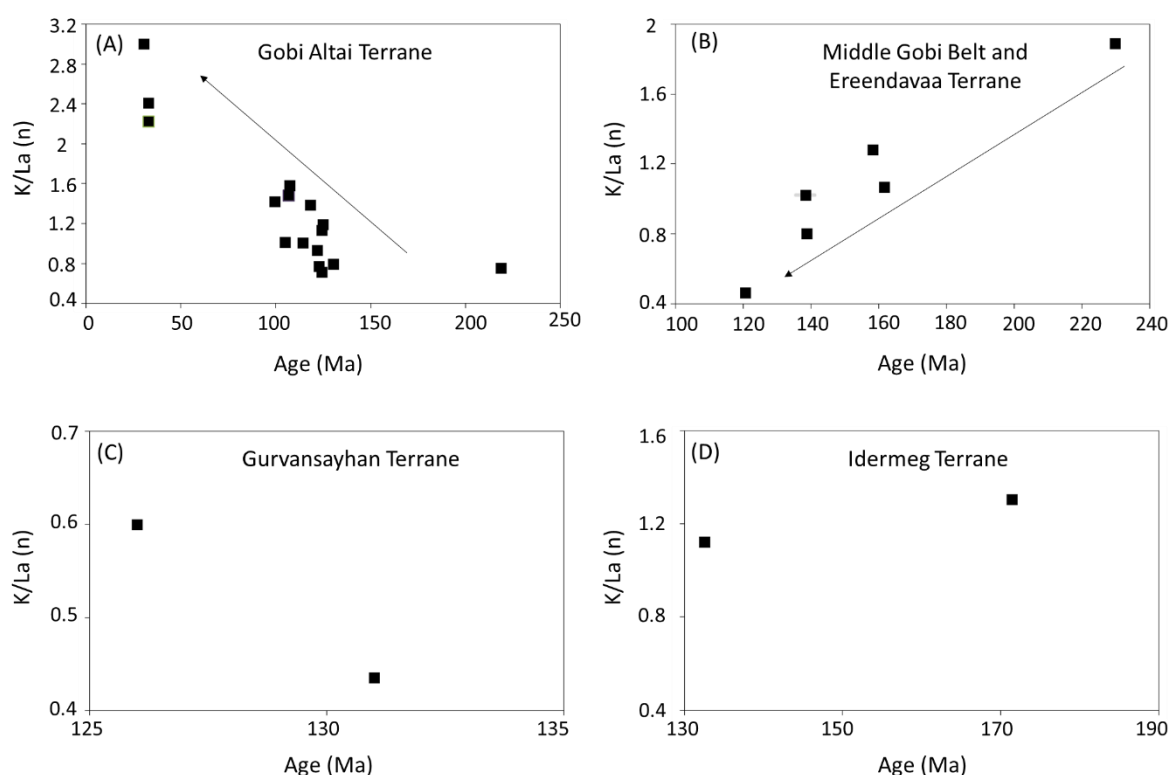


Figure 4.8: Primitive mantle-normalised (Sun and McDonough, 1989) K/La vs. Age; all age data from ^{40}Ar - ^{39}Ar dating. Terrane info from Badarch et al. (2002). Additional ^{40}Ar - ^{39}Ar data taken from: Graham et al. (2001); Dash et al. (2015) and Sheldrick et al. (2018).

4.5.2 ΔNb through time and space

As discussed by Fitton et al. (1997), ΔNb values ($\Delta Nb = 1.74 + \log (Nb/Y) - 1.92 \log (Zr/Y)$; equation 11) are “insensitive to the effects of variable degrees of mantle melting, source depletion through melt extraction, crustal contamination of the magmas, or subsequent

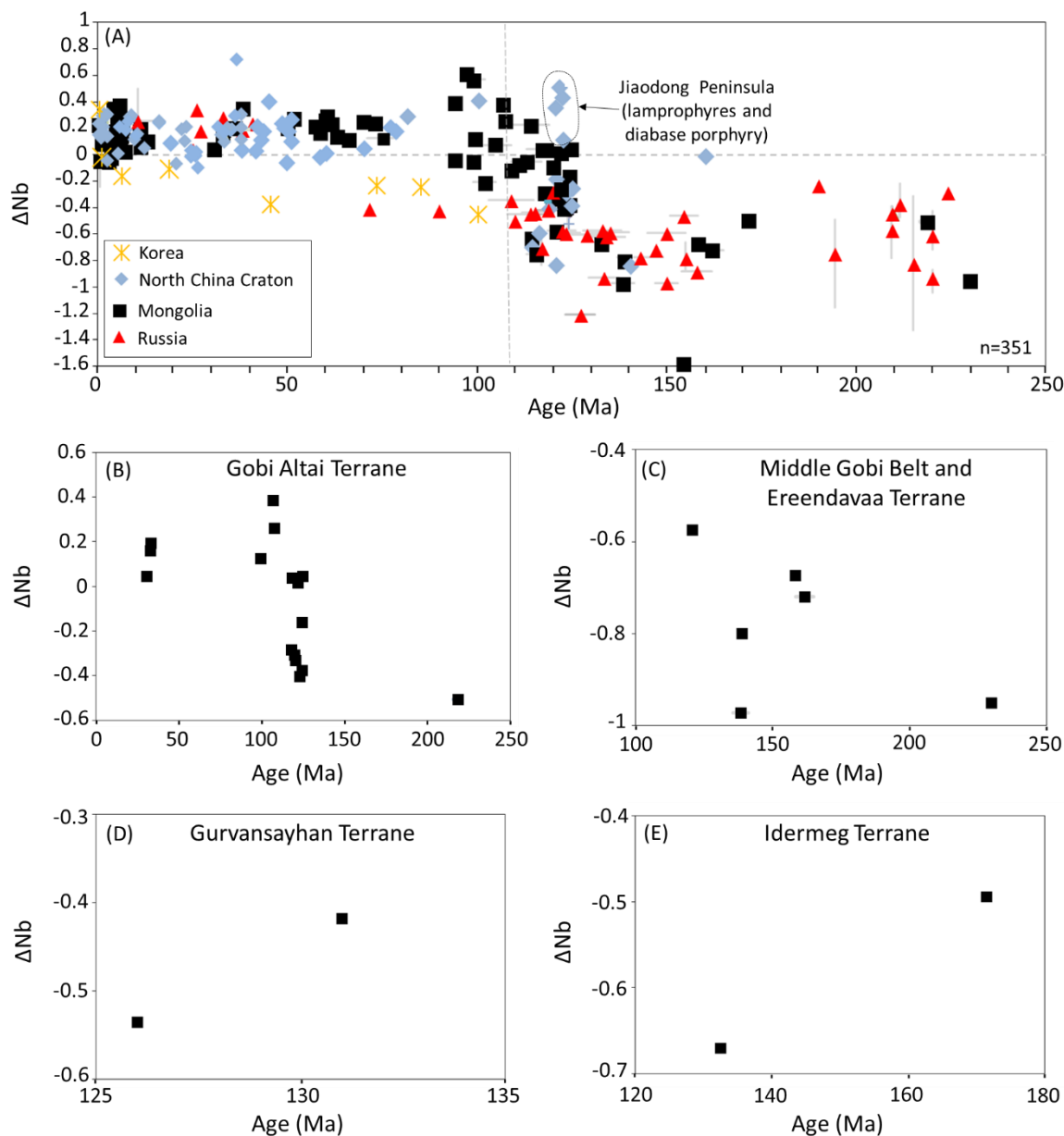


Figure 4.9: ΔNb ($\Delta Nb = 1.74 + \log (Nb/Y) - 1.92 \log (Zr/Y)$) vs. Age of the dated Mongolian and Chinese (North China Craton) melts. Range bars show the minimum and maximum values; however, range bars are normally less than the size of the data point. Data from: this study; Pouclet et al. (1994); Kim et al., (1999); Sagong et al. (2001); Zhang et al. (2002); Zhang and Zheng (2003); Pei et al. (2004); Johnson et al. (2005); Tang et al. (2006); Vorontsov et al. (2007 A&B); Gao et al. (2008); Liu et al. (2008) and references therein; Ying et al. (2008); Zhang et al. (2008); Andryuschenko et al. (2010); Ying et al. (2010); Ho et al. (2011); Wang et al. (2011); Kuang et al. (2012); Xu et al. (2012); Zhang et al. (2012); Chen et al. (2013); Ma et al. (2014; 2016); Zhao et al. (2014); Dash et al. (2015); appendix from Yarmolyuk et al. (2015); Gurban-Saikhan Range, Borzongiin-Govi depression, Dush Uul, South Gobi Area, Khotgor, Mushgai Well Area, Zuun-Bogd Range, Ikh-Bogd Range, Bayan-Tsagan Range, Khara-Argalant and Dund-Argalant Range, Chandman, Lower Okhon River, Khanui River and Ugii Lake) and Li et al. (2017). Due to abundant dated Korean Quaternary volcanism, this data has been averaged for visual aesthetics (Pouclet et al. (1994); Kim et al., (1999)). Figures 8 B-E only use samples with ^{40}Ar - ^{39}Ar radiometric dates.

alteration". Therefore, ΔNb values are used to assess source characteristics of volcanic samples from Korea, the North China Craton, Mongolia and Russia (**Fig. 4.9**). Positive ΔNb values are consistent with a source from the asthenospheric mantle or lithospheric mantle which is not depleted in HFSEs such as Nb. Alternatively, negative ΔNb values are consistent with a source depleted in Nb, such as a metasomatised SCLM. Detailed studies and modelling on sample specific localities also emphasise that crustal contamination is unlikely to cause the significant depletions in Nb (Sheldrick et al., 2018). To further extend the dataset, K/Ar dating results are now also included in the initial comparisons but where possible, only the dated sample, from the different localities, is used in the comparison. Where this was not possible (e.g., no geochemical data for the dated sample), then all the data was averaged from the locality and range bars show the minimum and maximum values for each point/locality. Analytical error bars for the radiometric dating results are also shown. To further evaluate the role of crustal contamination and source characteristics, MgO/SiO₂ vs. ΔNb values is considered more fully in Figure 4.10.

Most samples from Mongolia and China that are older than 107 Ma have negative ΔNb values (**Fig. 4.9**). It is interesting that asthenospheric melts from the Jiaodong Peninsula have an asthenospheric signature and are 122 Ma (zircon U-Pb radiometric dating; Ma et al. 2016). Whether these asthenospheric melts reflect a period of greater asthenospheric upwelling (122-126 Ma) is uncertain – however, this period of volcanism does correspond with the greatest period of Mesozoic magmatism in the North China Craton and elsewhere in Mongolia (e.g., He. 2014; Dash et al., 2015; Sheldrick et al., 2018). Generally, melts younger than 107 Ma from Mongolia and the North China Craton change to positive ΔNb values. Overall, samples between 140 - 107 Ma, show increasing ΔNb values as they young. This trend might reflect less involvement from a subduction-preconditioned subcontinental lithospheric mantle and crust, coupled with increasing asthenospheric input. Melts on the Gobi Altai terrane (**Fig. 4.9B**), and possibly the Middle Gobi Belt and Ereendavaa terrane (**Fig. 4.9C**), show increasing ΔNb values as they become younger; this is consistent with a progressive change in mantle source composition through time.

Melts from Russia (**Fig. 4.9A**) have a similar trend to those from Mongolia and the North China Craton; melts older than 107 Ma have negative ΔNb values, while those younger than ~40 Ma have positive ΔNb values. More data is required to assess whether Russia, like

Mongolia and the North China Craton, has abundant magmatism with positive ΔNb values between 40-107 Ma. It is interesting that the limited data for Korea (Poucllet et al., 1994; Kim et al., 1999; Zhang et al., 2016) suggest that asthenospheric melts do not appear until the Quaternary, despite models invoking combined processes involving the Palaeo-Pacific plate (e.g., Bars et al., 2018).

There is, generally, a clear correlation between MgO (Fig. 4.10A) and SiO₂ (Fig. 4.10B) vs. ΔNb values. However, there are also many samples with similar levels of MgO and SiO₂ with

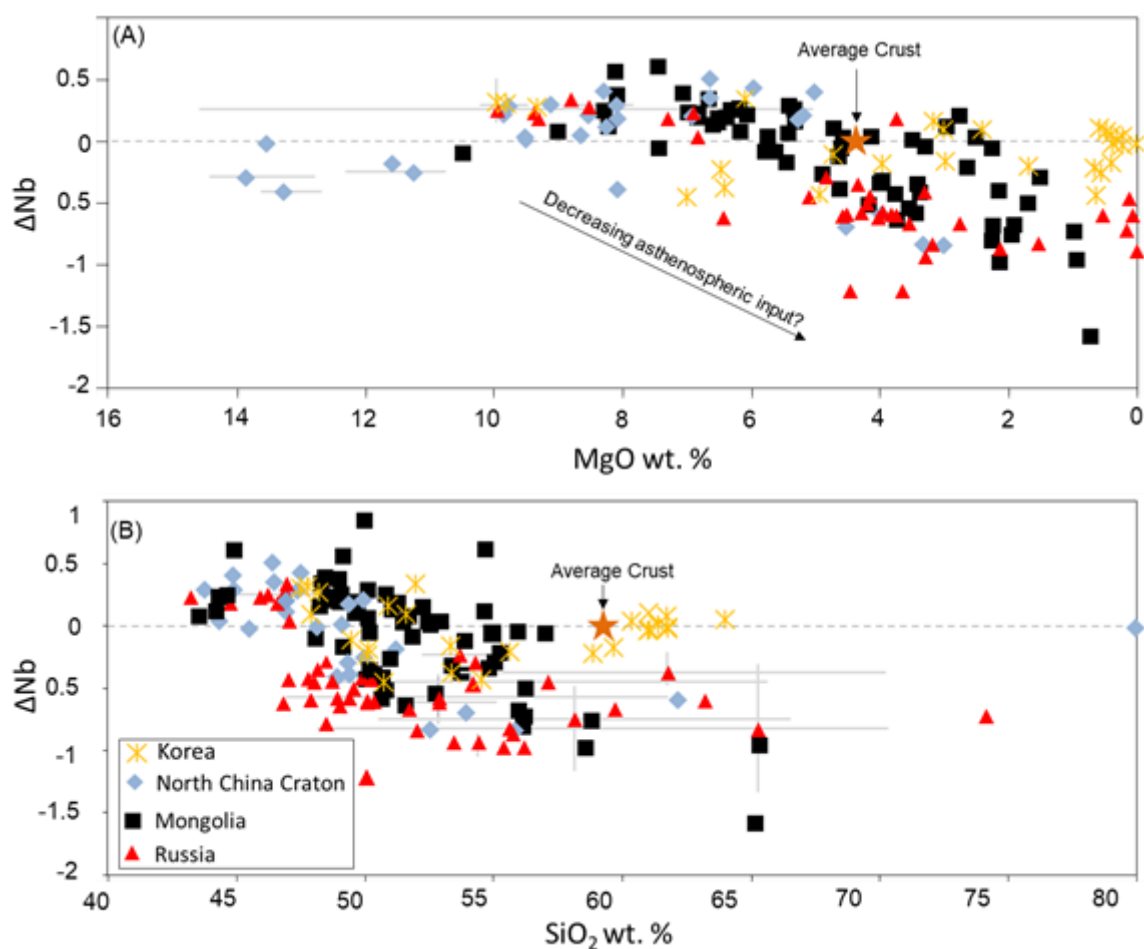


Figure 4.10: (A) MgO and (B) SiO₂ vs. ΔNb ($\Delta Nb = 1.74 + \log (Nb/Y) - 1.92 \log (Zr/Y)$). Range bars show the minimum and maximum values; however, range bars are normally less than the size of the data point. Data from: this study; Poucllet et al. (1994); Kim et al., (1999); Zhang et al. (2002); Zhang and Zheng (2003); Pei et al. (2004); Johnson et al. (2005); Vorontsov et al. (2007 A&B); Gao et al. (2008); Liu et al. (2008) and references therein; Zhang et al. (2008); Andryuschenko et al. (2010); Ying et al. (2010); Kuang et al. (2012); Ma et al. (2014; 2016); Dash et al. (2015); appendix from Yarmolyuk et al. (2015; Gurvan-Saikhan Range, Borzongiin-Govi depression, Dush Uul, South Gobi Area, Khotgor, Mushgai Well Area, Zuun-Bogd Range, Ikh-Bogd Range, Bayan-Tsagan Range, Khara-Argalant and Dund-Argalant Range, and Chandman); Zhang et al. (2016) and Li et al. (2017). The average crust value is from Rudnick and Fountain (1995).

negative and positive ΔNb values. Therefore, it seems likely that the negative ΔNb values reflect a source control with varying amounts of crustal input. The clear link between less

MgO and higher SiO₂ with the greatest negative ΔNb values emphasise changes in the style of magmatism through time (i.e. younger = less SiO₂ rich).

4.5.3 $^{87}\text{Sr}/^{86}\text{Sr}_{(t)}$ isotopes through time and space

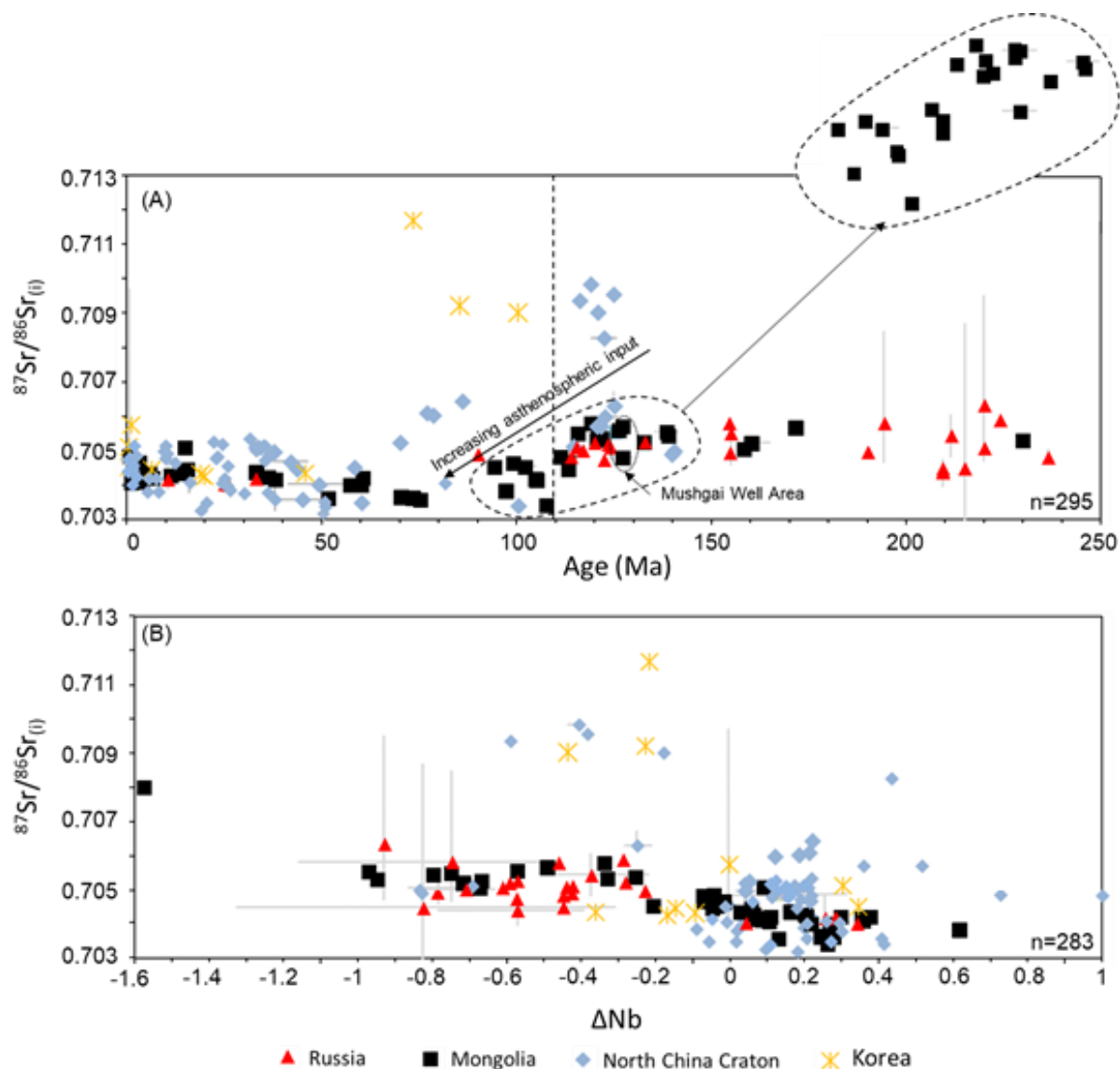


Figure 4.11: (A) Age and (B) ΔNb ($\Delta Nb = 1.74 + \log(Nb/Y) - 1.92 \log(Zr/Y)$) vs. $^{87}\text{Sr}/^{86}\text{Sr}_{(t)}$. Range bars show the minimum and maximum values (from localities where samples had to be averaged); however, range bars are normally less than the size of the data point. Data from: this study; Pouclet et al. (1994); Kim et al., (1999); Sagong et al. (2001); Zhang et al. (2002); Zhang and Zheng (2003); Pei et al. (2004); Johnson et al. (2005); Tang et al. (2006); Vorontsov et al. (2007 A&B); Gao et al. (2008); Liu et al. (2008) and references therein; Zhang et al. (2008); Andryuschenko et al. (2010); Ying et al. (2010); Ho et al. (2011); Wang et al. (2011); Kuang et al. (2012); Xu et al. (2012); Zhang et al. (2012); Ma et al. (2014; 2016); Zhao et al. (2014); Dash et al. (2015); appendix from Yarmolyuk et al. (2015); Gurvan-Saikhan Range, Borzongiin-Govi depression, Dush Uul, South Gobi Area, Khotgor, Mushgai Well Area, Zuun-Bogd Range, Ikh-Bogd Range, Bayan-Tsagan Range, Khara-Argalant and Dund-Argalant Range, Chandman, Lower Okhon River, Khanui River and Ugii Lake), Zhang et al. (2016) and Li et al. (2017). Due to abundant dated Korean Quaternary volcanism, this data has been averaged for visual aesthetics (Pouclet et al. (1994); Kim et al., (1999)).

The samples for Mongolia and the North China Craton trend to decreasing $^{87}\text{Sr}/^{86}\text{Sr}_{(t)}$ values as they become younger (Fig. 4.11A), with $^{87}\text{Sr}/^{86}\text{Sr}_{(t)}$ values frequently being <0.705 for

samples younger than ~107 Ma. Despite samples between 70-86 Ma from the North China Craton (**Fig. 4.11A**) having relatively high (compared to Mongolian samples) $^{87}\text{Sr}/^{86}\text{Sr}_{(i)}$ values (>0.705), these were interpreted to be asthenospheric mantle melts (Zhang et al. 2008). Samples >107 Ma from Russia also show $^{87}\text{Sr}/^{86}\text{Sr}_{(i)}$ values that are frequently >0.705 while samples <40 Ma have $^{87}\text{Sr}/^{86}\text{Sr}_{(i)}$ values that are <0.705 (more data is required to assess between 40-107 Ma). All localities generally trend to lower $^{87}\text{Sr}/^{86}\text{Sr}_{(i)}$ values with increasing ΔNb values (**Fig 4.11B**).

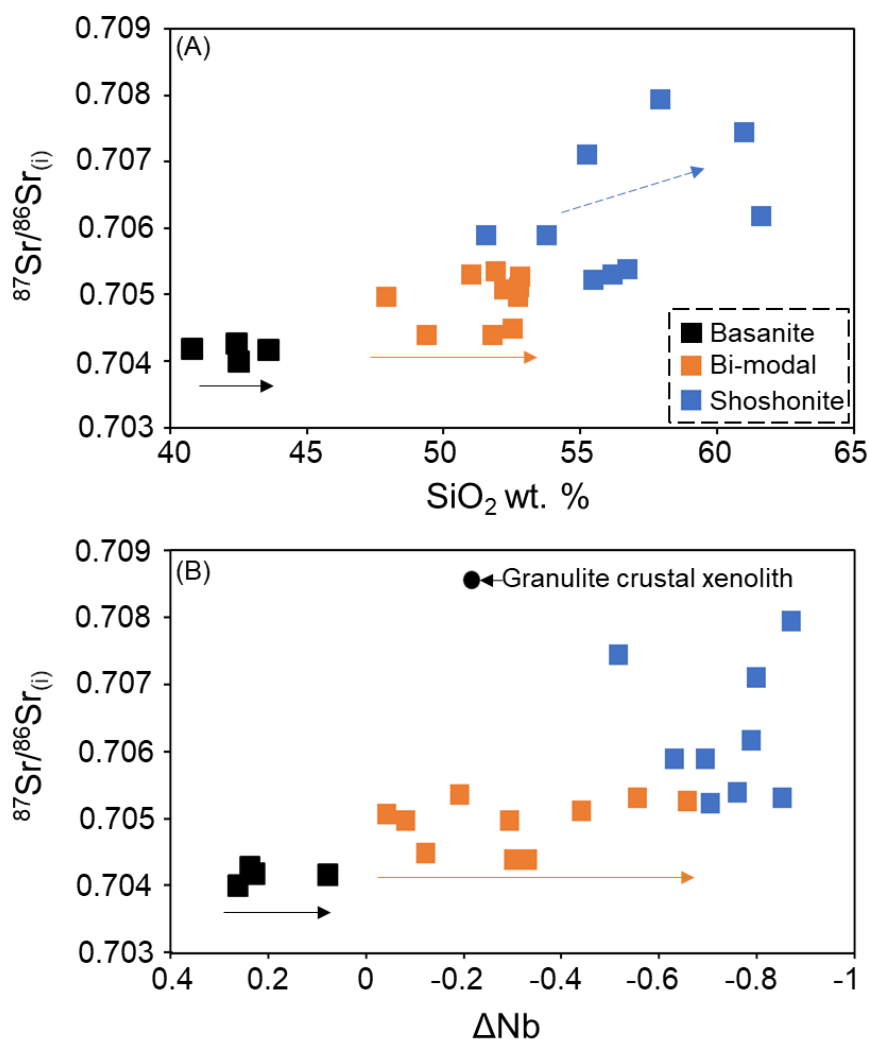


Figure 4.12: (A) SiO_2 and (B) ΔNb ($\Delta\text{Nb} = 1.74 + \log(\text{Nb}/\text{Y}) - 1.92 \log(\text{Zr}/\text{Y})$) vs. $^{87}\text{Sr}/^{86}\text{Sr}_{(i)}$. The Mongolian volcanic samples are from Dash et al. (2015) and the crustal xenolith (TB95-2.5) is from Barry et al. (2003).

Although crustal contamination may have increased $^{87}\text{Sr}/^{86}\text{Sr}_{(i)}$ values the data is best explained to reflect source controls. To emphasise this statement, I will now concentrate on a dataset from Mongolia (Dash et al. 2015); these samples underwent isotope analysis and were collected from only a few sample localities which have a range of SiO_2 compositions (thus allowing late-stage crustal contamination processes to be considered).

These data were separated into three categories by Dash et al. (2015) reflecting different source compositions: (1) basanite (~104 Ma); (2) bi-modal (~116 Ma) and (3) shoshonite (~116 Ma). The basanite and bi-modal samples do not show much variation between SiO_2 and ΔNb vs. $^{87}\text{Sr}/^{86}\text{Sr}_{(i)}$ values (**Fig. 4.12**) which is not indicative of significant late-stage crustal contamination processes. Some samples from the shoshonite series which have high SiO_2 (>55 wt. %) and large negative ΔNb values might be part of a trend consistent with crustal contamination.

Therefore, although crustal contamination would have likely modified $^{87}\text{Sr}/^{86}\text{Sr}_{(i)}$ values to some extent, it appears that this may have been minimal for the Mongolian samples. Thus, the change in $^{87}\text{Sr}/^{86}\text{Sr}_{(i)}$ values with time likely reflects a change in source composition; probably reflecting less involvement from the subcontinental lithospheric mantle (which may have been modified by recycled crustal components), increasing asthenospheric mantle input and finally lithospheric replacement (e.g., Barry et al., 2003; Zhang et al., 2002). Further discussion on AFC processes is considered below (section 4.5.4).

4.5.4 $\epsilon\text{Nd}_{(i)}$ values through time and space

Calculated $\epsilon\text{Nd}_{(i)}$ values for samples from Russia, Mongolia, the North China Craton and Korea are now compared to evaluate source variation (**Fig. 4.13**).

The samples from Mongolia, between 90-113 Ma, show a trend of decreasing $\epsilon\text{Nd}_{(i)}$ values with increasing age; samples older than 113 Ma have low or negative $\epsilon\text{Nd}_{(i)}$ values (**Fig. 4.13**; 1.1 to -2.6). However, the samples between 60-107 Ma consistently have high $\epsilon\text{Nd}_{(i)}$ values (average of 3.5 ± 0.91). All Mongolian samples younger than 104 Ma are from central Mongolia (**Fig. 4.5**); samples younger than 50 Ma trend to negative $\epsilon\text{Nd}_{(i)}$ values with decreasing age and then finally increase again. Mongolian samples older than 107 Ma clearly plot outside the “Mongolian sample field” – which incorporates samples <107 Ma – thus highlighting geochemical variability with age (**Fig. 4.14A**). Chinese samples have a trend comparable to the Mongolian samples although samples younger than 50 Ma show a range of $\epsilon\text{Nd}_{(i)}$ values (**Fig. 4.13**; 5.9 to -3.9).

Russian Cenozoic (<50 Ma) asthenospheric samples (Johnson et al., 2005; Andryushchenko et al., 2009) have positive $\epsilon\text{Nd}_{(i)}$ values (**Fig. 4.13**), while samples older than 50 Ma have predominantly negative $\epsilon\text{Nd}_{(i)}$ values (average = -0.5 ± 1.5). The limited data suggests source

variability between Mongolian and Russian Cenozoic samples; the Russian Cenozoic samples have $\epsilon\text{Nd}_{(i)}$ values consistent with an asthenospheric mantle source (**Fig. 4.13 & 14A**). More data on Russian volcanism, between 50-100 Ma, is required to compare with the Mongolian samples between this period. The Korean samples are not very comparable to the Mongolian samples – samples frequently have large negative $\epsilon\text{Nd}_{(i)}$ values (for samples >50 Ma) or have positive $\epsilon\text{Nd}_{(i)}$ values for samples younger than 50 Ma (**Fig. 4.13**).

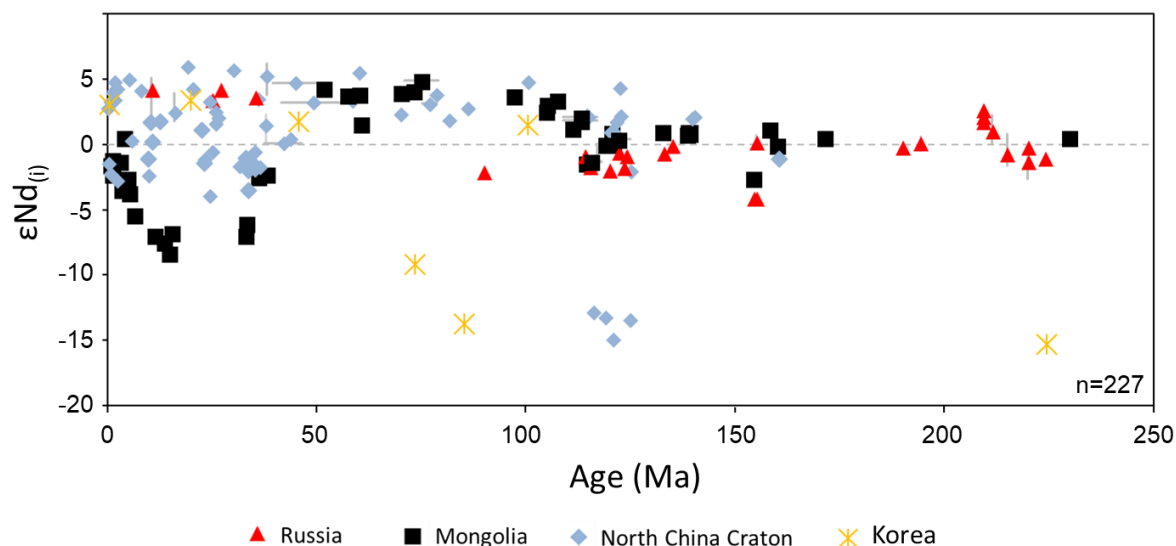


Figure 4.13: $\epsilon\text{Nd}_{(i)}$ vs. Age of the dated Russian, Mongolian, Chinese (North China Craton) and Korean melts. Range bars show the minimum and maximum values (from localities where samples had to be averaged); however, error bars are normally less than the size of the data point. Data from: this study; Pouclet et al. (1994); Sagong et al. (2001); Zhang et al. (2002); Zhang and Zheng (2003); Pei et al. (2004); Johnson et al. (2005); Tang et al. (2006); Vorontsov et al. (2007 A&B); Gao et al. (2008); Liu et al. (2008) and references therein, Zhang et al. (2008); Andryuschenko et al. (2010); Ying et al. (2010); Ho et al. (2011); Wang et al. (2011); Kuang et al. (2012); Xu et al. (2012); Zhang et al. (2012); Chen et al. (2013); Ma et al. (2014; 2016); Zhao et al. (2014); Dash et al. (2015); appendix from Yarmolyuk et al. (2015); Gurvan-Saikhan Range, Borzongiin-Govi depression, Dush Uul, South Gobi Area, Khotgor, Mushgai Well Area, Zuun-Bogd Range, Ikh-Bogd Range, Bayan-Tsagan Range, Khara-Argalant and Dund-Argalant Range, Chandman, Lower Okhon River, Khanui River and Ugii Lake) and Li et al. (2017).

Figure 4.14B ($^{87}\text{Sr}/^{86}\text{Sr}_{(i)}$ vs. $\epsilon\text{Nd}_{(i)}$) separates the Mongolian and Chinese (North China Craton) samples into three categories: (1) <50 Ma; (2) 50-107 Ma and (3) >107 Ma. This figure highlights the similarities between the Mongolian and Chinese samples; although there is some overlap between some of the Chinese samples <50 Ma and those samples between ≥ 50 -107. The Mongolian and Chinese samples >107 Ma form a distinct group.

Assimilation-fractional crystallisation modelling (DePaolo, 1981) results are shown (**Fig. 4.14B**) using sample 07CL09 from Xu et al. (2012) as the initial composition (this sample has high $\epsilon\text{Nd}_{(i)}$ and low $^{87}\text{Sr}/^{86}\text{Sr}_{(i)}$ values). Two different modelled curves are calculated using r -values (assimilation against fractionation rate) of 0.3 and 0.7. The amount of F (mass of magma/initial mass of magma) is shown next to the curves and is in 10% intervals (0-90 %).

The D-values for Sr and Nd are 1.13 and 0.17 respectively (this affects the z-value, where $z = \frac{r+D-1}{r-1}$). A granulite crustal xenolith (TB95-2.5) from Barry et al. (2003) is used as the contaminator.

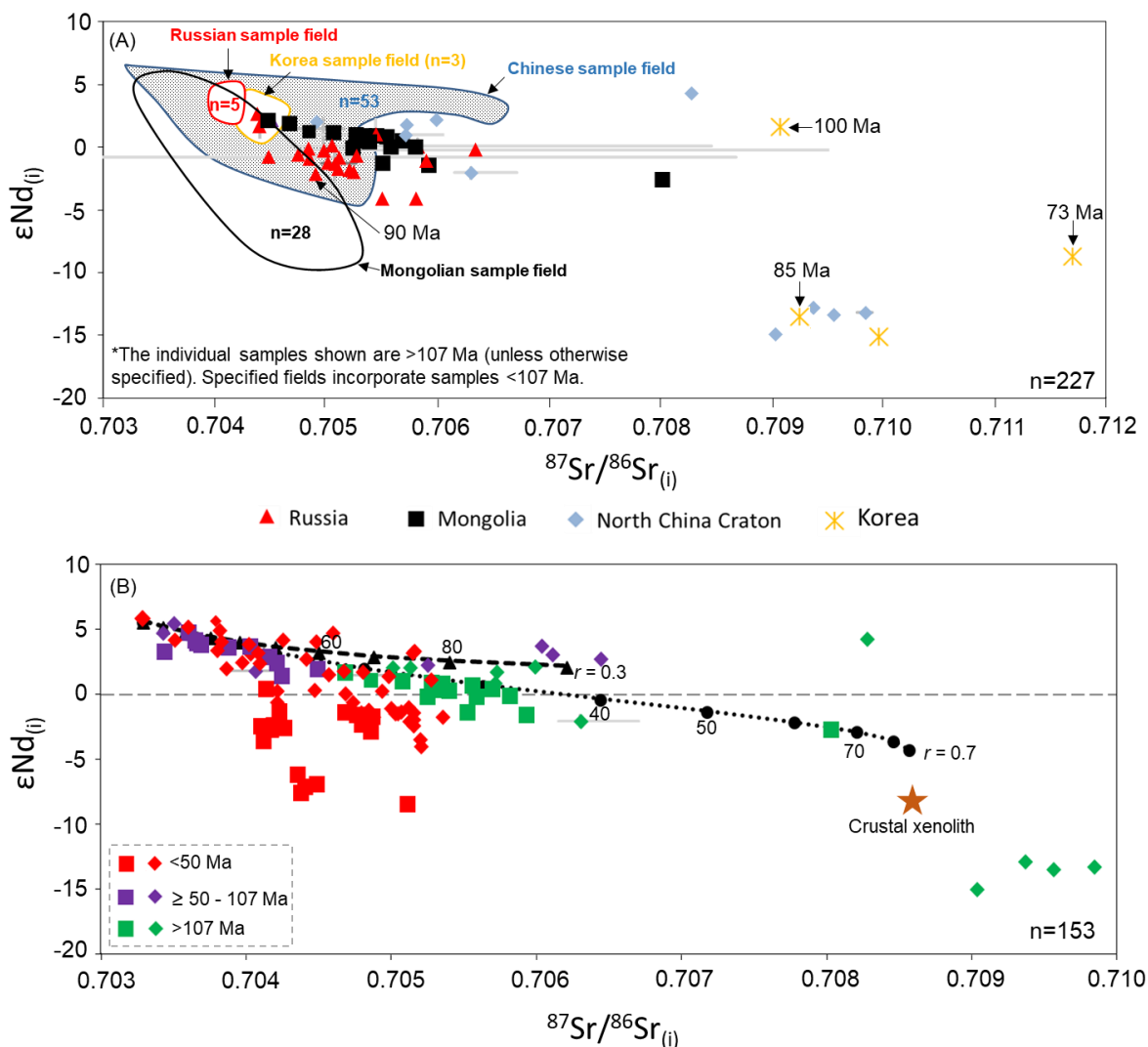


Figure 4.14: (A) $^{87}\text{Sr}/^{86}\text{Sr}_{(i)}$ vs. $\epsilon\text{Nd}_{(i)}$ of the dated Russian, Mongolian, Chinese (North China Craton) and Korean melts. Samples <107 Ma (unless specified) are shown as fields. (B) $^{87}\text{Sr}/^{86}\text{Sr}_{(i)}$ vs. $\epsilon\text{Nd}_{(i)}$ of the dated Mongolian (squares) and North China Craton (diamonds) samples. Range bars show the minimum and maximum values (from localities where samples had to be averaged); however, error bars are normally less than the size of the data point. Data sources are from the same citations stated in the Figure 13 caption. Sample 05MZL13 from Ying et al. (2010) was not included on the diagram ($^{87}\text{Sr}/^{86}\text{Sr}_{(i)} = 0.7145$; $\epsilon\text{Nd}_{(i)} = -1$ and age =160 Ma). (B) Two AFC modelling curves are calculated using the equations from DePaolo (1981) which use an r value (where r signifies assimilation against fractionation rate) of 0.3 and 0.7; D value for Sr and Nd is 1.13 and 0.17 respectively; starting composition is sample 07CL09 (Xu et al. 2012) and the contaminator is a granulite crustal xenolith (TB95-2.5) from Barry et al. (2003). The amount of F (mass of magma/initial mass of magma) is shown as 10% tick marks (0-90 %).

The AFC modelling results indicate that with an r -value of 0.3, a significant amount of magma would have to crystallise (~70-90 %), to go from the starting composition, to a composition like samples that are >107 Ma (Fig. 4.14B). Yet this AFC model would also predict samples to be very enriched in Nd (>200 ppm) after 80% crystallisation (Fig. 4.15)

and is therefore not an adequate explanation. Furthermore, this model has produced $\epsilon\text{Nd}_{(i)}$ values that are still more positive than samples >107 Ma. The AFC modelling curve that uses an r -value of 0.7 (i.e. very highly favours crustal assimilation) suggests that most samples >107 Ma could be explained by $<40\%$ crystallisation (**Fig. 4.14B**). However, whether such a large crustal assimilation rate occurred is questionable (e.g., petrological observations do not report abundant crustal xenoliths). Furthermore, samples <50 Ma have negative $\epsilon\text{Nd}_{(i)}$ (despite having positive ΔNb values) that are greater than the AFC modelling curves – thus this AFC model could only produce the negative $\epsilon\text{Nd}_{(i)}$ values if a contaminator with much greater negative $\epsilon\text{Nd}_{(i)}$ was utilised (yet this contaminator could not have a large negative ΔNb value either). Finally, for the Mongolian samples to go from negative, to positive, and then back to negative $\epsilon\text{Nd}_{(i)}$ values (as the samples young) via crustal assimilation processes alone seems highly unlikely. Therefore, the change in $\epsilon\text{Nd}_{(i)}$ and $^{87}\text{Sr}/^{86}\text{Sr}_{(i)}$ with time is consistent with source variation, varying degrees of asthenospheric input, and to a lesser extent, crustal contamination.

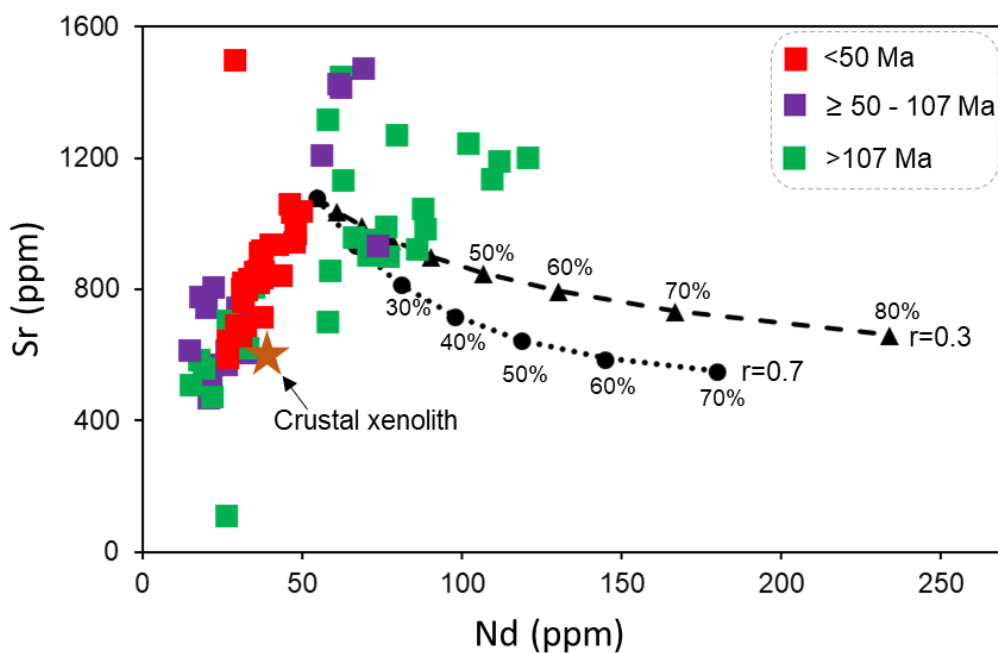


Figure 4.15: Nd vs. Sr (ppm) for the dated Mongolian samples. Additional data from Dash et al. (2015) and Yarmolyuk et al. (2015). Two AFC modelling curves are calculated using the equations from DePaolo (1981) which use an r value (where r signifies assimilation against fractionation rate) of 0.3 and 0.7; D value for Sr and Nd is 1.13 and 0.17 respectively; starting composition is sample 07CL09 (Xu et al. 2012) and the contaminator is a granulite crustal xenolith (TB95-2.5) from Barry et al. (2003). The amount of F (mass of magma/initial mass of magma) is shown as 10% tick marks with labels next to the curves.

The similarities between the Mongolian and North China Craton magmatism with time suggests similar geological processes occurred, perhaps reflecting a related genesis.

4.5.5 Pb isotopes through time and space

Calculated $^{206}\text{Pb}/^{204}\text{Pb}_{(i)}$, $^{207}\text{Pb}/^{204}\text{Pb}_{(i)}$ and $^{208}\text{Pb}/^{204}\text{Pb}_{(i)}$ values for samples from Russia, Mongolia and the North China Craton are compared (Fig. 4.16). Due to limited data the Korean volcanism is omitted from this comparison.

The $^{206}\text{Pb}/^{204}\text{Pb}_{(i)}$ vs. $^{207}\text{Pb}/^{204}\text{Pb}_{(i)}$ values for the Mongolian samples have again been separated into groups based on age (Fig. 4.16A), with samples >107 Ma having higher $^{207}\text{Pb}/^{204}\text{Pb}_{(i)}$ values than those <107 Ma, likely reflecting an enriched source and/or

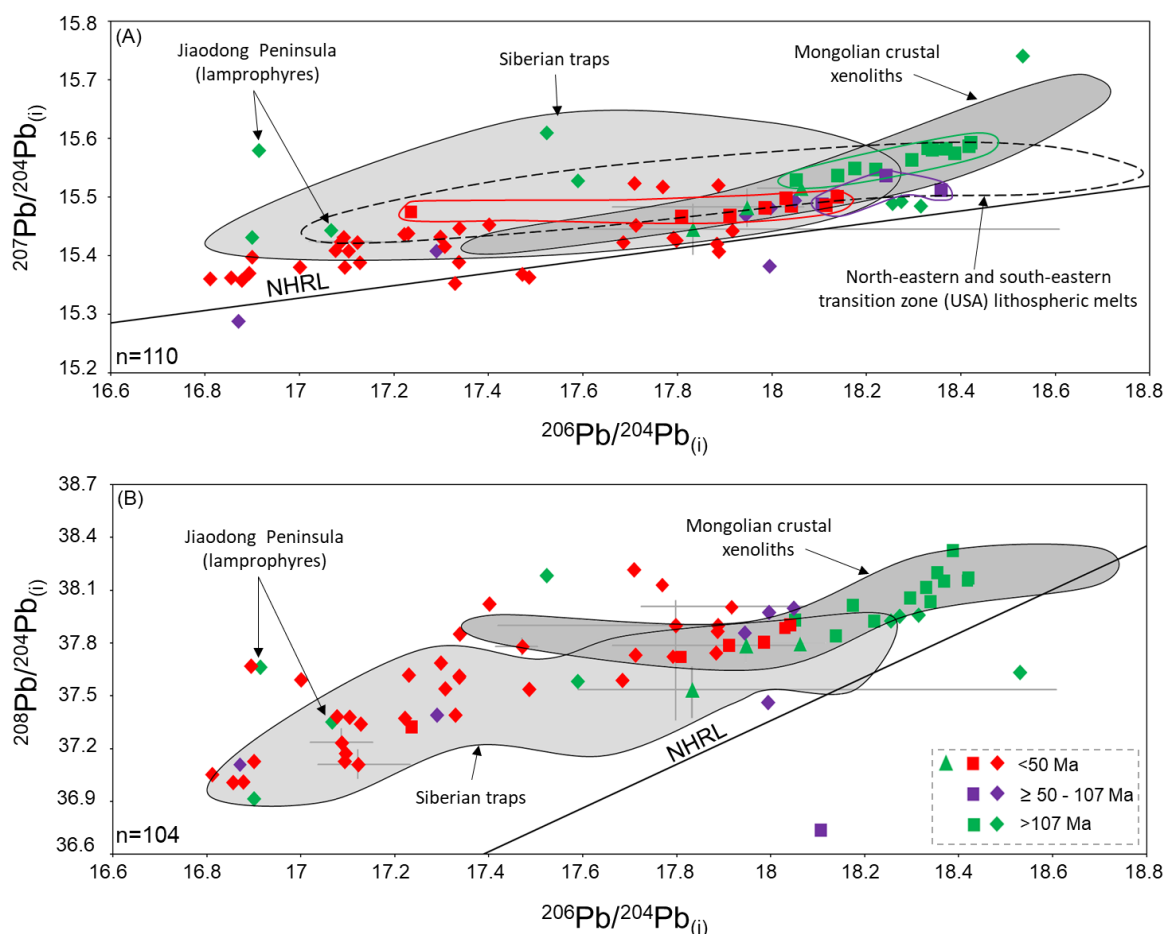


Figure 4.16: (A) $^{206}\text{Pb}/^{204}\text{Pb}_{(i)}$ vs. $^{207}\text{Pb}/^{204}\text{Pb}$ and (B) $^{206}\text{Pb}/^{204}\text{Pb}_{(i)}$ vs. $^{208}\text{Pb}/^{204}\text{Pb}$. Data sources: this study; Zhang et al. (2002); Barry et al. (2003); Zhang and Zheng (2003); Tang et al. (2006); Vorontsov et al. (2007); Ying et al. (2008); Zhang et al. (2008); Ho et al. (2011); Wang et al. (2011); Xu et al. (2012); Zhang et al. (2012); Ma et al. (2014); Zhao et al. (2014); Yarmolyuk et al. (2015). Range bars show the minimum and maximum values. Triangles are Russian samples, squares are Mongolian samples and diamonds are Chinese samples. Siberian traps field from data ($n=53$) within Wooden et al. (1993); north-eastern and south-eastern transition zone (USA) lithospheric melts from data ($n=17$) within Kempton et al. (1991); Mongolian crustal xenolith field from data ($n=11$) within Barry et al. (2003).

possibly more crustal input. The >107 Ma samples have $^{206}\text{Pb}/^{204}\text{Pb}_{(i)}$ vs. $^{207}\text{Pb}/^{204}\text{Pb}_{(i)}$ values similar to lithospheric mantle melts from the Basin-and-Range, USA (Fig. 4.16A; Kempton et al. 1993) and to Mongolian crustal xenoliths (Fig. 4.16A; Barry et al. 2003). The Mongolian samples <50 Ma trend to lower $^{206}\text{Pb}/^{204}\text{Pb}_{(i)}$ values. Other than sample TCS 59.2

(a high-Si adakite which has its petrogenesis discussed in chapter three), the samples >107 Ma are interpreted as lithospheric mantle melts with crustal and asthenospheric input (e.g., Sheldrick et al., 2018). This is consistent with geochemical signatures discussed earlier in this chapter. The distinct groupings for the Mongolian samples is consistent with the interpretation of different sources (e.g., asthenospheric mantle and lithospheric mantle).

The limited data from Russia (Vorontsov et al. 2007; Ust-Sukharinskii, Ulantui, Saranskii, and Zunnemeti fields), which has samples >107 Ma, have lower $^{207}\text{Pb}/^{204}\text{Pb}_{(i)}$ values than the Mongolian samples. The Chinese samples show a range of $^{206}\text{Pb}/^{204}\text{Pb}_{(i)}$ vs. $^{207}\text{Pb}/^{204}\text{Pb}_{(i)}$ values and thus it is not particularly easy to separate different groupings based on age with these radiogenic Pb ratios alone.

The $^{206}\text{Pb}/^{204}\text{Pb}_{(i)}$ vs. $^{208}\text{Pb}/^{204}\text{Pb}_{(i)}$ values for the Mongolian samples (**Fig. 4.16B**) also have distinct groupings (although there is only one sample between 50 and 107 Ma). Notably, the samples >107 Ma have lower $^{208}\text{Pb}/^{204}\text{Pb}_{(i)}$ values than those samples <50 Ma. The Russian samples also have similar $^{208}\text{Pb}/^{204}\text{Pb}_{(i)}$ values to the Mongolian samples despite having a range in $^{206}\text{Pb}/^{204}\text{Pb}_{(i)}$ values. The Chinese samples show a range of $^{206}\text{Pb}/^{204}\text{Pb}_{(i)}$ vs. $^{208}\text{Pb}/^{204}\text{Pb}_{(i)}$ values although many samples >107 Ma have lower ratios than samples <50 Ma – plus two notable outliers from the Jiadong Peninsula are interpreted as asthenospheric mantle melts (Ma et al. 2014) and are thus unusual for this period in the North China Craton.

4.5.6 $\epsilon\text{Hf}_{(i)}$ values through time and space

Calculated $\epsilon\text{Hf}_{(i)}$ values for samples from Russia, Mongolia and the North China Craton are compared (**Fig. 4.17**).

Samples >107 Ma have lower $\epsilon\text{Hf}_{(i)}$ values than the Mongolian asthenospheric mantle derived sample (TB95-7.1.6) at 107 Ma. This difference in $\epsilon\text{Hf}_{(i)}$ values for samples >107 Ma with the asthenospheric sample at ~107 Ma is consistent with source variation and thus supports earlier interpretations. Unfortunately, there is a lack of data to compare samples between 50 and 107 Ma. However, the high $\epsilon\text{Hf}_{(i)}$ values (>8) at ~50 Ma is consistent with asthenospheric mantle input.

The limited Mongolian and North China Craton data possibly indicates that from 50 Ma there is decreasing $\epsilon\text{Hf}_{(i)}$ (as the samples young). The $\epsilon\text{Hf}_{(i)}$ values finally increase again; this is a similar trend to previously discussed $\epsilon\text{Nd}_{(i)}$ values (Fig. 4.13).

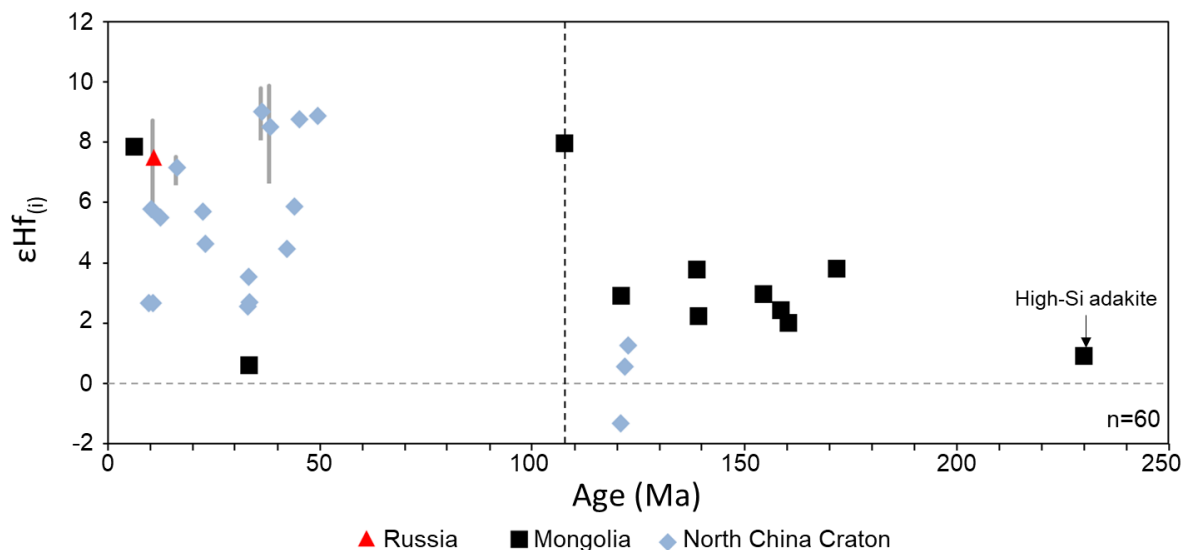


Figure 4.17: $\epsilon\text{Hf}_{(i)}$ vs. Age of the Russian, Mongolian and Chinese (North China Craton) volcanism. Range bars show the minimum and maximum values (from sample localities where data had to be averaged). Vertical dashed line at 107 Ma to indicate start of dominant asthenospheric magmatism. Data sources: this study; Barry et al. (2003); Johnson et al. (2005); Wang et al. (2011); Zhang et al. (2012) Ma et al. (2014, 2016) and Li et al. (2017). Sample JILT-1 (Ma et al. 2014; Jiaodong Peninsula), dated at 120.8 Ma (interpreted from subduction-enriched lithospheric mantle) is excluded for diagram cosmetics ($\epsilon\text{Hf}_{(i)} = -26.4$).

The combination of decreasing $\epsilon\text{Hf}_{(i)}$ and $\epsilon\text{Nd}_{(i)}$ values (between 50-30 Ma) is interesting and indicates increasing lithospheric input. Yet this lithosphere must be different from samples >107 Ma. As discussed in Chapter 2, Cenozoic samples (Mongolian and North China Craton basaltic rocks) have geochemical characteristics consistent with pyroxenite source lithology. Thus, one possible theory is that a switch to pyroxenite source melting occurred in Mongolia ~50 Ma, which was then accompanied by increasing asthenospheric input again (around 30 Ma), as the volcanism gets younger.

The lack of Hf isotope data on the Russian volcanism makes comparison studies through time difficult – the Russian Cenozoic samples from Vitim have positive $\epsilon\text{Hf}_{(i)}$ consistent with asthenospheric mantle input (Johnson et al. 2005).

4.6. DISCUSSION

4.6.1 Comments on the mantle plume hypothesis

Yarmolyuk et al. (2015) propose that a mantle plume is responsible for continuous Mesozoic and Cenozoic magmatism across the South Khangai Volcanic Region (SKVR). Here I take the opportunity to discuss the following statements in this article:

- (1) Volcanism in the SKVR was in an intraplate setting separated from other volcanic fields in Central Asia.
- (2) “The occurrence of chains of magmatic fields correspond to systematic migrations of magmatic centres during the region evolution” (Yarmolyuk et al., 2015). In other words, the mantle plume hypothesis predicts systematic age successions due to a lithospheric slab migrating over the plume.

To aid this discussion it is useful to include the sketch map from Yarmolyuk et al. (2015) which proposes a temporal migration of volcanic centres (**Fig. 4.18**).

The closure of the Mongol-Okhotsk Ocean occurred sometime between the Late Jurassic (~155 Ma) and beginning of the Early Cretaceous (~120 Ma) (e.g., Zonenshain et al., 1990; Kravchinsky et al., 2002; van der Voo et al., 2015) and therefore the SKVR was likely in an intraplate setting which agrees with statement 1.

However, this chapter has demonstrated that there is much geochemical similarity between the Mesozoic volcanism in the North China Craton and central Mongolia. To summarise:

- Most volcanism >107 Ma in the North China Craton and Mongolia has geochemical signatures (see sections 4.5.2-4.5.6) consistent with a subcontinental lithospheric mantle source (e.g., low ΔNb , high $^{87}Sr/^{86}Sr_{(i)}$, low $\epsilon Nd_{(i)}$ and low $\epsilon Hf_{(i)}$). Both Mongolia and the North China Craton has evidence for increasing asthenospheric input throughout the Mesozoic (e.g., **Fig. 4.9 & 4.11**).
- A dramatic switch to asthenospheric volcanism occurs in both Mongolia and the North China Craton at ~107 Ma (**Fig. 4.9-4.17**).
- Both Mongolia and the North China Craton show changes in geochemical signatures at around 50 Ma (e.g., **Fig. 4.13, 4.14 & 4.17**).

The remarkable geochemical similarities between the Mesozoic volcanism in Mongolia and the North China Craton indicates that there may be a related genesis. Therefore, I reject the hypothesis that the volcanism in the SKVR is completely independent from other volcanic fields in Central Asia. Furthermore, the appearance of asthenospheric melts in Mongolia and the North China Craton at a similar time interval suggests some large-scale

process was responsible for asthenospheric upwelling because distances between asthenospheric magmatism >1600 km - this leads to the discussion of statement 2.

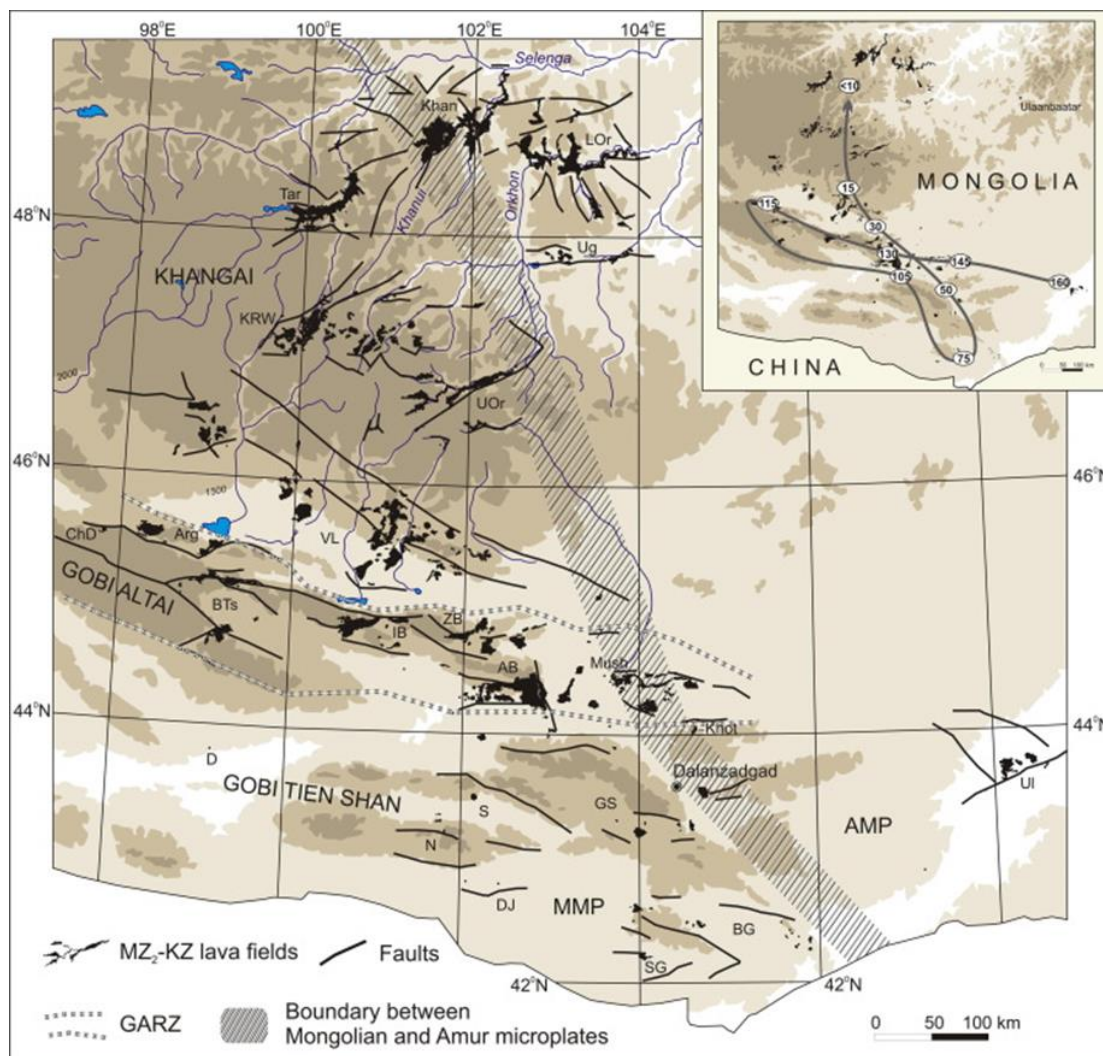


Figure 4.18: Sketch map from Yarmolyuk et al. (2015) of Mongolian volcanic fields; Inset diagram shows the temporal migration of volcanic centres.

Yarmolyuk et al. (2015) propose that there is a temporal migration of volcanic centres across Central Mongolia (**Fig. 4.18**; see the insert figure). As discussed previously, there is magmatism >107 Ma in both central and eastern Mongolia with a lithospheric mantle source signature. The new ^{40}Ar - ^{39}Ar dates (**Fig. 3.7 & 4.4**) show that (**Fig. 4.5**) if this volcanism is linked, then the age distribution of Mesozoic volcanism disagrees with the migration path proposed by Yarmolyuk et al. (2015). Furthermore, if we accept that the Mesozoic volcanism in both the North China Craton and Mongolia share a related genesis then this contests the migration path proposed by Yarmolyuk et al. (2015).

Finally, a proposed temporal migration of volcanic centres, due to a stationary mantle plume (hot spot), does not agree with plate reconstructions (e.g., Wu et al. 2017; **Fig. 1.5**).

Overall, the mantle plume hypothesis proposed by Yarmolyuk et al. (2015) would not work with a regional magmatic model (e.g., Sheldrick et al., 2018) and does not agree with plate reconstruction models (e.g., Wu et al., 2017).

4.6.2 Towards an integrated model for the Mesozoic volcanism

Mesozoic volcanism occurs in both Mongolia and the North China Craton during, or after, the closure of the Mongol-Okhotsk Ocean and the Palaeo-Asian Ocean (e.g., Zorin, 1999; Chen et al., 2000; Chen et al., 2009; Windley et al., 2010; Seton et al., 2012). Such large-scale ocean closures likely metasomatised overlying lithospheric mantle. Much of the Mesozoic volcanism >107 Ma in Mongolia and the North China Craton is interpreted to be derived from subduction-enriched subcontinental lithospheric mantle (e.g., Gao et al., 2008; Liu et al., 2008; Ma et al., 2014; Sheldrick et al., 2018). The proximity of this >107 Ma volcanism to either the Mongol-Okhotsk Suture or Solonker Suture possibly reflects modified lithospheric mantle from these ocean closures.

If there was southward subduction of the Mongol-Okhotsk slab it is unclear how far it extended. However, the Mongol-Okhotsk suture is closer (<500 km) to Mongolian Mesozoic magmatism than the Palaeo-Pacific slab (>2000 km) where models invoke great distances of flat-subduction (e.g., Bars et al. 2018). New seismic evidence has been used to interpret a southward-dipping slab associated with the Palaeo-Asian Oceanic slab (Zhang et al. 2018) and the north-dipping thrust belt in the Baolidao belt indicates contemporaneous north-dipping convergence (Xiao et al., 2003). The combined subducted slabs of the Mongol-Okhotsk and Palaeo-Asian oceans could help isolate volcanism by controlling lithospheric architecture and how any upwelling mantle disperses (e.g., Barry et al., 2017).

The Mongolian and North China Craton Mesozoic magmatism has a geochemical signature consistent with increasing asthenospheric input with time, and a gradual stripping of the lithosphere (**Fig. 4.7-4.9** & Sheldrick et al. 2018, and references therein). Finally, this lithosphere was stripped enough at ~107 Ma for asthenospheric magmatism to dominate in both Mongolia and the North China Craton (**Fig. 4.9-4.7**).

Numerical modelling of convective erosion and peridotite melt interaction was done by He (2014) which discussed possible implications for destruction of the North China Craton. In

this model, to explain the most abundant volcanism (135-115 Ma), the formation of an extensive mantle wedge is required, due to a stagnating Pacific plate beneath the North China Craton. Slab dehydration would then reduce the viscosity of the asthenosphere and may result in small-scale upwellings within the upper mantle and convection of the mantle wedge. As the asthenosphere ascends, it may cause compression of the rheological boundary layer and consequently increases the temperature gradient within this layer. This convection and excess heat causes lithospheric thinning. The lowering of melting temperature by peridotite-melt interaction can help accelerate lithospheric thinning and, when combined with convective erosion, can result in significant thinning of a cratonic lithosphere (e.g., with a mantle viscosity of 10^{18} - 10^{19} Pa s and a peridotite melting temperature of 1000-1100°C a lithosphere could be thinned over tens of millions of years but at normal asthenospheric temperatures). In such a model, a combination of vigorous upper mantle convection, peridotite-melt interaction and local delamination results in abundant magmatism and lithospheric thinning (He, 2014, 2015).

However, could the model by He (2014) be applied to a stagnating Mongol-Okhotsk and/or Palaeo-Asian Ocean slab too? Zircon $^{206}\text{Pb}/^{238}\text{U}$ data constrain the final closure of the Palaeo-Asian Ocean to be between 296 and 234 Ma (Chen et al., 2009). While the closure of the Mongol-Okhotsk Ocean occurred sometime between the Late Jurassic (~155 Ma) and beginning of the Early Cretaceous (~120 Ma) (e.g., e.g., Zonenshain et al., 1990; Kravchinsky et al., 2002; van der Voo et al., 2015).

Slab dehydration would likely have occurred when the Mongol-Okhotsk and Palaeo-Asian Ocean slabs were subducting. Palaeomagnetic data suggests that the Mongol-Okhotsk ocean was 4700 km wide in the late Permian (Kravchinsky et al. 2002) and thus there would have been much subduction and potentially lots of slab dehydration.

Minimal volcanism occurred in Mongolia and the North China Craton >150 Ma compared with ~135-107 Ma. The volcanism >150 Ma would have traversed through a thick lithosphere, which may have inhibited high-degree partial melting and melt migration to the surface (e.g., Xu, 2001; Sheldrick et al. 2018). This thick lithosphere may have also helped prevent back-arc spreading and lithospheric extension (He, 2014).

During the most abundant Mesozoic magmatism in Mongolia and the North China Craton (135-115 Ma) there was possibly the combined effect of multiple dehydrating slabs associated with the Mongol-Okhotsk, Palaeo-Asian and Izanagi subduction which may have also controlled asthenospheric upwelling dispersal. Thus, a model is proposed where all these slabs are dehydrating together, which reduces the mantle viscosity, resulting in vigorous convection and lithospheric thinning. The closure of the Mongol-Okhotsk Ocean may also have provided the necessary conditions for delamination processes in Mongolia.

From ~107-50 Ma asthenospheric magmatism dominated in Mongolia and the North China Craton. What caused these asthenospheric upwellings is uncertain. Whether it is possible for slab roll-back, from the Palaeo-Pacific plate, to trigger largescale asthenospheric upwelling in Mongolia and the North China Craton would make for interesting future research work. Cenozoic basalts in the North China Craton, such as in the Bohai Bay Basin, have attributed slab roll-back and lithospheric thinning to their genesis (e.g., He, 2014). However, the Cenozoic volcanism in Mongolia is >1500 km away from the Bohai Bay Basin (about the same distance as London to Rome).

CHAPTER 5

CONCLUDING REMARKS AND FURTHER WORK

5.1. OVERALL THESIS CONCLUSIONS

Chapter two used major- and trace-element data, Sr-Nd-Pb-Hf isotopes and $^{40}\text{Ar}/^{39}\text{Ar}$ radiometric dating analysis results to conduct a detailed localised investigation on Mesozoic volcanism from the Gobi Altai. This chapter tested for a change in the depth of melting by considering changes in the garnet signature with time and incorporated non-modal batch melt modelling results. Additionally, Zn/Fe ratios were also utilised to consider changes in magmatic processes through time (depth of melting/metasomatism/source composition). These results were also compared with Cenozoic volcanic samples from the Basin-and-Range (USA), and Western Anatolia (Turkey), to compare magmatism from similar geodynamic scenarios. Furthermore, FC3MS values were used to consider the involvement of pyroxenite as a source rock for Mongolian and Chinese Mesozoic and Cenozoic samples. This chapter concluded that the Gobi Altai volcanism had geochemical signatures consistent with a metasomatised SCLM being stripped away and increasing involvement from the asthenospheric mantle through time. The FC3MS values suggested that the Mongolian Cenozoic volcanism might be from a pyroxenite source, while results were inconclusive for the Mesozoic volcanism.

Chapter three introduced new low-Si and high-Si adakites south of the Mongol-Okhotsk suture. The low-Si adakites are interpreted as being derived from a lithospheric mantle wedge that has undergone metasomatism by slab melts. This mantle was likely metasomatised by a southward-subducting Mongol-Okhotsk slab associated with the closure of the Mongol-Okhotsk Ocean. However, the fractionation of late-stage accessory minerals, such as zircon and apatite caused the adakite-like HREE depletion. Two alternative models were proposed to explain the petrogenesis of the high-Si adakite samples: (1) a southward-subducting Mongol-Okhotsk slab underwent partial melting during the closure of the Mongol-Okhotsk Ocean with minor assimilation of mantle and crustal material; or (2) basaltic underplating of a thickened (>50 km; >1.5 GPa), eclogite lower crust, foundered into the underlying mantle, assimilated minor mantle material and finally underwent crustal contamination. This chapter also introduced new Mesozoic

shoshonitic and high-K trachyandesite lavas with arc-like geochemical signatures (collectively referred to as Group 1). Overall, this chapter argues that a southward-subducting Mongol-Okhotsk slab contributed to magmatic processes by causing metasomatism of the overlying lithosphere and controlling the dispersal of magmatic upwelling.

Chapter four used an extensive compilation of radiometric dated volcanic samples from Eastern Asia (Russia, Mongolia, NCC and NE China, and Korea) to assess geochemical source variations throughout the Mesozoic and Cenozoic. This chapter aimed to bring the conclusions from previous chapters and consider what this might mean more regionally for East Asian Mesozoic and Cenozoic volcanism. New major- and trace-element data, Sr-Nd-Pb-Hf isotopes and $^{40}\text{Ar}/^{39}\text{Ar}$ radiometric dating analysis was done on volcanic rocks collected from central and eastern Mongolia. Volcanism from Mongolia and the NCC share similar geochemical characteristics through time – with Mesozoic magmatism >107 Ma being predominantly derived from a metasomatised SCLM and has lower ΔNb , $\epsilon\text{Nd}_{(t)}$, $\epsilon\text{Hf}_{(t)}$ and higher $^{87}\text{Sr}/^{86}\text{Sr}_{(t)}$ values than volcanism between ~107-50 Ma from the asthenospheric mantle. AFC modelling indicates that it is unlikely that crustal contamination produced these geochemical signatures. Furthermore, the geochemistry indicates increasing asthenospheric input throughout the Mesozoic (~220-107 Ma), with the lithosphere being stripped away enough by 107 Ma for asthenospheric mantle derived magmatism to predominate. The removal of SCLM and presence of asthenospheric volcanism at ~107 Ma under Mongolia, NE China and the NCC indicates holistic processes for Mesozoic magmatism and is inconsistent with the mantle plume migration path previously proposed for Mongolia (Yarmolyuk et al., 2015). Whether a switch to asthenospheric magmatism happened in Eastern Russia at the same time remains unclear, nevertheless, the removal of SCLM in Eastern Russia during the Mesozoic might reflect large-scale holistic processes in Eastern Asia. Such stripping of SCLM and increasing asthenospheric input would be consistent with a model invoking convective erosion (and localised delamination) above multiple subducted slabs (bi-modal Mongol-Okhotsk slabs, bi-modal Palaeo-Asian slabs and Palaeo-Pacific slab). These subducted slabs could have trapped and controlled the dispersal of Mesozoic asthenospheric upwelling across Eastern Asia; but what drove such large-scale Mesozoic asthenospheric upwelling remains uncertain.

5.2. FURTHER WORK

5.2.1 *Constraining Mesozoic magmatism across Eastern Asia*

To further assess whether a switch to asthenospheric magmatism occurred at a similar time in Russia (~107 Ma) like Mongolia and Northern China, better age constraints are required on the Mesozoic Russian magmatism. At present, most dating techniques on the Russian Mesozoic magmatism utilise K-Ar and Rb-Sr isochron techniques (see chapter 1 and 4) which are susceptible to erroneous results due to sample alteration processes. For example, two Mesozoic volcanic samples from the Russian Khilok graben (Motninskoe) have negative ΔNb values (dated by K-Ar techniques; 90 and 71 Ma) unlike samples from Mongolia and Northern China (see chapter 4). However, it's difficult to assess whether these two anomalous samples are valid due to the susceptibility of K-Ar dating techniques to alteration processes.

By extension, research from Yarmolyuk et al. (2015) and Bars et al. (2018) utilised K-Ar dating techniques on Mesozoic samples from central Mongolia. It's the view of this author, that utilising such dating methods on rocks which have likely undergone alteration should be avoided. This statement is significant considering researchers use these dating results to account for precise magmatic age progression models (e.g., Wang et al., 2006a; Yarmolyuk et al. 2015).

Furthermore, models advocating Mesozoic Palaeo-Pacific slab roll-back (e.g., Ma et al., 2014; Bars et al., 2018) focus on magmatism from eastern Russia, Mongolia and the North China Craton. Such a model would predict an age progression, with a younging direction eastwards for Mesozoic volcanism (e.g., from oldest to youngest: Mongolia, China, and North Korea). This study did not identify any obvious age progression (Chapter 4). However, a major drawback from testing this model is the lack of data from North Korea. Therefore, to better constrain regional (and local) magmatic processes, much work could be done on constraining the timing of North Korean volcanism (e.g., see Wang et al., 2006a).

5.2.2 *Additional Hf isotope analysis*

Chapter 4 compared Hf isotope analysis versus the age of volcanic samples from across Eastern Asia - the advantage of using this isotope system is its robustness to mobility

processes (e.g., Barry et al., 2006). However, very little data is available compared to Sr-Nd-Pb isotope systems. This is particularly true for Eastern Russia, where no Hf isotope results were found in the literature for Mesozoic samples and only limited data for the Cenozoic (i.e., just volcanic samples from Vitim volcanic field). With regards to Mongolia and the North China Craton, there is no existing Hf data for volcanic samples between 106-50 Ma. In Mongolia, I constrain a switch to asthenospheric-dominated volcanism at 107 Ma, with the Hf data, with samples from Tsost Magmatic Field. However, further analysis could be done on samples from Dych Gol (Dash et al., 2015; ^{40}Ar - ^{39}Ar dating) to further confirm this switch at around 107 Ma in eastern Mongolia.

$\epsilon\text{Nd}_{(t)}$ isotopes versus age show a U-shaped trend for Mongolian Cenozoic samples (chapter 4; **Fig. 4.17**). This trend may also be evident in the $\epsilon\text{Hf}_{(t)}$ isotopes (the limited sample data is consistent with this trend; $n=2$). However, more data is required to assess this. Furthermore, a lot of Cenozoic samples from Mongolia were collected north of the Mongol-Okhotsk suture reflecting a different terrane amalgamation to southern Mongolia. Overall, a more regional analysis is required to test whether this U-shaped trend simply reflects melting from a different terrane source composition, or reflects changes in melting processes, or both.

5.2.3 Constraining the style and closure time of the Mongol-Okhotsk Ocean

How and when the Mongol-Okhotsk Ocean closed is still an ongoing research question (see Fritzell et al., 2015 for a good overview). Current palaeogeographic reconstructions (e.g., Van der Voo et al., 2015) attempt to model how this ocean closed despite not knowing where the Mongol-Okhotsk suture terminates in western/central Mongolia. Therefore, an exciting project would involve detailed investigations trying to identify/confirm the true extent of the Mongol-Okhotsk suture. Often, these first-principle investigations discover other important scientific results too and it's the view of this author, that constraining how and when the Mongol-Okhotsk Ocean closed is one of the biggest geological scientific questions remaining to be answered for East Asian tectonics.

5.2.4 Modelling magmatic upwelling from slab roll-back processes

How far from a flat-slab roll-back process can asthenospheric upwelling be generated? For Mesozoic asthenospheric upwelling to have occurred in central Mongolia (e.g., see chapter

2 for more details) from Palaeo-Pacific slab roll-back, asthenospheric upwelling would be occurring >2000 km from the Palaeo-Pacific active margin and likely significant distances from the subducted flat-slab edge. Today, one of the most studied extensive flat-slabs is that associated with the Nazca Ridge (Inca Plateau), which has a length of ~1500 km (e.g., Huangfu et al., 2016); however, this flat-slab is young (43-30 Ma) which is favourable for flat-slab generation processes. Just how far can a flat-slab extend, and is it possible to model just how far asthenospheric upwelling can be generated, from the slab edge, during slab roll-back processes? Furthermore, would such a process explain the Cenozoic asthenospheric upwellings in Eastern Asia too? The next stage of testing this East Asian magmatic slab roll-back model would benefit from a combined geochemical study and numerical modelling approach.

Further geochemical work could focus on intraplate volcanism from the border of China/North Korea (e.g., the Changbaishan volcanic field; see Guo et al., 2018 for a good review). The Changbaishan volcanic field (CHVF) represents the largest active volcanic system in an intraplate setting in NE Asia. From a geodynamic point, the CHVF is ca. 1400 km west of the Japan Trench, where the Pacific plate subducts beneath the eastern Eurasian continent and becomes stagnant in the mantle transition zone. The CHVF, according to seismic studies (Huang and Zhao, 2006) is situated above the Pacific flat-slab. The unusual geodynamic setting of the CHVF makes it an ideal laboratory for understanding the interplays between the subducted slab and continental intraplate volcanism. Therefore, the CHVF would be useful for comparative purposes.

Abbreviation list

AFC: Assimilation-fractional crystallisation

CAOB: Central Asian Orogenic Belt

CAB: Continental arc basalt

CHVF: Changbaishan volcanic field

HFSE: High-field strength element

HMA: High-magnesium andesite

HREE: Heavy rare earth element

HSA: High-Si adakite

LILE: Large-ion lithophile element

LREE: Light rare earth element

LOI: Loss on ignition

LSA: Low-Si adakite

MORB: Mid-ocean ridge basalt

MOS: Mongol-Okhotsk suture

NCC: North China Craton

N-MORB: Normal mid-ocean ridge basalt

OIB: Ocean island basalt

REE: Rare-earth element

SCLM: Subcontinental lithospheric mantle

SI: Saturation index

Equation list

Equation 1:

Mg-number: $100 \times \left(\frac{\text{MgO}}{40.3}\right) / \left(\left(\frac{\text{MgO}}{40.3}\right) + \left(\frac{\text{FeO}}{71.85}\right)\right)$. FeO is calculated using a $\text{Fe}_2\text{O}_3/\text{FeO}$ ratio of 0.2: $\text{FeO} = \left(\frac{\text{Fe}_2\text{O}_3(\text{T})}{\left(1 + \left(\frac{0.2}{1.111}\right)\right)}\right) / 1.111$.

Equation 2: Fitton et al. (1991)

Saturation Index: $100(\text{Si} - (\text{Al} + \text{Fe}_2 + \text{Mg} + 3\text{Ca} + 11\text{Na} + 11\text{K} + \text{Mn} - \text{Fe}_3 - \text{Ti} - 4\text{P})/2)$ where Si, Al etc. are weight percent oxides divided by their respective molecular weights

Equation 3: Neumann et al. (1954)

Rayleigh fractional crystallisation modelling: $\frac{C_l}{C_o} = F^{D-1}$. C_l = trace element concentration in the liquid (melt). C_o = trace element concentration in the original rock before melting began. F = Wt. fraction of melt produced = melt/(melt + rock).

Equation 4: DePaolo (1981)

AFC trace element modelling equation: $\frac{C_m}{C_m^0} = F^{-z} + \left(\frac{r}{r-1}\right) \frac{C_a}{zC_m^0} (1 - F^{-z})$.

Equation 5: DePaolo (1981)

AFC isotope modelling equation: $\varepsilon_m = \frac{\left(\frac{r}{r-1} \frac{C_a}{z} (1-F^{-z}) \varepsilon_a + C_m^0 F^{-z} \varepsilon_m^0\right)}{\frac{r}{r-1} \frac{C_a}{z} (1-F^{-z}) + C_m^0 F^{-z}}$

Equation 4 and 5 (AFC modelling equations): where C_m^0 is the element concentration of the initial magma prior to fractionation and assimilation, C_a is the element concentration of the contaminator and C_m is the concentration of the element in the magma after AFC. ε_a is the isotope ratio of the wallrock, ε_m^0 is the isotope ratio of the original magma and

ε_m is the isotope ratio concentration after AFC. Where r represents assimilation/fractionation ratio and F = mass of magma/initial mass of magma.

Equation 6: Sheldrick et al. (2018)

Bulk crustal assimilation: $Ca = \frac{(Cp \times 100) + (CC \times \% \text{ volume assimilated})}{(100 + \% \text{ volume of CC assimilated})}$. Where Ca is the composition of the lava after assimilation, Cp is the composition of the parental lava and CC is the composition of the contaminant.

Equation 7: Shaw (1970)

Non-modal batch melting: $\frac{C_l}{C_o} = \frac{1}{(D_o + F(1-P))}$. Where C_l is the concentration in the liquid, C_o is the concentration in the solid, D_o is the bulk partition coefficient at the onset of melting, F is the weight fraction of melt formed and P is the bulk partition coefficient of phases entering the melt.

Equation 8: Yang and Zhou (2013)

FC3MS = $\text{FeO}_T/\text{CaO} - 3 \times \text{MgO}/\text{SiO}_2$. Where the oxides are in Wt. %.

Equation 9: Niu et al. (1999)

$Y^{72} = Y_{Data} + \sum_{n=1}^N M_n (X_{72}^n - X_{Data}^n)$. Where n refers to the n^{th} term of the polynomial equation.

Equation 10: Davidson et al. (2012)

$\frac{Dy}{Dy^*} = \frac{Dy_n}{La_n^{4/13} Yb_n^{9/13}}$. Where n = chondrite normalised.

Equation 11: Fitton et al. (1997)

$$\Delta\text{Nb values } (\Delta\text{Nb} = 1.74 + \log (\text{Nb}/\text{Y}) - 1.92 \log (\text{Zr}/\text{Y}))$$

Reference list

- Aldanmaz, E., J. A. Pearce, M. F. Thirlwall, and J. G. Mitchell. "Petrogenetic evolution of late Cenozoic, post-collision volcanism in western Anatolia, Turkey." *Journal of Volcanology and Geothermal Research* 102, no. 1 (2000): 67-95.
- Andryushchenko, S.V., Vorontsov, A.A., Yarmolyuk, V.V. and Sandimirov, I.V., 2010. Evolution of Jurassic–Cretaceous magmatism in the Khambin volcanotectonic complex (western Transbaikalia). *Russian Geology and Geophysics*, 51(7), pp.734-749.
- Aguillón-Robles, A., Calmus, T., Benoit, M., Bellon, H., Maury, R.C., Cotten, J., Bourgois, J. and Michaud, F., 2001. Late Miocene adakites and Nb-enriched basalts from Vizcaino Peninsula, Mexico: Indicators of East Pacific Rise subduction below southern Baja California?. *Geology*, 29(6), pp.531-534.
- Atherton, M.P. and Petford, N., 1993. Generation of sodium-rich magmas from newly underplated basaltic crust. *Nature*, 362(6416), p.144.
- Badarch, G., Cunningham, W.D. and Windley, B.F., 2002. A new terrane subdivision for Mongolia: implications for the Phanerozoic crustal growth of Central Asia. *Journal of Asian Earth Sciences*, 21(1), pp.87-110.
- Baksi. 2006. Guidelines for assessing the reliability of $^{40}\text{Ar}/^{39}\text{Ar}$ plateau ages: Application to ages relevant to hotspot tracks. DOI: <http://www.mantleplumes.org/ArAr.html>
- Bars, A., Miao, L., Fochin, Z., Baatar, M., Anaad, C. and Togtokh, K., 2018. Petrogenesis and tectonic implication of the Late Mesozoic volcanic rocks in East Mongolia. *Geological Journal*.
- Barry, T.L., 1999. *Origins of Cenozoic basalts in Mongolia: a chemical and isotope study* (Doctoral dissertation, Geology).
- Barry, T.L., Davies, J.H., Wolstencroft, M., Millar, I.L., Zhao, Z., Jian, P., Safonova, I. and Price, M., 2017. Whole-mantle convection with tectonic plates preserves long-term global patterns of upper mantle geochemistry. *Scientific reports*, 7(1), p.1870.
- Barry, T.L., Pearce, J.A., Leat, P.T., Millar, I.L. and Le Roex, A.P., 2006. Hf isotope evidence for selective mobility of high-field-strength elements in a subduction setting: South Sandwich Islands. *Earth and Planetary Science Letters*, 252(3-4), pp.223-244.
- Barry, T. L., Saunders, A. D., Kempton, P. D., Windley, B. F., Pringle, M. S., Dorjnamjaa, D., & Saandar, S. (2003). Petrogenesis of Cenozoic basalts from Mongolia: evidence for the role of asthenospheric versus metasomatized lithospheric mantle sources. *Journal of Petrology*, 44(1), 55-91.
- Barry, T.L., Ivanov, A.V., Rasskazov, S.V., Demonterova, E.I., Dunai, T.J., Davies, G.R. and Harrison, D., 2007. Helium isotopes provide no evidence for deep mantle involvement in widespread Cenozoic volcanism across Central Asia. *Lithos*, 95(3), pp.415-424.
- Batkishig, B., Noriyoshi, T. and Greg, B., 2010. Magmatism of the Shuteen Complex and Carboniferous subduction of the Gurvansaikhan terrane, South Mongolia. *Journal of Asian Earth Sciences*, 37(5-6), pp.399-411.
- Bea, F., Pereira, M.D. and Stroh, A., 1994. Mineral/leucosome trace-element partitioning in a peraluminous migmatite (a laser ablation-ICP-MS study). *Chemical Geology*, 117(1-4), pp.291-312.
- BEARD, J.S. and LOFGREN, G.E., 1991. Dehydration melting and water-saturated melting of basaltic and andesitic greenstones and amphibolites at 1, 3, and 6. 9 kb. *Journal of Petrology*, 32(2), pp.365-401.
- Bennett, S.L., Blundy, J. and Elliott, T., 2004. The effect of sodium and titanium on crystal-melt partitioning of trace elements. *Geochimica et Cosmochimica Acta*, 68(10), pp.2335-2347.

- Berzina, A.P., Gimon, V.O., Nikolaeva, I.V., Paleskii, S.V. and Travin, A.V., 2009. Basites of the polychronous magmatic center with the Erdenetiyn-Ovoo porphyry Cu-Mo deposit (northern Mongolia): petrogeochemistry, $^{40}\text{Ar}/^{39}\text{Ar}$ geochronology, geodynamic position, and related ore formation. *Russian Geology and Geophysics*, 50(10), pp.827-841.
- Bird, Peter. "Initiation of intracontinental subduction in the Himalaya." *Journal of Geophysical Research: Solid Earth* 83.B10 (1978): 4975-4987.
- Blundy, J.D., Robinson, J.A.C. and Wood, B.J., 1998. Heavy REE are compatible in clinopyroxene on the spinel lherzolite solidus. *Earth and Planetary Science Letters*, 160(3), pp.493-504.
- Bradshaw, T.K., Hawkesworth, C.J. and Gallagher, K., 1993. Basaltic volcanism in the Southern Basin and Range: no role for a mantle plume. *Earth and Planetary Science Letters*, 116(1-4), pp.45-62.
- Bryant, J.A., Yogodzinski, G.M. and Churikova, T.G., 2011. High-Mg# andesitic lavas of the Shisheisky Complex, Northern Kamchatka: implications for primitive calc-alkaline magmatism. *Contributions to Mineralogy and Petrology*, 161(5), pp.791-810.
- Castillo, Paterno R. "An overview of adakite petrogenesis." *Chinese science bulletin* 51, no. 3 (2006): 257-268.
- Chakraborty, K.R., 1980. On the evolution of the nepheline to hypersthene normative alkali basaltic rocks of Kuantan, Pahang, Peninsular Malaysia. *Geological Society of Malaysia Bulletin*, 13, pp.79-86.
- Chen, B., Jahn, B.M., Wilde, S. and Xu, B., 2000. Two contrasting Palaeozoic magmatic belts in northern Inner Mongolia, China: petrogenesis and tectonic implications. *Tectonophysics*, 328(1-2), pp.157-182.
- Chen, B., Jahn, B.M. and Suzuki, K., 2013. Petrological and Nd-Sr-Os isotopic constraints on the origin of high-Mg adakitic rocks from the North China Craton: Tectonic implications. *Geology*, 41(1), pp.91-94.
- Chen, B., Jahn, B.M. and Tian, W., 2009. Evolution of the Solonker suture zone: constraints from zircon U–Pb ages, Hf isotopic ratios and whole-rock Nd–Sr isotope compositions of subduction-and collision-related magmas and forearc sediments. *Journal of Asian Earth Sciences*, 34(3), pp.245-257.
- Chen, S.S., Fan, Q.C., Zhao, Y.W. and Shi, R.D., 2013. Geochemical characteristics of basalts in Beilike area and its geological significance, Inner Mongolia. *Acta Petrologica Sinica*, 29(8), pp.2695-2708.
- Chen, L.H. and Zhou, X.H., 2005. Subduction-related metasomatism in the thinning lithosphere: Evidence from a composite dunite-orthopyroxenite xenolith entrained in Mesozoic Laiwu high-Mg diorite, North China Craton. *Geochemistry, Geophysics, Geosystems*, 6(6).
- Chen, Y., Xu, B., Zhan, S. and Li, Y., 2004. First mid-Neoproterozoic palaeomagnetic results from the Tarim Basin (NW China) and their geodynamic implications. *Precambrian Research*, 133(3), pp.271-281.
- Cocks, L.R.M. and Torsvik, T.H., 2007. Siberia, the wandering northern terrane, and its changing geography through the Palaeozoic. *Earth-Science Reviews*, 82(1), pp.29-74.
- Cogné, J.P., Kravchinsky, V.A., Halim, N. and Hankard, F., 2005. Late Jurassic-Early Cretaceous closure of the Mongol-Okhotsk Ocean demonstrated by new Mesozoic palaeomagnetic results from the Trans-Baikal area (SE Siberia). *Geophysical Journal International*, 163(2), pp.813-832.
- Condie, K.C., 2005. TTGs and adakites: are they both slab melts?. *Lithos*, 80(1-4), pp.33-44.
- Cunningham, D., 2013. Mountain building processes in intracontinental oblique deformation belts: Lessons from the Gobi Corridor, Central Asia. *Journal of Structural Geology*, 46, pp.255-282.
- Dash, B., Yin, A., Jiang, N., Tseveendorj, B. and Han, B., 2015. Petrology, structural setting, timing, and geochemistry of Cretaceous volcanic rocks in eastern Mongolia: Constraints on their tectonic origin. *Gondwana Research*, 27(1), pp.281-299.

Davidson, J., Turner, S. and Plank, T., 2012. Dy/Dy*: variations arising from mantle sources and petrogenetic processes. *Journal of Petrology*, 54(3), pp.525-537.

Davis, F.A., Humayun, M., Hirschmann, M.M. and Cooper, R.S., 2013. Experimentally determined mineral/melt partitioning of first-row transition elements (FRTE) during partial melting of peridotite at 3GPa. *Geochimica et Cosmochimica Acta*, 104, pp.232-260.

Davies, J.H. and von Blanckenburg, F., 1995. Slab breakoff: a model of lithosphere detachment and its test in the magmatism and deformation of collisional orogens. *Earth and Planetary Science Letters*, 129(1-4), pp.85-102.

Dawson, J.B. and Hinton, R.W., 2003. Trace-element content and partitioning in calcite, dolomite and apatite in carbonatite, Phalaborwa, South Africa. *Mineralogical Magazine*, 67(5), pp.921-930.

Defant, M.J. and Drummond, M.S., 1990. Derivation of some modern arc magmas by melting of young subducted lithosphere. *nature*, 347(6294), p.662.

Defant, M.J., Jackson, T.E., Drummond, M.S., De Boer, J.Z., Bellon, H., Feigenson, M.D., Maury, R.C. and Stewart, R.H., 1992. The geochemistry of young volcanism throughout western Panama and southeastern Costa Rica: an overview. *Journal of the Geological Society*, 149(4), pp.569-579.

DEFANT, M.J., RICHERSON, P.M., DE BOER, J.Z., STEWART, R.H., MAURY, R.C., BELLON, H., DRUMMOND, M.S., FEIGENSON, M.D. and JACKSON, T.E., 1991. Dacite genesis via both slab melting and differentiation: petrogenesis of La Yeguada volcanic complex, Panama. *Journal of Petrology*, 32(6), pp.1101-1142.

DePaolo, D.J., 1981. Trace element and isotopic effects of combined wallrock assimilation and fractional crystallisation. *Earth and planetary science letters*, 53(2), pp.189-202.

DeVor, Richard E., Tsong-how Chang, and John W. Sutherland. *Statistical quality design and control: contemporary concepts and methods*. New York: Macmillan, 1992.

Donskaya, T.V., Gladkochub, D.P., Mazukabzov, A.M., De Waele, B. and Presnyakov, S.L., 2012. The Late Triassic Kataev volcanoplutonic association in western Transbaikalia, a fragment of the active continental margin of the Mongol-Okhotsk Ocean. *Russian Geology and Geophysics*, 53(1), pp.22-36.

Donskaya, T.V., Windley, B.F., Mazukabzov, A.M., Kröner, A., Sklyarov, E.V., Gladkochub, D.P., Ponomarchuk, V.A., Badarch, G., Reichow, M.K. and Hegner, E., 2008. Age and evolution of late Mesozoic metamorphic core complexes in southern Siberia and northern Mongolia. *Journal of the Geological Society*, 165(1), pp.405-421.

Dostal, J. and Chatterjee, A.K., 2000. Contrasting behaviour of Nb/Ta and Zr/Hf ratios in a peraluminous granitic pluton (Nova Scotia, Canada). *Chemical Geology*, 163(1-4), pp.207-218.

Dupuy, C., Liotard, J.M. and Dostal, J., 1992. Zr/Hf fractionation in intraplate basaltic rocks: carbonate metasomatism in the mantle source. *Geochimica et Cosmochimica Acta*, 56(6), pp.2417-2423.

Enkhtuvshin, H., U. Sawada, T. Eetaya, S. Eezumee, 1995. A petrological study on the late Mesozoic and Cenozoic volcanic rocks of the Mongolian Plateau. *Problems of Geology and Palaeontology of Mongolia*, 75-77.

Eizenhöfer, P.R., Zhao, G., Zhang, J. and Sun, M., 2014. Final closure of the Palaeo-Asian Ocean along the Solonker suture zone: Constraints from geochronological and geochemical data of Permian volcanic and sedimentary rocks. *Tectonics*, 33(4), pp.441-463.

Fan, W. M., Guo, F., Wang, Y. J., & Lin, G. (2003). Late Mesozoic calc-alkaline volcanism of post-orogenic extension in the northern Da Hinggan Mountains, northeastern China. *Journal of volcanology and geothermal research*, 121(1), 115-135.

- Fan, W.M., Guo, F., Wang, Y.J. and Zhang, M., 2004. Late Mesozoic volcanism in the northern Huaiyang tectono-magmatic belt, central China: partial melts from a lithospheric mantle with subducted continental crust relicts beneath the Dabie orogen?. *Chemical Geology*, 209(1), pp.27-48.
- Fitton, J.G., James, D. and Leeman, W.P., 1991. Basic magmatism associated with late Cenozoic extension in the western United States: Compositional variations in space and time. *Journal of geophysical Research: Solid earth*, 96(B8), pp.13693-13711.
- Foley, S.F., Barth, M.G. and Jenner, G.A., 2000. Rutile/melt partition coefficients for trace elements and an assessment of the influence of rutile on the trace element characteristics of subduction zone magmas. *Geochimica et Cosmochimica Acta*, 64(5), pp.933-938.
- Foley, S., Tiepolo, M. and Vannucci, R., 2002. Growth of early continental crust controlled by melting of amphibolite in subduction zones. *Nature*, 417(6891), p.837.
- Foulger, G.R., 2011. *Plates vs plumes: a geological controversy*. John Wiley & Sons.
- Fritzell, E.H., Bull, A.L. and Shephard, G.E., 2016. Closure of the Mongol–Okhotsk Ocean: insights from seismic tomography and numerical modelling. *Earth and Planetary Science Letters*, 445, pp.1-12.
- Fujimaki, H., 1986. Partition coefficients of Hf, Zr, and REE between zircon, apatite, and liquid. *Contributions to Mineralogy and Petrology*, 94(1), pp.42-45.
- Gale, A., Dalton, C.A., Langmuir, C.H., Su, Y. and Schilling, J.G., 2013. The mean composition of ocean ridge basalts. *Geochemistry, Geophysics, Geosystems*, 14(3), pp.489-518.
- Gao, S., Luo, T.C., Zhang, B.R., Zhang, H.F., Han, Y.W., Zhao, Z.D. and Hu, Y.K., 1998. Chemical composition of the continental crust as revealed by studies in East China. *Geochimica et Cosmochimica Acta*, 62(11), pp.1959-1975.
- Gao, S., Rudnick, R.L., Carlson, R.W., McDonough, W.F. and Liu, Y.S., 2002. Re–Os evidence for replacement of ancient mantle lithosphere beneath the North China craton. *Earth and Planetary Science Letters*, 198(3), pp.307-322.
- Gao, S., Rudnick, R.L., Yuan, H.L., Liu, X.M., Liu, Y.S., Xu, W.L., Ling, W.L., Ayers, J., Wang, X.C. and Wang, Q.H., 2004. Recycling lower continental crust in the North China craton. *Nature*, 432(7019), pp.892-897.
- Gao, S., Rudnick, R.L., Xu, W.L., Yuan, H.L., Liu, Y.S., Walker, R.J., Puchtel, I.S., Liu, X., Huang, H., Wang, X.R. and Yang, J., 2008. Recycling deep cratonic lithosphere and generation of intraplate magmatism in the North China Craton. *Earth and Planetary Science Letters*, 270(1), pp.41-53.
- Ge, W.C., 2005. Zircon U-Pb ages and its significance of the Mesozoic granites in the Wulanhao region, central Da Hinggan Mountain. *Acta Petrologica Sinica*, 21, pp.749-762.
- Graham, S.A., Cope, T., Johnson, C.L. and Ritts, B., 2012. Sedimentary basins of the late Mesozoic extensional domain of China and Mongolia. In *Regional geology and tectonics: Phanerozoic rift systems and sedimentary basins*. Elsevier Inc..
- Graham, S.A., Hendrix, M.S., Johnson, C.L., Badamgarav, D., Badarch, G., Amory, J., Porter, M., Barsbold, R., Webb, L.E. and Hacker, B.R., 2001. Sedimentary record and tectonic implications of Mesozoic rifting in southeast Mongolia. *Geological Society of America Bulletin*, 113(12), pp.1560-1579.
- Green, T.H., Blundy, J.D., Adam, J. and Yaxley, G.M., 2000. SIMS determination of trace element partition coefficients between garnet, clinopyroxene and hydrous basaltic liquids at 2–7.5 GPa and 1080–1200 C. *Lithos*, 53(3), pp.165-187.

- Guo, F., Fan, W., Li, C., Gao, X. and Miao, L., 2009. Early Cretaceous highly positive ϵNd felsic volcanic rocks from the Hinggan Mountains, NE China: origin and implications for Phanerozoic crustal growth. *International Journal of Earth Sciences*, 98(6), pp.1395-1411.
- Guo, X.Y., Zhang, H.Y., Wang, Y.Q., He, H.S., Wu, Z.F., Jin, Y.H., Zhang, Z.X. and Zhao, J.J., 2018. Comparison of the spatio-temporal dynamics of vegetation between the Changbai Mountains of eastern Eurasia and the Appalachian Mountains of eastern North America. *Journal of Mountain Science*, 15(1), pp.1-12.
- Halim, N., Kravchinsky, V., Gilder, S., Cogné, J.P., Alexyutin, M., Sorokin, A., Courtillot, V. and Chen, Y., 1998. A palaeomagnetic study from the Mongol–Okhotsk region: rotated Early Cretaceous volcanics and remagnetized Mesozoic sediments. *Earth and Planetary Science Letters*, 159(3), pp.133-145.
- Hansen, J., Skjerlie, K.P., Pedersen, R.B. and De La Rosa, J., 2002. Crustal melting in the lower parts of island arcs: an example from the Bremanger Granitoid Complex, west Norwegian Caledonides. *Contributions to Mineralogy and Petrology*, 143(3), pp.316-335.
- Hao, F., Zou, H., Gong, Z., Yang, S. and Zeng, Z., 2007. Hierarchies of overpressure retardation of organic matter maturation: Case studies from petroleum basins in China. *AAPG bulletin*, 91(10), pp.1467-1498.
- Hastie, A.R., Kerr, A.C., Pearce, J.A. and Mitchell, S.F., 2007. Classification of altered volcanic island arc rocks using immobile trace elements: development of the Th–Co discrimination diagram. *Journal of petrology*, 48(12), pp.2341-2357.
- Hauri, E.H., 1996. Major-element variability in the Hawaiian mantle plume. *Nature*, 382(6590), p.415.
- Hawkesworth, C., Turner, S., Gallagher, K., Hunter, A., Bradshaw, T. and Rogers, N., 1995. Calc-alkaline magmatism, lithospheric thinning and extension in the Basin and Range. *Journal of Geophysical Research: Solid Earth*, 100(B6), pp.10271-10286.
- He, L., 2014. Numerical modeling of convective erosion and peridotite-melt interaction in big mantle wedge: Implications for the destruction of the North China Craton. *Journal of Geophysical Research: Solid Earth*, 119(4), pp.3662-3677.
- He, L., 2015. Thermal regime of the North China Craton: Implications for craton destruction. *Earth-Science Reviews*, 140, pp.14-26.
- Hendrix, M.S., Graham, S.A., Amory, J.Y. and Badarch, G., 1996. Noyon Uul syncline, southern Mongolia: Lower Mesozoic sedimentary record of the tectonic amalgamation of central Asia. *Geological Society of America Bulletin*, 108(10), pp.1256-1274.
- Herzberg, C., 2006. Petrology and thermal structure of the Hawaiian plume from Mauna Kea volcano. *Nature*, 444(7119), p.605.
- Herzberg, C., Cabral, R.A., Jackson, M.G., Vidito, C., Day, J.M.D. and Hauri, E.H., 2014. Phantom Archean crust in Mangaia hotspot lavas and the meaning of heterogeneous mantle. *Earth and Planetary Science Letters*, 396, pp.97-106.
- Hofmann, A.W., 1988. Chemical differentiation of the Earth: the relationship between mantle, continental crust, and oceanic crust. *Earth and Planetary Science Letters*, 90(3), pp.297-314.
- Ho, K.S., Liu, Y., Chen, J.C., You, C.F. and Yang, H.J., 2011. Geochemical characteristics of Cenozoic Jining basalts of the western North China Craton: evidence for the role of the lower crust, lithosphere, and asthenosphere in petrogenesis. *Terrestrial, Atmospheric and Oceanic Sciences*, 22(1), pp.15-40.
- Huang, J. and Zhao, D., 2006. High-resolution mantle tomography of China and surrounding regions. *Journal of Geophysical Research: Solid Earth*, 111(B9).
- Huang, L., Liu, C.Y. and Kusky, T.M., 2015. Cenozoic evolution of the Tan–Lu Fault Zone (East China)—Constraints from seismic data. *Gondwana Research*, 28(3), pp.1079-1095.

- Huangfu, P., Wang, Y., Cawood, P.A., Li, Z.H., Fan, W. and Gerya, T.V., 2016. Thermo-mechanical controls of flat subduction: insights from numerical modeling. *Gondwana Research*, 40, pp.170-183.
- Hunt, A.C., Parkinson, I.J., Harris, N.B.W., Barry, T.L., Rogers, N.W. and Yondon, M., 2012. Cenozoic volcanism on the Hangai Dome, Central Mongolia: geochemical evidence for changing melt sources and implications for mechanisms of melting. *Journal of Petrology*, 53(9), pp.1913-1942.
- Irvine, T.N.J. and Baragar, W.R.A.F., 1971. A guide to the chemical classification of the common volcanic rocks. *Canadian journal of earth sciences*, 8(5), pp.523-548.
- Jahn, B.M., Capdevila, R., Liu, D., Vernon, A. and Badarch, G., 2004. Sources of Phanerozoic granitoids in the transect Bayanhongor–Ulaan Baatar, Mongolia: geochemical and Nd isotopic evidence, and implications for Phanerozoic crustal growth. *Journal of Asian Earth Sciences*, 23(5), pp.629-653.
- Jian, P., Liu, D., Kröner, A., Windley, B.F., Shi, Y., Zhang, F., Shi, G., Miao, L., Zhang, W., Zhang, Q. and Zhang, L., 2008. Time scale of an early to mid-Palaeozoic orogenic cycle of the long-lived Central Asian Orogenic Belt, Inner Mongolia of China: implications for continental growth. *Lithos*, 101(3-4), pp.233-259.
- Johnson, Cari L., Todd J. Greene, David A. Zinniker, J. Michael Moldowan, Marc S. Hendrix, and Alan R. Carroll. "Geochemical characteristics and correlation of oil and nonmarine source rocks from Mongolia." *AAPG bulletin* 87, no. 5 (2003): 817-846.
- Johnson, J.S., Gibson, S.A., Thompson, R.N. and Nowell, G.M., 2005. Volcanism in the Vitim volcanic field, Siberia: geochemical evidence for a mantle plume beneath the Baikal rift zone. *Journal of Petrology*, 46(7), pp.1309-1344.
- Kamber, B.S. and Collerson, K.D., 2000. Role of 'hidden' deeply subducted slabs in mantle depletion. *Chemical Geology*, 166(3-4), pp.241-254.
- Kay, S.M., Ramos, V.A. and Marquez, M., 1993. Evidence in Cerro Pampa volcanic rocks for slab-melting prior to ridge-trench collision in southern South America. *The journal of Geology*, 101(6), pp.703-714.
- Kedong, T. and Zhuyun, Y., 1993. Regional metamorphism and tectonic evolution of the Inner Mongolian suture zone. *Journal of Metamorphic Geology*, 11(4), pp.511-522.
- Kim, C.B., Turek, A., Chang, H.W., Park, Y.S. and Ahn, K.S., 1999. U-Pb zircon ages for Precambrian and Mesozoic plutonic rocks in the Seoul-Cheongju-Chooncheon area, Gyeonggi massif, Korea. *Geochemical Journal*, 33(6), pp.379-397.
- Kim, K.H., Tanaka, T., Nagao, K. and Jang, S.K., 1999. Nd and Sr isotopes and K-Ar ages of the Ulreungdo alkali volcanic rocks in the East Sea, South Korea. *Geochemical Journal*, 33(5), pp.317-341.
- Kroener, A. and Rojas-Agramonte, Y., 2014. THE ALTAIDS AS SEEN BY EDUARD SUESS, AND PRESENT THINKING ON THE LATE MESOPROTEROZOIC TO PALAEOZOIC EVOLUTION OF CENTRAL ASIA. *Austrian Journal of Earth Sciences*, 107(1).
- Kuang, Y.S., Wei, X., Hong, L.B., Ma, J.L., Pang, C.J., Zhong, Y.T., Zhao, J.X. and Xu, Y.G., 2012. Petrogenetic evaluation of the Laohutai basalts from North China Craton: Melting of a two-component source during lithospheric thinning in the late Cretaceous–early Cenozoic. *Lithos*, 154, pp.68-82.
- Lambart, S., Laporte, D. and Schiano, P., 2013. Markers of the pyroxenite contribution in the major-element compositions of oceanic basalts: Review of the experimental constraints. *Lithos*, 160, pp.14-36.
- Le Roux, V., Lee, C.T. and Turner, S.J., 2010. Zn/Fe systematics in mafic and ultramafic systems: Implications for detecting major element heterogeneities in the Earth's mantle. *Geochimica et Cosmochimica Acta*, 74(9), pp.2779-2796.

- Le Roux, V., Dasgupta, R. and Lee, C.T., 2011. Mineralogical heterogeneities in the Earth's mantle: Constraints from Mn, Co, Ni and Zn partitioning during partial melting. *Earth and Planetary Science Letters*, 307(3), pp.395-408.
- Liang, J. L., X. Ding, X. M. Sun, Z. M. Zhang, H. Zhang, and W. D. Sun. "Nb/Ta fractionation observed in eclogites from the Chinese continental scientific drilling project." *Chemical Geology* 268, no. 1-2 (2009): 27-40.
- Ling, M.X., Wang, F.Y., Ding, X., Zhou, J.B. and Sun, W., 2011. Different origins of adakites from the Dabie Mountains and the Lower Yangtze River Belt, eastern China: geochemical constraints. *International Geology Review*, 53(5-6), pp.727-740.
- Linnen, R.L., 1998. The solubility of Nb-Ta-Zr-Hf-W in granitic melts with Li and Li+ F; constraints for mineralization in rare metal granites and pegmatites. *Economic Geology*, 93(7), pp.1013-1025.
- Liu, H., Li, Y., He, H., Huangfu, P. and Liu, Y., 2018. Two-phase southward subduction of the Mongol-Okhotsk oceanic plate constrained by Permian-Jurassic granitoids in the Erguna and Xing'an massifs (NE China). *Lithos*, 304, pp.347-361.
- Liu, R.X., Chen, W.J., Sun, J.Z. and Li, D.M., 1992. The K-Ar age and tectonic environment of Cenozoic volcanic rock in China. *The age and geochemistry of Cenozoic volcanic rock in China*, pp.1-43.
- Liu, S., Hu, R.Z., Gao, S., Feng, C.X., Zhong, H., Qi, Y., Wang, T., Qi, L. and Feng, G., 2008b. K-Ar ages and geochemical+ Sr-Nd isotopic compositions of adakitic volcanic rocks, western Shandong Province, eastern China: Foundering of the lower continental crust. *International Geology Review*, 50(8), pp.763-779.
- Liu, W., Pan, X.F., Liu, D.Y. and Chen, Z.Y., 2009. Three-step continental-crust growth from subduction accretion and underplating, through intermediary differentiation, to granitoid production. *International Journal of Earth Sciences*, 98(6), pp.1413-1439.
- Liu, W., Siebel, W., Li, X.J. and Pan, X.F., 2005. Petrogenesis of the Linxi granitoids, northern Inner Mongolia of China: constraints on basaltic underplating. *Chemical Geology*, 219(1), pp.5-35.
- Liu, Y., Zong, K., Kelemen, P.B. and Gao, S., 2008a. Geochemistry and magmatic history of eclogites and ultramafic rocks from the Chinese continental scientific drill hole: subduction and ultrahigh-pressure metamorphism of lower crustal cumulates. *Chemical Geology*, 247(1), pp.133-153.
- Liu, S., Hu, R., Gao, S., Feng, C., Qi, Y., Wang, T., Feng, G. and Coulson, I.M., 2008b. U–Pb zircon age, geochemical and Sr–Nd–Pb–Hf isotopic constraints on age and origin of alkaline intrusions and associated mafic dikes from Sulu orogenic belt, Eastern China. *Lithos*, 106(3-4), pp.365-379.
- Liu, W., Pan, X.F., Liu, D.Y. and Chen, Z.Y., 2009. Three-step continental-crust growth from subduction accretion and underplating, through intermediary differentiation, to granitoid production. *International Journal of Earth Sciences*, 98(6), pp.1413-1439.
- Li, H.Y., Xu, Y.G., Ryan, J.G. and Whattam, S.A., 2017. Evolution of the mantle beneath the eastern North China Craton during the Cenozoic: Linking geochemical and geophysical observations. *Journal of Geophysical Research: Solid Earth*, 122(1), pp.224-246.
- Li, X.H., 2000. Cretaceous magmatism and lithospheric extension in Southeast China. *Journal of Asian Earth Sciences*, 18(3), pp.293-305.
- Li, X.H., Chung, S.L., Zhou, H., Lo, C.H., Liu, Y. and Chen, C.H., 2004. Jurassic intraplate magmatism in southern Hunan-eastern Guangxi: $^{40}\text{Ar}/^{39}\text{Ar}$ dating, geochemistry, Sr-Nd isotopes and implications for the tectonic evolution of SE China. *Geological Society, London, Special Publications*, 226(1), pp.193-215.
- Li, X.H., Long, W.G., Li, Q.L., Liu, Y., Zheng, Y.F., Yang, Y.H., Chamberlain, K.R., Wan, D.F., Guo, C.H., Wang, X.C. and Tao, H., 2010. Penglai zircon megacrysts: a potential new working reference material for microbeam determination of Hf–O isotopes and U–Pb age. *Geostandards and Geoanalytical Research*, 34(2), pp.117-134.

- Luhr, J.F., Carmichael, I.S. and Varekamp, J.C., 1984. The 1982 eruptions of El Chichón Volcano, Chiapas, Mexico: mineralogy and petrology of the anhydrite-bearing pumices. *Journal of Volcanology and Geothermal Research*, 23(1-2), pp.69-108.
- Ma, L., Jiang, S.Y., Hofmann, A.W., Dai, B.Z., Hou, M.L., Zhao, K.D., Chen, L.H., Li, J.W. and Jiang, Y.H., 2014. Lithospheric and asthenospheric sources of lamprophyres in the Jiaodong Peninsula: a consequence of rapid lithospheric thinning beneath the North China Craton?. *Geochimica et Cosmochimica Acta*, 124, pp.250-271.
- Ma, L., Jiang, S.Y., Hofmann, A.W., Xu, Y.G., Dai, B.Z. and Hou, M.L., 2016. Rapid lithospheric thinning of the North China Craton: New evidence from Cretaceous mafic dikes in the Jiaodong Peninsula. *Chemical Geology*, 432, pp.1-15.
- Ma, X.H., Chen, B., Lai, Y. and Lu, Y.H., 2009. Petrogenesis and mineralization chronology study on the Aolunhua porphyry Mo deposit, Inner Mongolia, and its geological implications. *Acta Petrologica Sinica*, 25(11), pp.2939-2950.
- Mallik, A. and Dasgupta, R., 2012. Reaction between MORB-eclogite derived melts and fertile peridotite and generation of ocean island basalts. *Earth and Planetary Science Letters*, 329, pp.97-108.
- Matzen, A.K., Baker, M.B., Beckett, J.R. and Stolper, E.M., 2013. The temperature and pressure dependence of nickel partitioning between olivine and silicate melt. *Journal of Petrology*, 54(12), pp.2521-2545.
- Martin, H., Smithies, R.H., Rapp, R., Moyen, J.F. and Champion, D., 2005. An overview of adakite, tonalite–trondhjemite–granodiorite (TTG), and sanukitoid: relationships and some implications for crustal evolution. *Lithos*, 79(1-2), pp.1-24.
- Mayer, B., Jung, S., Romer, R.L., Stracke, A., Haase, K.M. and Garbe-Schönberg, C.D., 2013. Petrogenesis of tertiary hornblende-bearing lavas in the Rhön, Germany. *Journal of Petrology*, 54(10), pp.2095-2123.
- McDonough, W.F. and Sun, S.S., 1995. The composition of the Earth. *Chemical geology*, 120(3-4), pp.223-253.
- McKenzie, D.A.N. and O'Nions, R.K., 1991. Partial melt distributions from inversion of rare earth element concentrations. *Journal of Petrology*, 32(5), pp.1021-1091.
- Meng, Q.R., 2003. What drove late Mesozoic extension of the northern China–Mongolia tract?. *Tectonophysics*, 369(3), pp.155-174.
- Menzies, M.A., Fan, W. and Zhang, M., 1993. Palaeozoic and Cenozoic lithoprobes and the loss of > 120 km of Archaean lithosphere, Sino-Korean craton, China. *Geological Society, London, Special Publications*, 76(1), pp.71-81.
- Menzies, M., Xu, Y., Zhang, H. and Fan, W., 2007. Integration of geology, geophysics and geochemistry: a key to understanding the North China Craton. *Lithos*, 96(1), pp.1-21.
- Morimoto, N., 1988. Nomenclature of pyroxenes. *Mineralogy and Petrology*, 39(1), pp.55-76.
- Moyen, J.F., 2009. High Sr/Y and La/Yb ratios: the meaning of the “adakitic signature”. *Lithos*, 112(3-4), pp.556-574.
- Neumann, H., Mead, J. and Vitaliano, C.J., 1954. Trace element variation during fractional crystallization as calculated from the distribution law. *Geochimica et Cosmochimica Acta*, 6(2-3), pp.90-99.
- Nie, F.J., Sun, Z.J., Li, C., Liu, Y.F., Lu, K.P., Zhang, K. and Liu, Y., 2011. Re–Os isotopic dating of molybdenite separates from Chalukou porphyry Mo polymetallic deposit in Heilongjiang Province. *Mineral Deposits*, 30(5), pp.829-836.
- Nielsen, R.L., Gallahan, W.E. and Newberger, F., 1992. Experimentally determined mineral-melt partition coefficients for Sc, Y and REE for olivine, orthopyroxene, pigeonite, magnetite and ilmenite. *Contributions to Mineralogy and Petrology*, 110(4), pp.488-499.

- Niu, Y., Collerson, K.D., Batiza, R., Wendt, J.I. and Regelous, M., 1999. Origin of enriched-type mid-ocean ridge basalt at ridges far from mantle plumes: The East Pacific Rise at 11 20' N. *Journal of Geophysical Research: Solid Earth*, 104(B4), pp.7067-7087.
- Niu, Y. and O'Hara, M.J., 2007. Global correlations of ocean ridge basalt chemistry with axial depth: a new perspective. *Journal of Petrology*, 49(4), pp.633-664.
- Orolmaa, D., Erdenesaihan, G., Borisenko, A.S., Fedoseev, G.S., Babich, V.V. and Zhmodik, S.M., 2008. Permian-Triassic granitoid magmatism and metallogeny of the Hangayn (central Mongolia). *Russian Geology and Geophysics*, 49(7), pp.534-544.
- Okamura, S., Martynov, Y.A., Furuyama, K. and Nagao, K., 1998. K–Ar ages of the basaltic rocks from Far East Russia: Constraints on the tectono-magmatism associated with the Japan Sea opening. *Island Arc*, 7(1-2), pp.271-282.
- Pearce, J.A., 1983. Role of the sub-continental lithosphere in magma genesis at active continental margins.
- Pei, F.P., Xu, W.L., Wang, Q.H., Wang, D.Y. and Lin, J.Q., 2004. Mesozoic basalt and mineral chemistry of the mantle-derived xenocrysts in Feixian, western Shandong, China: constraints on nature of Mesozoic lithospheric mantle. *Geological Journal of China Universities*, 10(1), pp.88-97.
- Peng, P., Zhai, M., Guo, J., Zhang, H. and Zhang, Y., 2008. Petrogenesis of Triassic post-collisional syenite plutons in the Sino-Korean craton: an example from North Korea. *Geological Magazine*, 145(5), pp.637-647.
- Pouclot, A., Lee, J.S., Vidal, P., Cousens, B. and Bellon, H., 1994. Cretaceous to Cenozoic volcanism in South Korea and in the Sea of Japan: magmatic constraints on the opening of the back-arc basin. *Geological Society, London, Special Publications*, 81(1), pp.169-191.
- Qian, S.P., Ren, Z.Y., Zhang, L., Hong, L.B. and Liu, J.Q., 2015. Chemical and Pb isotope composition of olivine-hosted melt inclusions from the Hannuoba basalts, North China Craton: implications for petrogenesis and mantle source. *Chemical Geology*, 401, pp.111-125.
- Qin, F., 2008. The metallogenic epoch and source of ore-forming materials of the Xiaodonggou porphyry molybdenum deposit, Inner Mongolia. *Geosci. J. Graduate Sch. China Univ. Geosci.*, 22, pp.173-180.
- Raddick, M.J., Parmentier, E.M. and Scheirer, D.S., 2002. Buoyant decompression melting: A possible mechanism for intraplate volcanism. *Journal of Geophysical Research: Solid Earth*, 107(B10).
- Rapp, R.P., Shimizu, N., Norman, M.D. and Applegate, G.S., 1999. Reaction between slab-derived melts and peridotite in the mantle wedge: experimental constraints at 3.8 GPa. *Chemical Geology*, 160(4), pp.335-356.
- Rapp, R.P., Watson, E.B. and Miller, C.F., 1991. Partial melting of amphibolite/eclogite and the origin of Archean trondhjemites and tonalites. *Precambrian Research*, 51(1-4), pp.1-25.
- Rapp, R.P. and Watson, E.B., 1995. Dehydration melting of metabasalt at 8–32 kbar: implications for continental growth and crust-mantle recycling. *Journal of Petrology*, 36(4), pp.891-931.
- Reichow, M.K., Litvinovsky, B.A., Parrish, R.R. and Saunders, A.D., 2010. Multi-stage emplacement of alkaline and peralkaline syenite–granite suites in the Mongolian–Transbaikalian Belt, Russia: evidence from U–Pb geochronology and whole rock geochemistry. *Chemical Geology*, 273(1), pp.120-135.
- Richards, J.P. and Kerrich, R., 2007. Special paper: adakite-like rocks: their diverse origins and questionable role in metallogenesis. *Economic geology*, 102(4), pp.537-576.
- Rudnick, R.L. and Fountain, D.M., 1995. Nature and composition of the continental crust: a lower crustal perspective. *Reviews of geophysics*, 33(3), pp.267-309.
- Rudnick, R.L. and Gao, S., 2003. Composition of the continental crust. *Treatise on geochemistry*, 3, p.659.

- Rudnick, R.L., McDonough, W.F. and Chappell, B.W., 1993. Carbonatite metasomatism in the northern Tanzanian mantle: petrographic and geochemical characteristics. *Earth and Planetary Science Letters*, 114(4), pp.463-475.
- Rushmer, T., 1991. Partial melting of two amphibolites: contrasting experimental results under fluid-absent conditions. *Contributions to Mineralogy and Petrology*, 107(1), pp.41-59.
- Sagong, H., Kwon, S.T., Cheong, C.S. and Choi, S.H., 2001. Geochemical and isotopic studies of the Cretaceous igneous rocks in the Yeongdong Basin, Korea: implications for the origin of magmatism in pull-apart basin. *Geosciences Journal*, 5(3), p.191.
- Sajona, F.G., Bellon, H., Maury, R., Pubellier, M., Cotten, J. and Rangin, C., 1994. Magmatic response to abrupt changes in geodynamic settings: Pliocene—Quaternary calc-alkaline and Nb-enriched lavas from Mindanao (Philippines). *Tectonophysics*, 237(1-2), pp.47-72.
- Samoylov, V.S., and M.M. Arkelyants, 1989. The late Mesozoic magmatism of the Gobi Altai region and its structural position. *Geotectonics* 23, 268-275.
- Schilling, J.G., 1973. Iceland mantle plume: geochemical study of Reykjanes Ridge. *Nature*, 242(5400), p.565.
- Sengör, A.C. and Natal'in, B.A., 1996. Turcic-type orogeny and its role in the making of the continental crust. *Annual Review of Earth and Planetary Sciences*, 24(1), pp.263-337.
- Sen, C. and Dunn, T., 1994. Dehydration melting of a basaltic composition amphibolite at 1.5 and 2.0 GPa: implications for the origin of adakites. *Contributions to Mineralogy and Petrology*, 117(4), pp.394-409.
- Sheldrick, T.C., Barry, T.L., Van Hinsbergen, D.J. and Kempton, P.D., 2018. Constraining lithospheric removal and asthenospheric input to melts in Central Asia: A geochemical study of Triassic to Cretaceous magmatic rocks in the Gobi Altai (Mongolia). *Lithos*, 296, pp.297-315.
- Stern, C.R. and Kilian, R., 1996. Role of the subducted slab, mantle wedge and continental crust in the generation of adakites from the Andean Austral Volcanic Zone. *Contributions to mineralogy and petrology*, 123(3), pp.263-281.
- Sturm, R., 2002. PX-NOM—an interactive spreadsheet program for the computation of pyroxene analyses derived from the electron microprobe. *Computers & Geosciences*, 28(4), pp.473-483.
- Sun, S.S. and McDonough, W.S., 1989. Chemical and isotopic systematics of oceanic basalts: implications for mantle composition and processes. *Geological Society, London, Special Publications*, 42(1), pp.313-345.
- Smith, D.J., 2014. Clinopyroxene precursors to amphibole sponge in arc crust. *Nature Communications*, 5, p.4329.
- Tang, Y.J., Zhang, H.F. and Ying, J.F., 2006. Asthenosphere—lithospheric mantle interaction in an extensional regime: implication from the geochemistry of Cenozoic basalts from Taihang Mountains, North China Craton. *Chemical Geology*, 233(3), pp.309-327.
- Taylor, S.R. and McLennan, S.M., 1985. The continental crust: Its evolution and composition. *London: Blackwell*.
- Tran, T.H., Polyakov, G.V., Tran, T.A., Borisenko, A.S., Izokh, A.E., Balykin, P.A., Ngo, T.P. and Pham, T.D., 2016. *Intraplate magmatism and metallogeny of North Vietnam*. Springer International Publishing.
- Tomurtogoo, O., Windley, B.F., Kröner, A., Badarch, G. and Liu, D.Y., 2005. Zircon age and occurrence of the Adaatsag ophiolite and Muron shear zone, central Mongolia: constraints on the evolution of the Mongol—Okhotsk ocean, suture and orogen. *Journal of the Geological Society*, 162(1), pp.125-134.
- Tuff, J. and Gibson, S.A., 2007. Trace-element partitioning between garnet, clinopyroxene and Fe-rich picritic melts at 3 to 7 GPa. *Contributions to Mineralogy and Petrology*, 153(4), pp.369-387.

- Van der Voo, R., van Hinsbergen, D.J., Domeier, M., Spakman, W. and Torsvik, T.H., 2015. Latest Jurassic–earliest Cretaceous closure of the Mongol–Okhotsk Ocean: A palaeomagnetic and seismological-tomographic analysis. *Geological Society of America Special Papers*, 513, pp.589–606.
- Van Hinsbergen, D.J., Cunningham, D., Straathof, G.B., Ganerød, M., Hendriks, B.W. and Dijkstra, A.H., 2015. Triassic to Cenozoic multi-stage intra-plate deformation focused near the Bogd Fault system, Gobi Altai, Mongolia. *Geoscience Frontiers*, 6(5), pp.723–740.
- Vervoort, J.D., Patchett, P.J., Blichert-Toft, J. and Albarède, F., 1999. Relationships between Lu–Hf and Sm–Nd isotopic systems in the global sedimentary system. *Earth and Planetary Science Letters*, 168(1), pp.79–99.
- Vorontsov, A.A., Yarmolyuk, V.V., Lykhin, D.A., Dril, S.I., Tatarnikov, S.A. and Sandimirova, G.P., 2007A. Magmatic sources and geodynamics of the early Mesozoic Northern Mongolia–Western Transbaikalia rift zone. *Petrology*, 15(1), pp.35–57.
- Vorontsov, A.A. and Yarmolyuk, V.V., 2007B. The evolution of volcanism in the Tugnuï-Khilok sector of the western Transbaikalia rift area in the Late Mesozoic and Cenozoic. *Journal of Volcanology and Seismology*, 1(4), pp.213–236.
- Wang, F., Zhou, X.H., Zhang, L.C., Ying, J.F., Zhang, Y.T., Wu, F.Y. and Zhu, R.X., 2006a. Late Mesozoic volcanism in the Great Xing'an Range (NE China): timing and implications for the dynamic setting of NE Asia. *Earth and Planetary Science Letters*, 251(1), pp.179–198.
- Wang, H., Xu, Z., Lu, X., Fu, B., Lu, J., Yang, X. and Zhao, Z., 2016b. Two-types of Early Cretaceous adakitic porphyries from the Luxi terrane, eastern North China Block: Melting of subducted Palaeo-Pacific slab and delaminated newly underplated lower crust. *Lithos*, 240, pp.140–154.
- Wang, T., Guo, L., Zhang, L., Yang, Q., Zhang, J., Tong, Y. and Ye, K., 2015. Timing and evolution of Jurassic–Cretaceous granitoid magmatism in the Mongol–Okhotsk belt and adjacent areas, NE Asia: Implications for transition from contractional crustal thickening to extensional thinning and geodynamic settings. *Journal of Asian Earth Sciences*, 97, pp.365–392.
- Wang, T., Zheng, Y., Li, T. and Gao, Y., 2004. Mesozoic granitic magmatism in extensional tectonics near the Mongolian border in China and its implications for crustal growth. *Journal of Asian Earth Sciences*, 23(5), pp.715–729.
- Wang, W., Xu, W.L., Ji, W.Q., Yang, D.B. and Pei, F.P., 2006b. Late Mesozoic and Palaeogene basalts and deep-derived xenocrysts in eastern Liaoning province, China: constraints on nature of lithospheric mantle. *Geological Journal of China Universities*, 12(1), pp.30–40.
- Wang, W., Xu, W.L., Wang, D.Y., Ji, W.Q., Yang, D.B. and Pei, F.P., 2007. Caiyuanzi Palaeogene basalts and deep-derived xenocrysts in eastern Liaoning, China: constraints on nature and deep process of the Cenozoic lithospheric mantle. *Journal of Mineralogy and Petrology*, 27(1), pp.63–70.
- Wang, X.A., Xu, Z.Y., Liu, Z.H. and Zhou, K., 2012. Petrogenesis and tectonic setting of the K-feldspar granites in Chaihe area, central Greater Xing'an Range: constraints from petro-geochemistry and zircon U–Pb isotope chronology. *Acta Petrologica Sinica*, 28, pp.2647–55.
- Wang, Y., Zhao, Z.F., Zheng, Y.F. and Zhang, J.J., 2011. Geochemical constraints on the nature of mantle source for Cenozoic continental basalts in east-central China. *Lithos*, 125(3), pp.940–955.
- Watanabe, Y. and Stein, H.J., 2000. Re–Os ages for the Erdenet and Tsagaan Suvarga porphyry Cu–Mo deposits, Mongolia, and tectonic implications. *Economic geology*, 95(7), pp.1537–1542.
- Wilhem, C., Windley, B.F. and Stampfli, G.M., 2012. The Altaids of Central Asia: a tectonic and evolutionary innovative review. *Earth-Science Reviews*, 113(3–4), pp.303–341.
- Winther, K.T., Newton, R.C., 1991. Experimental melting of hydrous low-K tholeiite: evidence on the origin of Archaean cratons. *Bull. Geol. Soc. Denmark* 39, 213–228.

- Winther, K.T., 1996. An experimentally based model for the origin of tonalitic and trondhjemitic melts. *Chemical Geology*, 127(1-3), pp.43-59.
- Winchester, J.A. and Floyd, P.A., 1977. Geochemical discrimination of different magma series and their differentiation products using immobile elements. *Chemical geology*, 20, pp.325-343.
- Windley, B.F., Maruyama, S. and Xiao, W.J., 2010. Delamination/thinning of sub-continental lithospheric mantle under Eastern China: The role of water and multiple subduction. *American Journal of Science*, 310(10), pp.1250-1293.
- Wolf, M.B. and Wyllie, P.J., 1994. Dehydration-melting of amphibolite at 10 kbar: the effects of temperature and time. *Contributions to Mineralogy and Petrology*, 115(4), pp.369-383.
- Wu, H.Y., Zhang, L.C., Zhou, X.H. and Chen, Z.G., 2008. Geochronology and geochemical characteristics of late mesozoic andesites in the Central Da-Hinggan Mountains, and its genesis.
- Wu, G., Chen, Y.J., Zhao, Z.H., Zhao, T.P., Li, Z.T. and Zhang, Z., 2009. Geochemistry, zircon SHRIMP U-Pb age and petrogenesis of the East Luoguhe granites at the northern end of the Great Hinggan Range. *Acta Petrologica Sinica*, 25(2), pp.233-247.
- Wu, L., Kravchinsky, V.A., Gu, Y.J. and Potter, D.K., 2017. Absolute reconstruction of the closing of the Mongol-Okhotsk Ocean in the Mesozoic elucidates the genesis of the slab geometry underneath Eurasia. *Journal of Geophysical Research: Solid Earth*, 122(7), pp.4831-4851.
- Xie, H., Tian, J.C., Wu, L.W., Zhu, Y.T., Wu, C.H., Shen, K., Gu, W.J. and Zhang, F., 2011. Age of ore-forming granites in Aershan area of Inner Mongolia and its significance for prospecting. *Journal of Jilin University (Earth Science Edition)*, 41(5), pp.1432-40.
- Xiong, X.L., Adam, J. and Green, T.H., 2005. Rutile stability and rutile/melt HFSE partitioning during partial melting of hydrous basalt: implications for TTG genesis. *Chemical Geology*, 218(3-4), pp.339-359.
- Xiong, X., Keppler, H., Audéat, A., Ni, H., Sun, W. and Li, Y., 2011. Partitioning of Nb and Ta between rutile and felsic melt and the fractionation of Nb/Ta during partial melting of hydrous metabasalt. *Geochimica et Cosmochimica Acta*, 75(7), pp.1673-1692.
- Xiong, X.L., Li, X.H., Xu, J.F., Li, W.X., Zhao, Z.H., Wang, Q. and Chen, X.M., 2003. Extremely high-Na adakite-like magmas derived from alkali-rich basaltic underplate: the Late Cretaceous Zhantang andesites in the Huichang Basin, SE China. *Geochemical Journal*, 37(2), pp.233-252.
- Xu, J.F., Shinjo, R., Defant, M.J., Wang, Q. and Rapp, R.P., 2002. Origin of Mesozoic adakitic intrusive rocks in the Ningzhen area of east China: Partial melting of delaminated lower continental crust?. *Geology*, 30(12), pp.1111-1114.
- Xu, J.F., Wang, Q. and Yu, X.Y., 2000. Geochemistry of high-Mg andesites and adakitic andesite from the Sanchazi block of the Mian-Lue ophiolitic melange in the Qinling Mountains, central China: evidence of partial melting of the subducted Palaeo-Tethyan crust. *Geochemical Journal*, 34(5), pp.359-377.
- Xu, Z., Zhao, Z.F. and Zheng, Y.F., 2012. Slab–mantle interaction for thinning of cratonic lithospheric mantle in North China: geochemical evidence from Cenozoic continental basalts in central Shandong. *Lithos*, 146, pp.202-217.
- Xu, Z. and Zheng, Y.F., 2017. Continental basalts record the crust-mantle interaction in oceanic subduction channel: A geochemical case study from eastern China. *Journal of Asian Earth Sciences*.
- Yan, C., Sun, Y., Lai, Y. and Ma, X., 2011. LA-ICP-MS zircon U-Pb and molybdenite Re-Os isotope ages and metallogenic geodynamic setting of Banlashan Mo deposit, Inner Mongolia. *Mineral Deposits*, 30(4), pp.616-634.

- Yang, F., Santosh, M. and Kim, S.W., 2018. Mesozoic magmatism in the eastern North China Craton: Insights on tectonic cycles associated with progressive craton destruction. *Gondwana Research*.
- Yan, J., Chen, J.F., Xie, Z., Yang, G., Yu, G. and Qian, H., 2005. Geochemistry of Late Mesozoic basalts from Kedoushan in the Middle and Lower Yangtze regions: Constraints on characteristics and evolution of the lithospheric mantle. *Geochimica*, 34(5), pp.455-469.
- Yang, J.H., Wu, F.Y., Shao, J.A., Wilde, S.A., Xie, L.W. and Liu, X.M., 2006. Constraints on the timing of uplift of the Yanshan Fold and Thrust Belt, North China. *Earth and Planetary Science Letters*, 246(3-4), pp.336-352.
- Yang, J. and Wu, F., 2009. Triassic magmatism and its relation to decratonization in the eastern North China Craton. *Science in China Series D: Earth Sciences*, 52(9), pp.1319-1330.
- Yang, Z.F. and Zhou, J.H., 2013. Can we identify source lithology of basalt?. *Scientific reports*, 3, p.1856.
- Yarmolyuk, V.V., Kovalenko, V.I., Kozakov, I.K., Sal'nikova, E.B., Bibikova, E.V., Kovach, V.P., Kozlovsky, A.M., Kotov, A.B., Lebedev, V.I., Eenjin, G. and Fugzan, M.M., 2008, November. The age of the Khangai batholith and the problem of batholith formation in Central Asia. In *Doklady Earth Sciences* (Vol. 423, No. 1, pp. 1223-1228). MAIK Nauka/Interperiodica.
- Yarmolyuk, V.V., Kovalenko, V.I., Sal'nikova, E.B., Budnikov, S.V., Kovach, V.P., Kotov, A.B. and Ponomarchuk, V.A., 2002. Tectono-magmatic zoning, magma sources, and geodynamics of the Early Mesozoic Mongolia-Transbaikal Province. *Geotectonics*, 36(4), pp.293-311.
- Yarmolyuk, V.V., Kudryashova, E.A., Kozlovsky, A.M., Lebedev, V.A. and Savatenkov, V.M., 2015. Late Mesozoic–Cenozoic intraplate magmatism in Central Asia and its relation with mantle diapirism: Evidence from the South Khangai volcanic region, Mongolia. *Journal of Asian Earth Sciences*, 111, pp.604-623.
- Ying, J.F., Zhou, X.H., Zhang, L.C., Wang, F. and Zhang, Y.T., 2010. Geochronological and geochemical investigation of the late Mesozoic volcanic rocks from the Northern Great Xing'an Range and their tectonic implications. *International Journal of Earth Sciences*, 99(2), pp.357-378.
- Zhang, H.F., Sun, M., Zhou, X.H., Fan, W.M., Zhai, M.G. and Yin, J.F., 2002. Mesozoic lithosphere destruction beneath the North China Craton: evidence from major-, trace-element and Sr-Nd-Pb isotope studies of Fangcheng basalts. *Contributions to Mineralogy and Petrology*, 144(2), pp.241-254.
- Zhang, H.F., Sun, M., Zhou, X.H. and Ying, J.F., 2005. Geochemical constraints on the origin of Mesozoic alkaline intrusive complexes from the North China Craton and tectonic implications. *Lithos*, 81(1-4), pp.297-317.
- Zhang, H. and Zheng, J., 2003. Geochemical characteristics and petrogenesis of Mesozoic basalts from the North China Craton: a case study in Fuxin, Liaoning Province. *Chinese Science Bulletin*, 48(9), pp.924-930.
- Zhang, J.H., Ge, W.C., Wu, F.Y., Wilde, S.A., Yang, J.H. and Liu, X.M., 2008. Large-scale Early Cretaceous volcanic events in the northern Great Xing'an Range, northeastern China. *Lithos*, 102(1), pp.138-157.
- Zhang, K.J., 2014. Genesis of the Late Mesozoic Great Xing'an range Large Igneous Province in eastern central Asia: a Mongol–Okhotsk slab window model. *International Geology Review*, 56(13), pp.1557-1583.
- Zhang, J., Zhang, H.F., Ying, J.F., Tang, Y.J. and Niu, L.F., 2008. Contribution of subducted Pacific slab to Late Cretaceous mafic magmatism in Qingdao region, China: a petrological record. *Island Arc*, 17(2), pp.231-241.
- Zhang, S.H., Zhao, Y., Song, B., Hu, J.M., Liu, S.W., Yang, Y.H., Chen, F.K., Liu, X.M. and Liu, J., 2009. Contrasting Late Carboniferous and Late Permian–Middle Triassic intrusive suites from the northern margin of the North China craton: Geochronology, petrogenesis, and tectonic implications. *Geological Society of America Bulletin*, 121(1-2), pp.181-200.

- Zhang, Y.B., Sun, S.H. and Mao, Q., 2006. Mesozoic O-type adakitic volcanic rocks and its petrogenesis, palaeotectonic dynamic and mineralization significance of the eastern side of southern Da Hinggan, China. *Acta Petrologica Sinica*, 22, pp.2289-2304.
- Zhang, K.J., 2014. Genesis of the Late Mesozoic Great Xing'an range Large Igneous Province in eastern central Asia: a Mongol–Okhotsk slab window model. *International Geology Review*, 56(13), pp.1557-1583.
- Zhenhua, Z., LinSu, L., Yongjun, Y. and Tao, L., 2010. Petrogenesis of the Early Cretaceous A-type granite in the Huanggang Sn-Fe deposit, Inner Mongolia: Constraints from zircon U-Pb dating and geochemistry. *Acta Petrologica Sinica*, 26(12), pp.3521-3537.
- Zhao, Z.H., Xiong, X.L., Wang, Q., Wyman, D.A., Bao, Z.W., Bai, Z.H. and Qiao, Y.L., 2008. Underplating-related adakites in Xinjiang Tianshan, China. *Lithos*, 102(1), pp.374-391.
- Zhao, D., Pirajno, F., Dobretsov, N.L. and Liu, L., 2010. Mantle structure and dynamics under East Russia and adjacent regions. *Russian Geology and Geophysics*, 51(9), pp.925-938.
- Zhou, J.Y., 1998. The bimodal volcanic rocks in the Huichang Basin, Jiangxi Province and their tectonic setting. *Volcanology and Mineral Resources*, 19, pp.12-23.
- Zhang, H., Li, Q., Ye, Z., Gong, C. and Wang, X., 2018. New seismic evidence for continental collision during the assembly of the Central Asian Orogenic Belt. *Journal of Geophysical Research: Solid Earth*.
- Zhang, J., Zhang, H.F., Ying, J.F., Tang, Y.J. and Niu, L.F., 2008. Contribution of subducted Pacific slab to Late Cretaceous mafic magmatism in Qingdao region, China: a petrological record. *Island Arc*, 17(2), pp.231-241.
- Zhang, W.H., Zhang, H.F., Fan, W.M., Han, B.F. and Zhou, M.F., 2012. The genesis of Cenozoic basalts from the Jining area, northern China: Sr–Nd–Pb–Hf isotope evidence. *Journal of Asian Earth Sciences*, 61, pp.128-142.
- Zhao, Y.W., Fan, Q.C., Zou, H. and Li, N., 2014. Geochemistry of Quaternary basaltic lavas from the Nuomin volcanic field, Inner Mongolia: Implications for the origin of potassic volcanic rocks in Northeastern China. *Lithos*, 196, pp.169-180.
- Zhou, Z., Barrett, P.M. and Hilton, J., 2003. An exceptionally preserved Lower Cretaceous ecosystem. *Nature*, 421(6925), pp.807-814.
- Zhou, H.W., Zhong, Z.Q., Ling, W.L., Zhong, G.L. and Xu, Q.D., 1998. Sm-Nd isochron for the amphibolites within Taihua complex from Xiao Qinling area, Western Henan and its geological implications. *Geochimica*, 27(4), pp.367-372
- Zindler, A. and Hart, S., 1986. Chemical geodynamics. *Annual review of earth and planetary sciences*, 14(1), pp.493-571.
- Zonenshain, L.P., 1990. Geology of the USSR: a plate tectonic synthesis. *Geodynamic Monograph*, 21, p.242.
- Zorin, Y.A., 1999. Geodynamics of the western part of the Mongolia–Okhotsk collisional belt, Trans-Baikal region (Russia) and Mongolia. *Tectonophysics*, 306(1), pp.33-56.

Appendix A

Samples and analytical methods (XRF and ICP-MS)

The whole-rock samples were crushed in a fly press and then powdered in an agate Tema swig mill. Careful picking of any amygdales was undertaken to remove any presence in the crushed samples. Major elements were determined on fusion beads made from pre-ignited powders which were fused with lithium metaborate flux (80% Li metaborate and 20% Li tetraborate) in a ratio of 1:5. Then 32mm diameter pressed powdered briquettes (10g mixed with 7% PVA soln, as binding agent) were used to analyse for elements Rb, Ba, Nb, Sr, Zn, Ni, Sc, V, Co, Cr, Zr and Y. The major and trace elements were analysed at the University of Leicester by X-ray fluorescence (XRF) spectrometry using an ARL 8420 wavelength-dispersive system fitted with a Rh anode X-ray tube and a Philips PW1400 spectrometer with a W anode tube.

Th, U, La, Ce, Pb, Pr, Nd, Sm, Hf, Ta, Eu, Gd, Tb, Dy, Ho, Er, Tm, Yb and Lu concentrations were determined by inductively coupled plasma mass spectrometry (ICP-MS) at the University of Leicester. International standards BCR-1 (basalt) and JG-3 (granodiorite), an in-house standard WS1-b (basalt) and blank were analysed with every unknown sample batch (maximum of 16 unknown samples).

Some elements have been analysed by both XRF and ICP-MS techniques and comparisons are made to crosscheck the data. R^2 values have been calculated (Figure 2) for some elements of various concentrations (Ba, Nb, Ce and Nd). Where R^2 calculates the proportion of variance and is the square of r (Pearson product moment correlation coefficient). Where r is:

$$r = \frac{\sum (x - \bar{x})(y - \bar{y})}{\sqrt{\sum (x - \bar{x})^2 \sum (y - \bar{y})^2}}$$

Where x and y are the samples mean average. The coefficient of determination for R^2 ranges from 0

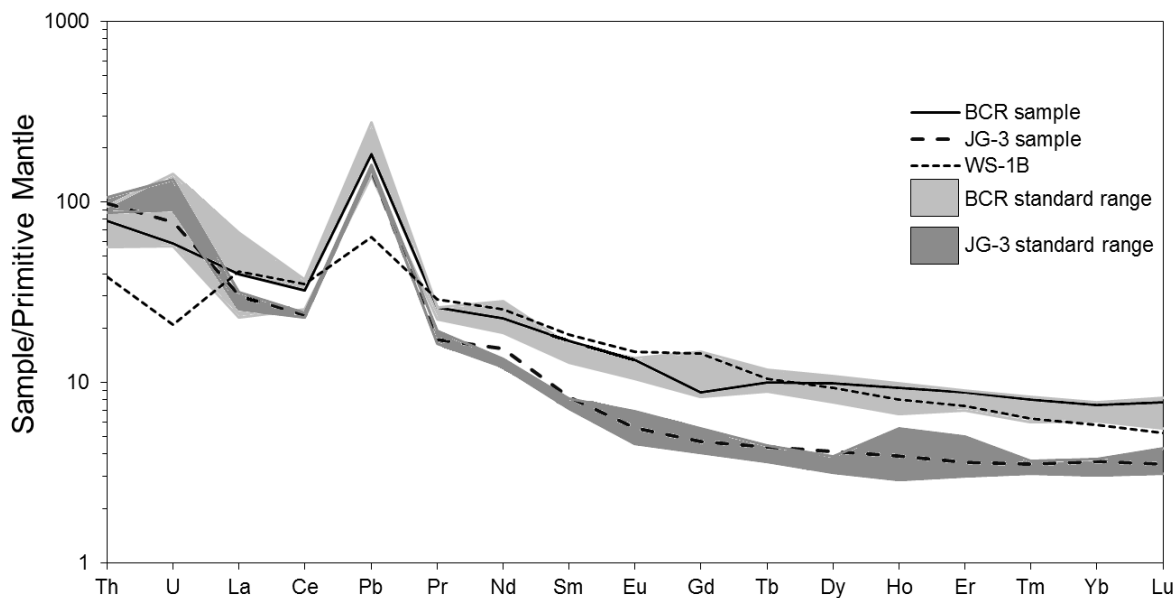


Figure 1: A primitive mantle-normalised trace element variation diagram with the different standards plotted; normalisation values are from Sun and McDonough (1989). The analysed standards are in good agreement with the reference range for these samples.

to 1. Where 0 indicates no relationship and 1 is a perfect relationship. The high R^2 numbers (0.94 to 0.99) indicates a good agreement between the XRF and ICP-MS data.

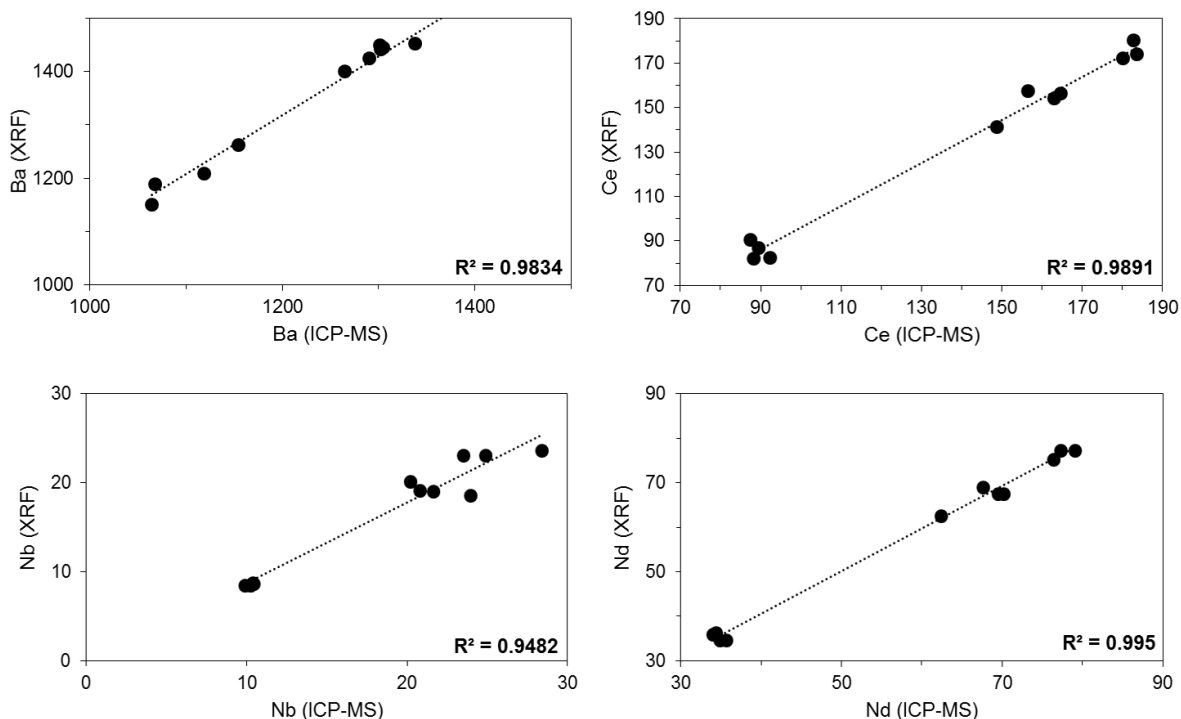


Figure 2: Trace element variation diagrams showing the XRF and ICP-MS data plotted against each other. Calculated R^2 values are also shown on each plot.

Isotope (Sr-Nd-Pb-Hf) preparation:**Dissolution and column chemistry**

150- 200 mg of sample was weighed into 15ml Savillex teflon beakers and leached in 5 mls of 6M HCl at 60°C for 2 hours. After discarding the leachate, the samples were washed and centrifuged twice in mQ water, dried and reweighed. Mixed ^{149}Sm - ^{150}Nd and ^{176}Lu - ^{177}Hf isotope tracers were weighed and added to the samples. 1-2mls of 2x quartz-distilled 16M HNO_3 and 5-6 mls of 29M HF were added, and the sample beakers were left closed on a hotplate at 140°C overnight. After evaporating to dryness, a further 1-2 mls of HNO_3 were added, and the samples were left on the hotplate closed overnight. The samples were then converted to chloride form using 10 mls of 2x quartz-distilled HCl. The samples were then dissolved in c. 2 ml of 1M HCl + 0.1M HF in preparation for column chemistry, and centrifuged.

A second aliquot of sample was weighed into 15ml Savillex beakers, leached and dissolved as above prior to Pb separation and analysis.

Primary column separation

Primary columns consisting of 2 ml of Eichrom AG50x8 cation exchange resin in 10ml Biorad Poly-Prep columns were used to separate bulk high field strength elements (HFSE: Ti, Hf, Zr), a fraction containing Sr, Ca and Rb, and a bulk rare-earth element (REE) fraction.

Samples were loaded onto the columns in c. 1.5 mls of 1M HCl + 0.1M HF, and the HFSE were immediately eluted in 10 mls of 1M HCl + 0.1M HF. This fraction was evaporated to dryness in preparation for separation of Hf (step 4, below). Sr, Ca and Rb were eluted in 30 mls of 1.5M HCl, and evaporated to dryness in preparation for separation of Rb and Sr (Step 5, below). Finally, the REE were eluted in 10 mls of 6M HCl and evaporated to dryness in preparation for separation of Sm, Nd and Lu (Step 6, below).

Separation of Hf

Hafnium separation followed a procedure adapted from Münker et al. (2001). HFSE concentrates from the primary columns were dissolved in c. 2 mls of 6M HCl and loaded onto columns packed with 1 ml of EICHRON LN-SPEC ion exchange resin packed into 10ml Biorad Poly-Prep columns. Matrix elements were eluted in 10-20 mls of 6M HCl, and 2 * 2

mls of milliQ water was then passed through the column to remove HCl from the columns prior to subsequent elution steps involving peroxide (mixing of HCl and peroxide would result in immediate elution of HFSE from the columns). The columns were then washed with several 10ml column volumes of a solution containing citric acid, nitric acid and peroxide. In this medium, titanium citrate complexes show a distinctive bright orange colour, allowing Ti to be quantitatively removed from the column by repeated washing. Once all traces of Ti were removed from the columns, 5mls of peroxide-free citric acid + nitric acid solution were eluted, again in order to avoid mixing of peroxide with HCl solutions. Zr was then washed from the columns using 50-80 ml of 6M HCl + 0.06M Hf. Finally, Hf was collected in 10 mls of 6M HCL + 0.2M HCl.

Separation of Sr

Samples from the primary column separation were dried down and taken up in c. 2 mls of 2.5M HCl and pipetted onto quartz-glass columns containing 4mls of AG50x8 cation exchange resin. Matrix elements were washed off the column using 48 mls of calibrated 2.5M HCl, and discarded. Sr was collected in 12 mls of 2.5M HCl, and evaporated to dryness.

Separation of Sm, Nd and Lu from the bulk REE fraction

Sm and Nd were separated using 2mls of EICHRON LN-SPEC ion exchange resin packed into 10ml Biorad Poly-Prep columns. The bulk REE fraction was dissolved in 200 microlitres of 0.2M HCl and loaded onto the columns. La, Ce and Pr were eluted using a total of 14mls of 0.2M HCl. Nd was collected in 3mls of 0.3M HCl and Sm was collected in 3.5mls of 0.6M HCl. The middle rare-earth elements were eluted in 50 mls of 2.5 M HCl, and finally Lu (+ some residual Yb) was collected in 10 mls of 6M HCl. Sm, Nd and Lu fractions were evaporated to dryness in preparation for mass spectrometry.

Separation of Pb

Dissolved samples for Pb were converted to bromide form using 2 mls of concentrated HBr. Pb was separated using using columns containing 100 microlitres of Dowex AG1x8 anion exchange resin using standard bromide separation methods.

Mass spectrometry

Lu analysis

Lu fractions were dissolved in 1 ml of 2% HNO₃ prior to analysis on a Thermo-Electron Neptune mass spectrometer, using a Cetac Aridus II desolvating nebuliser. 0.006 l/min of nitrogen were introduced via the nebulizer in addition to Ar in order to minimise oxide formation. The instrument was operated in static multicollection mode, with cups set to monitor ¹⁷⁶Er, ¹⁷⁷Er, ¹⁷²Yb, ¹⁷³Yb, ¹⁷⁵Lu, ¹⁷⁶Lu+Hf+Yb, ¹⁷⁷Hf and ¹⁷⁹Hf. Standard sample cones and X-skimmer cones were used, giving a typical signal of c. 600 V/ppm Lu. 1% dilutions of each sample were tested prior to analysis, and samples diluted to c. 20ppb prior to the addition of c. 20ppb of Er. Data reduction followed Lapen et al. 2004, using a ratio of 0.6841 for ¹⁶⁷Er/¹⁶⁶Er to correct ¹⁷⁶Lu/¹⁷⁵Lu for mass fractionation using an exponential law. ¹⁷⁶Yb and ¹⁷⁶Hf interferences on ¹⁷⁶Lu were monitored using ¹⁷³Yb and ¹⁷⁷Hf respectively; ¹⁷⁶Yb/¹⁷³Yb and ¹⁷⁶Hf/¹⁷⁷Hf were corrected for mass bias using ¹⁶⁷Er/¹⁶⁶Er = 0.6841 before interference corrections were made. During the period of analysis, Ames Lu gave a value for ¹⁷⁶Lu/¹⁷⁵Lu of 0.02658 ± 0.00002 (2-sigma, n=59), which lies within analytical uncertainty of the value obtained by Lapen et al. (0.02656 ± 0.00003, 2-sigma).

Hf analysis

Hf fractions were dissolved in 1 ml of 2% HNO₃ + 0.1M HF, prior to analysis on a Thermo-Electron Neptune mass spectrometer, using A Cetac Aridus II desolvating nebuliser. 0.006 l/min of nitrogen were introduced via the nebulizer in addition to Ar in order to minimise oxide formation. The instrument was operated in static multicollection mode, with cups set to monitor ¹⁷²Yb, ¹⁷³Yb, ¹⁷⁵Lu, ¹⁷⁶Lu+Hf+Yb, ¹⁷⁷Hf, ¹⁷⁸Hf, ¹⁷⁹Hf and ¹⁸⁰Hf.

1% dilutions of each sample were tested prior to analysis, and samples diluted to c. 20ppb. Standard sample cones and X-skimmer cones were used, giving a typical signal of c. 800-1000 V/ppm Hf. Correction for ¹⁷⁶Yb on the ¹⁷⁶Hf peak was made using reverse-mass-bias correction of the ¹⁷⁶Yb/¹⁷³Yb ratio empirically derived using Hf mass-bias corrected Yb-doped JMC475 solutions (Nowell and Parrish, 2001). ¹⁷⁶Lu interference on the ¹⁷⁶Hf peak was corrected by using the measured ¹⁷⁵Lu and assuming ¹⁷⁶Lu/¹⁷⁵Lu = 0.02653. The column procedure used to separate Hf effectively removes most Yb and Lu, so these corrections are minimal. Spike-stripping was carried out using an iterative algorithm. Data are reported relative to ¹⁷⁹Hf/¹⁷⁷Hf = 0.7325.

The Hf standard solution JMC475 was analysed during each analytical session and sample $^{176}\text{Hf}/^{177}\text{Hf}$ ratios are reported relative to a value of 0.282160 for this standard (Nowell and Parrish, 2001). Eleven analyses of JMC475 gave a mean $^{176}\text{Hf}/^{177}\text{Hf}$ value of 0.282146 ± 0.000007 (1-sigma). Typical external precision for a single day's analysis was in the range between 13-22 ppm.

Sm analysis

Sm fractions were loaded onto one side of an outgassed double Re filament assembly using dilute (0.6M) HCl, and analysed in a Thermo Scientific Triton mass spectrometer in static collection mode. Replicate analysis of the BCR-2 rock standard across the time of analysis gave a mean Sm concentration of 6.27 ± 0.11 ppm (1-sigma, n=2)

Nd analysis

Nd fractions were loaded onto one side of an outgassed double Re filament assembly using dilute HCl, and analysed in a Thermo Scientific Triton mass spectrometer in multi-dynamic mode. Data are normalised to $^{146}\text{Nd}/^{144}\text{Nd} = 0.7219$. 17 analyses of the JND-i standard gave a value of 0.512104 ± 0.000004 (10.4 ppm, 1-sigma). All other standard and sample data is quoted relative to a value of 0.512115 for this standard. One analyses of the BCR-2 rock standard gave $^{143}\text{Nd}/^{144}\text{Nd} = 0.512634 \pm 0.000004$ (1-sigma).

Sr analysis

Sr fractions were loaded onto outgassed single Re filaments using a TaO activator solution and analysed in a Thermo-Electron Triton mass spectrometer in multi-dynamic mode. Data are normalised to $^{86}\text{Sr}/^{88}\text{Sr} = 0.1194$. 16 analyses of the NBS987 standard gave a value of 0.710260 ± 0.000006 (9 ppm, 1-sigma). Sample data is normalised using a preferred value of 0.710250 for this standard.

Pb analysis

Prior to Pb isotope analysis each sample was spiked with a thallium solution, which was added to allow for the correction of instrument-induced mass bias. Samples were then introduced into a Thermo Scientific Neptune Plus multicollector ICP-MS using an Aridus II desolvating nebuliser. For each sample, five ratios were simultaneously measured ($^{206}\text{Pb}/^{204}\text{Pb}$, $^{207}\text{Pb}/^{204}\text{Pb}$, $^{208}\text{Pb}/^{204}\text{Pb}$, $^{207}\text{Pb}/^{206}\text{Pb}$ and $^{208}\text{Pb}/^{206}\text{Pb}$). Each individual

acquisition consisted of 75 sets of ratios, collected at 5-second integrations, following a 60 second de-focused baseline.

The precision and accuracy of the method was assessed through repeat analysis of an NBS 981 Pb reference solution (also spiked with thallium). The average values obtained for each of the measured NBS 981 ratios were then compared to the known values for this reference material (Thirlwall, 2002). All sample data were subsequently normalised, according to the relative daily deviation of the measured reference value from the true, with the aim of cancelling out the slight daily variations in instrumental accuracy, allowing the direct comparison of the data obtained during different analytical sessions. Internal uncertainties (the reproducibility of the measured ratio) were propagated relative to the external uncertainty.

References

- Nowell, G.M. & Parrish, R.R. (2001) Simultaneous acquisition of isotope compositions and parent/daughter ratios by non-isotope dilution-mode plasma ionisation multi-collector mass spectrometry (PIMMS). *In Plasma Source Mass Spectrometry: The New Millennium* (Holland, G. & Tanner, S.D. eds) *Royal Soc. Chem., Spec. Publ.* **267**, 298-310.
- Lapen, T.J., Mahlen, N.J., Johnson, C.M. & Beard, B.L. (2004) High Precision Lu and Hf isotope analysis of both spiked and unspiked samples: a new approach. *Geochemistry, Geophysics, Geosystems*, **5(1)**, 1-17. doi:10.1029/2003GC000582.
- Münker, C., Weyer, S., Scherer, E., Mezger, K., 2001. Separation of high field strength elements (Nb, Ta, Zr, Hf) and Lu from rock samples for MC-ICPMS measurements. *Geochem. Geophys. Geosyst.* **2**. doi:10.1029/2001GC000183.

Ar-Ar dating preparation:

Sample Preparation

The samples were crushed using a pestle and mortar and the crushate was sieved and washed repeatedly in de-ionised water to remove dust and clay particles from the surfaces of all the size fractions. Using a binocular microscope, the groundmass was picked, selecting pieces free from alteration. The picked separates were cleaned ultrasonically in acetone and de-ionised water, dried using the hot plate, and packaged in aluminium foil packets of ca. 10mm x 10mm in size prior to irradiation.

Irradiation

Samples were irradiated at the McMaster Nuclear Reactor (McMaster University, Canada) for 120 hours. Cadmium shielding was used and the samples were held in position 8D. Neutron flux was monitored using biotite mineral standard GA1550 which has an age of 99.738 ± 0.104 Ma (Renne et al 2011). Standards were packed for irradiation, either side of the unknown samples and analysed using the single grain fusion method using a 1059nm CSI fibre laser and a MAP215-50 mass spectrometer. The J Values were then calculated by linear extrapolation between the 2 measured J values, the values for each sample are shown in the data table (appendix A) and a 1% error on J is used.

Analysis

The irradiated samples were loaded into an ultra-high vacuum system and a 1059nm CSI fibre laser was focussed into the sample chamber and was used to step-heat the samples.

After passing through a liquid nitrogen trap, extracted gases were cleaned for 5 minutes using 2 SAES AP-10 getters, one at 450°C and one at room temperature, following which the gases were let into a Nu Instrumnets mass spectrometer for measurement, the mass discrimination value was measured at 295 for $^{40}\text{Ar}/^{36}\text{Ar}$. System blanks were measured before and after every one or two sample analyses. Gas clean-up and inlet is fully automated, with measurement of ^{40}Ar , ^{39}Ar , ^{38}Ar , ^{37}Ar , and ^{36}Ar , each for ten scans, and the final measurements are extrapolations back to the inlet time.

Data Reduction

The system blanks measured before and after every one or two sample analysis were subtracted from the raw sample data. Results were corrected ^{37}Ar and ^{39}Ar decay, and

neutron-induced interference reactions. The following correction factors were used: $(^{39}\text{Ar}/^{37}\text{Ar})_{\text{Ca}} = 0.00065 \pm 0.00000325$, $(^{36}\text{Ar}/^{37}\text{Ar})_{\text{Ca}} = 0.000265 \pm 0.000001325$, and $(^{40}\text{Ar}/^{39}\text{Ar})_{\text{K}} = 0.0085 \pm 0.0000425$; based on analyses of Ca and K salts. Ages were calculated using the atmospheric $^{40}\text{Ar}/^{36}\text{Ar}$ ratio of 298.56 (Lee et al., 2006) and decay constants of Renne et al., (2011). All data corrections were carried out using an Excel macro and ages were calculated using Isoplot 3 (Ludwig, 2003). All ages are reported at the 2σ level and include a 1% error on the J value.

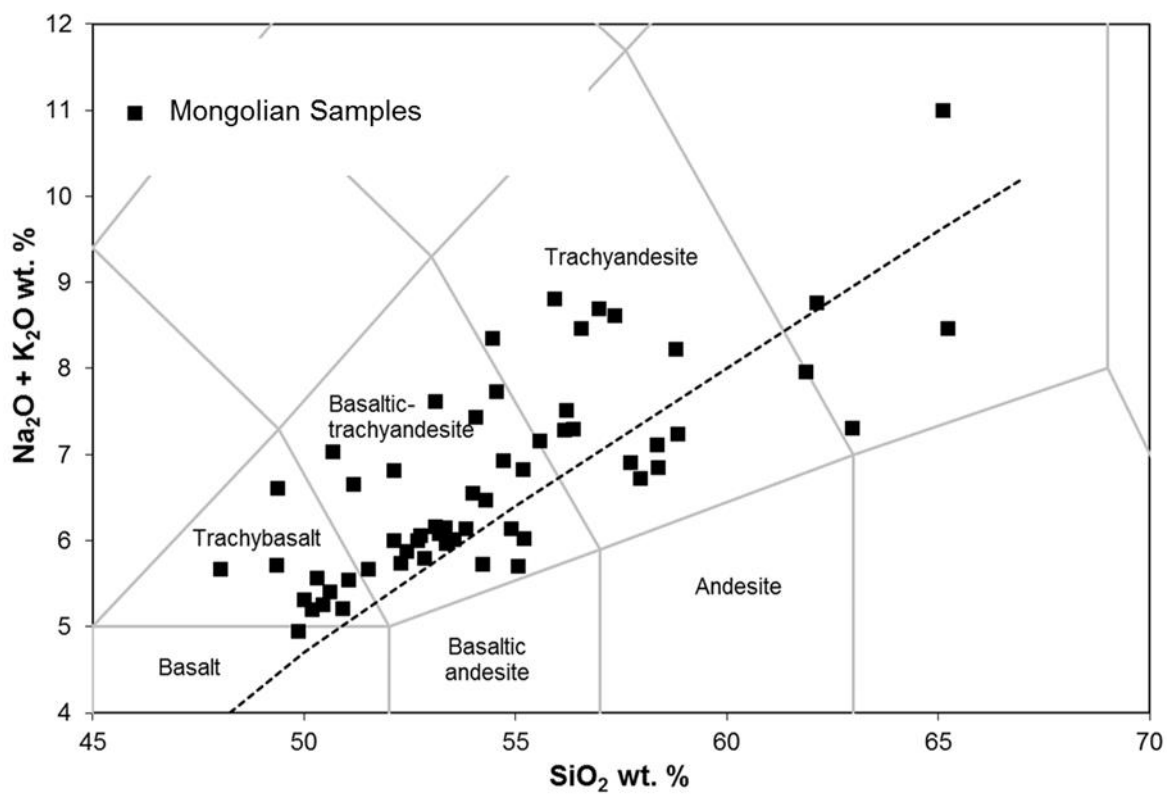
Appendix B: New Mongolian samples plotted on a TAS diagram

Figure 1: A TAS diagram (from Le Bas et al. 1986) plotting the same samples as on the immobile element plot (**Fig. 4.6**).